Universidade do Minho

Escola de Engenharia

Filipa Juliana Fernandes Castro

Process Intensification for the Production of Hydroxyapatite Nanoparticles

Doutoramento em Bioengenharia

Trabalho efetuado sob a orientação de:

Doutor José António Couto Teixeira

Doutor António Augusto Martins de Oliveira Soares Vicente

Abril de 2013

To my parents, for all the encouragement and support

ACKNOWLEDGEMENTS

The achievement of this PhD thesis has been a real challenge and would not have been possible without the help of some people. I had the opportunity to be part of the MIT-Portugal Program and to collaborate with several laboratories (IBB - Institute for Biotechnology and Bioengineering, Centre for Biological Engineering, University of Minho, Braga, Portugal; LEPAE - Laboratory for Process, Environmental and Energy Engineering, Faculty of Engineering of the University of Porto, Porto, Portugal; Jensen Research Group - Department of Chemical Engineering, Massachusetts Institute of Technology, Cambridge, United States of America). The collaboration with these institutions allowed me to deepen my scientific knowledge and feed my taste for research, learning from the best in each research area. It also enabled me to learn new techniques and refine my critical thinking. I had excellent scientific discussions but also made real friends. Therefore I would like to sincerely thank the people who have been part of this journey for their support and dedication over the last four years.

Firstly, I would like to thank my supervisors, Professor José António Teixeira and Professor António Vicente, for their continuous guidance and encouragement throughout the last few years, and for letting me pursue my ideas. They have been inspiring and most supportive at difficult times. Above all, I thank them for allowing me to continue this journey and stimulating my interest in research.

I thank particularly Professor Fernando Rocha and Doctor António Ferreira for accepting and embracing me as part of the great family of LEPAE. I thank them for their orientation, availability, commitment, support, dedication and valuable contributions in guiding this work. Their expertise, availability to discuss ideas and willingness to give of their knowledge were fundamental. I also thank them for their friendship.

I also would like to thank Professor Klavs Jensen and all the members of the Jensen Research Group for my wonderful learning experience. I would like to specially thank Simon Kuhn for his orientation and support in the laboratory, and Baris Unal for many discussions on microfluidics and crystallization, and for carrying out FTIR measurements.

I thank Dr. Speakman, Dr. Shiahn Chen and Patrick Boisvert for supporting me with the X-ray and SEM measurements, and with the interpretation of the results. I am also thankful to Dr Jorge Ferreira from LNEG (Laboratório Nacional de Energia e Geologia, Portugal) for carrying out the X-ray measurements and to Liliana Pereira from the department of Chemical Engineering of FEUP (Faculty of Engineering of the University of Porto) for carrying the Ca/P measurements.

I thank all my lab mates at LEPAE, Berta Estevinho, Cecília Ferreira, Rosa Crespo and Issam Khaddour for sharing with me part of my three wonderful years in this laboratory. I specially thank Cecília and Berta for their valuable cooperation and support. I also thank my lab mates at IBB, namely for material support. I thank all my colleagues from the first year of the doctoral program, particularly Geisa Lopes, Fabiana Fernandes, Silvia Mihaila and Swarna Pandian for sharing with me a wonderful life experience in Cambridge.

Finally, special thanks to my family, especially to my parents for all their love and dedication, and to my grandmother for her affection.

I thank Fernando for his love, friendship and patience, and his unconditional support and help to overcome all my difficulties over the past four years.

This work was supported by the Portuguese Foundation for Science and Technology (SFRH/BD/42992/2008) through the MIT-Portugal Program, Bioengineering Systems Focus Area.

FCT Fundação para a Ciência e a Tecnologia
MINISTÉRIO DA CIÊNCIA, TECNOLOGIA E ENSINO SUPERIOR

ABSTRACT

Precipitation processes are widely used in chemical industry for the production of particulate solids. In these processes, the chemical and physical nature of synthesized particles is of key importance. The traditional stirred tank batch reactors are affected by non-uniform mixing of reactants, often resulting in broad particle size distribution.

The main objective of this thesis was to apply meso and microreactors for the synthesis of hydroxyapatite (HAp) nanoparticles under near-physiological conditions of pH and temperature, in order to overcome the limitations associated with stirred tank batch reactors. Meso and microreactors offer unique features in comparison with conventional chemical reactors. Their high surface-to-volume ratio enables enhanced heat and mass transfer, as well as rapid and efficient mixing. In addition to low consumption of reagents, meso and microreactors are usually operated in continuous flow, making them attractive tools for high throughput experimentation.

Precipitation of HAp was first studied in a stirred tank batch reactor, mixing being assured by a novel metal stirrer. HAp was synthetized by mixing diluted aqueous solutions of calcium hydroxide and orthophosphoric acid at 37 °C. After process optimization, a suspension of HAp nanoparticles with pH close to 7 was obtained for a mixing molar ratio Ca/P=1.33. The precipitation process was characterized by three stages: precipitation of amorphous calcium phosphate, transformation of amorphous calcium phosphate into HAp and growth of HAp crystals. The reaction system was further characterized based on equilibrium equations. The resolution of the system, which was possible with the knowledge of three process variables (temperature, pH and calcium concentration), allowed identifying and quantifying all the chemical species present in solution. The proposed model was validated by comparing the experimental and theoretical conductivity.

Precipitation of HAp was then investigated in a meso oscillatory flow reactor (meso-OFR). The mesoreactor was first operated batchwise in a vertical tube and experiments were performed under the same conditions of temperature, reactants concentration and power density applied in the stirred tank batch reactor. Despite hydrodynamic conditions being not directly comparable, it was possible to assess the effectiveness of both reactors in terms of

mixing and quality of the precipitated particles. The experimental results show the advantages of the meso-OFR over the stirred tank due to the production, about four times faster, of smaller and more uniform HAp nanoparticles. Afterwards, continuous-flow precipitation of HAp was carried out in one meso-OFR and in a series of eight meso-OFRs. Experiments were carried out using fixed frequency (f) and amplitude (x_0), varying only the residence time. HAp nanoparticles were successfully obtained in both systems, mean particle size and aggregation degree of the prepared HAp particles decreasing with decreasing residence time.

In the present work continuous-flow precipitation of HAp was also investigated in two ultrasonic microreactors. Initially, the process was carried out in a tubular microreactor immersed in an ultrasonic bath, where single-phase (laminar) and gas-liquid flow experiments were both performed. Continuous-flow precipitation of HAp in single-phase flow was then done in a Teflon microreactor with integrated piezoelectric actuator. Rod-like shape HAp nanoparticles were yielded in both reactors under near-physiological conditions of pH and temperature. Further, particles showed improved characteristics, namely in terms of size, shape, particle aggregation and crystallinity.

In summary, scale-down of the HAp precipitation process has resulted in the formation of HAp nanoparticles with improved characteristics when compared with HAp particles prepared in a stirred tank batch reactor. Therefore, we believe that the work developed can be a useful contribution to the development of a platform for the continuous production of high quality HAp nanoparticles.

RESUMO

Os processos de precipitação são amplamente usados na indústria química para a produção de partículas sólidas. Neste tipo de processo, a natureza química e física das partículas sintetizadas é fundamental. Os tradicionais reatores descontínuos tipo tanque agitado apresentam problemas na homogeneização da mistura dos reagentes, resultando geralmente numa larga distribuição de tamanho de partículas.

O principal objetivo desta tese consistiu no uso de meso e microreatores na síntese de nanopartículas de hidroxiapatite (HAp) sob condições próximas das condições fisiológicas de pH e temperatura, de forma a ultrapassar as limitações associadas aos reatores descontínuos tipo tanque agitado. Os meso e microreatores possuem características únicas em comparação com os reatores químicos convencionais. A sua elevada razão superfície/volume possibilita uma melhor transferência de calor e massa, assim como uma mistura rápida e eficiente. Para além do baixo consumo de reagentes, os meso e microreatores são geralmente operados em fluxo contínuo, tornando-os uma ferramenta atrativa para a experimentação de alto rendimento.

Em primeiro lugar, a precipitação de HAp foi estudada num reator descontínuo tipo tanque agitado, sendo a mistura assegurada por um novo agitador de metal. A HAp foi sintetizada a 37 ° C, a partir da mistura de soluções aquosas diluídas de hidróxido de cálcio e de ácido ortofosfórico. Após a otimização do processo, uma suspensão de nanopartículas de HAp com um pH próximo de 7 foi obtida para uma razão molar Ca/P inicial de 1.33. O processo de precipitação foi caracterizado por três fases: a precipitação de fosfato de cálcio amorfo, a transformação de fosfato de cálcio amorfo em HAp e crescimento de cristais de HAp. O sistema reacional foi caracterizado recorrendo a equações de equilíbrio. A resolução numérica do sistema foi possível com o conhecimento de três variáveis de processo (temperatura, pH e concentração de cálcio) possibilitando, deste modo, a identificação e quantificação de todas as espécies químicas presentes em solução. O modelo proposto foi validado comparando os valores de condutividade experimental e teórico.

De seguida, investigou-se a precipitação de HAp num mesoreator de fluxo oscilatório (meso-OFR). O mesoreator foi primeiramente operado em descontínuo num tubo vertical sob as

mesmas condições de temperatura, concentração de reagentes e densidade de potência usadas no reator descontínuo tipo tanque agitado. Apesar das condições hidrodinâmicas não serem diretamente comparáveis, foi possível avaliar a eficácia de ambos os reatores em termos de mistura e qualidade das partículas precipitadas. Segundo os resultados experimentais, as nanopartículas de HAp são menores e mais uniformes quando obtidas no meso-OFR, acresce ainda o facto de a sua produção ser quatro vezes mais rápida neste tipo de reator. Posteriormente, a precipitação em contínuo de HAp foi realizada usando um meso-OFR e uma série de oito meso-OFRs. As experiências foram realizadas usando uma frequência (f) e uma amplitude (x_0) fixas, variando apenas o tempo de residência. Nanopartículas de HAp foram obtidas com sucesso em ambos os sistemas, sendo que o tamanho médio e o grau de agregação das partículas de HAp preparadas diminui com a diminuição do tempo de residência.

No decorrer da presente investigação foi tambéem estudada a precipitação em contínuo de HAp usando dois microreatores ultra-sónicos. Inicialmente, realizou-se o processo num microreator tubular imerso num banho de ultra-sons, usando fluxo laminar e segmentado. A precipitação de HAp em fluxo laminar foi posteriormente estudada num microreator de Teflon com um atuador piezoeléctrico integrado. Em ambos os reatores geraram-se nanopartículas de HAp em forma de bastonete, em condições próximas das condições fisiológicas de pH e de temperatura. Além disso, as partículas apresentaram características melhoradas, nomeadamente em termos de tamanho, forma, grau de agregação e cristalinidade.

Em resumo, a redução da escala do processo de precipitação de HAp resultou na formação de nanopartículas de HAp com características melhoradas quando comparadas com as partículas obtidas num reator descontínuo tipo tanque agitado. Desta forma, acreditamos que o trabalho desenvolvido pode ser um importante contributo para o desenvolvimento de uma plataforma para a produção contínua de nanopartículas de HAp de elevada qualidade.

LIST OF PUBLICATIONS

This thesis is based on the work presented in the following publications:

Castro, F., A. Ferreira, F. Rocha, A. Vicente and J.A. Teixeira. 2012. “Characterization of intermediate stages in the precipitation of hydroxyapatite at 37 °C.” *Chemical Engineering Science* 77: 150-156.

Castro, F., S. Kuhn, K. Jensen, A. Ferreira, F. Rocha, A. Vicente and J.A. Teixeira. 2013. “Continuous-flow precipitation of hydroxyapatite in ultrasonic microsystems.” *Chemical Engineering Journal* 215-216: 979-987.

Castro, F., S. Kuhn, K. Jensen, A. Ferreira, F. Rocha, A. Vicente and J.A. Teixeira. 2013. “Process intensification and optimization for hydroxyapatite nanoparticles production.” *Chemical Engineering Science*, In Press.

The following paper has been sent to the AIChE Journal:

Castro F, Ferreira A, Rocha F, Vicente A and Teixeira JA. 2013. “Precipitation of hydroxyapatite at 37 °C in a meso oscillatory flow reactor operated in batch at constant power density.”

The following paper has been sent to Industrial & Engineering Chemistry Research:

Castro, F.; Ferreira, A.; Rocha, F.; Vicente, A.; and Teixeira, J.A. 2013. “Continuous-flow precipitation of hydroxyapatite at 37 °C in a meso oscillatory flow reactor.”

CONTENTS

LIST OF FIGURES

LIST OF TABLES

LIST OF GENERAL NOMENCLATURE

Notation

a – activity

a^* - activity of a saturated solution

A – surface area of the crystal

B - constant of Debye-Huckel (at 37 °C)

c – concentration of the solute in solution

c^* - equilibrium saturation concentration

C_i – concentration of species i, mol.dm^{-3}

Ca/P – calcium to phosphate molar ratio

C_D baffle discharge coefficient

Δc – concentration driving force

$\Delta c/c^*$ - relative supersaturation

d_0 – orifice diameter, m

d_i – internal diameter of the reactor, m

D - diameter of the tube, m

D_0 - diameter of the constriction, m

D_s - diameter of the stirrer, m

D_t - diameter of the tank, m

f - oscillation frequency, Hz

f_c – geometric correction factor

F_1 – blue absorption peak

F_2 – neutral zone absorption

F_1-F_2 – Abs, parameter used for the construction of the calibration curve Abs *versus* pH

g – order of the overall crystal growth process

ΔG – Gibbs free energy

ΔG_{het} – Gibbs free energy of the critical nucleus in the heterogeneous process

$\Delta G_{\underline{hom}}$ – Gibbs free energy of the critical nucleus in the homogeneous process

h - height of the tank, m

J – rate of nuclei formation

k_B – Boltzmann constant

K – conductivity, S.cm^{-1}

K_G – overall crystal growth coefficient

K_{sp} – product solubility

l – baffles spacing

L – crystal size

m – mass of solid deposited in time t

N - speed of the stirrer, s^{-1}

N_B - number of constrictions per unit length, m^{-1}

N_P - power number of the stirrer

P/V - power density, $W.m^{-3}$

r – size of the cluster

r_c – critical size of the cluster

R – gas constant

Re_0 – oscillatory Reynolds number

Re_n – net flow Reynolds number

R_G – linear growth rate

S – fundamental supersaturation/supersaturation ratio

S_t – Strouhal number

T – absolute temperature

x_0 oscillation amplitude, m (center-to-peak)

Greek letters

α - baffle free area ratio

δ – baffle thickness

λ_i – molar ionic conductivity of species i, $S.cm^2.mol^{-1}$

ρ - fluid density, $kg.m^{-3}$

Ω – specific volume of a growth unit

σ – supersaturation

σ_{HAp} – supersaturation HAp

τ_i – induction time

θ – diffraction angle, deg.

μ – chemical potential

$\Delta\mu$ – chemical potential difference between the solution phase and the crystalline phase

μ_0 – standard potential

μ_1 – chemical potential of a given substance in solution (state 1)

μ_2 – chemical potential of a given substance in the crystal (state 2)

γ – solid-liquid interfacial energy

ω - oscillation angular frequency, rad.s^{-1}

Abbreviations

ACP – amorphous calcium phosphate

α-TCP – alpha tricalcium phosphate

β-TCP – beta tricalcium phosphate

DCPA – dicalcium phosphate dehydrate

DCPD – dicalcium phosphate anhydrous

EDTA - Ethylenediamine tetraacetic acid

FTIR – Fourier transform infrared spectroscopy

GLF – gas-liquid flow

HAp (or OHAp) – hydroxyapatite

IEP – isoelectric point

OCP – octacalcium phosphate

OFM – oscillatory flow mixing

OFR – oscillatory flow reactor

PI – process intensification

ppm – parts per million

Rpm – rotation per minute

SEM – scanning electron microscopy

SPF – single-phase flow

SPC - smooth periodic constriction

TCA – total calcium in solution

TPO – total phosphate in solution

XRD – X-ray diffraction

1 INTRODUCTION

This chapter presents the topics addressed in this PhD thesis, especially the importance of the unit operation of precipitation in the chemical industry for particulate solids production. A particular emphasis will be done to the hydroxyapatite (HAp) system precipitation. This first approach aims at demonstrating the scientific, technological and economic interests of the topics studied and that motivated the development of this thesis. Finally, the general objectives are listed and a summary of the organization of the thesis is presented, including identification of the general contents of each chapter.

1.1 Crystallization/Precipitation in the chemical industry

Crystallization is one of the oldest chemical engineering operations to have been exploited commercially (Stanley 2006; Söhnel and Garside 1992). In particular, crystallization by precipitation, also defined as reactive crystallization (Demopoulos 2009), where the formation of the solid product is via a chemical reaction, is of considerable industrial importance (Söhnel and Garside 1992). It has been widely used for the formation of particulate solids of magnetic and electronic materials, catalysts, ceramics and pharmaceutical powders (Rodríguez-clemente et al. 1999; Jones et al. 2005; Oliveira 2007; Demopoulos 2009). Precipitation also stands out because of its simplicity, low cost, and easy application in industrial production (Kawase and Miura 2007; Liu et al. 2001; Ying et al. 2008).

However, the science of reactive precipitation still remains poorly understood (Sultana 2010). During reactive precipitation, high levels of supersaturation are generated (Wang and Fox 2003). In this case, fast or very fast chemical reactions and very fast nucleation kinetics are often involved, leading to the simultaneous occurrence of nucleation and growth as well as the presence of secondary processes such as ageing and agglomeration (Söhnel and Garside 1992). Therefore, mixing effects are significant in determining the distribution of supersaturation and subsequently the product properties, namely phase purity, morphology, size, and particle size distribution (Aimable et al. 2011; Stanley 2006; Wang and Fox 2003).

Stirred tank batch reactors are conventionally used for solid particulate synthesis (Khan et al. 2004). Several disadvantages are associated with the implementation of wet chemical synthesis in stirred tank reactors, namely in terms of the reproducibility of the process and product quality. The resulting product often has wide size distribution due to non-uniform reaction conditions in the reactor (Mersmann 1999; Ying et al. 2008). Stirred tank batch reactors are usually characterized by heterogeneous spatial and temporal distributions of process parameters such as temperature and concentration, and thus a variable supersaturation environment (Demopoulos 2009). Those are intrinsically related to mixture quality and intensity achieved in stirred tanks. The problem becomes magnified as the scale of operation increases since the control of mixing is very difficult in large vessels (Jones et al. 2005;

Jongen et al. 2003), and can be particularly pronounced in fast precipitation systems owing to the very fast reaction kinetics (Jones et al. 2005).

1.2 Calcium phosphate system

Calcium phosphates are widely used in biomedical applications, since their chemical composition is roughly equivalent to that of the inorganic matrix of human bone. Among them, special attention has been paid to HAp, $Ca_5(PO_4)_3OH$, due to its exceptional biocompatibility, bioactivity and osteoconductivity (He and Huang 2007). Actually, difficulties have been encountered in producing stoichiometric HAp at body temperature and normal pH, principally nanoparticles with a precise control size (Wang et al. 1998). This can be explained by the complexity of the calcium phosphate system, the structure of HAp particularly prone to ion substitution and the role of kinetic factors, which, depending on the experimental conditions, prevail over thermodynamic factors (Koutsopoulos 2002). One of the most important properties of calcium phosphate salts is solubility. It is solubility that determines the direction of many reactions that involve calcium phosphates, like dissolution, precipitation, hydrolysis and phase transformation. The quantity of calcium phosphates dissolved in a unit volume of solution varies with changes in the synthesis parameters, namely changes in the pH (Chow and Eanes 2001). At body temperature and pH between 4 and 12, HAp is the most stable calcium phosphate salt, this is, the least soluble calcium phosphate salt (Elliot 1994). However, other calcium phosphate phases may form, given that they possess much higher crystallization rate compared to HAp (Oliveira 2007).

1.3 Thesis motivation and aim

The systems available for HAp production at the moment do not guarantee the stoichiometrical equilibrium, mainly due to the way reagents are mixed, leading to hydrodynamic characteristics that impede the creation of optimal conditions for the production of HAp with controlled properties. Even small differences in stoichiometry, morphology or size may affect the chemical, biological and physical behavior of the material (Tadic et al. 2002). This calls for the development of a system that provides an efficient and intense mixing, and in particular micromixing, essential to obtain HAp crystals with specific properties.

Meso and microreactors offer several advantages over traditional stirred tank batch reactors, namely reduced capital, energy costs and exposure to toxic or hazardous materials (Jähnisch et al. 2004), making them interesting tools for high throughput and screening experimentation. Scaled-down reactors present high surface to volume ratio that enhances heat and mass transfer, and vastly improves fluid mixing, allowing a better control over the reaction steps that govern particle size distribution, i.e., nucleation and growth, and thereby improving the monodispersity of synthesized nanoparticles (Jähnisch et al. 2004; Hessel 2009). In that way, scaled-down reactors appear as good candidates to promote ideal conditions for the controllability of HAp particles properties.

The problem addressed in this project is finding out how to obtain HAp crystals with a precise controlled size, a controlled and narrow size distribution and a high purity. HAp particles shall be produced with high specific surface area, narrow crystal size distribution and low concentration of secondary products, providing a matrix with the best conditions for bone related cells growth. Thus, in addition to the main objective stated above, the following specific objectives can be identified:

- Understanding of the HAp precipitation process mechanism;
- Physico-chemical characterization of the HAp precipitation process;
- Adaptation of smaller reaction systems compared to conventional ones for the production of HAp crystals that:
    - minimize mass transfer and hydrodynamics limitations to obtain HAp with high yields;
    - allow better product consistency and reproducibility;
    - reduce energy and operating costs;
    - allow easy scale-up procedures.

1.4 Thesis outline

This thesis is organized in eight chapters. In this first chapter motivation, research aims and thesis outline are described. Chapter 2 presents a summary of the basic principles of the crystallization/precipitation process, and the particular case of the HAp system. It also summarizes the current methods and reactors employed for the production of HAp via precipitation. Furthermore, an overview of the main advantages of miniaturization is outlined. The main experimental results are presented from Chapter 3 to Chapter 7. Chapter 3 presents the study of the HAp precipitation at 37 °C for different mixing Ca/P molar ratios in a stirred tank batch reactor. It describes the process adopted to synthesize HAp via the chemical precipitation technique, by mixing a saturated calcium hydroxide aqueous solution with an orthophosphoric acid aqueous solution. The mechanism of the optimized HAp precipitation process is studied and HAp powders characteristics are compared with a commercial HAp. In Chapter 4, the reaction system of the optimized HAp precipitation process is modeled based on mass balance and equilibrium equations. In the following chapters, the same HAp precipitation system is studied in different scaled-down reactors. Chapter 5 and Chapter 6 explore the feasibility of a meso oscillatory flow reactor (meso-OFR) to improve the precipitation process of HAp, operated in both batch and in continuous modes, respectively. The meso reactor consists in a glass tube provided with smooth periodic cavities, operating under oscillatory flow mixing (OFM), where mixing intensity is controlled by oscillation frequency (f) and amplitude (x_0). Chapter 5 refers to the HAp precipitation process in the mesoreactor operated in batch at constant power density. Experiments were performed under the same conditions of temperature (37 °C), reactants concentration and power density applied in the stirred tank batch reactor studied in Chapter 3. The constant power density applied to both reactors was used as the reference criterion. The effectiveness of both mixing methods for a given power input is investigated in terms of reaction time and characteristics of the precipitated particles. The prepared HAp particles are also compared with a commercial HAp. Concerning Chapter 6, it investigates the continuous-flow HAp precipitation under near-physiological conditions of pH and temperature in the meso-OFR and in the scaled-up meso-OFR, being the throughput of the mesoreactor increased by associating in series eight vertical meso-ORFs. The influence of residence time on HAp particles characteristics is also studied and HAp particles characteristics are compared with HAp particles prepared in the stirred tank batch reactor and in the meso-OFR operated in batch, as well as with a commercial HAp. Chapter 7 shows the ability of two ultrasonic microreactors for continuous-flow HAp precipitation under the same conditions used in the meso-OFR. Precipitation of HAp was first carried out in a tubular microreactor immersed in an ultrasonic bath, where single-phase (laminar) and segmented gas-liquid flow were both evaluated. The single-phase flow study was then conducted in a novel microfluidic device. It consists of a Teflon stack microreactor with an integrated piezoelectric element, thereby allowing the direct transmission of ultrasound to the reactor. HAp particles prepared in this system were compared with HAp particles obtained in the previous reactors studied and a commercial HAp. Finally, Chapter 8 is dedicated to the main conclusions of the thesis, recommendations and suggestions for future work.

1.5 References

Aimable, A., N. Jongen, A. Testino, M. Donnet, J. Lemaître, H. Hofmann, and P. Bowen. 2011. “Precipitation of Nanosized and Nanostructured Powders: Process Intensification and Scale-Out Using a Segmented Flow Tubular Reactor (SFTR).” *Chemical Engineering & Technology* 34 (3): 344–352.

Chow, L.C., and E.D Eanes. 2001. *Octacalcium Phosphate*. Monograph. Basel: Karger.

Demopoulos, G.P. 2009. “Aqueous Precipitation and Crystallization for the Production of Particulate Solids with Desired Properties.” *Hydrometallurgy* 96 (3): 199–214.

Elliot, J.C. 1994. *Structure and Chemistry of the Apatites and Other Calcium Orthophosphates*. Amsterdam: Elsevier.

He, Q. J., and Z. L. Huang. 2007. “Template-directed Growth and Characterization of Flowerlike Porous Carbonated Hydroxyapatite Spheres.” *Crystal Research and Technology* 42 (5): 460–465.

Hessel, V. 2009. “Novel Process Windows - Gate to Maximizing Process Intensification via Flow Chemistry.” *Chemical Engineering & Technology* 32 (11): 1655–1681.

Jones, A., S. Rigopoulos, and R. Zauner. 2005. “Crystallization and Precipitation Engineering.” *Computers & Chemical Engineering* 29 (6): 1159–1166.

Jongen, N., M. Donnet, P. Bowen, J. Lemaître, H. Hofmann, R. Schenk, C. Hofmann, et al. 2003. “Development of a Continuous Segmented Flow Tubular Reactor and the ‘Scale-out’ Concept - In Search of Perfect Powders.” *Chemical Engineering and Technology* 26: 303–305.

Jähnisch, K., V. Hessel, H. Löwe, and M. Baerns. 2004. *Chemistry in Microstructured Reactors. Angewandte Chemie (International Ed. in English)*. Vol. 43.

Khan, S., A. Günther, M. Schmidt, and K. F. Jensen. 2004. “Microfluidic Synthesis of Colloidal Silica.” *Langmuir : the ACS Journal of Surfaces and Colloids* 20 (20): 8604–11.

Koutsopoulos, S. 2002. “Synthesis and Characterization of Hydroxyapatite Crystals: a Review Study on the Analytical Methods.” *Journal of Biomedical Materials Research* 62 (4): 600–12.

Mersmann, A. 1999. “Crystallization and Precipitation.” *Chemical Engineering and Processing: Process Intensification* 38: 345–353.

Oliveira, C. 2007. "Precipitação Do Fosfato Dicálcico : Caracterização Experimental e Modelização". PhD Thesis. Faculty of Engineering of the University of Porto.

Rodríguez-clemente, R., J. Gómez-morales, A. López-macipe, J. García-Carmona, M. Ocaña, and C. J. Serna. 1999. "Solid Particles Formation from Solutions , an Intellectual and Industrial Meeting Point and Challenge." *Contributions to Science* 1 (1): 63–77.

Stanley, S.J. 2006. "Tomographic Imaging During Reactive Precipitation in a Stirred Vessel: Mixing with Chemical Reaction." *Chemical Engineering Science* 61 (24): 7850–7863.

Söhnel, O. and J. Garside. 1992. *Precipitation: Basic Principles and Industrial Applications* Oxford: Butterworth-Heinemann.

Sultana, M. 2010. "Microfluidic Systems for Continuous Crystallization of Small Organic Molecules". PhD Thesis. Massachusetts Institute of Technology .

Tadic, D., F. Peters, and M. Epple. 2002. "Continuous Synthesis of Amorphous Carbonated Apatites." *Biomaterials* 23 (12): 2553–9.

Wang, L., and R. O. Fox. 2003. "Application of in Situ Adaptive Tabulation to CFD Simulation of Nano-particle Formation by Reactive Precipitation." *Chemical Engineering Science* 58 (19): 4387–4401.

Wang, M., R. Joseph, and W. Bonfield. 1998. "Hydroxyapatite-polyethylene Composites for Bone Substitution: Effects of Ceramic Particle Size and Morphology." *Biomaterials* 19 (24): 2357–66.

Ying, Y., G. Chen, Y Zhao, S. Li, and Q. Yuan. 2008. "A High Throughput Methodology for Continuous Preparation of Monodispersed Nanocrystals in Microfluidic Reactors." *Chemical Engineering Journal* 135 (3): 209–215.

Zhao, C.-X., L. He, S. Z. Qiao, and A. P.J. Middelberg. 2011. "Nanoparticle Synthesis in Microreactors." *Chemical Engineering Science* 66 (7): 1463–1479.

2 LITERATURE REVIEW

In this chapter the basic concepts considered to pursuit this doctoral dissertation are reviewed. Firstly, fundamental aspects related to the crystallization/precipitation processes are discussed, namely mechanisms and physical and chemical aspects of precipitation. Then, the target system, HAp, is characterized in terms of its structure, its composition and chemical properties with respect to solubility in aqueous solutions and reactions. Finally, methodologies commonly used for the production of HAp, as well as the current reactors used and their limitations are reviewed.

2.1 Crystallization/Precipitation processes

2.1.1 Definition

Crystallization consists in converting a substance or several substances from amorphous, gaseous or liquid state to crystalline state, being chemical potential difference the driving force of the process (Oliveira 2007). As to the term 'precipitation', it commonly refers to fast crystallization (Mullin 2001) (**Table 2.1**). Sometimes, it also implies an irreversible process, i.e. supersaturation is obtained by a chemical reaction between two soluble components, leading to a very sparingly soluble specie that precipitates directly (Oliveira 2007; Mersmann 1995). Another distinguishing feature of precipitation processes is that they are generally initiated at high supersaturation, resulting in rapid nucleation and growth of solid phases and the consequent creation of large numbers of very small primary crystals (Mullin 2001) (see **Table 2.1**). Finally, precipitation processes, as all crystallization processes, consist of three basic steps (supersaturation, nucleation and growth) usually followed by secondary steps such as ripening, ageing or agglomeration that can cause major changes on the final product (Mullin 2001; Söhnel and Garside 1992).

Table 2.1. Comparison between crystallization and precipitation processes (adapted from Oliveira, 2007).

	Crystallization	**Precipitation**
Definition	Solid phase formation	Fast crystallization
Solubility	Great extent, from medium to high	Low
Achievement of supersaturation	Various ways	Dilution and reaction
Relative supersaturation	Low	High
Product morphology	Well-defined	Not well-defined (generally amorphous material)
Size of the crystalline product	Big	Small
Nucleation mechanism	Secondary	Primary
Nucleation rate	Low	High
Nucleation order	Low	High
Growth rate	Variable in a large range (0.005 – 0.5 μm.s^{-1})	Low (0.005 – 0.05 μm.s^{-1})
Controllability	Controllable	Difficult to control

2.1.2 Modes of crystallization

The driving force for any crystallization/precipitation process is the development of supersaturation (Söhnel and Garside 1992). The main techniques used to achieve supersaturation include changing solution temperature (cooling), evaporation of solvent (evaporation), addition of antisolvent and chemical reaction (reactive crystallization) (Mullin 2001). These processes are described below (Pedrosa 1995; Sultana 2010):

- Cooling: it is commonly used in systems whose solubility increases with rising temperature. The solution temperature is lowered below the saturation temperature for that solution leading to the formation of the solid phase. The end product usually exhibits high purity.

- Evaporation: it is used in systems whose solubility values are not influenced by temperature or whose solubility decreases with increasing former. Supersaturation is achieved by evaporation of the solvent which results in an increase in concentration. This can be done by heating a solution to its boiling point. This technique is slow and has been the first to be applied.
- Addition of antisolvent: a solution of the compound to be crystallized is mixed with an antisolvent. The solubility of the compound is lower in the mixed solvent system compared to that in the original solution and so supersaturation is created. Efficient mixing is essential in this technique, since antisolvent crystallization involves the mixing of a solution with an antisolvent. Another important feature of this method lies on the fact that one can operate at ambient temperature.
- Chemical reaction: supersaturation can be achieved by chemical reaction, by adding one reactant solution to a stirred solution of another. The end product is formed in concentrations exceeding the solubility, i.e. supersaturation is generated, and so precipitation of the desired product occurs. The characteristics of the resulting product depend essentially on the way reactants are mixed.

2.1.3 Crystallization/Precipitation mechanisms

2.1.3.1 Role of supersaturation

A saturated solution is in thermodynamic equilibrium with the solid phase, at a specified temperature. As to the term supersaturation, it refers to a solution that contains more of the dissolved material than could be dissolved by the solvent under normal circumstances (Mullin 2001).

The state of supersaturation is an essential requirement for all crystallization operations (Söhnel and Garside 1992; Mullin 2001; Oliveira 2007; Sultana 2010). The relationship between supersaturation and spontaneous crystallization has been represented on a solubility-supersolubility diagram (**Figure 2.1**).

The diagram (see **Figure 2.1**) can be described in terms of three distinct zones (Mullin 2001):

- the stable zone of an undersaturated solution where no nucleation or crystal growth is possible. Existing crystals will simply dissolve;

- the supersaturated metastable zone where growth may occur but spontaneous nucleation does not, and;
- the labile supersaturated zone of spontaneous and rapid nucleation.

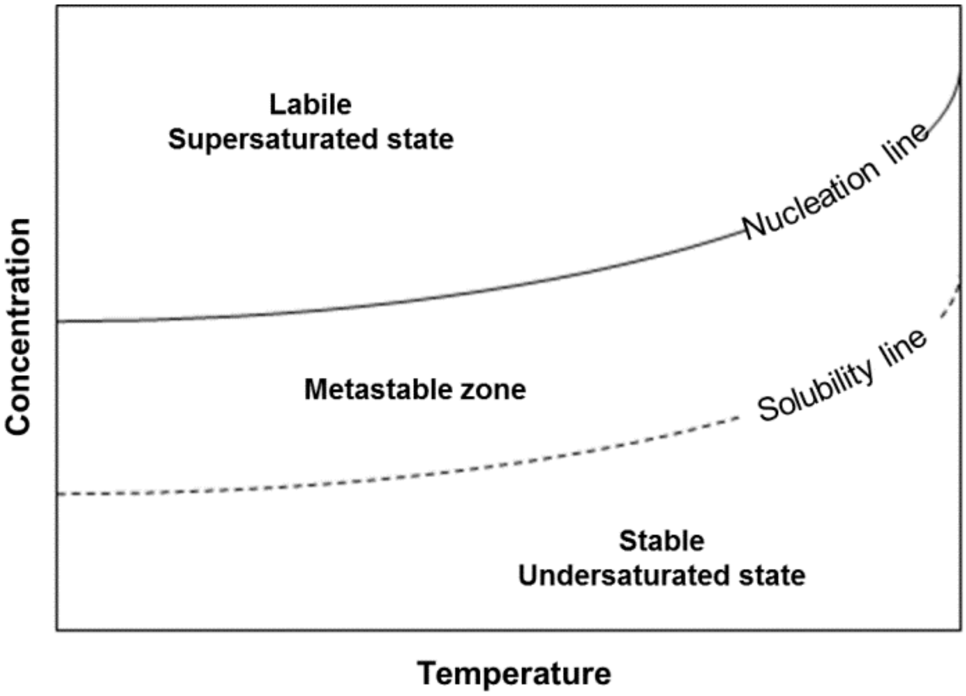

Figure 2.1. The solubility-supersolubility diagram.

In thermodynamic terms, the fundamental driving force for crystallization can be defined as the difference between the chemical potential of the given substance in solution (state 1) and the crystal (state 2) (Mullin 2001):

$$\sigma = \Delta\mu = \mu_1 - \mu_2 \qquad (2.1)$$

writing the chemical potential, μ, in terms of the standard potential, μ_0, and the activity, *a*:

$$\mu = \mu_0 + RT \ln a \qquad (2.2)$$

where *R* is the gas constant and *T* is the absolute temperature.

The fundamental dimensionless driving force for crystallization may therefore be expressed as:

$$\frac{\Delta\mu}{RT} = \ln\left(\frac{a}{a^*}\right) = \ln S \qquad (2.3)$$

where a^* is the activity of a saturated solution and S is the fundamental supersaturation.

Supersaturation, σ, can also be expressed in terms of solution concentrations, since the values of activity are generally not known. Among the most common expressions of supersaturation, σ, are the concentration driving force, Δc, the supersaturation ratio, S, and the relative supersaturation $\Delta c/c^*$:

$$\sigma = \Delta c = c - c^* \qquad (2.4)$$

$$\sigma = S = \frac{c}{c^*} \qquad (2.5)$$

$$\sigma = \frac{\Delta c}{c^*} = S - 1 \qquad (2.6)$$

where c is the concentration of the solute in solution and c^* is the equilibrium saturation concentration at the given temperature.

Supersaturation is the key variable among all the factors that affect crystal nucleation and growth (**Figure 2.2**), directly influencing both physical (crystal size distribution) and chemical (purity) properties of the final products (Söhnel and Garside 1992).

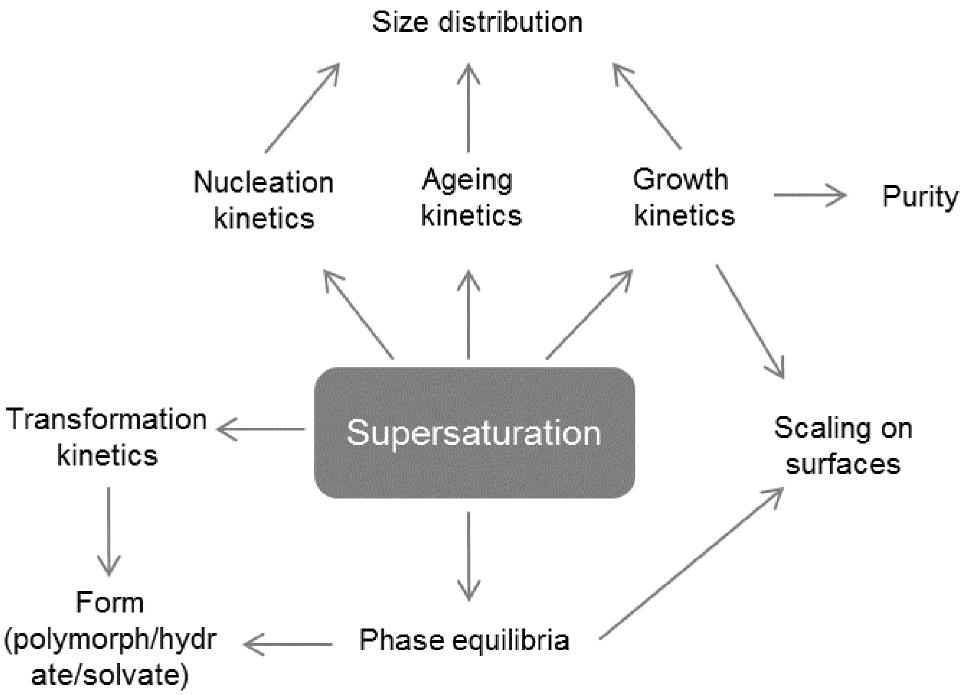

Figure 2.2. The role os supersaturation in precipitation processes (adapted from Söhnel and Garside 1992).

2.1.3.2 Nucleation and crystal growth

In the following paragraph, nucleation and crystal growth are reviewed and treated as independent processes. However, it must be highlighted that both events take place simultaneously during precipitation, at least for a part of the overall process (Söhnel and Garside 1992).

- *Nucleation*

The condition of supersaturation is *per se* not sufficient to initiate crystallization in a given system. Before crystals can develop there must exist in the solution a number of minute solid bodies, known as nuclei, that act as centers of crystallization (Mullin 2001). The conditions that are favorable for nucleus formation, as well as the kinetics of their formation, are the subject of nucleation theory. The various mechanisms are schematically represented in **Figure 2.3**:

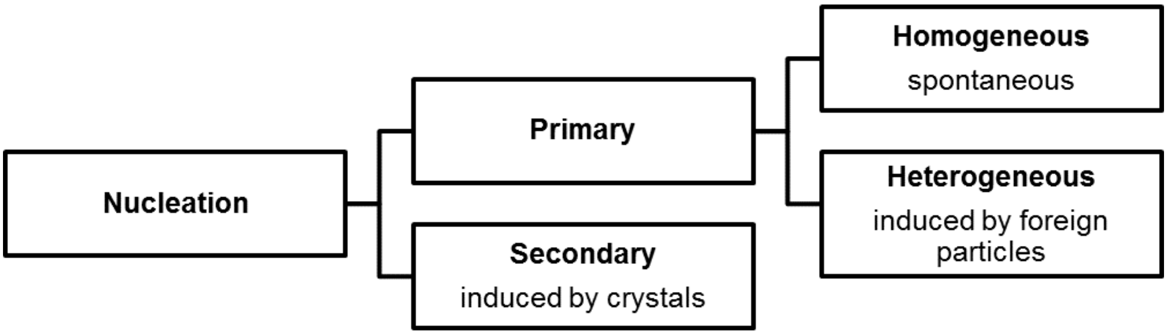

Figure 2.3. Mechanisms of nucleation (adapted from Mullin, 2001).

In primary nucleation, formation of the new solid phase is not influenced by the presence of the solid phase being formed. Primary nucleation can be either homogeneous nucleation, where formation of the solid phase is not brought about the presence of any solid phase, or heterogeneous nucleation, where formation of new solid phase particles is triggered by the presence of a foreign solid phase. Secondary nucleation is the mechanism by which formation of the solid phase is initiated by the presence of solid phase of the crystallizing material itself (Mullin 2001).

Homogeneous nucleation

Primary nucleation is believed to be initiated in a series of bimolecular collisions that forms an aggregate of a small number of molecules, “embryos”, of the dissolved material. Embryos below a critical cluster size (r_c), are unstable and may disintegrate, whereas embryos that exceed this critical cluster size will become stable nuclei and will grow (**Figure 2.4**):

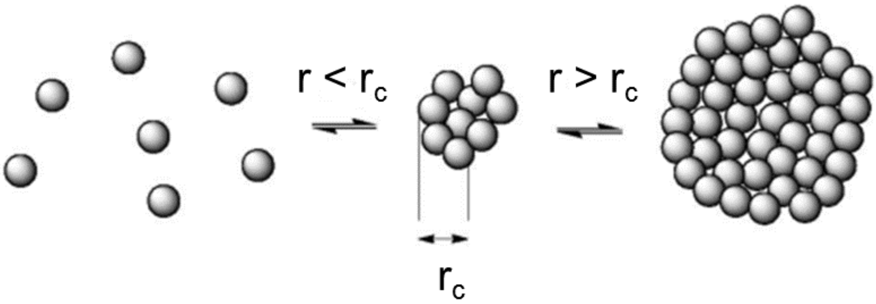

Figure 2.4. The process of nucleation.

The classical nucleation theory states that the change in the Gibbs free energy (ΔG) required to form a nucleus of radius r is given by the equation:

$$\Delta G(r) = \left(\frac{4\pi r^3}{3\Omega}\right) k_B T ln(1+\sigma) + 4\pi r^2 \gamma \tag{2.7}$$

where r is the size of the cluster, Ω is the specific volume of a growth unit, γ is the solid-liquid interfacial energy, k_B is the Boltzmann constant and σ is the relative supersaturation.

Consequently, the free energy, ΔG, increases with the cluster size, r, until a maximum is reached at r_c, which marks the nucleation event. As the new phase grows larger than r_c, the free energy decreases without bound (**Figure 2.5**).

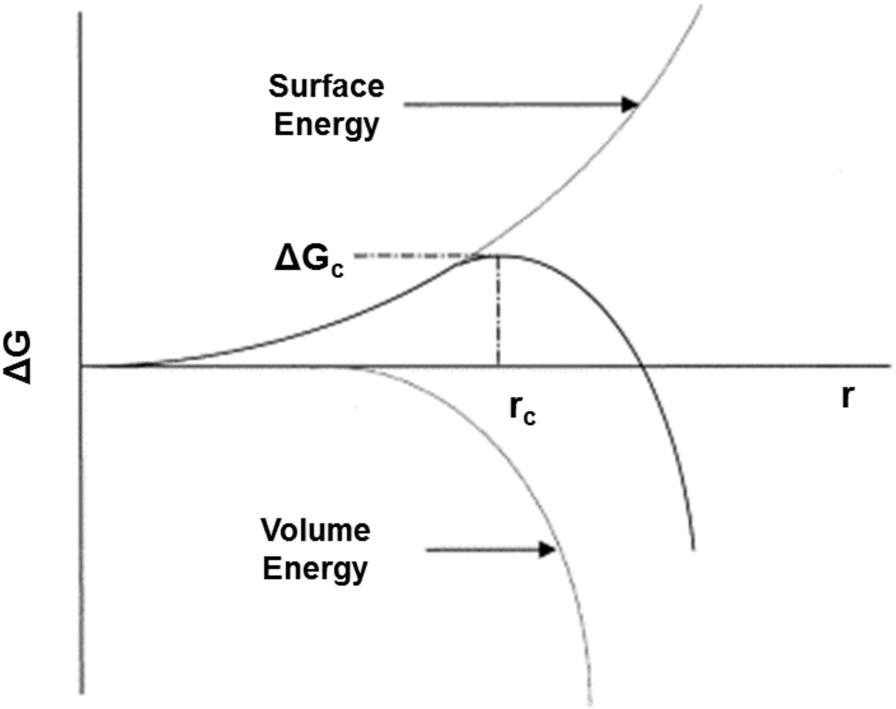

Figure 2.5. Gibbs free energy change of nucleation as a function of the cluster size.

The rate of nuclei formation, J, defined as the number of clusters that grow further than the critical size and so become crystals, is given by the equation:

$$J = J_0 \exp\left(\frac{-\Delta G}{k_B T}\right) \tag{2.8}$$

Since the activation energy is a decreasing function of the supersaturation, the rate of nucleation increases with the increase of the supersaturation.

Heterogeneous nucleation

The nucleation process is usually enhanced by the presence of impurity particles, ions or foreign surfaces. These lower the nucleation energy barrier. The Gibbs free energy of the critical nucleus that forms through heterogeneous nucleation, ΔG_{het}, is expressed by:

$$\Delta G_{c,het} = f_c G_{c,hom} \tag{2.9}$$

where ΔG_{hom} is the Gibbs free energy of the critical nucleus in the homogeneous process and f_c is a geometric correction factor.

Secondary nucleation

During precipitation, secondary nucleation may occur by different mechanisms. These were summarized in Söhnel and Garside (1992). However, in precipitation of sparingly soluble substances, the contribution of secondary nucleation is overshadowed by primary mechanisms, thereby in most cases secondary nucleation needs not to be considered during precipitation (Söhnel and Garside 1992).

Induction time

In the case of unseeded crystallization, the kinetics of nucleation can be measured with the induction time τ_i. It corresponds to the time that passes until the first nucleus is formed in the supersaturated solution. The induction time decreases rapidly with the increase of the degree of relative supersaturation. The higher the relative supersaturation, the sooner the crystallization will start.

❖ *Crystal growth*

Once an ordered structure is formed by nucleation, crystal growth occurs through a 2-dimensional molecular self-assembling, where the solute molecules from the supersaturated solution are added to the solid phase. Solute molecules migrate from the bulk solution to the crystal surface, adsorb, diffuse around the surface to find a suitable site, and are finally integrated into the crystal lattice. According to the Kossel model (**Figure 2.6**), adsorption of growth units may occur at three possible sites:

- ledge sites – incorporation at a flat surface (terrace) having only one site of intermolecular interaction available;

- step sites – incorporation at a surface having two sites of intermolecular interaction available;
- kink sites – three possible sites of intermolecular interactions.

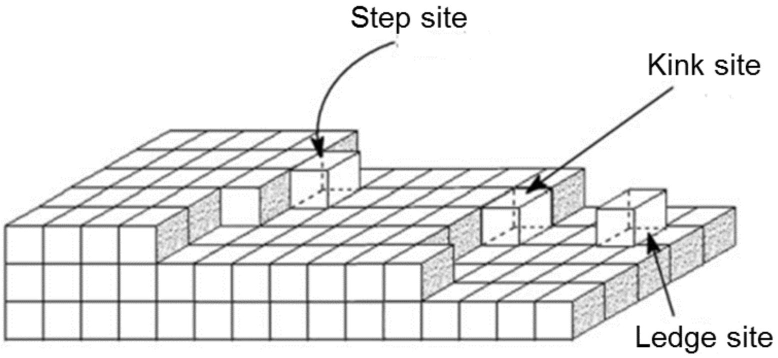

Figure 2.6. Kossel's model of a growing crystal surface.

If crystal size is characterized by a characteristic dimension, L, its linear growth rate, R_G, can be defined as:

$$R_G = \frac{dL}{dt} \tag{2.10}$$

$$R_G = \frac{1}{A} \times \frac{dm}{dt} = K_G\,(c - c^*)^g \tag{2.11}$$

where m is the mass of solid deposited in time t, A is the surface area of the crystal, c is the concentration of the solute in solution (supersaturated), c^* is the equilibrium saturation concentration, K_G is an overall crystal growth coefficient and g is usually referred as the "order" of the overall crystal growth process.

When the mass transfer is not limiting, surface integration is the rate limiting step of crystal growth. In this case, the growth mechanism can be classified into three main categories: continuous growth mechanism, birth and spread mechanism and screw dislocation mechanism. These have been thoroughly reviewed by Mullin (2001).

2.1.4 Chemical aspects of precipitation

Chemical reactions taking place during precipitation are frequently more complex than is implied by a simple stoichiometric equation. Product formation can result from a number of consecutive reactions in solution, each having a different rate (Mersmann 1995). For example, according to the Ostwald's law of stages, the formation of a thermodynamically stable phase will be preceded by that of a number of less stable (metastable) phases possessing greater energy than the stable phase provided that the formation of solid proceeds sufficiently quickly (Söhnel and Garside 1992). This has been confirmed by the behavior of several systems, including the formation of HAp, which is generally preceded by the formation of a metastable phase such as amorphous calcium phosphate or octacalcium phosphate, depending upon the prevailing reaction conditions (van Kemenade and de Bruyn 1987).

It is important to develop a full kinetic description of precipitation and to ensure that kinetic equations refer to the controlling reaction. Further, it is imperative to control the purity of a product that is applied as bone substitute. In this case, it is intended to obtain a low concentration of secondary products from the HAp formation reaction, once those products may be detrimental for cell growth.

2.1.5 Physical aspects of precipitation

2.1.5.1 Particle size distribution

Particle size distribution is a critical quality parameter for many industrial processes. The efficiency of any process for the production of crystals relies on the size, shape and size distribution, as they affect downstream processes such as filtration and drying and determine the product quality (Sultana 2010). Particle size distribution obtained during precipitation is influenced by many processes, including rates of nucleation and growth, and secondary steps such as agglomeration (Söhnel and Garside 1992; Mullin 2001).

The physical properties of the HAp particles play an important role in interacting with the cells in the human body (Bystrov et al. 2011). Therefore, it is important to control particle size distribution and achieve as narrow a distribution as possible, once it allows a better uniformity of cell growth around the HAp particles (Wang et al. 1998; Cai and Tang 2008; Dorozhkin 2010).

2.1.5.2 Influence of mixing

Both nucleation and growth processes are greatly influenced by mixing conditions. Many parameters depend on stirring intensity, such as the induction period, the number and morphology of the particles being formed. Besides, the manner and rate at which the reactants are mixed together influences precipitation rate, average size and width of the size distribution of particles being formed. Several processes need to be considered when precipitation results from mixing of two separate reacting solutions (Söhnel and Garside 1992):

- mixing of reactants, which takes place at different scales, ranging from macroscopic scale (macromixing - acts at the scale of the whole vessel) to microscopic scale (micromixing – acts at the molecular level) (Zauner and Jones 2002);
- formation of the precipitated substance by chemical reaction between the reactants;
- nucleation of the solid phase and crystal growth of the particle formed.

Although in many cases the first two steps are assumed to be fast enough not to limit the kinetics of nucleation and crystal growth, their influence cannot be neglected. Because of very fast nucleation, mixing becomes particularly important in precipitation processes (Shekunov and York 2000) and particularly micromixing once it regulates the mixing phenomena at the molecular level, which is the scale where reactions occur (Silva et al. 2008). Besides, at very high supersaturations the characteristic reaction time is of the same order of magnitude or even smaller than mixing time. When this situation prevails, the course of the mixing process helps to determine the course of supersaturation. This explains why mixing conditions affect crystal shape, purity, crystallinity, and in some cases, even the phase modification (e.g., polymorph) that is formed.

2.1.6 Secondary steps

Various processes can further affect the physical and chemical properties of the precipitate phase during contact with the mother liquor. According to Nývlt et al. (1985), these processes are: recrystallization, isothermal recrystallization (also ripening or Ostwald ripening), ageing and agglomeration.

Secondary processes are of particular importance for the formation of the final product size distribution, particularly the agglomeration phenomenon. It arises if crystals stick together to generate new, larger particles (Mersmann 1995). Among agglomeration types, one generally observes aggregation without supersaturation, i.e. formation of a cluster of crystals linked by weak cohesion forces (van der Waals), or agglomeration in the presence of supersaturation, i.e. collision then aggregation between crystals followed by the formation of crystalline bridges (**Figure 2.7**).

Figure 2.7. Schematic representation of aggregation and agglomeration phenomena.

As mentioned above, precipitation processes are characterized by rapid nucleation and growth, resulting thus in the formation of a large number of primary particles that remain in the submicron range. The behavior of colloidal particles in this size range is governed by interfacial forces, which result from the balance between attractive van der Waals forces and repulsive electrostatic forces of the charged particles (Kind 2002). These forces can result in an overall repulsion or attraction between particles. In precipitation processes, the resulting particles are usually secondary particles, i.e. particles built by the agglomeration of the fine primary ones. Key parameters in particle agglomeration phenomenon include the hydrodynamic conditions, the size of the particles and the nature of the surrounding liquid (Kind 2002; Mersmann 1995).

2.2 Hydroxyapatite (HAp) system

2.2.1 Calcium phosphates

Calcium phosphates are widely used as bone substitute materials due to their chemical similarity to the mineral component of bones and teeth (Viswanath and Ravishankar 2008; Dorozhkin 2010; Wang and Nancollas 2008). By definition, all calcium phosphates consist of three major chemical elements: calcium (oxidation state +2), phosphorus (oxidation state +5), and oxygen (oxidation state -2). They are mostly sparingly soluble in water, but all dissolve in acids.

Table 2.2 presents some of the known calcium phosphates, including their standard abbreviation and their major properties. In general, the lower the Ca/P molar ratio, the more acidic and soluble the calcium phosphate phase (Wang and Nancollas 2008).

Table 2.2. Calcium phosphate salts, name, standard abbreviation, chemical formula, Ca/P molar ratio and solubility.

Name	**Standard abbreviation**	**Chemical formula**	**Ca/P molar ratio**	**Solubility at 37 °C, -log (K_{sp})**
Dicalcium phosphate dehydrate	DCPD	$CaHPO_4.2H_2O$	1.00	6.73
Dicalcium phosphate anhydrous	DCPA	$CaHPO_4$	1.00	6.04
Octacalcium phosphate	OCP	$Ca_8H_2(PO_4)_6.5H_2O$	1.33	98.6
Amorphous calcium phosphate	ACP	$Ca_xH_y(PO_4)_z.nH_2O$	1.20 – 2.20	Cannot be measured precisely
α-Tricalcium phosphate	α-TCP	$\alpha\text{-}Ca_3(PO_4)_2$	1.50	28.5
β-Tricalcium phosphate	β-TCP	$\beta\text{-}Ca_3(PO_4)_2$	1.50	29.6
Hydroxyapatite	HAp, HA or OHAp	$Ca_5(PO_4)_3OH$	1.67	117.2

Among existing calcium phosphates, hydroxyapatite (HAp) remains the most intensely studied bioceramic owing to its similarity to natural bone (Kumta et al. 2005; Wang and Nancollas 2008; Oliveira 2007). In addition to being non-toxic, HAp is biocompatible, i.e. not recognized as foreign material in the body and, most importantly, it exhibits both bioactive behavior and integrates into living tissue by the same processes active in remodeling healthy bone. More to the point, HAp is also known to be osteoconductive (able to provide a scaffold or template for new bone formation) and support osteoblast adhesion and proliferation (Dorozhkin 2010).

2.2.2 HAp properties (structure, composition and phase stability)

2.2.2.1 Structure

Crystals of HAp may have either monoclinic or hexagonal unit cells. From the thermodynamic aspect, the monoclinic form is more stable and corresponds to stoichiometric HAp (Leventouri 2006). In the monoclinic phase (space group $P2_1/b$, lattice parameters a = 9.4214, $b = 2a$, c = 6.8814 Å, γ = 120°), the OHs occur in columns on the screw axis, pointing upward and downward in alternate, nearest-neighbor columns (**Figure 2.8**) (Wang and Nancollas 2008; Corno et al. 2006).

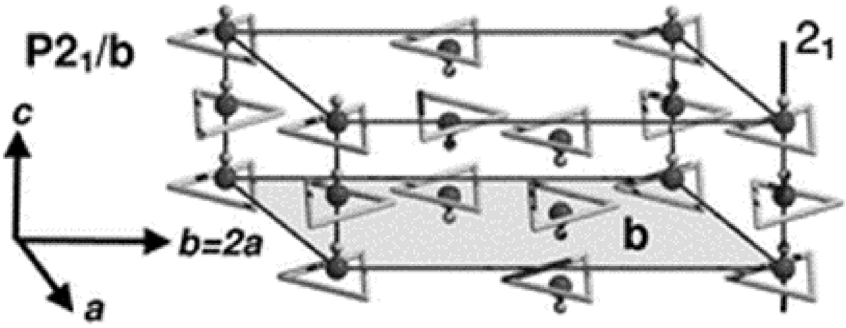

Figure 2.8. Monoclinic $P2_1/b$ HAp structure. P, O and Ca atoms not relevant for the scheme have been omitted for clarity. Ca atoms are at the vertices of triangles around each hydroxyl group (adapted from Corno et al., 2006).

The hexagonal form of HAp (space group $P6_3/m$, lattice parameters a = 9.4176, $b = a$, c = 6.8814 Å, β = 120°) (**Figure 2.9**), generally atributed to nonstoichiometric HAp (Leventouri 2006) and found in biological apatites, has a structure similar to the monoclinic form, but with columns of calcium and hydroxide groups located in parallel channels. Ion substitution can readily occur in these channels, and this may account for the high degree of substitution found in natural apatites (Wang and Nancollas 2008; Elliot 1994).

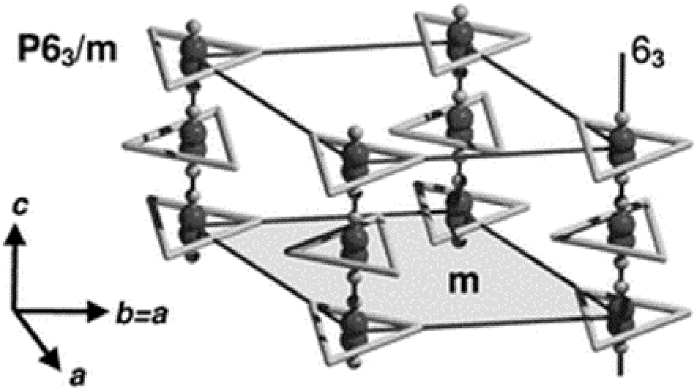

Figure 2.9. Hexagonal P6$_3$/m HAp structure. P, O and Ca atoms not relevant for the scheme have been omitted for clarity. Ca atoms are at the vertices of triangles around each hydroxyl group (adapted from Corno et al., 2006).

2.2.2.2 Composition

HAp, $Ca_5(PO_4)_3OH$, is a compound with a variable composition existing over Ca/P molar ratios from 1.67 for stoichiometric to $\approx$1.5 for fully calcium deficient HAp (Wang and Nancollas 2008), and sometimes even outside this range (Elliot 1994). As to biological apatites, they have multiple substitutions and deficiencies at all ionic sites. Of particular importance is the carbonate substitution in B-type carbonate HAp, where carbonate substitutes for the phosphate ion (Leventouri 2006).

2.2.2.3 Phase stability

The stability of calcium phosphate (CaP) phases in contact with aqueous solutions can be understood in terms of a typical solubility phase diagram in which solubility isotherms are expressed as plots of log [Ca] as a function of pH (**Figure 2.10**). According to this diagram, for a given pH value, any salt whose isotherm lies below another, will be relatively more stable and so less soluble (Fernández et al. 1999). One can also observe that at 37 °C, HAp is the least soluble salt down to a pH 4.2, e.g. it is the most stable calcium phosphate for pH between 4.2 and 12 at body temperature (Elliot 1994). However, kinetic factors are also important in determining the likelihood of the formation of preferred crystal phases in solutions supersaturated with respect to several different phases (Wang and Nancollas 2008; Koutsopoulos 2002). The formation of HAp is much slower than that of either OCP or DCPD, and during simultaneous phase formation, a larger portion of the kinetically favored phase may be observed, even though it has a much smaller thermodynamic driving force. The balance between kinetic and thermodynamic factors is, therefore, very important in discussing the likelihood of precursor formation during calcium phosphate precipitation.

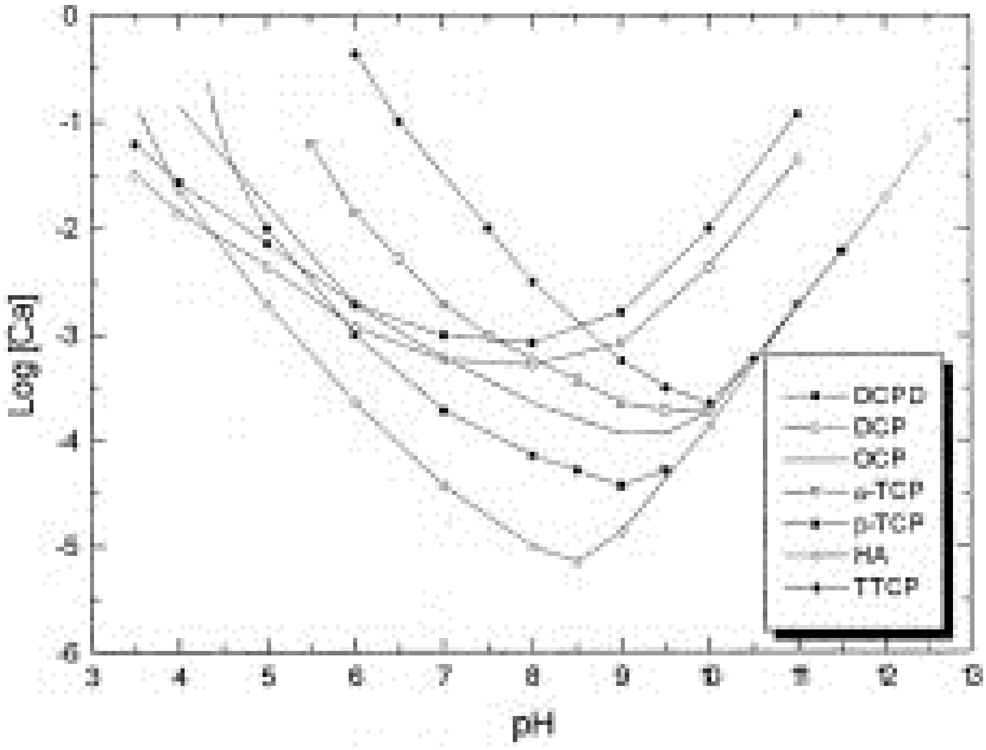

Figure 2.10. Solubility isotherms of calcium phosphates in the system $Ca(OH)_2$-H_3PO_4-H_2O at 37 ºC (Fernández et al., 1999).

2.3 Processes for HAp synthesis

2.3.1 Methods

Many methods have been reported for HAp synthesis, including solid state reactions, sol-gel crystallization, hydrothermal processing, layer hydrolysis of other calcium phosphate salts and wet chemical reactions (Koutsopoulos 2002; Ferraz et al. 2004; Saeri et al. 2003). The synthesis of HAp from the precipitation route stands out because of its simplicity, low cost, and easy application in industrial production (Liu et al. 2001).

Depending on the precipitation conditions, like stirring speed, reactants addition rate, Ca/P molar ratio, reaction temperature and pH, one can obtain HAp particles with different morphology, size and purity (Elliot 1994; Ferreira et al. 2003). In most of the works, precipitation of HAp is carried out at high temperature and high pH (Gomez-Morales et al. 2001; Liu et al. 2001; Koutsopoulos 2002). Investigations on the precipitation of HAp at low temperatures (Bernard et al. 1999; Afshar et al. 2003; Saeri et al. 2003) and at physiological conditions of temperature and pH (Koutsoukos and Nancollas 1981; Inskeep and Silvertooth 1988; Ishikawa et al. 1994; Ashok et al. 2003; Kumta et al. 2005) have also been reported. Besides, HAp synthesis is generally conducted at high supersaturations, resulting most of the times in the formation of non-stoichiometric products (van Kemenade and de Bruyn 1987; Koutsopoulos 2002; Clarkin et al. 2007). Direct precipitation of HAp has only been observed for low reactants concentrations, that is, slightly supersaturated or undersaturated aqueous solutions with respect to precursor phase (Seckler et al. 1999; Boskey and Posner 1976).

2.3.2 Reactors

Conventionally, precipitation processes are achieved in stirred tank batch reactors for both production, research and development (Sultana 2010; Shirure et al. 2005). Several disadvantages are associated with the implementation of precipitation in such system, namely in terms of the reproducibility of the process and product quality (Silva et al. 2008). Such system is characterized by heterogeneous spatial and temporal distributions of process parameters such as temperature and concentration, giving rise to a variable supersaturation environment (Demopoulos 2009; Sultana 2010) and affecting thus the final product properties. Actually, mixing problems have been encountered in stirred tank batch reactors (Silva et al. 2008; Sultana 2010; Jones et al. 2005; Jongen et al. 2003). Macromixing is achieved by intensive stirring, but micromixing is not at all controlled. Micromixing regulates mixing phenomena at the molecular level, which is the scale at which the reactions occur, and it is thus a key factor for the production of HAp particles with controlled characteristics. Besides, the product from batch precipitation often has wide size distribution due to inhomogeneous mixing and broad residence time distribution (Kawase and Miura 2007; Jones et al. 2005).

Due to the limitations of stirred tank batch reactors, various systems have been used for the precipitation of HAp in order to obtain a better control over reaction conditions. Among them, semi-batch configuration (Gomez-Morales et al. 2001)has been used to overcome homogeneity problems in the distribution of supersaturation in the vessel. Indeed, the precipitant is added in a controlled manner to ensure constant supersaturation (Demopoulos 2009). Continuous stirred tank reactors (CSTR) have also been used (Gomez-Morales et al. 2001), since they offer a stable supersaturation due to their steady state operation (Demopoulos 2009). Such system usually results in fine particles of wide size distribution

(Demopoulos 2009). Recently, micro devices have been applied for the continuous-flow precipitation of HAp in order to solve the mixing problems associated to stirred tank batch reactors. Various configurations have been applied, ranging from a simple tubular reactor (Fujii et al. 2011), to which a mixing part is sometimes added that is generally T-shaped (Yang et al. 2010), to more complex systems (Yang et al. 2010; Silva et al. 2008; Kandori et al. 2011; Shum et al. 2009). The use of tubular microreactors is very interesting because of the relative easy use, but the problems of parabolic velocity profile or channel clogging limit its use at the industrial level (Jongen et al. 2003). Yang et al. (2010) studied a microporous tube-in-tube microchannel reactor that in addition to promote better mixing conditions also aims at obtaining a high throughput method, essential to the transition of microreactor technology from lab-scale to industrial-scale chemical processes. Silva et al. (2008) work also attempts to implement an industrial technology for the preparation of HAp nanoparticles. The reactor developed, the NETmix reactor, is a static mixer, consisting of a network of interconnected chambers and channels. Its main advantages include the ability to control mean residence time and mixing intensity.

2.4 Process intensification

2.4.1 Definition

Process intensification (PI) is commonly mentioned as one of the most promising development paths for the chemical processing industry and one of the most important progress areas for chemical engineering research (Górak and Stankiewicz 2011). PI can be defined as “any chemical engineering development that leads to a substantially smaller, cleaner, safer and more energy efficient technology” (González-Bello et al. 2011). It aims at adapting the process to chemical reaction that is to obtain: higher yields and better product consistency and repeatability; energy savings and decreased operating costs; reduced capital expenditure; flexible production capacity and safer processes. Through PI it should be possible to make the most efficient use of the process environment; to reduce waste by-product formation; to use smaller reaction systems compared to conventional ones; to obtain easy scale-up or scale-down systems just by adjusting the number of reaction units. The goal is to reach intrinsic kinetics of phenomena by minimizing heat and mass transfer, and hydrodynamic limitations. For that, four main strategies can be used (Bakker and Dekker 2003), as shown in **Figure 2.11**.

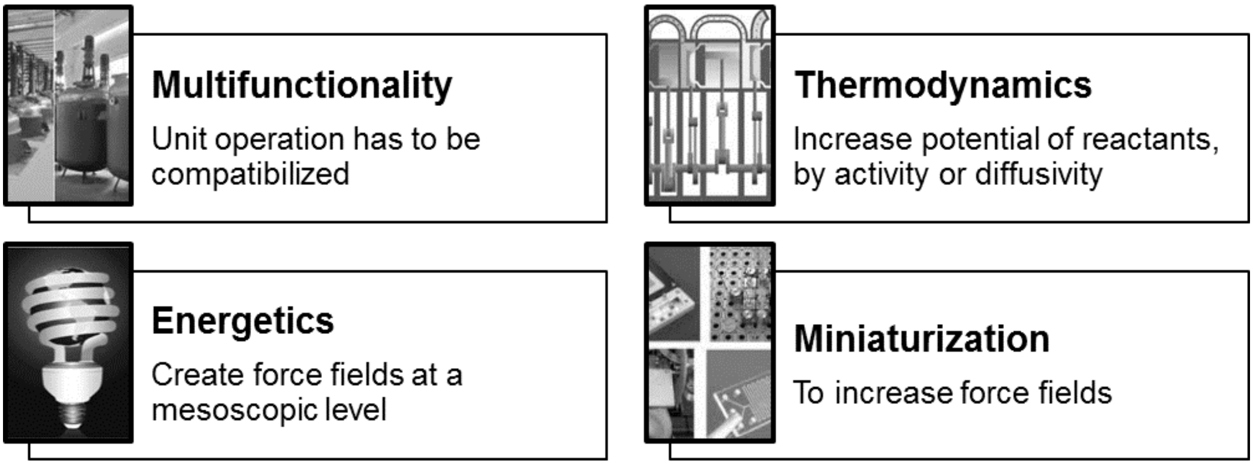

Figure 2.11. Strategies for process intensification.

These strategies aim at:

- combining in a single unit several unit operations (Multifunctionality), namely through the use of multi-functional reactors;
- using alternative solvents (Thermodynamics) such as ionic liquids;
- using alternative energy resources such as microwaves or acoustic fields (Energetics)
- using micro and meso-scale systems (Miniaturization).

2.4.2 Miniaturization

Miniaturization is a relatively young research field, in which micro and meso-scale systems are included. The first microchannel device was described in a German patent from 1986 (González-Bello et al. 2011). A microstructured reactor is generally defined as a reactor with three-dimensional structures, the inner dimensions of which are under a millimeter in size (Jähnisch et al. 2004), while meso systems are under a millimeter to centimeter in size (Li and Ananthasuresh 2002).

Scaling down offers several advantages (**Figure 2.12**), namely reduced capital, energy costs and exposure to toxic or hazardous materials (Jähnisch et al. 2004; Pohar and Plazl 2009), making micro- and mesoreactors interesting tools for high throughput and screening experimentation. Their high surface to volume ratio enhances heat and mass transfer (Jähnisch et al. 2004; Pohar and Plazl 2009; González-Bello et al. 2011; Hessel 2009). Besides, mixing times in micromixers (down to several milliseconds) are generally smaller than in conventional systems (Jähnisch et al. 2004). Therefore, miniaturization allows for a precise control of reaction with improved conversions, selectivities and yields of desired products. It also provides an opportunity to integrate heat transfer, fluid mixing and chemical reaction in the same unit and thereby reducing the number of other components. Further, scalability and optimization are also significantly easier (González-Bello et al. 2011; Jongen et al. 2003).

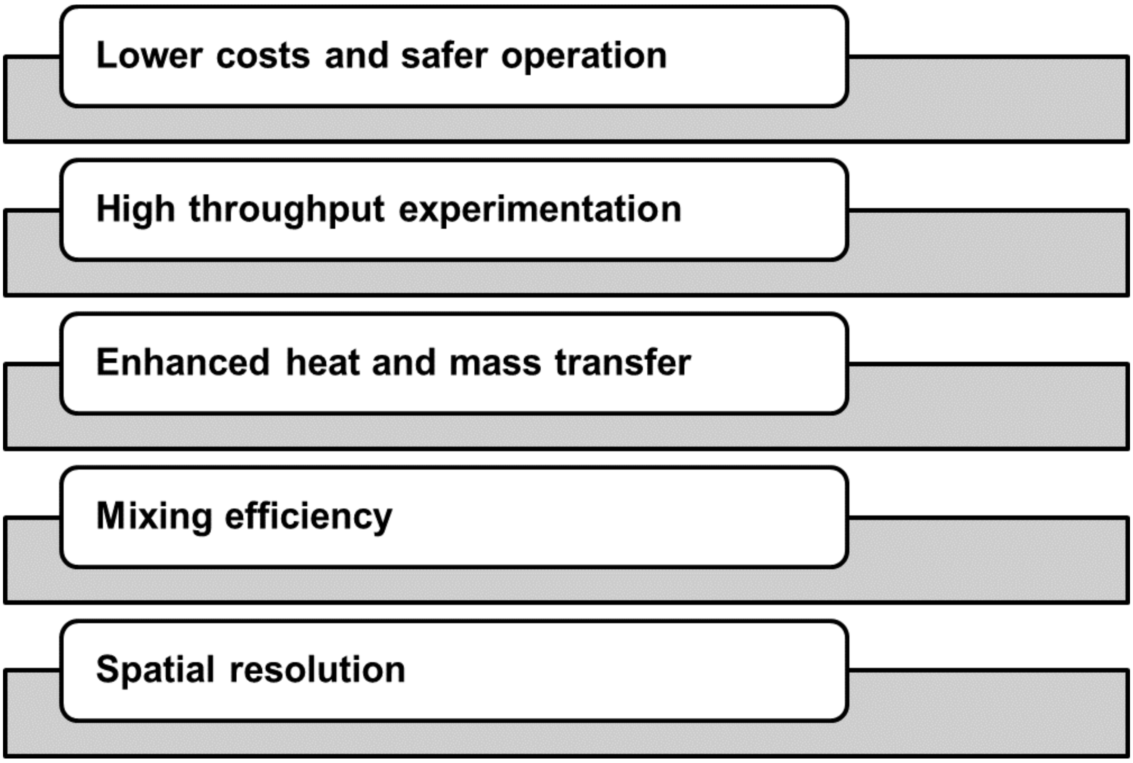

Figure 2.12. Main advantages of miniaturization.

2.5 References

Afshar, A, M Ghorbani, N Ehsani, M Saeri, and C Sorrell. 2003. “Some Important Factors in the Wet Precipitation Process of Hydroxyapatite.” *Materials & Design* 24 (3): 197–202.

Ashok, M, N. Meenakshi Sundaram, and S. Narayana Kalkura. 2003. “Crystallization of Hydroxyapatite at Physiological Temperature.” *Materials Letters* 57 (13-14): 2066–2070.

Bakker, R., and M. Dekker. 2003. *Reengineering the Chemical Processing Plant*.

Bernard, L, M Freche, J L Lacout, and B Biscans. 1999. “Preparation of Hydroxyapatite by Neutralization at Low Temperature — Influence of Purity of the Raw Material.” *Powder Technology* 103: 19–25.

Boskey, L., and A. Posner. 1976. “Formation of Hydroxyapatite at Low Supersaturation.” *The Journal of Physical Chemistry* 80 (1): 40–45.

Bystrov, V .S., E. Paramonova, Y. Dekhtyar, A. Katashev, A. Karlov, N. Polyaka, A. V. Bystrova, A. Patmalnieks, and A. L. Kholkin. 2011. “Computational and Experimental Studies of Size and Shape Related Physical Properties of Hydroxyapatite Nanoparticles.” *Journal of Physics. Condensed Matter* 23.

Cai, Y., and R. Tang. 2008. “Calcium Phosphate Nanoparticles in Biomineralization and Biomaterials.” *Journal of Materials Chemistry* 18 (32): 3775.

Clarkin, O. M., M. R. Towler, G. M. Insley, and M. E. Murphy. 2007. “Phase Transformations of Calcium Phosphates Formed in Wet Field Environments.” *Journal of Materials Science* 42 (19): 8357–8362.

Corno, M., C. Busco, B. Civalleri, and P Ugliengo. 2006. “Periodic Ab Initio Study of Structural and Vibrational Features of Hexagonal Hydroxyapatite Ca10(PO4)6(OH)2.” *Physical Chemistry Chemical Physics* 6: 2464–2472.

Demopoulos, G.P. 2009. “Aqueous Precipitation and Crystallization for the Production of Particulate Solids with Desired Properties.” *Hydrometallurgy* 96 (3): 199–214.

Dorozhkin, S. V. 2010. “Calcium Orthophosphates as Bioceramics: State of the Art.” *Journal of Functional Biomaterials* 1 (1): 22–107.

Elliot, J.C. 1994. *Structure and Chemistry of the Apatites and Other Calcium Orthophosphates*. Amsterdam: Elsevier.

Fernández, E., F. J. Gil, M. P. Ginebra, F. C. Driessens, J. A. Planell, and S M Best. 1999. "Calcium Phosphate Bone Cements for Clinical Applications. Part I: Solution Chemistry." *Journal of Materials Science. Materials in Medicine* 10 (3): 169–76.

Ferraz, M. P., F. J. Monteiro, and C. M. Manuel. 2004. "Hydroxyapatite Nanoparticles: A Review of Preparation Methodologies." *Journal of Applied Biomaterials & Biomechanics : JABB* 2 (2): 74–80.

Ferreira, A, C. Oliveira, and F. Rocha. 2003. "The Different Phases in the Precipitation of Dicalcium Phosphate Dihydrate." *Journal of Crystal Growth* 252 (4): 599–611.

Fujii, E., K. Kawabata, Y. Nakazaki, Y. Tanizawa, Y. Shirosaki, S. Hayakawa, and A. Osaka. 2011. "Fabrication of Hydroxyapatite with Controlled Morphology in a Micro-reactor." *Journal of the Ceramic Society of Japan* 119 (1386): 116–119.

Gomez-Morales, J., J. Torrent-Burgues, and R. Rodriguez-Clemente. 2001. "Crystal Size Distribution of Hydroxyapatite Precipitated in a MSMPR Reactor." *Crystal Research and Technology* 36 (8-10): 1065–1074.

González-Bello, O.J., A. Unzurrunzaga, S. Pérez, M. Belsué, and S. Gil-Rio. 2011. "Process Intensification Based on Structured Technologies : Fabrication Method of Microchannel Reactor and Its Potential Use in Industrial Reactions." In *9th Green Chemistry Conference. AN INTERNATIONAL EVENT.* Alcalá de Henares - Spain.

Górak, A., and A. Stankiewicz. 2011. "Intensified Reaction and Separation Systems." *Annual Review of Chemical and Biomolecular Engineering* 2 (1): 431–451.

Hessel, V. 2009. "Novel Process Windows - Gate to Maximizing Process Intensification via Flow Chemistry." *Chemical Engineering & Technology* 32 (11): 1655–1681.

Inskeep, W. P., and J. C. Silvertooth. 1988. "Kinetjcs of Hydroxyapatite Precipitation at pH 7 . 4 to 8 . 4 *." *Geochimica Et Cosmochimica Acta* 52: 1883–1893.

Ishikawa, K, E. D. Eanes, and M. S. Tung. 1994. "The Effect of Supersaturation on Apatite Crystal Formation in Aqueous Solutions at Physiologic pH and Temperature." *Journal of Dental Research* 73 (8): 1462–1469.

Jones, A., S. Rigopoulos, and R. Zauner. 2005. "Crystallization and Precipitation Engineering." *Computers & Chemical Engineering* 29 (6): 1159–1166.

Jongen, N., M. Donnet, P. Bowen, J. Lemaître, H. Hofmann, R. Schenk, C. Hofmann, et al. 2003. "Development of a Continuous Segmented Flow Tubular Reactor and the 'Scale-out' Concept - In Search of Perfect Powders." *Chemical Engineering and Technology* 26: 303–305.

Jähnisch, K., V. Hessel, H. Löwe, and M. Baerns. 2004. *Chemistry in Microstructured Reactors. Angewandte Chemie* 43.

Kandori, K., T. Kuroda, S. Togashi, and E. Katayama. 2011. "Preparation of Calcium Hydroxyapatite Nanoparticles Using Microreactor and Their Characteristics of Protein Adsorption." *Journal of Physical Chemistry B* 115: 653–659.

Kawase, M., and K. Miura. 2007. "Fine Particle Synthesis by Continuous Precipitation Using a Tubular Reactor." *Advanced Powder Technology* 18 (6): 725–738.

van Kemenade, M.J.J.M., and P.L. de Bruyn. 1987. "A Kinetic Study of Precipitation from Supersaturated Calcium Phosphate Solutions." *Journal of Colloid and Interface Science* 118 (2): 564–585.

Kind, M. 2002. "Colloidal Aspects of Precipitation Processes ." *Chemical Engineering Science* 57: 4287–4293.

Koutsopoulos, S. 2002. "Synthesis and Characterization of Hydroxyapatite Crystals: a Review Study on the Analytical Methods." *Journal of Biomedical Materials Research* 62 (4): 600–12.

Koutsoukos, P G, and G H Nancollas. 1981. "THE MORPHOLOGY OF HYDROXYAPATITE CRYSTALS GROWN IN AQUEOUS SOLUTION AT 37°C." *Journal of Crystal Growth* 55: 369–375.

Kumta, P. N, C. Sfeir, D.-H. Lee, D. Olton, and D. Choi. 2005. "Nanostructured Calcium Phosphates for Biomedical Applications: Novel Synthesis and Characterization." *Acta Biomaterialia* 1 (1): 65–83.

Leventouri, T. 2006. "Synthetic and Biological Hydroxyapatites: Crystal Structure Questions." *Biomaterials* 27 (18): 3339–42.

Li, J., and G. K. Ananthasuresh. 2002. "Three-dimensional Low-temperature Co-fired Ceramic Shells for Miniature Systems Applications." *Journal of Micromechanics and Microengineering* 12: 198–203.

Liu, C, Y Huang, W Shen, and J Cui. 2001. "Kinetics of Hydroxyapatite Precipitation at pH 10 to 11." *Biomaterials* 22 (4): 301–6.

Mersmann, A. 1995. *Crystallization Technology Handbook*. New York: Marcel Dekker.

Mullin, J.W. 2001. *Crystallization*. Fourth. Oxford: Reed Educational and professional publishing Ltd.

Oliveira, C. 2007. "Precipitação Do Fosfato Dicálcico : Caracterização Experimental e Modelização". PhD Thesis. Faculty of Engineering of the University of Porto.

Pedrosa, A. M. C. 1995. “Precipitação Do Gluconato De Sódio Com Solventes Orgânicos”. I.S.T., Lisboa.

Pohar, A, and I Plazl. 2009. “Process Intensification Through Microreactor Application” 23 (4): 537–544.

Saeri, M, A. Afshara, M. Ghorbania, N. Ehsania, and C.C. Sorrellb. 2003. “The Wet Precipitation Process of Hydroxyapatite.” *Materials Letters* 57: 4064–4069.

Seckler, M M, M Danese, S Derenzo, J V Valarelli, M Giulietti, and R Rodríguez-clemente. 1999. “Influence of Process Conditions on Hydroxyapatite Crystallinity Obtained by Direct Crystallization.” *Materials Research* 2 (2): 59–62.

Shekunov, B.Yu, and P York. 2000. “Crystallization Processes in Pharmaceutical Technology and Drug Delivery Design.” *Journal of Crystal Growth* 211 (1-4): 122–136.

Shirure, V. S., A. S. Pore, and V. G. Pangarkar. 2005. “Intensification of Precipitation Using Narrow Channel Reactors : Magnesium Hydroxide Precipitation.” *Society*: 5500–5507.

Shum, H. C., A. Bandyopadhyay, S. Bose, and D. A. Weitz. 2009. “Double Emulsion Droplets as Microreactors for Synthesis of Mesoporous Hydroxyapatite.” *Chemistry of Materials* 21: 5548–5555.

Silva, V. M. T. M., P. A. Quadros, P. E. M. S. C. Laranjeira, M. M. Dias, and J. C. B. Lopes. 2008. “A Novel Continuous Industrial Process for Producing Hydroxyapatite Nanoparticles.” *Journal of Dispersion Science and Technology* 29 (4): 542–547.

Sultana, M. 2010. “Microfluidic Systems for Continuous Crystallization of Small Organic Molecules”. PhD Thesis. Massachusetts Institute of Technology .

Söhnel, O., and J. Garside. 1992. *Precipitation: Basic Principles and Industrial Applications* Oxford: Butterworth-Heinemann.

Viswanath, B, and N Ravishankar. 2008. “Controlled Synthesis of Plate-shaped Hydroxyapatite and Implications for the Morphology of the Apatite Phase in Bone.” *Biomaterials* 29 (36): 4855–63.

Wang, L., and G. H. Nancollas. 2008. “Calcium Orthophosphates: Crystallization and Dissolution.” *Chemical Reviews* 108 (11): 4628–69.

Wang, M., R. Joseph, and W. Bonfield. 1998. “Hydroxyapatite-polyethylene Composites for Bone Substitution: Effects of Ceramic Particle Size and Morphology.” *Biomaterials* 19 (24): 2357–66.

Yang, Q., J.-X. Wang, L. Shao, Qi-A. Wang, F. Guo, J.-F. Chen, L. Gu, and Y.-T. An. 2010. “High Throughput Methodology for Continuous Preparation of Hydroxyapatite

Nanoparticles in a Microporous Tube-in-Tube Microchannel Reactor.” *Industrial & Engineering Chemistry Research* 49: 140–147.

Zauner, R., and A. G. Jones. 2002. “On the Influence of Mixing on Crystal Precipitation Processes — Application of the Segregated Feed Model.” *Chemical Engineering Science* 57: 821–831.

3 CHARACTERIZATION OF INTERMEDIATE STAGES IN THE PRECIPITATION OF HAp AT 37 °C IN A STIRRED TANK BATCH REACTOR

Precipitation of HAp was carried out by mixing a saturated calcium hydroxide aqueous solution with an orthophosphoric acid aqueous solution at 37 ºC. In order to promote optimal conditions for the production of HAp with high yields, mixing of the reaction medium was assured by a novel metal stirrer. Different experimental conditions were studied varying the mixing Ca/P molar ratio from 1.00 to 1.67. After process optimization, a suspension of HAp particles with pH close to 7 was obtained for a mixing molar ratio Ca/P = 1.33. The precipitation process was then characterized as a function of pH and calcium concentration, revealing the existence of three different stages. The precipitate formed in each stage was characterized by scanning electron microscopy and X-ray diffraction.

3.1 Introduction

Several methods have been used for the preparation of HAp by precipitation, namely using nitrate, ammonium and phosphate ions. Beyond the use of polluting agents, these methods also require additional experimental steps to eliminate by-products resulting from the reaction. This section refers to a simple and non-polluting method. It consists in preparing HAp from neutralization between calcium hydroxide with orthophosphoric acid:

$$5Ca(OH)_2 + 3H_3PO_4 \rightarrow Ca_5(PO_4)_3OH \downarrow + 9H_2O \qquad (3.1)$$

However, it is difficult to control the reaction conditions necessary to obtain a powder with the desired characteristics, since calcium hydroxide is slightly soluble in water and the state of the orthophosphate ions depends on pH (**Figure 3.1**).

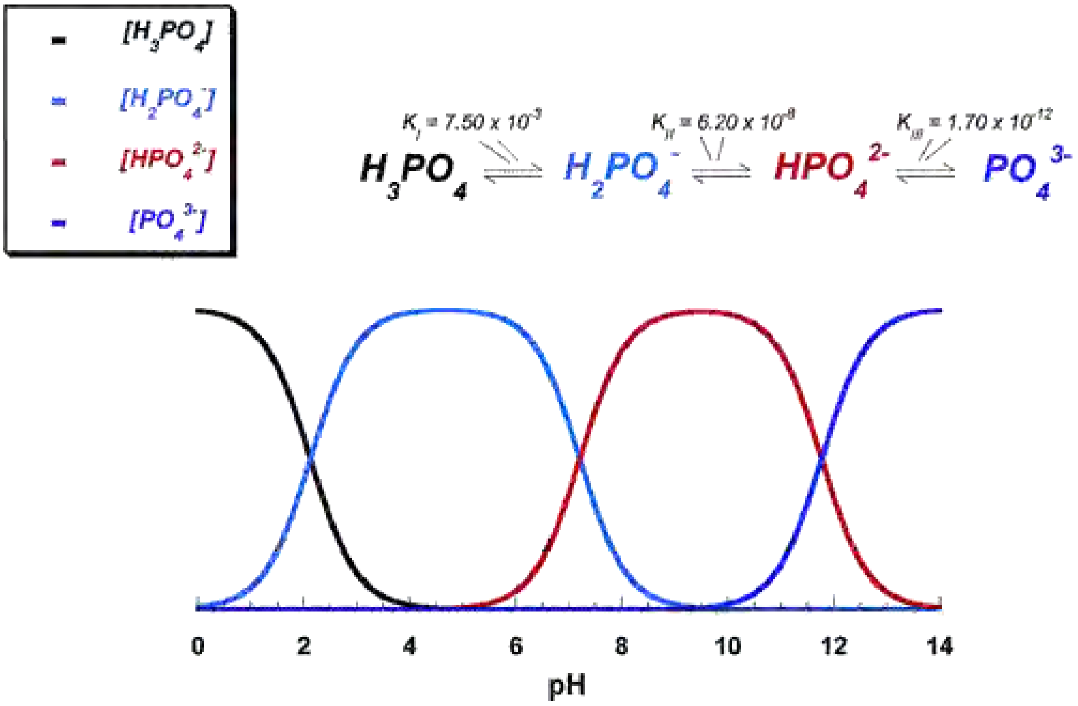

Figure 3.1. pH variation of ionic concentrations in triprotic equilibrium for phosphoric acid solutions (Lynn and Bonfield 2005).

To overcome this limitation, most of the works have focused on the control of pH to favor the presence of the PO_4^{3-} ions and thus avoid the formation of other calcium phosphates. In Osaka et al. (1991) and Bernard et al. (2000) works, the authors studied the influence of the acid addition rate on the HAp powder properties and on the calcium hydroxide dissolution rate, respectively, demonstrating that maintenance of an alkaline reaction medium is fundamental to favor the formation of stoichiometric HAp. Nevertheless, for the synthesis of HAp for medical purposes, there is a concern in preparing HAp under conditions that are more conductive to the survival of cells. The preparation has to follow specific criteria, namely about pH and temperature conditions (Kumta et al. 2005).

In this section, a simple methodology for the synthesis of HAp from diluted solutions at 37 ºC is reported. For that, a saturated calcium hydroxide aqueous solution was mixed with an orthophosphoric acid aqueous solution, without maintaining a fixed pH. In this way, a homogeneous solution of hydroxide and calcium ions shall be obtained, avoiding the formation of local concentration gradients, while maximizing HAp precipitation process. Further, reagents were mixed by a novel metal stirrer, designed in order to obtain an efficient and intense mixing of the reaction medium. The influence of the mixing Ca/P molar ratio on the powder properties and on the final pH value was studied, the optimum conditions being derived for obtaining stable HAp nanoparticles under near-physiological conditions of temperature and pH, i.e., HAp particles suitable for bone substitution application. Finally, the intermediate stages for the optimized HAp precipitation process were described.

3.2 Material and methods

3.2.1 HAp preparation

HAp precipitation was carried out in a cylindrical batch reactor (**Figure 3.2**) made of glass, with 100 mm in diameter and 250 mm in height, where temperature was regulated by a water jacket and a thermostatic bath maintained at 37 ºC. The agitation was assured by a novel metal stirrer (see **Figure 3.2**) and kept at 270 rpm. The designed stirrer is provided by 16 agitators along its length in order to obtain an efficient and intense mixing of the reaction medium.

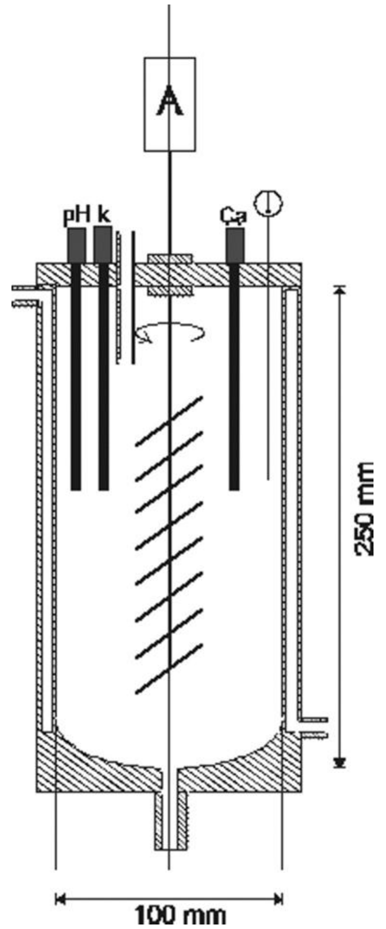

Figure 3.2. Experimental precipitation apparatus.

HAp was synthesized by the mixing of equal volumes (0.5 dm^3) of a saturated calcium hydroxide (Riedel-de Haën, 96%) aqueous solution and an orthophosphoric acid (Pronalab, 85%) aqueous solution, with different mixing Ca/P molar ratios (1.00, 1.33 and 1.67).

A 19.3 mmol.dm^{-3} calcium hydroxide aqueous solution, that is, a saturated calcium hydroxide aqueous solution at T = 37 ºC (Perry and Green 1997) was prepared. To facilitate the dissolution of calcium hydroxide, the solution was agitated in a closed vessel for 24 hours at 500 rpm, and at 25 ºC, as its solubility decreases with the increase of temperature (Johannsen and Rademacher 1999). Calcium concentration was then confirmed by EDTA (Riedel-de Haën, 99%) titration. Both saturated calcium hydroxide aqueous solution and orthophosphoric acid aqueous solution were prepared with ultra pure water, and ionic force was adjusted by the addition of 6 mL of KCl (Panreac, 99.5%) 4 mol.dm^{-3} solution.

Precipitation started by the quick addition (≈ 26 mL.s^{-1}) of the orthophosphoric acid aqueous solution to the saturated calcium hydroxide aqueous solution. The concentration of the orthophosphoric acid aqueous solution varied from 11.5 mmol.dm^{-3} to 19.3 mmol.dm^{-3}, so as to obtain different mixing Ca/P molar ratios.

Calcium concentration, pH, temperature and conductivity were continuously measured (inoLab pH/cond level 3, WTW) and recorded for about 6 hours. The different electrodes were calibrated with buffer solutions. pH calibration was made with two buffer solutions (Hanna Instruments) with pH=7.01 and pH=10.01 at 25 ºC. Regarding calcium electrode (inolab Ca 800, WTW), its calibration was done using standard solutions of 5 and 50 ppm of calcium. Those were prepared from $CaCl_2$ (Merck proanalysis, 98%) and ionic force was adjusted by the addition of 6 mL of KCl (Panreac, 99.5%) 4 mol.dm^{-3} solution per 500 mL of standard solution.

3.2.2 Powder characterization

Samples were withdrawn at different time intervals, filtered (membrane of 0.2 µm pore size, Gelman Sciences, USA), washed twice with ultra-pure water and dried at T = 60 ºC during 24 h. The particles obtained were then characterized by XRD (PanAlytical X'Pert PRO Alfa-1 diffractometer with $\lambda_{CuK\alpha}$=1.54056 Å), FTIR (Bomem MB-154S) and SEM (FEI Quanta 400FEG ESEM/EDAX Genesis X4M with an accelerating voltage of 15 kV and 20 kV), where samples were covered by a 10 nm layer of gold. For particle size distribution (LS 230, Beckman Coulter), cryo-SEM (JEOL JSM 6301F/Oxford INCA Energy 350/Gatan Alto 2500 with an accelerating voltage of 15 kV) and zeta potential measurements (Malvern Nano ZetaSizer), suspensions were collected at the end of each experiment and directly analyzed. As to the Ca/P molar ratio of the final product, total phosphorus was quantified by the ascorbic acid method (spectrophotometer PG Instruments Ltd. T60 UV/VIS) and calcium was measured by atomic absorption spectroscopy (spectrometer GBC 932Plus).

3.3 Results and Discussion

3.3.1 HAp precipitation process

From a thermodynamic point of view, the existing conditions favor the spontaneous precipitation of HAp, since it is the most stable calcium phosphate for pH between 4 and 12 at body temperature (Elliot 1994). But considering the kinetics it does not mean that HAp is the only calcium phosphate to precipitate (Koutsopoulos 2002). Thus, to reduce the influence of the kinetic factors, precipitation of HAp was performed from diluted solutions so as to obtain low supersaturations. Indeed, at low supersaturations homogeneous formation of the most stable phase is to be expected as the solution would be saturated or even undersaturated with respect to the other phases (van Kemenade and de Bruyn 1987). As it was referred above, calcium hydroxide is slightly soluble in water and generally a suspension with aggregates of undissolved calcium hydroxide is obtained. Therefore, through the use of diluted solutions it is intended to get a homogeneous solution of hydroxide and calcium ions in order to avoid the formation of local concentration gradients, so allowing a better control of the reaction conditions.

3.3.2 HAp precipitation process for mixing molar ratios Ca/P = 1.00, 1.33 and 1.67

The pH of the reaction medium was continuously measured during the precipitation process for all operating conditions (**Figure 3.3**). Initial pH, corresponding to the pH of the saturated aqueous solution of calcium hydroxide, was high (>12) and similar to the expected value (Safavi and Nakayama 2000). After the addition of the orthophosphoric acid aqueous solution, pH decreased and reached a plateau at approximately 10.8, 8.2 and 6.2 for Ca/P = 1.67, 1.33 and 1.00, respectively. Then, pH decreased slowly and stabilized, showing that the majority of the reaction is completed after, approximately, 10000 s. Further, for Ca/P = 1.33, pH stabilized near 7, as intended.

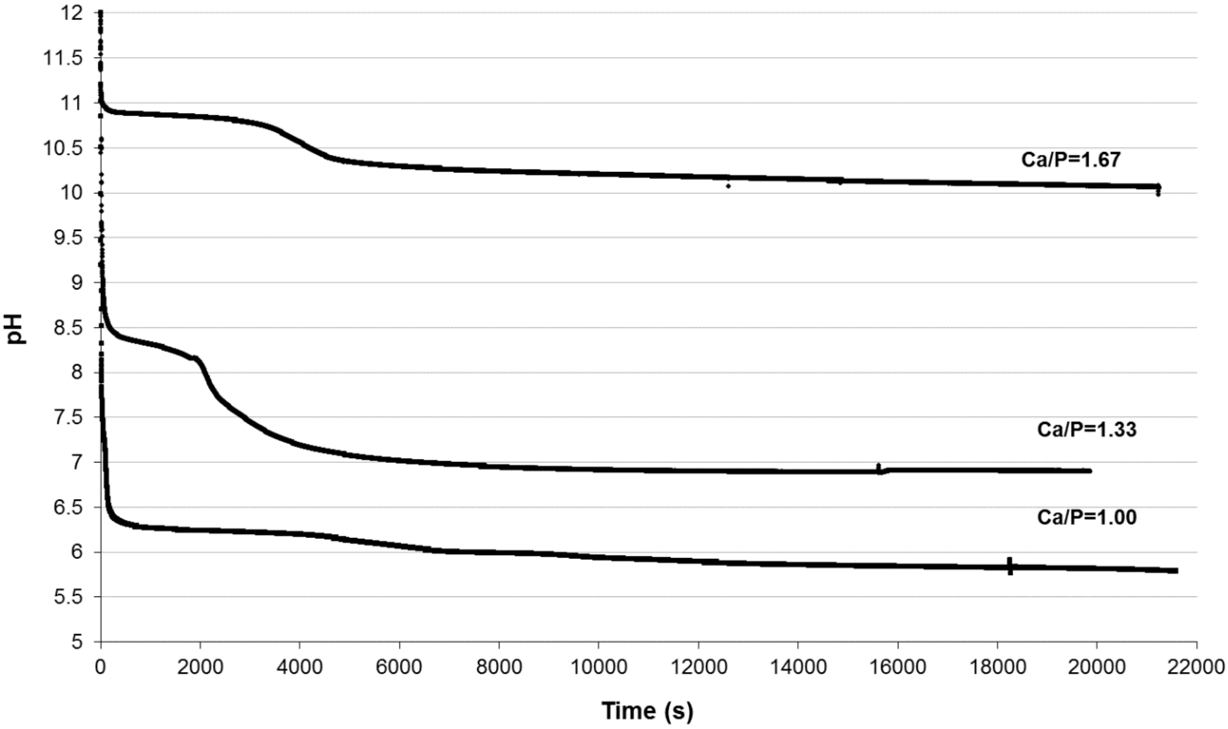

Figure 3.3. Variation of pH with time during HAp precipitation at *T* = 37 ºC for different mixing Ca/P molar ratios.

XRD patterns of the final products are shown in **Figure 3.4**. Formation of single-phased HAp was verified, since characteristic peaks of HAp are evidenced in diffraction patterns. Moreover, XRD patterns exhibit broad diffraction peaks, namely at 26 º2θ and 30 to 34 º2θ, suggesting the presence of amorphous phase or considerably small particles (Tadic et al. 2002). Besides, XRD patterns obtained are similar to XRD patterns of biological apatites, which also present broad diffraction peaks, characteristic of small crystallites (Marković et al. 2011).

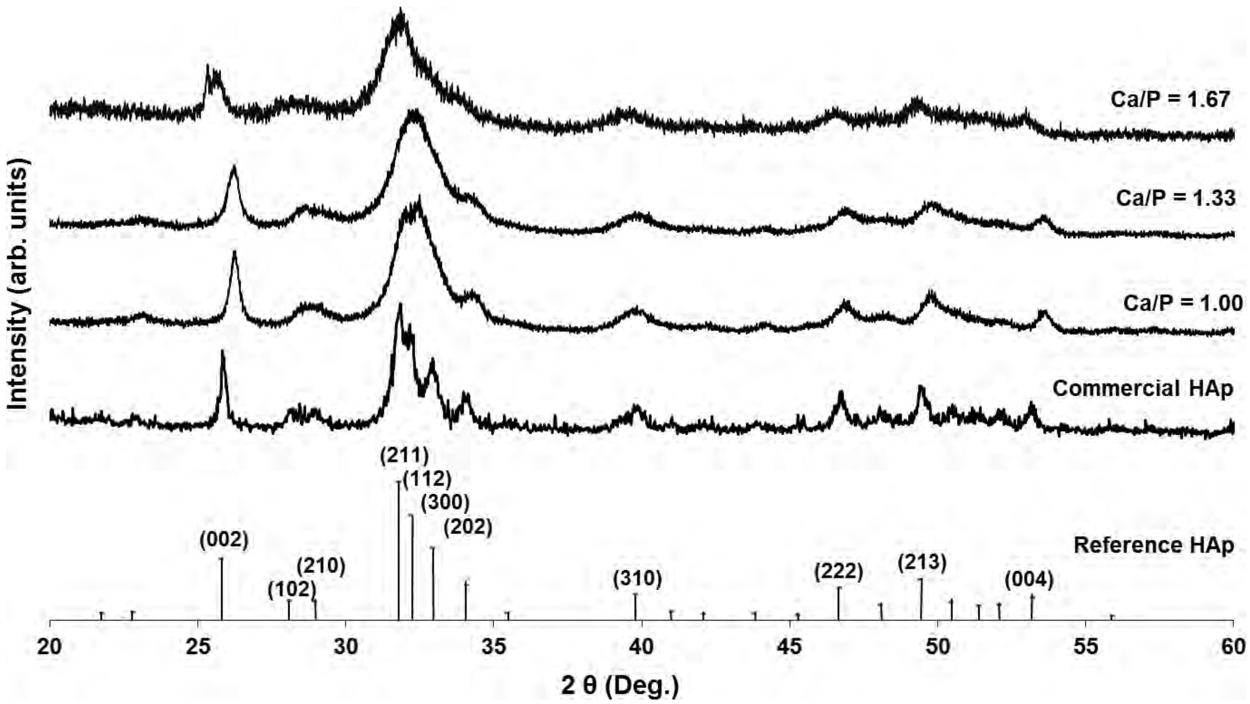

Figure 3.4. XRD patterns of the products formed during HAp precipitation at *T* = 37 ºC for different mixing Ca/P molar ratios.

Functional groups of HAp were confirmed by FTIR analysis (**Figure 3.5**). Bands for the hydroxyl group, OH^-, and for the phosphate group, PO_4^{3-}, although not well resolved, are exhibited. Moreover, spectra exhibit a broad band from approximately 3700 to 3000 cm^{-1} and a peak at 1643 cm^{-1}, revealing the existence of adsorbed water on the HAp particles, which can be justified by the low drying temperature (60 ºC) and the absence of a ripening (ageing) treatment (Koutsopoulos 2002; Osaka et al. 1991; Zhou et al. 2008). The peak assigned to stretching mode of OH^- (around 3571 cm^{-1}) is weak in the spectra of the products obtained with the mixing Ca/P molar ratios 1.33 and 1.00, and is not visible in the spectrum of the precipitate formed with the mixing Ca/P molar ratio 1.67. This can be due to the overlap with the broad peak of the adsorbed water on HAp particles (Ma and Zhu 2009). The peak related to vibrational mode of OH^- (around 630 cm^{-1}) is difficult to detect due to the quality of the signal in this region of the spectra. Concerning peaks assigned to vibrations of the phosphate group, PO_4^{3-}, the broadening of the phosphate characteristic bands at 900-1200 cm^{-1} and at 580-603 cm^{-1} may be explained by the small dimensions of HAp particles precipitated (Venkateswarlu et al. 2010). FITR spectra also exhibit carbonate bands, which can be explained by the absorption of CO_2 from air or water, once the reaction system was open to air. Carbonate bands were mainly observed in the spectra of the precipitate obtained for the larger mixing Ca/P molar ratio, since alkaline solutions readily absorb CO_2 (Osaka et al.

1991). In addition, carbonate band positions at approximately 1459, 1422 and 875 cm^{-1} for Ca/P = 1.33 and Ca/P = 1.00, and at 1424 and 875 cm^{-1} for Ca/P = 1.67, seem to indicate that the HAp formed is carbonated HAp of B-type, where the carbonate ions occupy the phosphate ions sites (Landi et al. 2003). Further, presence of peaks assigned to the hydrogen phosphate group, HPO_4^{2-} (Koutsopoulos 2002) are visible in all the spectra. This also may indicate the formation of calcium deficient HAps.

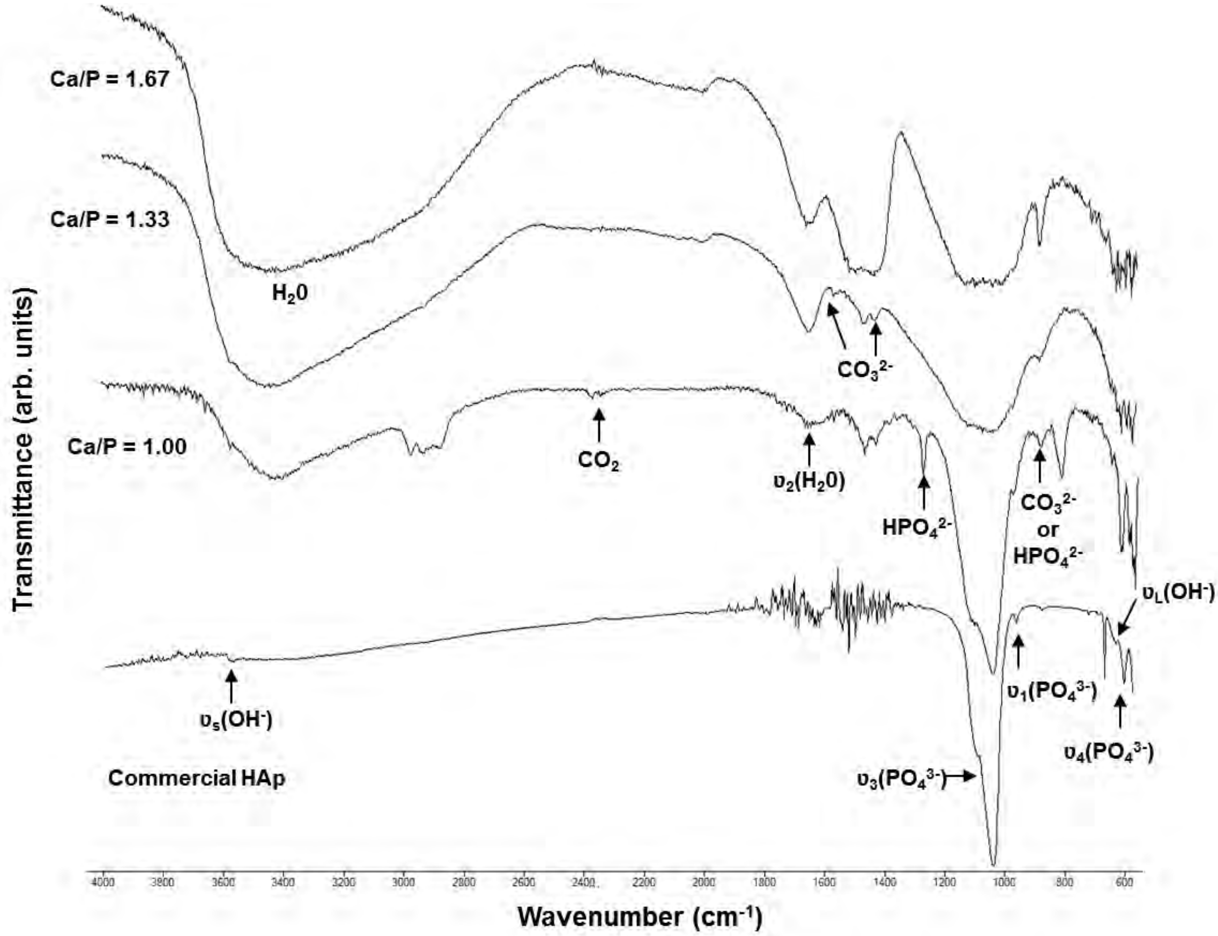

Figure 3.5. FTIR spectra of the products formed during HAp precipitation at *T* = 37 ºC for different mixing Ca/P molar ratios.

Precipitates were also characterized in terms of their final Ca/P molar ratio.

Table 3.1. Ca/P molar ratio of the final products formed for different mixing Ca/P molar ratios.

Mixing Ca/P	Final Ca/P
1.00	1.16 ± 0.02
1.33	1.78 ± 0.05
1.67	1.33 ± 0.04
Commercial HAp	1.811 ± 0.0025

According to **Table 3.1** precipitates obtained exhibit a Ca/P molar ratio different from the Ca/P molar ratio of stoichiometric HAp. Indeed, from XRD and FTIR analysis, HAps obtained are calcium-deficient and/or carbonated. For mixing Ca/P molar ratios of 1.00 and 1.67, it seems that the HAp obtained is calcium deficient, since their Ca/P molar ratio is lower than the stoichiometric value. Actually, HAp is a compound with a variable composition existing over Ca/P molar ratios from 1.67 for stoichiometric to $\approx$1.5 for fully calcium deficient HAp (Wang and Nancollas 2008), and sometimes even outside this range (Elliot 1994). The final Ca/P molar ratio of the precipitate obtained for a mixing Ca/P molar ratio of 1.00 is too low to be considered HAp. However, XRD and FTIR results show that the product formed is HAp. As to the Ca/P molar ratio of the final product obtained with a mixing Ca/P molar ratio of 1.33, it is higher than the stoichiometric value, showing thus the formation of a carbonated HAp of B-type (Landi et al. 2003; Kumta et al. 2005).

Based on the results presented above, the most promising experiment from the point of view of the objectives mentioned is the one with a mixing molar ratio Ca/P=1.33, as stable HAp nanoparticles were obtained under near-physiological conditions of temperature and pH.

3.3.3 Characterization of the HAp precipitation process for a mixing molar ratio Ca/P = 1.33

Supersaturation with respect to HAp, octacalcium phosphate (OCP) and beta-tricalcium phosphate (β-TCP) was calculated based on the ratio between the calcium concentration measured and the calcium concentration at equilibrium (**Figure 3.6**). The equilibrium concentration of calcium was determined using published solubility isotherms of the different calcium phosphate salts for the system $Ca(OH)_2$–H_3PO_4–H_2O at 37 ºC (Fernández et al. 1999). According to the existing conditions of pH and supersaturation (see **Figure 3.3** and **Figure 3.6**), the calcium phosphate to precipitate should be HAp.

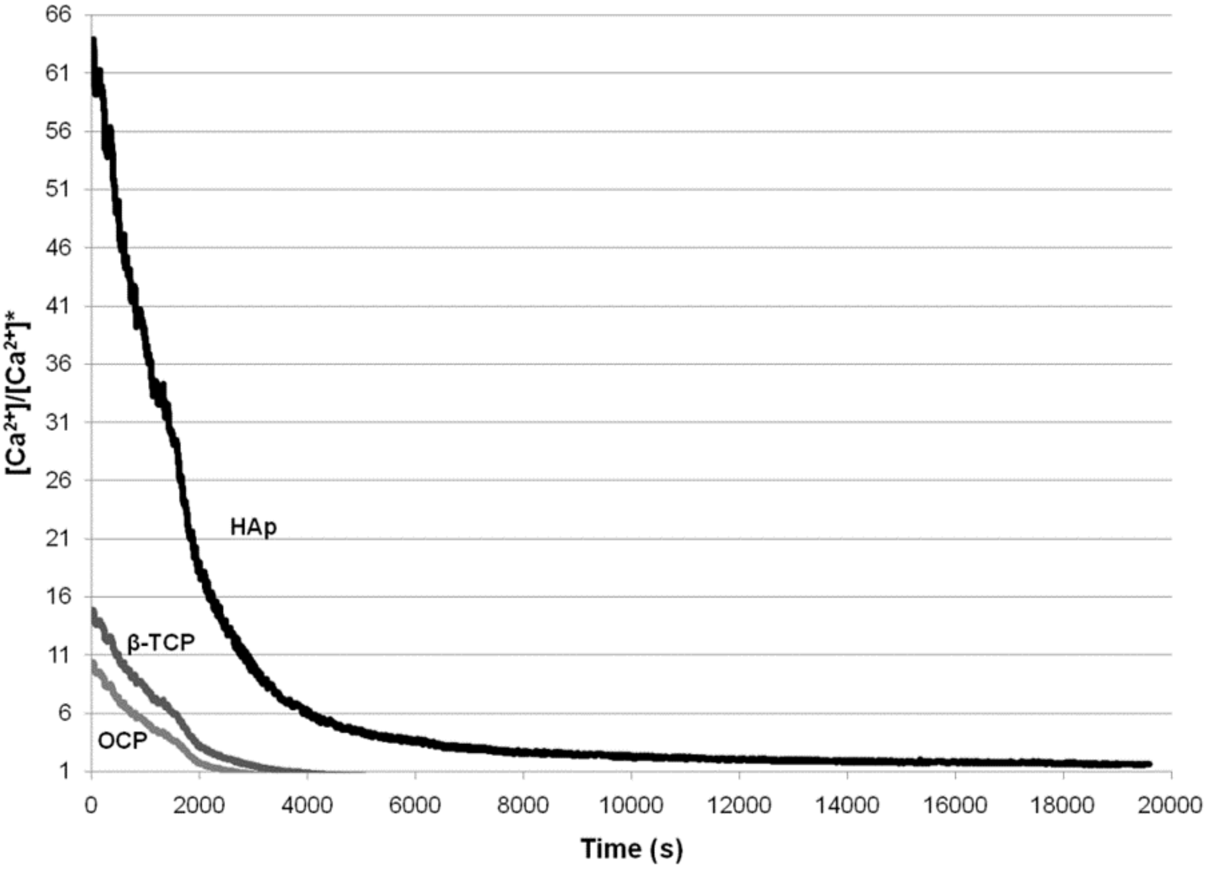

Figure 3.6. Variation of supersaturation with time with respect to HAp, OCP and β-TCP.

From **Figure 3.7**, three stages can be observed during HAp precipitation with a mixing molar ratio Ca/P=1.33.

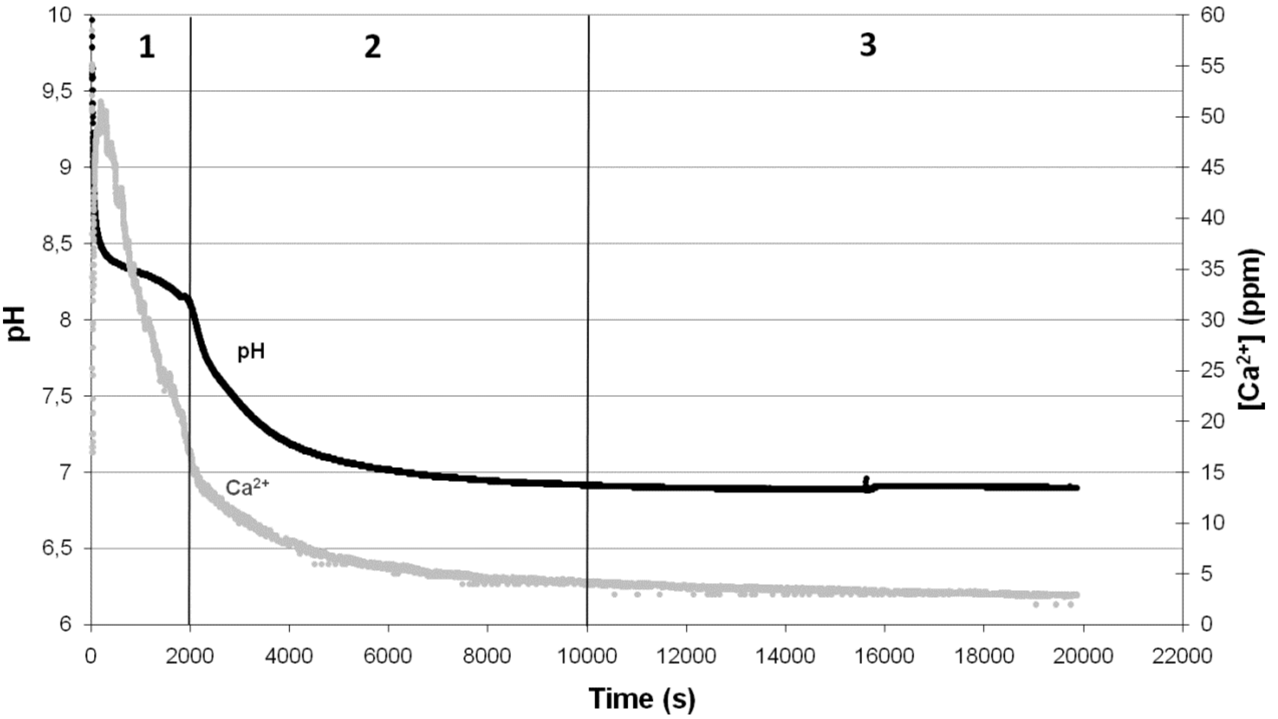

Figure 3.7. pH and $[Ca^{2+}]$ variation with time during HAp precipitation for a mixing molar ratio Ca/P=1.33.

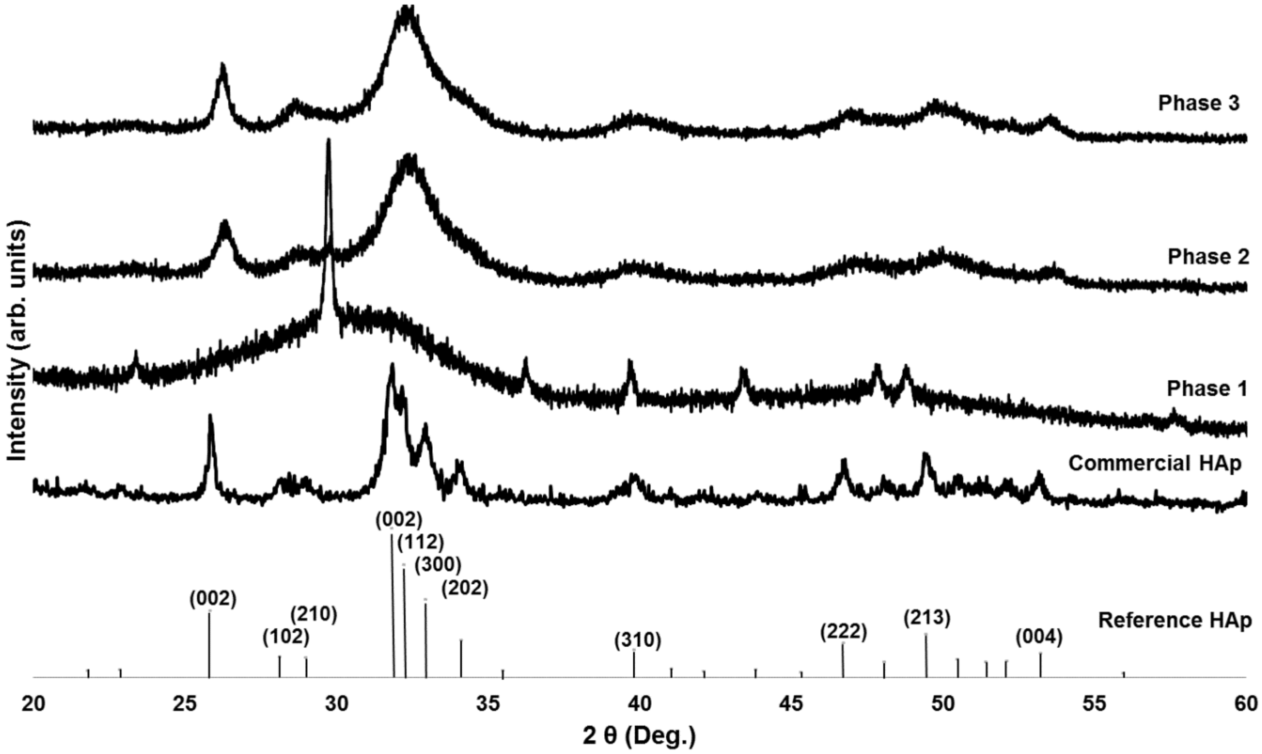

Figure 3.8. XRD patterns of the products formed in the different stages of HAp precipitation for a mixing molar ratio Ca/P=1.33.

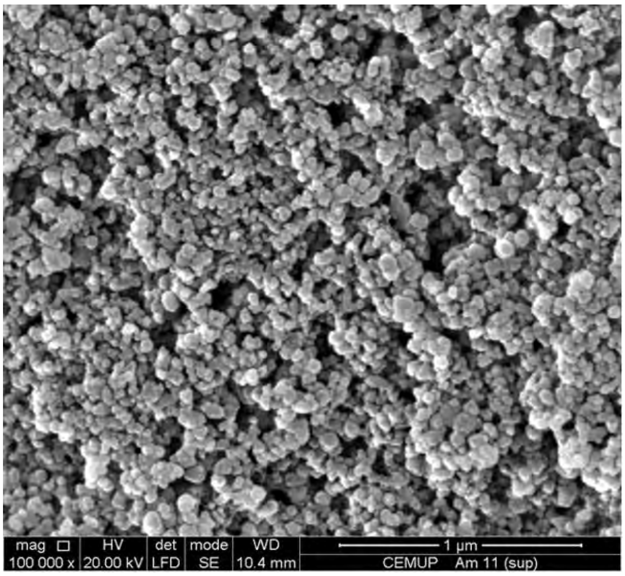

Figure 3.9. SEM image of the product formed in stage 1 of HAp precipitation for a mixing molar ratio Ca/P=1.33.

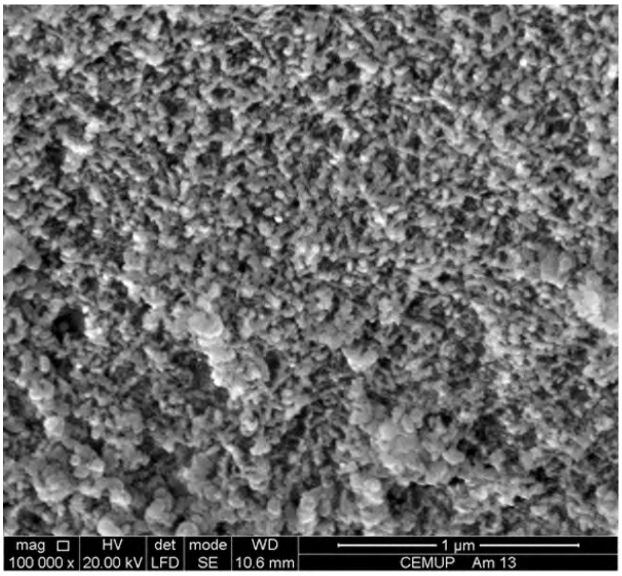

Figure 3.10. SEM image of the product formed in stage 2 of HAp precipitation for a mixing molar ratio Ca/P=1.33.

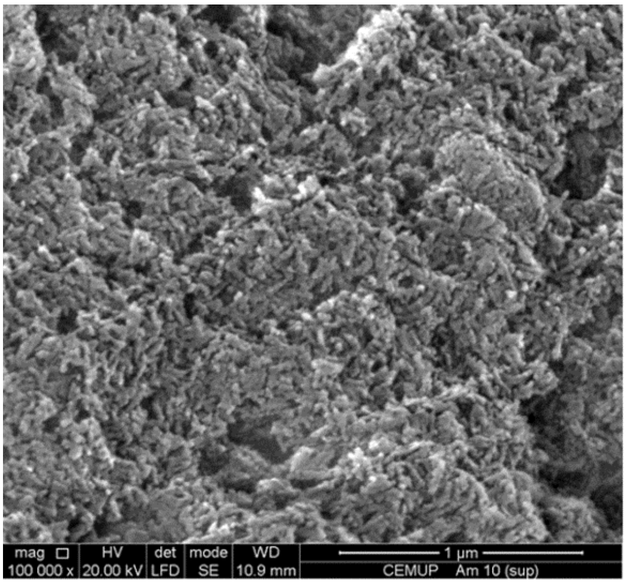

Figure 3.11. SEM image of the product formed in stage 3 of HAp precipitation for a mixing molar ratio Ca/P=1.33.

In stage 1, there is a decrease in pH (from approximately 12 to 8.2) followed by a period of stabilization, and a decrease in calcium concentration. Particles formed seem to be spherical with a diameter of approximately 20 nm and in an amorphous state (**Figure 3.9**). According to XRD results (**Figure 3.8**), precipitation of amorphous calcium phosphate $Ca_3(PO)_2$ (ACP) occurs, which can be described by the following equation:

$$3Ca(OH)_2 + 2H_3PO_4 \rightarrow Ca_3(PO_4)_2 \downarrow + 6H_2O \qquad (3.2)$$

During stage 2, it seems that transformation of ACP to HAp occurs. In fact, XRD results (see **Figure 3.8**) confirmed the presence of HAp. Regarding SEM images (**Figure 3.10**), particles with two distinguished forms are shown, one spherical with a diameter around 20 nm and similar to the particles observed in stage 1, and one more elongated, with approximately 20 nm width and 100 nm long. According to Equation 3, transformation of ACP to HAp causes consumption of calcium and hydroxide ions, which is experimentally verified (see **Figure 3.7**):

$$8Ca_3(PO_4)_2 + Ca^{2+} + 4OH^- + H_2O \rightarrow 5Ca_5(PO_4)_3OH + HPO_4^{2-} \qquad (3.3)$$

In stage 3, pH and [Ca^{2+}] stabilize, meaning that the majority of the growth process is completed and that the product formed is stable. **Figure 3.8** confirms that the product formed is HAp, the XRD curves of stage 2 and stage 3 being overlapped. In terms of morphology and size, **Figure 3.11** shows rod-like particles of about 20 nm width and 100 nm long.

Based on the results presented above, it seems that the precipitation process is characterized by formation of ACP and its subsequent conversion to HAp. Nevertheless and despite not being verified experimentally, formation of octacalcium phosphate $Ca_4H(PO_4)_3$ (OCP) could be expected, since the system is supersaturated with respect to OCP at the beginning of the experiment (see **Figure 3.6**). According to Equation (3.4), transformation of ACP into OCP requires an uptake of phosphate and hydrogen ions and a release of calcium into solution.

$$7Ca_3(PO_4)_2 + HPO_4^{2-} + 4H^+ \rightarrow 5Ca_4H(PO_4)_3 + Ca^{2+} \qquad (3.4)$$

But this is not confirmed by the experimental data, where a decrease of both calcium concentration and pH is observed. However, the possibility of OCP being a precursor remains, but it is so unstable that it is rapidly converted to HAp (Equation 3.5).

$$6Ca_4H(PO_4)_3 + Ca^{2+} + 8OH^- \rightarrow 5Ca_5(PO_4)_3OH + 3HPO_4^{2-} + 3H_2O \qquad (3.5)$$

Finally, final suspensions were characterized in terms of their behavior in solution (cryo-SEM) and in terms of size distribution (laser diffraction). From cryo-SEM image (**Figure 3.12**), it can be seen that HAp particles have the tendency to aggregate in solution, forming micrometric-size clusters, while based on SEM images (see **Figure 3.10** and **Figure 3.11**) HAp crystals have a size close to 100 nm. It also can be seen that the structures formed by those clusters have a porous nature.

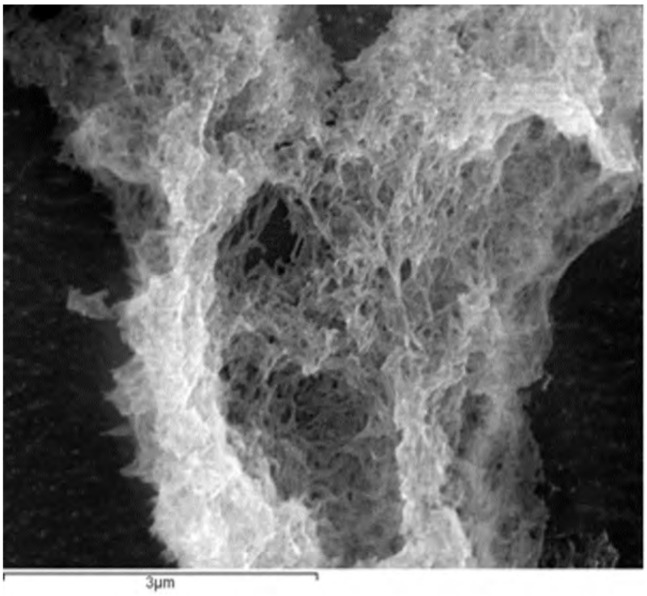

Figure 3.12. Cryo-SEM image of the final suspension obtained from HAp precipitation for a mixing molar ratio Ca/P=1.33.

It was chosen to present particle size distribution results as both volume and number distributions, allowing thus to detect the presence of aggregates and to study the size of the majority of the particles, respectively. Aggregates of HAp particles with sizes of several microns were also observed by Saeri et al. (2003). The granulometric analysis of HAp particles in volume (**Figure 3.13**a) revealed the formation of aggregates with an average equivalent diameter around 39.5 μm. From the laser analysis in number (**Figure 3.13**b), HAp crystals range in size from 0.052–0.229 μm and have a mean equivalent diameter of 0.128 μm, presenting a narrow size distribution curve, similar to the one presented in Gomes et al. (2009) work.

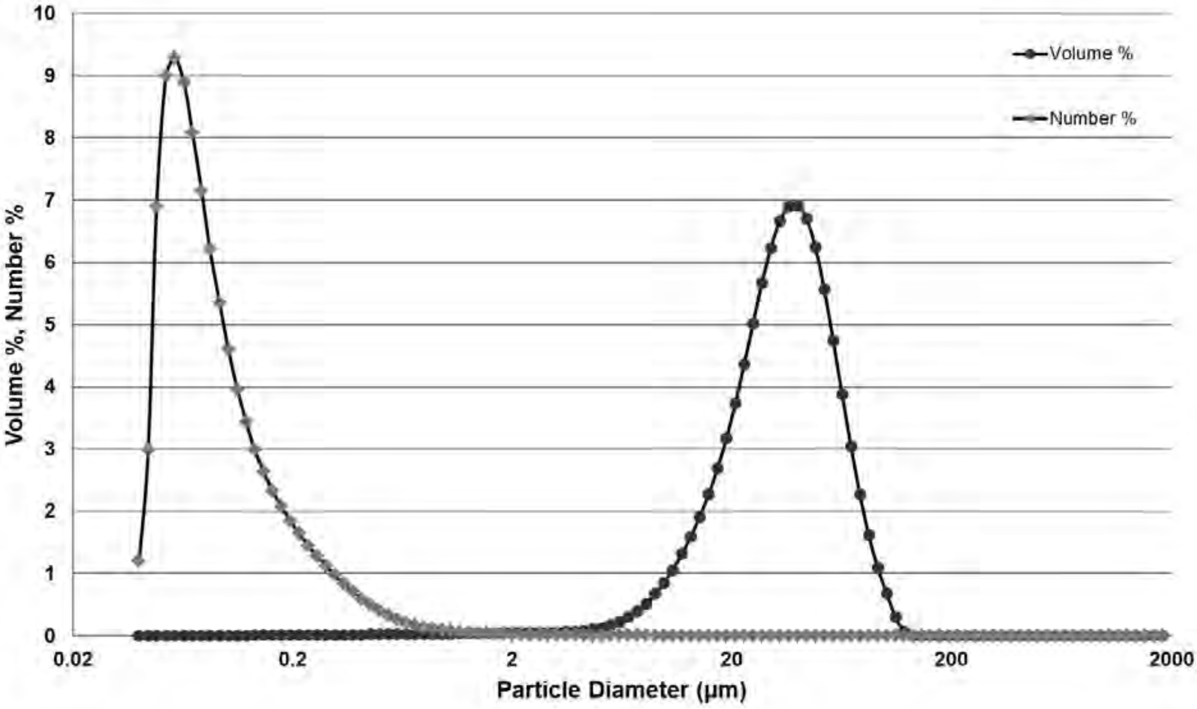

Figure 3.13. Particle size distribution of HAp particles obtained from HAp precipitation for a mixing molar ratio Ca/P=1.33: a) in volume; and b) in number.

Based on zeta potential measurements (**Table 3.2**), suspensions obtained are unstable. In the case of the product formed in stage 1, the agglomeration phenomenon can be justified by its amorphous state and particles dimensions, since they possess a high surface area to volume ratio, resulting in a high surface tension which they tend to lower by adhering to one another. The suspension seems to stabilize during the precipitation, as zeta potential value increases from stage 1 to stage 3. In fact, as crystals grow larger and become more stable, the surface tension decreases. However, zeta potential remains low indicating that the final suspension continues unstable. According to Bouyer et al. (2000), the isoelectric point (IEP) of HAp varies between 4 and 6, and the pH of the final suspension is approximately equal to 7, which is close to the IEP of HAp and can thus explain the instability of the suspension. It is important to mention that zeta potential values are widely dispersed, which is mainly due to the presence of aggregates with different sizes.

Table 3.2. Zeta potential measurements for the suspensions collected in stages 1 and 3 from HAp precipitation for a mixing molar ratio Ca/P=1.33.

	Suspension collected in stage 1	**Suspension collected in stage 3**
Zeta potential (mV)	2.99 ± 2.06	18.9 ± 4.1

3.4 Conclusion

This study describes a simple approach for the precipitation of HAp nanoparticles at 37 ºC. Experiments with different mixing Ca/P molar ratios (1.00, 1.33 and 1.67) were investigated. Formation of HAp single-phased was confirmed by XDR and FTIR, for all the experimental conditions used. Further, the resulting HAps were proved to be calcium-deficient and/or B-type carbonated. It also has been shown that for the mixing molar ratio Ca/P=1.33, stable HAp nanoparticles were obtained at a pH close to 7, which is particularly important in the preparation of HAp for medical purposes. The precipitation process was characterized, revealing the existence of three stages: precipitation of ACP, transformation of ACP to HAp, and growth of HAp. In addition, it was shown that the final product was composed of aggregates formed by nanoparticles with a rod-like shape of about 20 nm with and 100 nm long.

It is important to highlight that HAp particles produced in this work have characteristics (morphology, size and crystallinity) similar to particles already available in the market. But unlike other works, HAp precipitation was carried out at low temperature and without maintaining a fixed pH, so avoiding the use of additional chemical compounds and experimental steps. Finally, this work can be a useful contribution to other studies, namely because precipitation of HAp was studied in a reaction medium where pH is changing and also because the process was fully characterized, which is important for the understanding of the mechanism of HAp formation.

3.5 References

Bernard, L, M Freche, J.L Lacout, and B Biscans. 2000. “Modeling of the Dissolution of Calcium Hydroxyde in the Preparation of Hydroxyapatite by Neutralization.” *Chemical Engineering Science* 55 (23): 5683–5692.

Bouyer, E, F Gitzhofer, and M I Boulos. 2000. “Morphological Study of Hydroxyapatite Nanocrystal Suspension.” *Journal of Materials Science. Materials in Medicine* 11 (8): 523–31.

Elliot, J.C. 1994. *Structure and Chemistry of the Apatites and Other Calcium Orthophosphates*. Amsterdam: Elsevier.

Fernández, E., F. J. Gil, M. P. Ginebra, F. C. Driessens, J. A. Planell, and S. M. Best. 1999. “Calcium Phosphate Bone Cements for Clinical Applications. Part I: Solution Chemistry.” *Journal of Materials Science. Materials in Medicine* 10 (3): 169–76.

Gomes, P. J., V. M. T. M. Silva, P. A. Quadros, M. M. Dias, and J. C. B. Lopes. 2009. “A Highly Reproducible Continuous Process for Hydroxyapatite Nanoparticles Synthesis.” *Journal of Nanoscience and Nanotechnology* 9 (6): 3387–3395.

van Kemenade, M.J.J.M., and P.L. de Bruyn. 1987. “A Kinetic Study of Precipitation from Supersaturated Calcium Phosphate Solutions.” *Journal of Colloid and Interface Science* 118 (2): 564–585.

Koutsopoulos, S. 2002. “Synthesis and Characterization of Hydroxyapatite Crystals: a Review Study on the Analytical Methods.” *Journal of Biomedical Materials Research* 62 (4): 600–12.

Kumta, P. N., C. Sfeir, D.-H. Lee, D. Olton, and D. Choi. 2005. “Nanostructured Calcium Phosphates for Biomedical Applications: Novel Synthesis and Characterization.” *Acta Biomaterialia* 1 (1): 65–83.

Landi, E., G. Celotti, G. Logroscino, and A. Tampieri. 2003. “Carbonated Hydroxyapatite as Bone Substitute.” *Journal of the European Ceramic Society* 23 (15): 2931–2937.

Lynn, A.K., and W Bonfield. 2005. “A Novel Method for the Simultaneous, Titrant-Free Control of pH and Calcium Phosphate Mass Yield.” *Accounts of Chemical Research* 38 (3): 202–207.

Ma, M.-G., and J.-F. Zhu. 2009. “Solvothermal Synthesis and Characterization of Hierarchically Nanostructured Hydroxyapatite Hollow Spheres.” *European Journal of Inorganic Chemistry* (36): 5522–5526.

Marković, S., L. Veselinović, M. J. Lukić, L. Karanović, I. Bračko, N. Ignjatović, and D. Uskoković. 2011. “Synthetical Bone-like and Biological Hydroxyapatites: a Comparative Study of Crystal Structure and Morphology.” *Biomedical Materials* 6.

Osaka, A., Y. Miura, K. Takeuchi, M. Asada, and K. Takahashi. 1991. “Calcium Apatite Prepared from Calcium Hydroxide and Orthophosphoric Acid.” *Journal of Materials Science: Materials in Medicine* 2 (1): 51–55.

Perry, R. H.,Green, D. W., 1997. Perry's Chemical Engineers' Handbook.

Saeri, M, A. Afshara, M. Ghorbania, N. Ehsania, and C.C. Sorrellb. 2003. “The Wet Precipitation Process of Hydroxyapatite.” *Materials Letters* 57: 4064–4069.

Safavi, K., and T. A. Nakayama. 2000. “Influence of Mixing Vehicle on Dissociation of Calcium Hydroxide in Solution.” *Journal of Endodontics* 26 (11): 649–651.

Tadic, D., F. Peters, and M. Epple. 2002. “Continuous synthesis of Amorphous carbonated apatites.” *Biomaterials* 23 (12): 2553–2559.

Venkateswarlu, K., A. Chandra Bose, and N. Rameshbabu. 2010. “X-ray peak broadening studies of Nanocrystalline hydroxyapatite by Williamson–Hallanalysis.” *Physica B: Condensed Matter* 405 (20): 4256–4261.

Zhou, W., M. Wang, W. Cheung, B. Guo, and D. Jia. 2008. “Synthesis of Carbonated Hydroxyapatite Nanospheres Through Nanoemulsion.” *Journal of Materials Science: Materials in Medicine* 10 (1): 103–110.

4 MODELING OF THE PRECIPITATION OF HAp AT 37 ºC IN A STIRRED TANK BATCH REACTOR

In this chapter, the precipitation process of HAp studied in the previous chapter was modeled. For that, the reaction system was defined based on mass balance and equilibrium equations and calcium supersaturation. The resolution of the system of equations was possible due to the knowledge of three process variables: calcium concentration, pH and temperature. The resolution of the system allowed identifying and quantifying all the chemical species present in solution during the process. The proposed model was further validated with experimental conductivity data.

4.1 Introduction

It is generally recognized that the crystallization of many calcium phosphates involves the formation of metastable precursor phases that subsequently dissolve as the precipitation reaction proceeds (Wang and Nancollas 2008). Thus, complex intermediate phases can participate in the crystallization process. Indeed, by mixing a calcium hydroxide aqueous solution with an orthophosphoric acid aqueous solution for a mixing Ca/P molar ratio 1.33, the precipitation of HAp occurs after the initial precipitation of an intermediate metastable phase, amorphous calcium phosphate (ACP) (see 3.3.3). Although it was not experimentally verified, precipitation of HAp, under the present reaction conditions, generally involves the formation of one more precursor phase, octacalcium phosphate (OCP) (Wang and Nancollas 2008). Further, the results obtained show that the Ostwald rule of stages, which states that the least stable (most soluble phase) forms preferentially in a sequential precipitation (Wang and Nancollas 2008), is likely to be obeyed for the system studied. However, pH is another important parameter in determining the likelihood of the formation of calcium phosphate phases, once at high pH the precipitation of more acidic phases, such as DCPD and OCP, can be ruled out.

According to the results presented in the previous chapter, three stages were identified in the precipitation process of HAp at 37 °C in a stirred tank batch reactor, obtained from mixing of diluted aqueous solutions of calcium hydroxide and orthophosphoric acid with a mixing Ca/P molar ratio 1.33:

- spontaneous precipitation of ACP;
- transformation of ACP to HAp;
- growth of HAP.

Due to the complexity of the system, chemical species present in the solution over the precipitation process must be characterized and quantified. These determinations are based, typically, on electrochemical measurements or quantitative analysis data, with the lowest possible number of measurements for the determination of the composition and properties of the system.

Concentrations of the solutions may be determined directly or indirectly by measuring certain solution properties that are dependent upon concentration. Usually, density, viscosity, refractive index, and electrical conductivity are properties chosen for this purpose (Oliveira 2007). They can be measured with high accuracy, especially when measurements are made under controlled conditions.

The definition of the reaction system and the resolution of the system of equations resulting from mass balance and equilibrium equations, as well as calcium supersaturation, allowed identifying and quantifying all the chemical species present in solution during the process. Therefore, it allowed identifying the composition of the precipitate and its evolution with time.

4.2 Materials and Methods

4.2.1 Experimental procedure

Precipitation of HAp was performed at 37 °C in a 1 dm^3 stirred tank batch reactor, being the apparatus already described in the previous chapter. As mentioned in Chapter 3, HAp was synthesized by the mixing of equal volumes (0.5 dm^3) of a saturated calcium hydroxide (Riedel-de Haën, 96%) aqueous solution and an orthophosphoric acid (Pronalab, 85%) aqueous solution. Reactants solutions were prepared according to the protocol described in 3.2.1. Calcium concentration, pH, temperature and conductivity were continuously measured (inolab pH/cond level 3, WTW) and recorded. The initial Ca/P molar ratio used was 1.33 and the duration of the run varied according to the final conditions pretended. The maximum duration was about 6 h. At the end of each experiment, suspension samples were withdrawn, filtered and dried in order to determine the type of precipitate. Crystals were characterized in terms of composition (XRD) and morphology (SEM) (see 3.2.2).

4.2.2 Description of the system

Precipitation of HAp follows complex mechanisms of formation and growth involving numerous chemical species such as phosphate ions, and various calcium and phosphate complexes. The $Ca(OH)_2$-H_3PO_4-H_2O system, in accordance with the literature (Oliveira 2007; Tsuge et al. 1996; Lazić 1995), is defined by the following reactions:

$$\mathrm{H_2O\ (aq) \leftrightarrow H^+\ (aq) + \ OH^-(aq)} \tag{4.1}$$

$$\mathrm{H_3PO_4\ (aq) \leftrightarrow H^+(aq) + \ H_2PO_4{}^-(aq)} \tag{4.2}$$

$$\mathrm{H_2PO_4^-\ (aq) \leftrightarrow H^+(aq) + \ HPO_4{}^{2-}(aq)} \tag{4.3}$$

$$\mathrm{HPO_4^{2-}\ (aq) \leftrightarrow H^+(aq) + \ PO_4{}^{3-}(aq)} \tag{4.4}$$

$$\mathrm{CaHPO_4\ (aq) \leftrightarrow Ca^{2+}(aq) + \ HPO_4{}^{2-}(aq)} \tag{4.5}$$

$$\mathrm{CaPO_4^-\ (aq) \leftrightarrow Ca^{2+}(aq) + \ PO_4{}^{3-}(aq)} \tag{4.6}$$

$$\mathrm{CaH_2PO_4^+\ (aq) \leftrightarrow Ca^{2+}(aq) + \ H_2PO_4{}^-(aq)} \tag{4.7}$$

$$\mathrm{CaOH^+(aq) \leftrightarrow Ca^{2+}(aq) + \ OH^-(aq)} \tag{4.8}$$

$$\mathrm{Ca_5(PO_4)_3OH\ (s) \leftrightarrow \ 5Ca^{2+}(aq) + 3PO_4^{3-}\ (aq) + OH^-\ (aq)} \tag{4.9}$$

The concentration of each chemical species involved in the reaction system presented above was calculated from a system of equations comprising:
- mass balance equations;
- equilibrium equations;
- supersaturation with respect to HAp (supersaturation of calcium).

Supersaturation with respect to HAp was estimated from the calculation of the supersaturation of calcium, i.e from the ratio between the calcium concentration in the reaction medium and the equilibrium concentration of calcium for the existing conditions. The equilibrium concentration of calcium was determined from the solubility isotherm of

HAp (see 2.2.2.3, **Figure 2.10**), which relates the solubility of HAp (in terms of calcium concentration) in function of pH at a fixed temperature (37 °C) in the system $Ca(OH)_2$-H_3PO_4-H_2O.

The result is a system of non-linear algebraic equations, which can be solved iteratively making successive approximations of the ionic strength:

$$K_1 = y_1^2\,[H^+]\,[OH^-] \tag{4.10}$$

$$K_2 = \frac{y_1^2[H^+][H_2PO_4^-]}{[H_3PO_4]} \tag{4.11}$$

$$K_3 = \frac{y_2[H^+][HPO_4^{2-}]}{[H_2PO_4^-]} \tag{4.12}$$

$$K_4 = \frac{y_1y_3[H^+][PO_4^{3-}]}{y_2[HPO_4^{2-}]} \tag{4.13}$$

$$K_5 = \frac{y_2^2[Ca^{2+}][HPO_4^{2-}]}{[CaHPO_4]} \tag{4.14}$$

$$K_6 = \frac{y_2y_3[Ca^{2+}][PO_4^{3-}]}{y_1[CaPO_4^-]} \tag{4.15}$$

$$K_7 = \frac{y_2[Ca^{2+}][H_2PO_4^-]}{[CaH_2PO_4^+]} \tag{4.16}$$

$$K_8 = \frac{y_2[Ca^{2+}][OH^-]}{[CaOH^+]} \tag{4.17}$$

$$\sigma_{HAp}^9 = \frac{y_2^5[Ca^{2+}]^5y_3^3[PO_4^{3-}]^3y_1[OH^-]}{K_{spHAp}} \tag{4.18}$$

$$\sigma_{\mathrm{HAp}} = \frac{[\mathrm{Ca}^{2+}]}{10^{-(0.0067\mathrm{pH}^4 + 0.2237\mathrm{pH}^3 - 2.4647\mathrm{pH}^2 + 10.18\mathrm{pH} - 15.545)}} \quad (4.19)$$

$$\mathrm{TCA} = [Ca^{2+}] + [CaHPO_4] + [CaH_2PO_4^+] + [CaOH^+] + [CaPO_4^-] \quad (4.20)$$

$$\mathrm{TPO} = [H_3PO_4] + [H_2PO_4^-] + [HPO_4^{2-}] + [PO_4^{3-}] + [CaHPO_4] + [CaPO_4^-] + [CaH_2PO_4^+] \quad (4.21)$$

$$I = \frac{1}{2}([\mathrm{OH}^-] + [\mathrm{H_2PO_4^-}] + 4[\mathrm{HPO_4^{2-}}] + 9[\mathrm{PO_4^{3-}}] + [\mathrm{H}^+] + 4[\mathrm{Ca}^{2+}] + [\mathrm{CaPO_4^-}] + [\mathrm{CaOH}^+] + [\mathrm{CaH_2PO_4^+}]) \quad (4.22)$$

$$y_1 = 10^{\left(\frac{-0.52\sqrt{I}}{1+\sqrt{I}}\right)} \quad (4.23)$$

$$y_2 = 10^{\left(\frac{-4*0.52\sqrt{I}}{1+\sqrt{I}}\right)} \quad (4.24)$$

$$y_3 = 10^{\left(\frac{-9*0.52\sqrt{I}}{1+\sqrt{I}}\right)} \quad (4.25)$$

$$\mathrm{pH} = -\log(y_1[H^+]) \quad (4.26)$$

The activity coefficients were determined from the Debye-Huckel equation proposed by Davies (1962):

$$\log y = -B\, z_i^2 \log\frac{\sqrt{I}}{1+\sqrt{I}} - 0.3I \quad (4.27)$$

with B = 0.52 at T = 37 ºC

Table 4.1. Equilibrium constants for the chemical reactions of the $Ca(OH)_2$-H_3PO_4-H_2O system and solubility product for HAp.

Equilibrium constant, *T* (K)	**Reference**
$K_1 = 1 \times 10^{-14}$	(Song et al. 2002)
$K_2 = 10^{-\left(\frac{799.31}{T} + 0.013486 * T - 4.5535\right)}$	(Song et al. 2002)
$K_3 = 10^{-\left(\frac{1979.5}{T} + 0.019840 * T - 5.3541\right)}$	(Song et al. 2002)
$K_4 = 10^{-11.984}$	(Matsuya et al. 1996)
$K_5 = 10^{\left(\frac{-22188}{T} - 0.2554 * T + 148.15\right)}$	(Song et al. 2002)
$K_6 = 10^{-6.337}$	(Matsuya et al. 1996)
$K_7 = 10^{\left(\frac{-8413.5}{T} - 0.08660 * T + 53.335\right)}$	(Song et al. 2002)
$K_8 = 10^{-1.288}$	(Matsuya et al. 1996)
$K_{spHAp} = 10^{-\left(\frac{8219.41}{T} + 1.6657 + 0.098215 * T\right)}$	(Song et al. 2002)

Looking at the system of equations presented above (Equations (4.10) to (4.26)) one can conclude that this system is defined by 17 equations and 20 unknowns, containing therefore three degrees of freedom. As 3 process variables were continuously measured (temperature, pH and calcium concentration), a determinate system with 17 equations and 17 unknowns is thereby achieved. It is possible to manipulate Equations (4.10)-(4.26) to obtain a sequential resolution of the system and thus to describe the dynamics of all the chemical species present in solution in the stirred tank batch reactor. An application in MATLAB was developed to solve and monitor the process (see Appendix A.1).

To evaluate if the system of equations (Equations (4.10) to (4.26)) represents correctly the precipitation process studied, the solution conductivity was measured and compared with the conductivity, *K* ($S.cm^{-1}$), calculated using the estimated concentration of the chemical species, by the formula:

$$K = \sum \frac{C_i}{1000} \lambda_i \times 1.2356 \qquad (4.28)$$

where C_i is the concentration of each species ($mol.dm^{-3}$), λ_i the correspondent molar ionic conductivity ($S.cm^2.mol^{-1}$) and 1.2356 a correction factor.

The values of λ_i used (Oliveira 2007) are presented in **Table 4.2**. These values are for 25 °C, as it was not possible to find these values for 37 °C. Therefore, a correction factor (Equation (4.28)) was used for the calculation of the conductivity. This factor was estimated based on the existing difference between the ionic activity of KCl at 25 and 37 °C (Haynes 2012), since KCl has a preponderant weight in the estimation of the conductivity. Further, it was not possible to find the ionic conductivity for some species ($CaPO_4^-$, $CaH_2PO_4^+$ and $CaOH^+$). The concentration of these ions is very small, so the error in the calculation of the conductivity will not be very relevant. It should however be underlined that these ionic conductivities are ionic conductivities at infinite dilution. Typically, the ionic conductivities of highly concentrated solutions have lower values.

The use of KCl for the adjustment of ionic strength has to be considered in solving the system of equations. The amount added to each reactant solution (see 3.2.1) interferes significantly in the calculation of the conductivity. The concentration of KCl in the resulting solutions (0.048 mol.dm^{-3}) was obtained by measuring its conductivity. KCl concentration was estimated using tabulated values of the conductivity of KCl for different concentration (Haynes 2012).

Table 4.2. Equivalent ionic activities at 25 ºC (Oliveira, 2007).

Ion	**λ_i (S.cm^2.mol^{-1})**
H^+	349.65
OH^-	198
$H_2PO_4^-$	36
$1/2HPO_4^{2-}$	57
$1/3PO_4^{3-}$	92.8
$CaPO_4^-$	
$CaH_2PO_4^+$	
$CaOH^+$	
$1/2Ca^{2+}$	59.47
K^+	73.48
Cl^-	76.31

4.3 Results and Discussion

The variation with time of the continuously measured process variables (pH, [Ca^{2+}], and T) as well as the supersaturation with respect to HAp, σ_{HAp} or [Ca^{2+}]/[Ca^{2+}]*, are presented below.

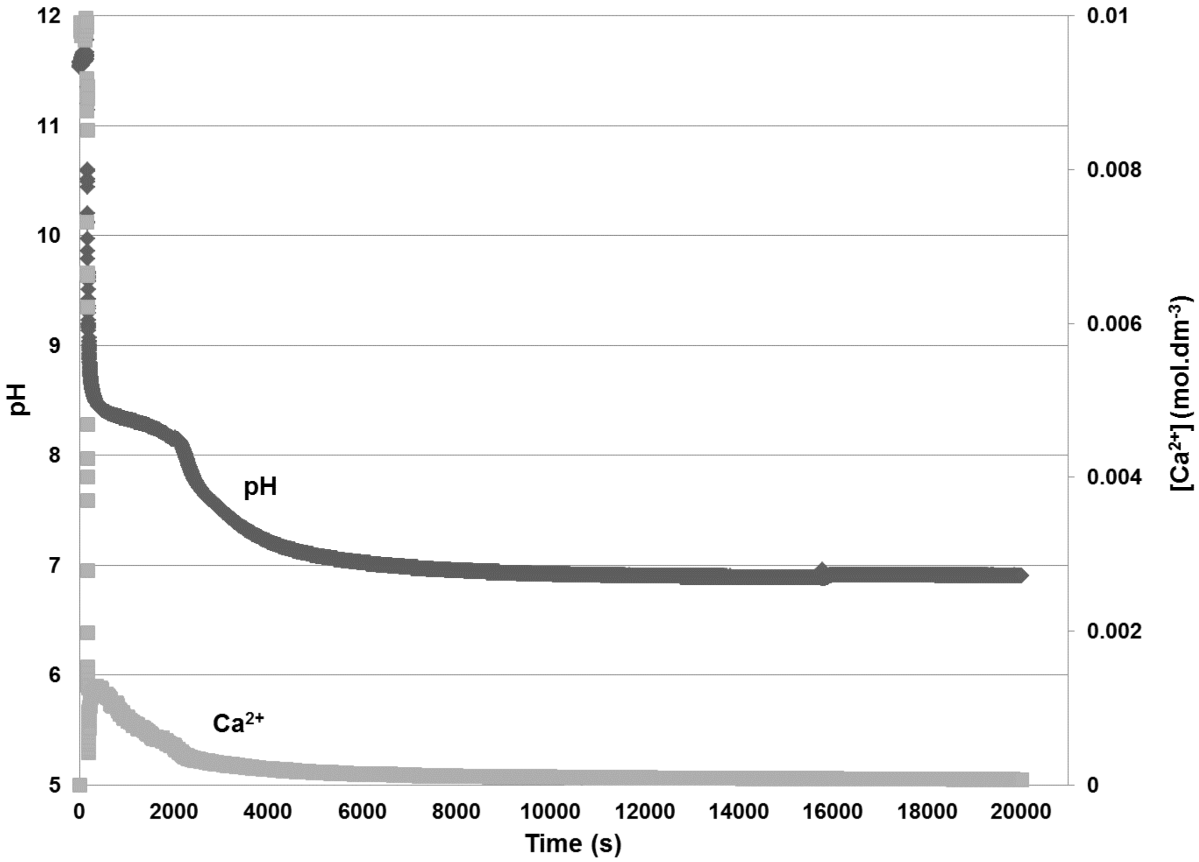

Figure 4.1. pH and [Ca^{2+}] variation with time during HAp precipitation.

The first instants are characterized by a pH drop (**Figure 4.1**) due to the addition of the orthophosphoric acid aqueous solution and to the consumption of OH^- ions for the formation of ACP, which was verified in the previous chapter. After, it reaches a first plateau at approximately 8.3, corresponding to the maturation of ACP (Uskoković and Uskoković 2011). Then, the pH value decreases again owing to the conversion of ACP to HAp and HAp growth, once both steps involve the consumption of OH^- ions (see 3.3.3). Finally, pH reaches a value close to 7 and stabilizes, suggesting the stabilization of the phase transformation. As to the calcium concentration, it initially decreases due to the addition of the orthophosphoric acid aqueous solution, and thereby due to the dilution of the calcium hydroxide solution. Then, for a short time, calcium concentration increases, which may be due to local concentration gradients and dissolution of the solid calcium hydroxide that remains in solution (see 3.2.1). Afterwards, [Ca^{2+}] decreases with two different slopes, the first stage corresponding to the precipitation of ACP and the second stage corresponding to the transformation of ACP to HAp and HAp growth.

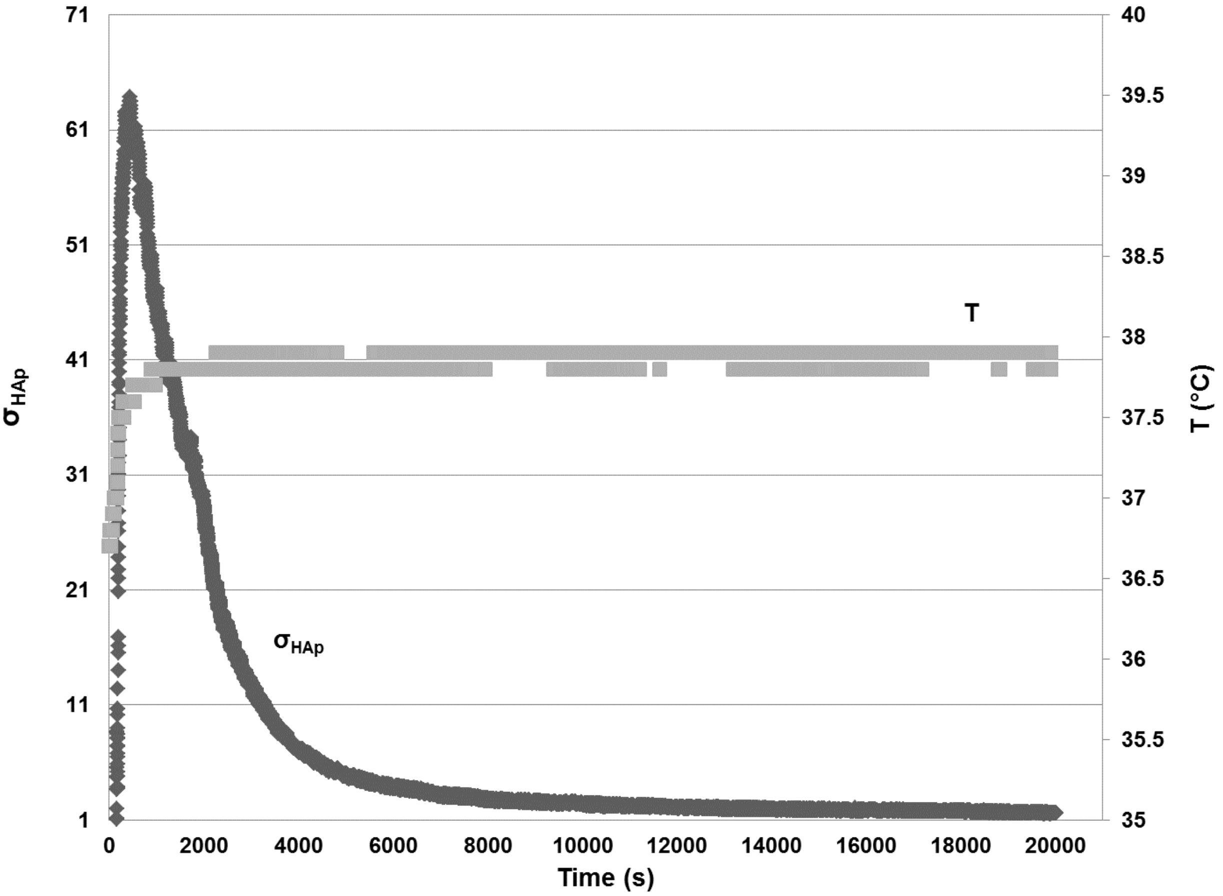

Figure 4.2. Variation of supersaturation and temperature with time with respect to HAp.

From **Figure 4.2**, one can see that the reaction medium keeps supersaturated with respect to HAp throughout the precipitation system. Indeed, σ_{HAp} remains above 1 that corresponds to the solubility of HAp. Below this limit, dissolution takes place (Uskoković and Uskoković 2011). However, one must take into account the fact that the solubility data, i.e. the calcium equilibrium concentration, was obtained from the literature (Fernández et al. 1999) for the system $Ca(OH)_2$-H_3PO_4-H_2O. Thereby, this value may be slightly different from the calcium equilibrium concentration in the system studied, since the presence of KCl in the reaction medium may influence the solubility of HAp (Chen et al. 2004; Oliveira 2007). As to the temperature, **Figure 4.2** shows that the reaction is exothermic since the temperature increases from approximately 36.7 to 37.9 °C during the precipitation process.

The results obtained from the resolution of the system of equations are presented below.

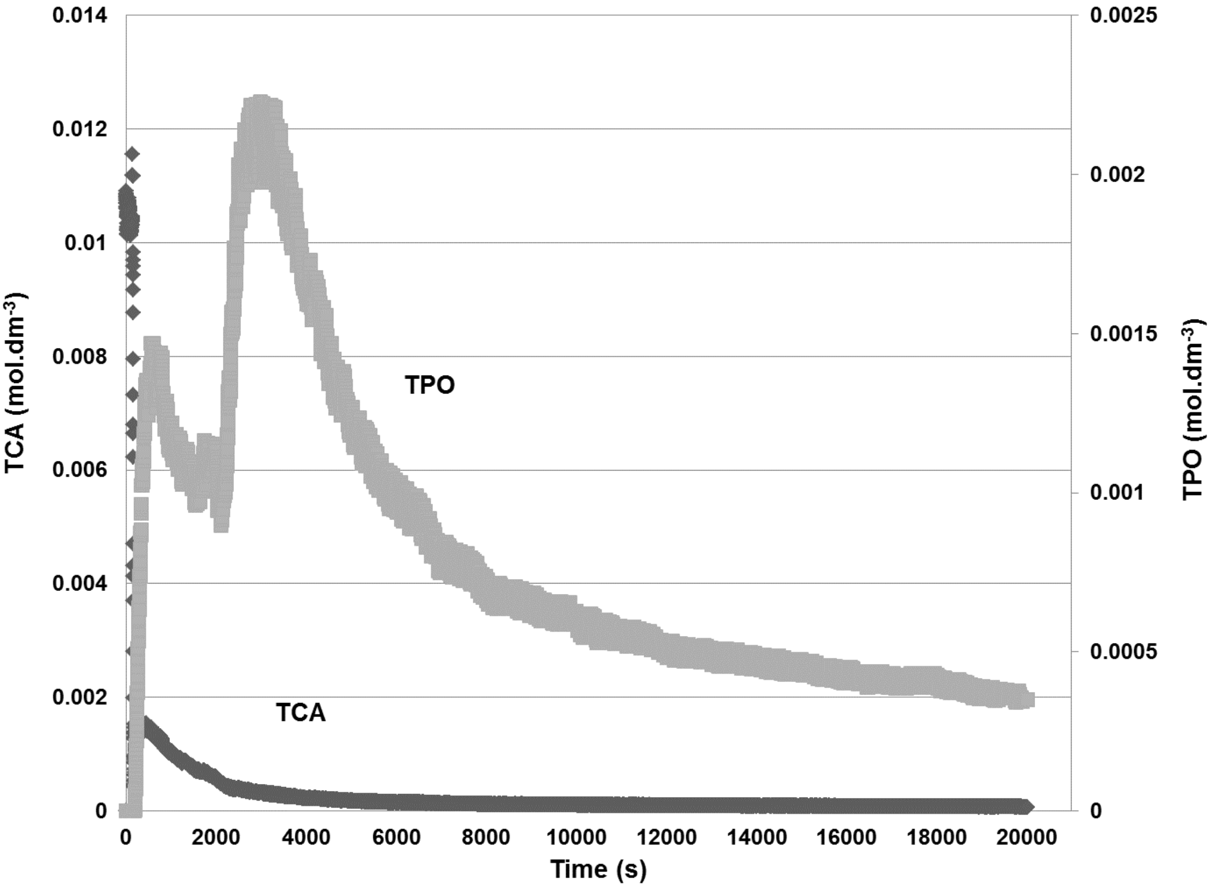

Figure 4.3. Variation of TCA and TPO with time.

Figure 4.3 shows that the total calcium in solution (TCA) decreases over the precipitation process, once calcium ions are consumed for the formation of calcium phosphates. In relation to TPO (see **Figure 4.3**), it increases in the first instants owing to the addition of orthophosphoric acid and its respective dissociation. Then, it decreases as phosphate ions are consumed during ACP precipitation (see 3.3.3). After, the total phosphate in solution increases due the conversion of ACP to HAp, since the transformation proceeds with the shift in the Ca/P molar ratio of the precipitate from 1-1.5 (Ca/P values for ACP) to 1.67 and therefore implying a release of PO_4^{3-} ions into the reaction medium (Uskoković and Uskoković 2011). Finally, TPO decreases due to the growth of HAp.

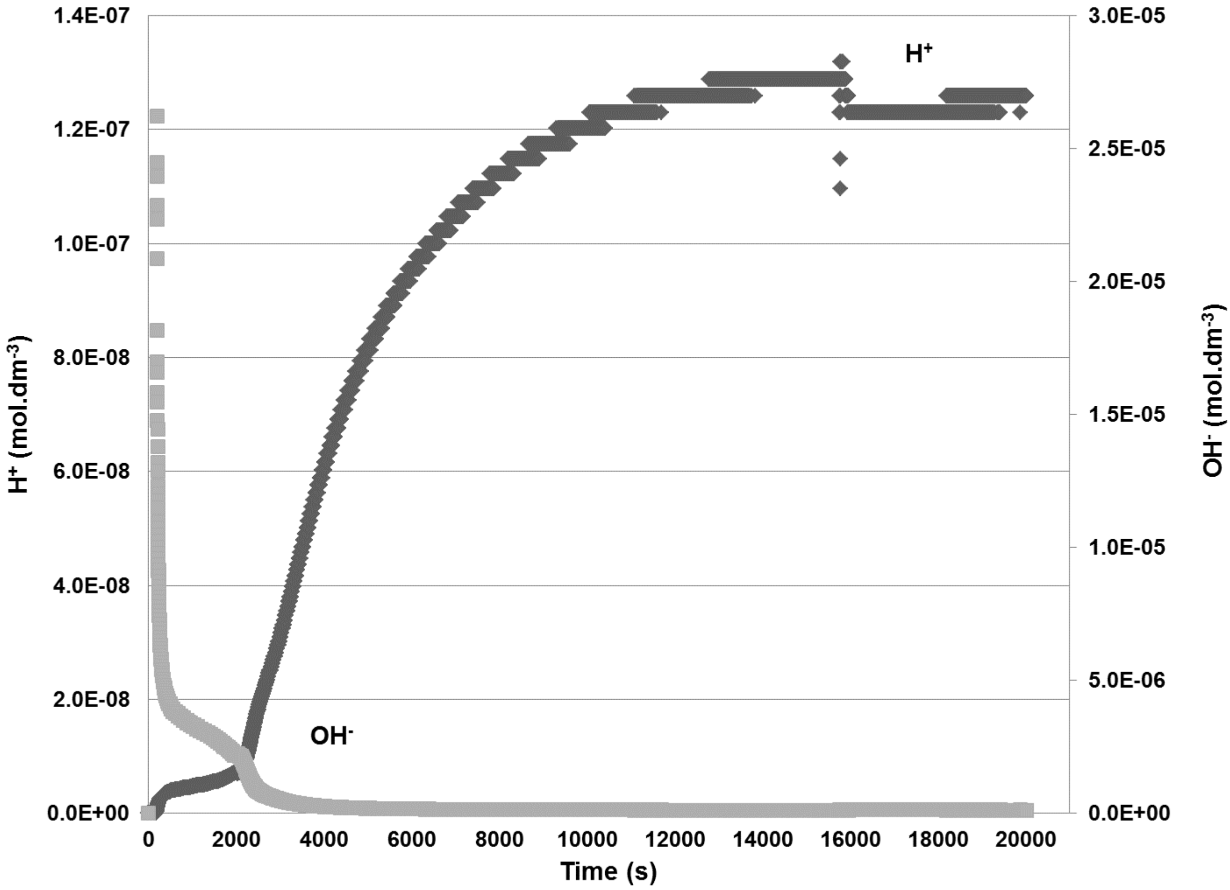

Figure 4.4. Variation of [H^+] and [OH^-] with time.

The value of [OH^-] decreases during HAp precipitation process once it is consumed, first for the formation of ACP, then during ACP transformation to HAp and finally for HAp growth (**Figure 4.4**). As to hydrogen ions, **Figure 4.4** shows that their concentration increases during the precipitation. Indeed, phosphate ions are necessary for the formation of calcium phosphate phases and these are obtained from orthophosphoric acid dissociation, which in its turn results in the release of H^+ ions.

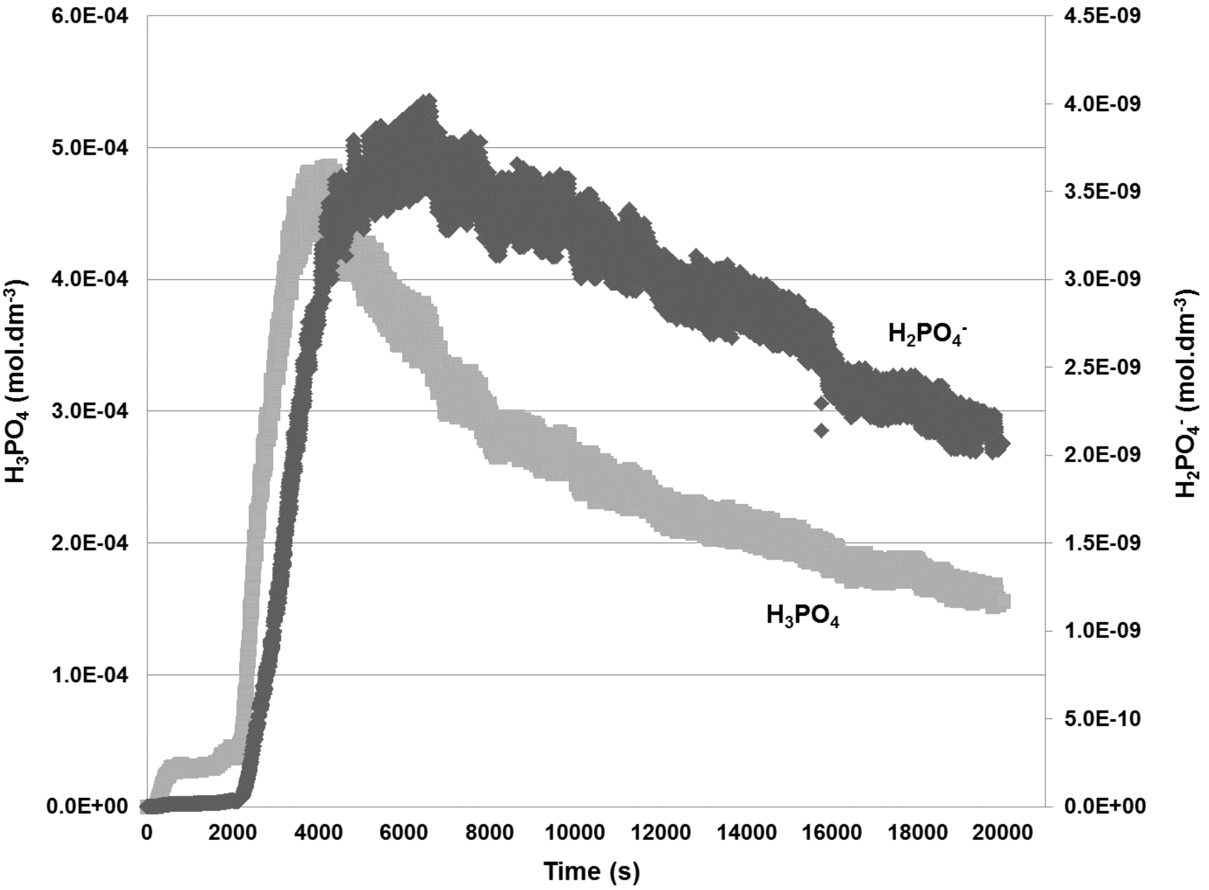

Figure 4.5. Variation of [H_3PO_4] and [$H_2PO_4^-$] with time.

The value of [H_3PO_4] is initially low as it is immediately dissociated for the release of phosphate ions, needed for the precipitation of ACP (**Figure 4.5**). Then, it increases due to the release of hydrogen phosphate ions (HPO_4^{2-}) during the transformation of ACP to HAp. Finally, it decreases, since phosphate ions are consumed for HAp growth. In relation to [$H_2PO_4^-$], it follows the same evolution as [H_3PO_4] (see **Figure 4.5**), for the same reasons mentioned above.

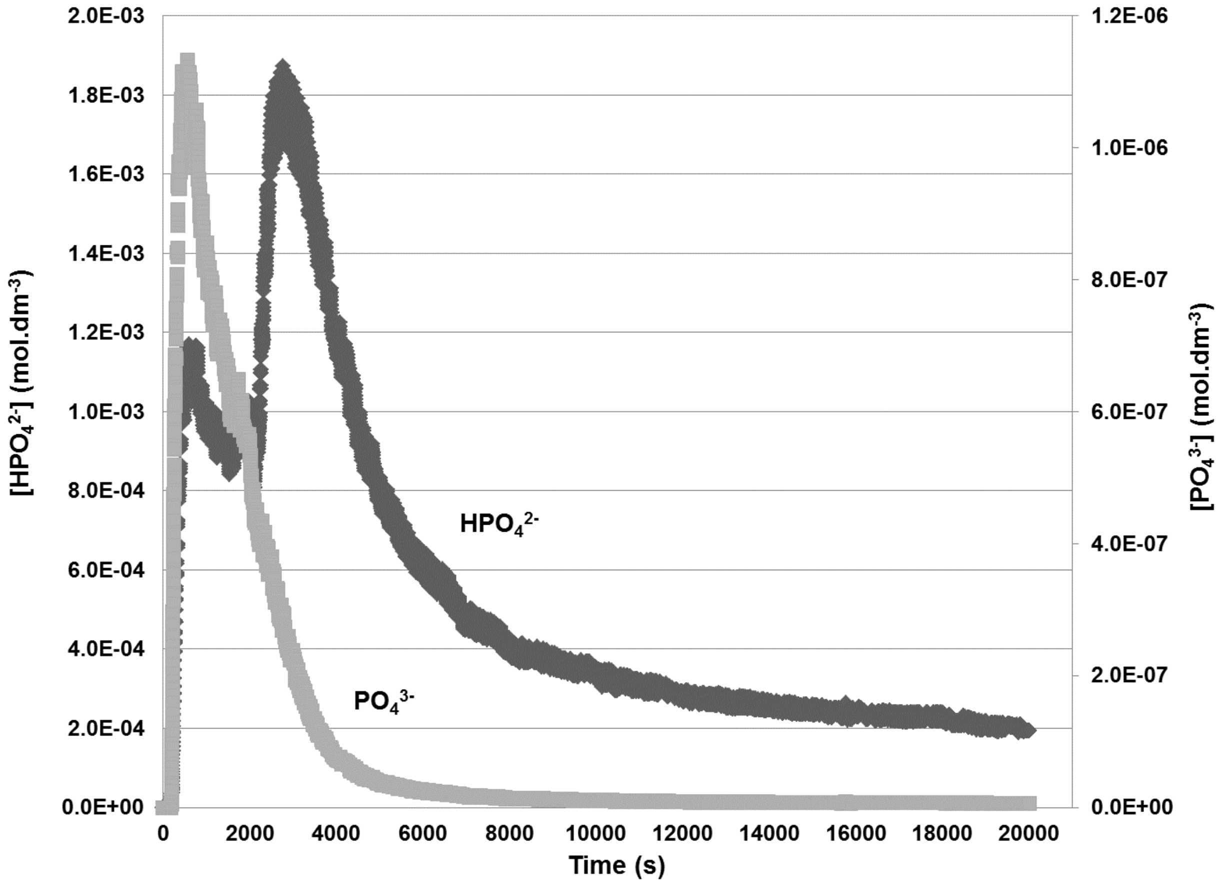

Figure 4.6. Variation of [HPO$_4^{2-}$] and [PO$_4^{3-}$] with time.

The value of [HPO$_4^{2-}$] increases at the beginning of the precipitation process (**Figure 4.6**) due to the addition of orthophosphoric acid and its subsequent dissociation. Then, it decreases as it is dissociated for the consumption of phosphate ions during the precipitation of ACP. After, it increases since it is released from the transformation of ACP to HAp (see 3.3.3). Finally, the concentration of hydrogen phosphate ions decreases once phosphate ions are consumed for the growth of HAp. [PO$_4^{3-}$] increases in the first instants owing to the addition of orthophosphoric acid and its subsequent dissociation (see **Figure 4.6**). Then, it decreases once it is consumed during ACP precipitation and HAp growth.

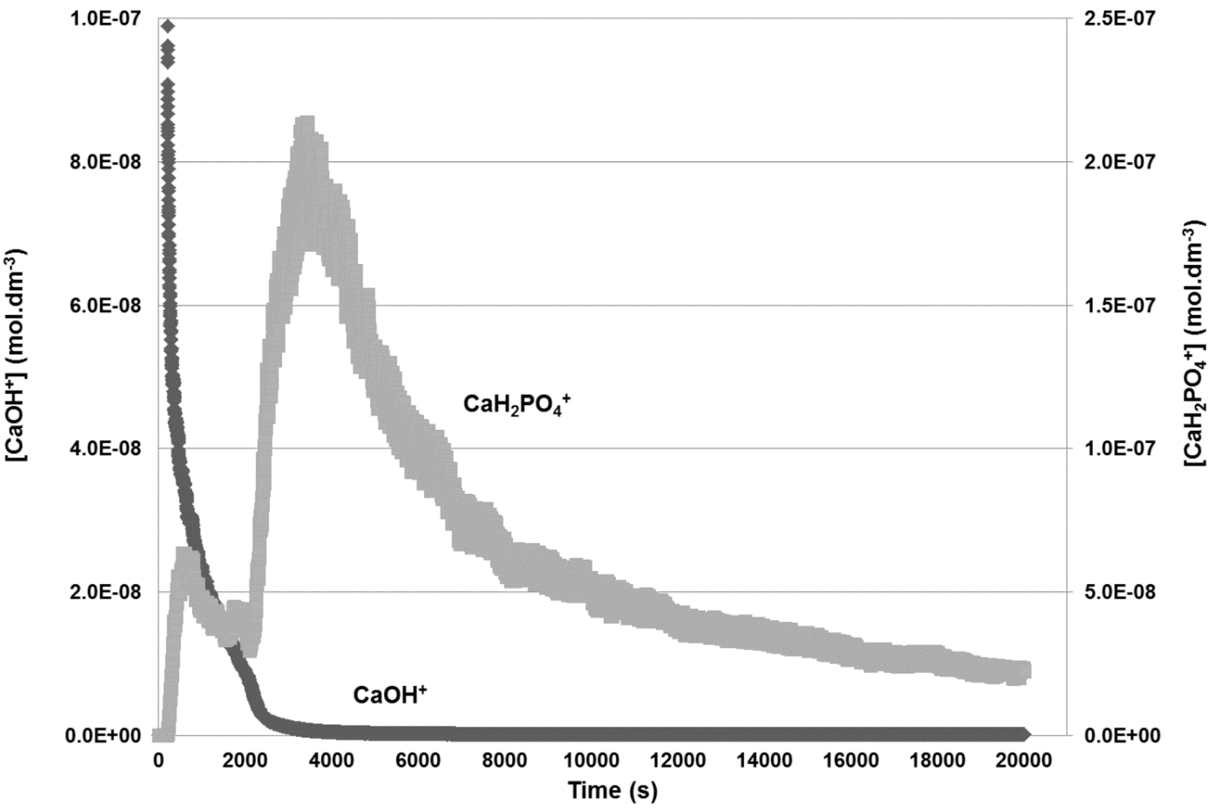

Figure 4.7. Variation of [$CaOH^+$] and [$CaH_2PO_4^+$] with time.

The value of [$CaOH^+$] decreases over the precipitation process (**Figure 4.7**), since calcium and hydroxyl ions are both consumed for the formation of ACP, transformation of ACP to HAp and HAp growth. As to [$CaH_2PO_4^+$], it increases at the beginning (see **Figure 4.7**) due to release $H_2PO_4^-$ ions from the dissociation of orthophosphoric acid. Afterwards, it decreases owing to the fact that calcium and phosphate ions are consumed for the formation of ACP. Then, it increases since hydrogen phosphate ions are released from the transformation of ACP to HAp. Finally, it decreases as phosphate ions are consumed for the growth of HAp.

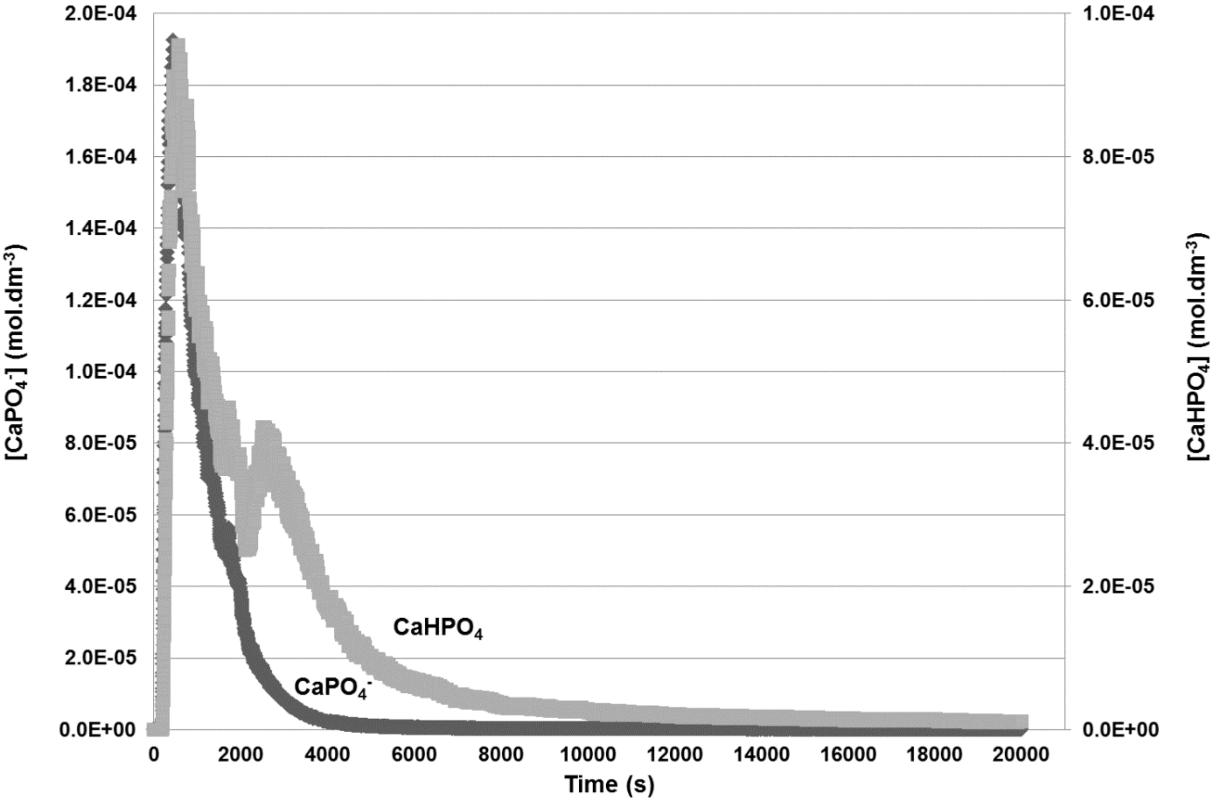

Figure 4.8. Variation of [$CaPO_4^-$] and [$CaHPO_4$] with time.

From **Figure 4.8** one can see that [$CaPO_4^-$] decreases during HAp precipitation once both calcium and phosphate ions are consumed. In relation to [$CaHPO_4$], it mainly decreases over the precipitation process (see **Figure 4.8**), although at approximately 2000 s an increase in [$CaHPO_4$] is observed. This is due to the release of hydrogen phosphate ions during the transformation of ACP to HAp.

After the estimation of the conductivity over time, the following graphic representation was obtained:

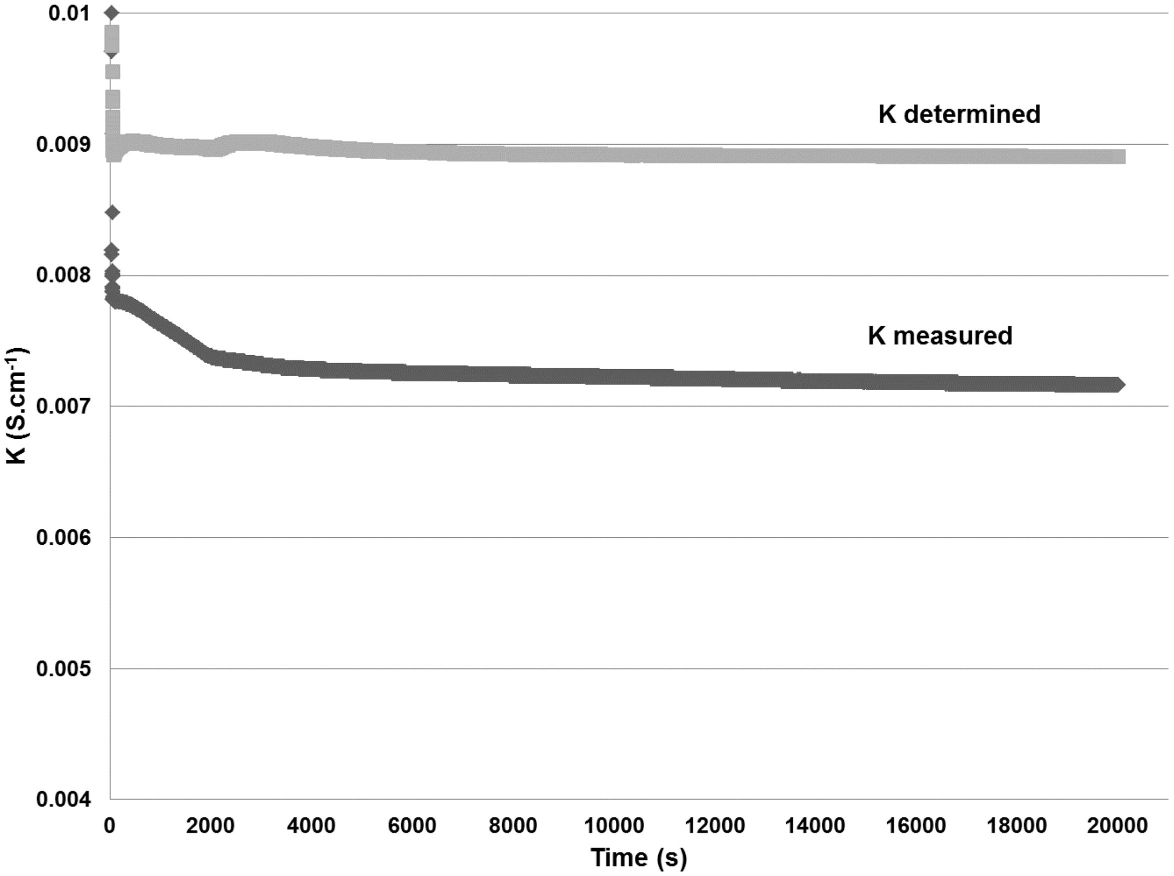

Figure 4.9. Variation of *K* with time.

Figure 4.9 shows that the conductivity obtained by solving the system of equations is relatively close to the experimental, proving that the system of equations represents well the precipitation process. The agreement in the early instants (until approximately 2000 s) is not as good, suggesting that the proposed system does not correctly apply in this situation. This can be explained by the fact that the system of equations used only assumes the formation of HAp from the beginning of the precipitation process. However, it was verified that the first phase that precipitates is ACP (see 3.3.3). Some of the equations of the proposed system could be replaced by others, including the definition of supersaturation of HAp by the equation defining the corresponding supersaturation of ACP, in order to set up a system of equations representative of the chemical system in the reaction medium. Nevertheless, it is important to refer that ACP composition is not easily known because of its metastable state.

The difference observed between the measured and the estimated value of the conductivity can be due to the fact that the ionic conductivities used are at infinite dilution. This fact may have a significant effect on the estimated conductivity and so, the calculated conductivity is higher than the measured one (**Figure 4.9**).

4.4 Conclusion

Precipitation of hydroxyapatite (HAp) at 37 °C for a mixing Ca/P molar ratio of 1.33 in a stirred tank batch reactor was modeled. The definition of the reaction system leads to a system of 17 equations (mass balance and equilibrium equations, and supersaturation of calcium) and 20 unknowns, whose resolution was possible with the knowledge of three of the process variables (temperature, pH and calcium concentration). The system allowed describing the dynamics of all the chemical species present in solution in the stirred tank batch reactor. Further, the results are consistent with the study conducted in the previous chapter, where the precipitation process of HAp was characterized by the precipitation of a metastable phase, ACP, its conversion to HAp and HAp growth.

The proposed model was validated with the measurement of the conductivity of the reaction medium and its comparison with the conductivity calculated from the estimated concentration of the chemical species, yielding a satisfactory agreement between the predicted value by the model and experimental data. However, the agreement is not as good in the early instants of the precipitation process, thereby the system cannot be correctly applied in this situation.

Therefore, the resolution of the system of equations gives a rather approximate indication of the precipitation process chemistry over time. Hence, this approach may be of particular interest for further study, i.e. the study of the whole mechanism of precipitation and growth.

4.5 References

Chen, Z.-F., B. W. Darvell, and V. W.-H. Leung. 2004. “Hydroxyapatite Solubility in Simple Inorganic Solutions.” *Archives of Oral Biology* 49 (5): 359–67.

Fernández, E., F. J. Gil, M. P. Ginebra, F. C. Driessens, J. Planell, and S. M. Best. 1999. “Calcium Phosphate Bone Cements for Clinical Applications. Part I: Solution Chemistry.” *Journal of Materials Science. Materials in Medicine* 10 (3): 169–76.

Haynes, W.M. 2012. *CRC Handbook of Chemistry and Physics*. 93RD ed.

Matsuya, S., S. Takagi, and L. C. Chow. 1996. “Hydrolysis of Tetracalcium Phosphate in H3P04 and KH2POa.” *Journal of Materials Science* 31: 3263–3269.

Oliveira, C. 2007. “Precipitação Do Fosfato Dicálcico : Caracterização Experimental e Modelização”. PhD Thesis. Faculty of Engineering of the University of Porto.

Lazić, S. 1995. “Microcrystallinehydroxyapatiteformation from Alkalinesolutions.” *Journal of Crystal Growth* 147 (1-2): 147–154.

Song, Y, H.H. Hahn, and E. Hoffmann. 2002. “The Effect of Carbonate on the Precipitation of Calcium Phosphate.” *Environmental Technology* 23 (2): 207–15..

Tsuge, H., S. Yoshizawa, and M. Tsuzuki. “Reactive Crystallization of Calcium Phosphate.” *Chemical Engineering Research & Design* 74 (7): 797–802.

Uskoković, V., and D. P. Uskoković. 2011. “Nanosized Hydroxyapatite and Other Calcium Phosphates: Chemistry of Formation and Application as Drug and Gene Delivery Agents.” *Journal of Biomedical Materials Research. Part B, Applied Biomaterials* 96 (1): 152–91.

Wang, L., and G. H. Nancollas. 2008. “Calcium Orthophosphates: Crystallization and Dissolution.” *Chemical Reviews* 108 (11): 4628–69.

5 PRECIPITATION OF HAp AT 37 °C IN A MESO OSCILLATORY FLOW REACTOR OPERATED IN BATCH AT CONSTANT POWER DENSITY

A meso oscillatory flow reactor (meso-OFR) was successfully applied for the precipitation of HAp nanoparticles. The reactor consists in a glass tube provided with smooth periodic cavities, operating under oscillatory flow mixing (OFM), where mixing intensity is controlled by the oscillation frequency (f) and amplitude (x_0). Mixing efficiency of the mesoreactor operated batchwise in a vertical tube was evaluated at constant power density. For that, variation of the hue values upon mixing was monitored both spatially and temporally. The best operating conditions for fast mixing and a more homogeneous reaction medium were verified for $f = 0.83$ Hz and $x_0 = 4.5$ mm. HAp precipitation was then carried out under these conditions at 37 °C for different mixing Ca/P molar ratios. HAp nanoparticles with a mean size of about 67 nm and a narrow size distribution were obtained. The prepared HAp nanoparticles were also compared with the HAp nanoparticles produced in the stirred tank batch reactor. Apart from hydrodynamics, the external conditions such as reactants concentration, temperature and power density were kept constant in both reactors. The obtained results show the advantages of the meso-OFR over the stirred tank due to the production, about four times faster, of smaller and more uniform HAp nanoparticles.

5.1 Introduction

Oscillatory flow reactors (OFRs) have been developed over the past two decades and proven to provide effective and uniform mixing (Phan and Harvey 2011). OFRs have been extensively studied in chemical engineering processes such as crystallization (Chew and Ristic 2005; Ristic 2007), polymerization (Ni et al. 1999; Ni et al. 2001), fermentation (Ni et al. 1995) and dispersion (Harvey et al. 2003; Ni et al. 2002a). The basic concept of the OFR is the application of periodic fluid oscillations to a cylindrical column containing evenly spaced orifice baffles (Reis 2006). **Figure 5.1** shows a schematic representation of a conventional OFR.

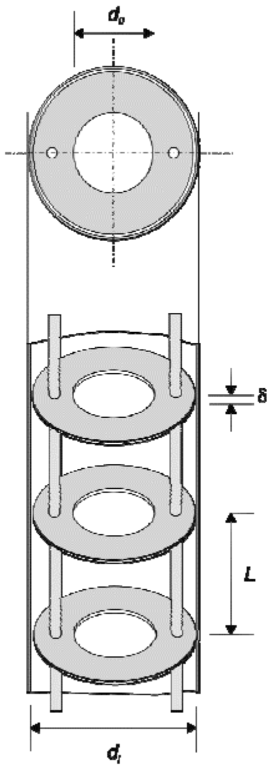

Figure 5.1. Schematic representation of cross section in an OFR: d_i – reactor internal diameter, l – baffles spacing, d_0 – orifice diameter, δ - baffle thickness (Reis 2006).

The OFR can be operated batchwise or continuously in horizontal or vertical tubes. The liquid or multiphase fluid is typically oscillated in the axial direction by means of diaphragms, bellows or pistons, at one or both ends of the tube (Ni et al. 2002b). The sharp edged baffles are fixed and distributed along the tube at a regular spacing (l). Another system for generation of flow oscillations is also common and has already been described (reciprocating plates column), which works by moving a set of baffles up and down from the top of the tube.

The oscillatory flow mixing (OFM) is an efficient mechanism, where fluid moves from the walls to the center of the tube. Due to the oscillations, the flow direction is periodically reversing, and this motion interacts with the baffles, forming vortices (**Figure 5.2**). Those periodically formed vortices can be controlled by a combination of geometrical and operational parameters, such as, baffle diameter, baffle spacing, oscillation frequency and amplitude (Ni et al. 2002b; Reis 2006). The result is a highly uniform mixing in the zones between successive baffles, in which the rates of axial and radial mixing are similar. This provides precise control of mixing, from gentle mixing to the most intense, and efficient heat and mass transfer.

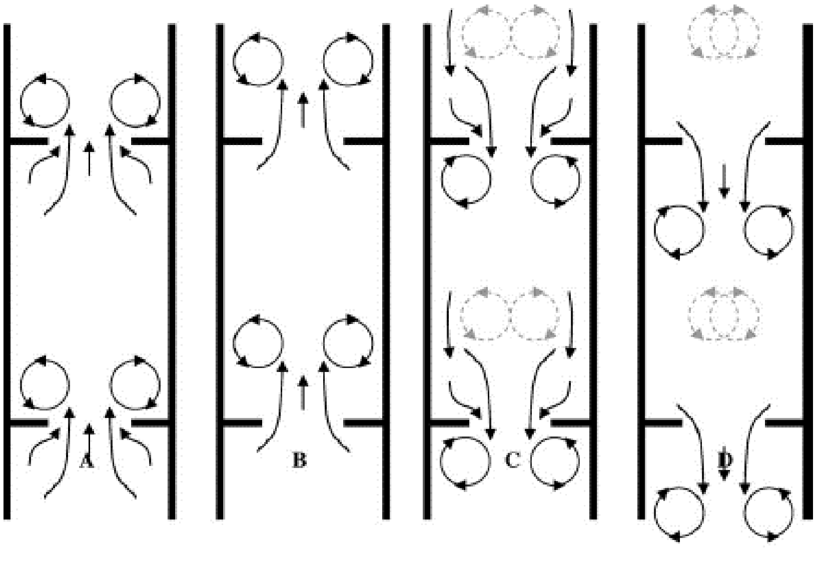

Figure 5.2. Mechanism of oscillatory flow mixing (OFM) in an OFR (Fitch et al. 2005). (A) Start of Up Stroke. (B) Maximum velocity in Up stroke, i.e. flow reversal. (C) Start of Down stroke. (D) Maximum velocity in Down stroke.

For a given baffle geometry, the fluid mechanical condition in an OFR operated in batch is controlled by the oscillatory Reynolds number, Re_o, and the Strouhal number, St, defined as (Ni et al. 2002b):

$$Re_0 = \frac{\rho D x_0 \omega}{\mu} \tag{5.1}$$

$$St = \frac{D}{4\pi x_0} \tag{5.2}$$

where D is the tube diameter (m), x_o the oscillation amplitude center-to-peak (m), ω the angular frequency of oscillation (=$2\pi f$), f the oscillation frequency (Hz), μ the dynamic viscosity of fluid (N.s.m^{-2}) and ρ the density of the liquid (kg.m^{-3}).

The oscillatory Reynolds number describes the intensity of mixing applied to the column, while the Strouhal number is the ratio of tube diameter to stroke length, measuring the effective eddy propagation (Lawton et al. 2009).

The “conventional” OFR geometry was redesigned by Reis et al. (2004) in order to be used in bioprocesses (Reis et al. 2004; Reis et al. 2005; Reis 2006). Aiming to reduce the high shear regions, that may be critical to some cell cultures, the sharp baffles were smoothed. The resulting reactor is composed by a straight tube and smooth periodic constrictions (SPCs) incorporated as a single piece, making it easy for sterilization (Reis 2006). Further, the meso OFR is a mesoscale (millilitre) device, reducing thus reagent requirements and waste. It can also be easily scaled up to the industrial scale (Lopes et al. 2011). In that way, the meso-(OFR) appears as a good candidate to promote ideal conditions for the controllability of HAp particles properties.

This section reports on the feasibility of a meso-OFR to improve the precipitation process of HAp under near-physiological conditions of temperature and pH, particularly important when preparing HAp for medical purposes (Kumta et al. 2005). First, mixing efficiency of the mesoreactor operated in batch in a vertical tube at a constant powder density (31.5 W.m^{-3}) was evaluated by monitoring the hue. HAp precipitation process was then studied for different mixing Ca/P molar ratios (1.00, 1.33 and 1.67). Experiments were performed under the same conditions of temperature (37 °C), reactants concentration and power density applied in the stirred tank batch reactor (see 3.2.1). The constant power density applied to both reactors was used as the reference criterion. The effectiveness of both mixing methods for a given power input was investigated in terms of reaction time and characteristics of the precipitated particles.

5.2 Materials and methods

5.2.1 Description of the experimental set-ups

5.2.1.1 The meso-OFR

The mesoreactor consists of a 35 cm long and 4.4 mm internal diameter glass jacketed tube (**Figure 5.3**) provided with smooth periodic cavities (SPC) (**Figure 5.4**), with an averaged baffle spacing of 13 mm and a baffle thickness of 6 mm. The diameter on the constricted zone (baffle internal diameter) is 1.6 mm, leading to a baffle free area of 13 % (Reis 2006). The reactor has an approximate volume of 4 mL.

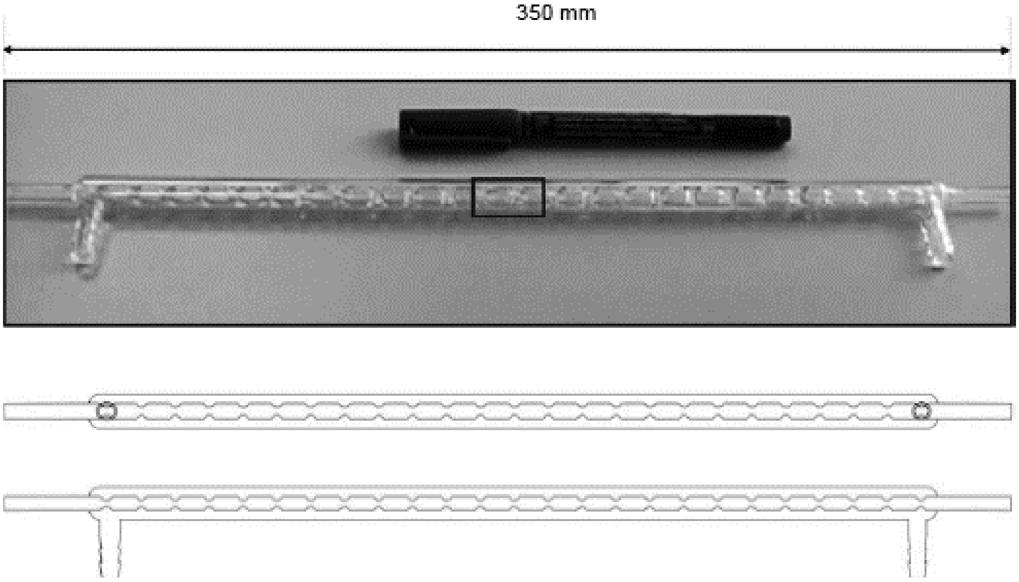

Figure 5.3. Geometry of the SPC tube composing the micro-bioreactor (Reis 2006).

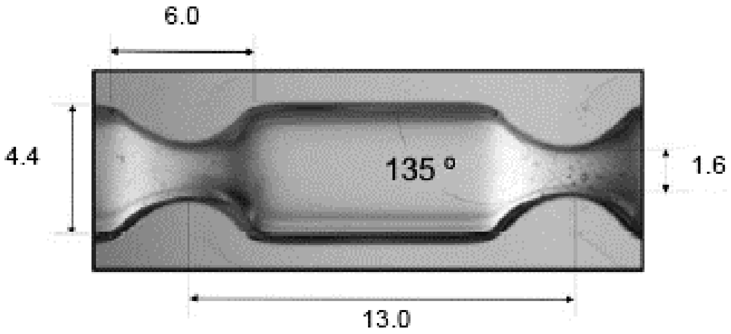

Figure 5.4. SPC tube geometry. All dimensions are in mm (Reis 2006).

5.2.1.2 The oscillating system

The fluid was oscillated using a novel oscillating system designed at LEPAE (Laboratory for Process, Environmental and Energy Engineering, Faculty of Engineering of the University of Porto). Oscillation amplitudes and frequencies were ranging from 1 to 4.5 mm and 0.83 to 3.67 Hz. The upper part of the oscillating system works, also, as a mixing chamber, minimizing by this way dead volume and thus enhance mixing of the reactants at the entrance of the mesoreactor.

5.2.1.3 Experimental apparatus for evaluation of mixing and HAp precipitation

The experimental set-up used for studying the mixing efficiency of the meso-OFR and HAp precipitation is presented in **Figure 5.5**.

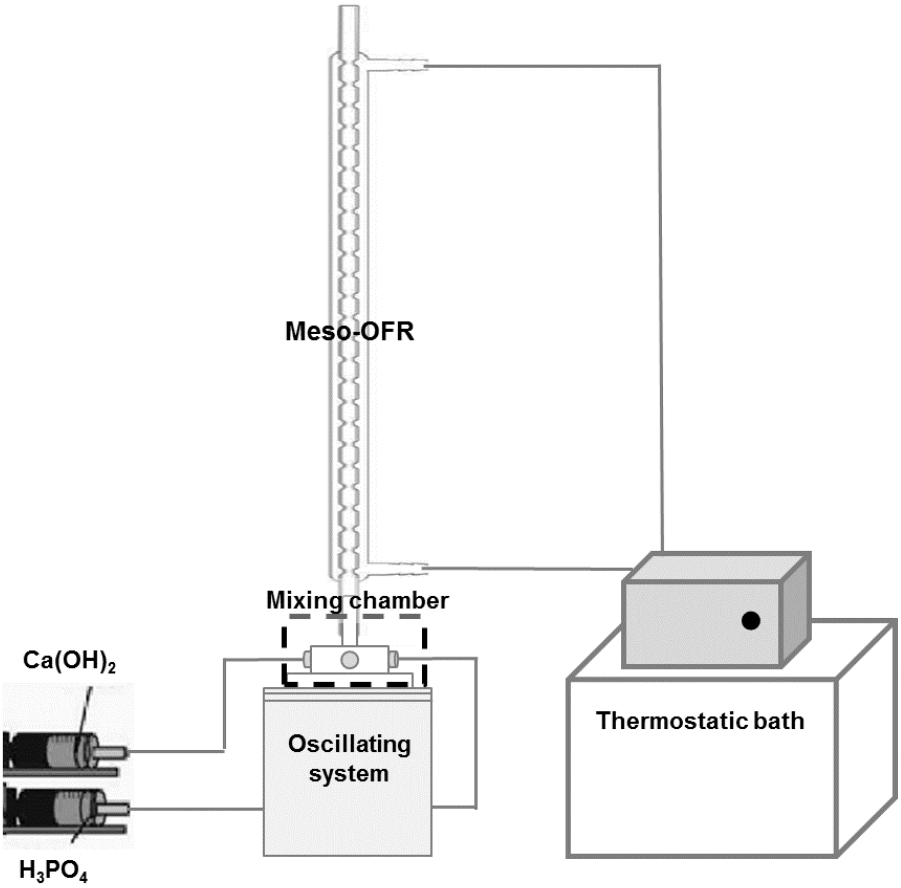

Figure 5.5. Experimental set-up for the mixing study and HAp precipitation.

The reactants were quickly (3 to 4 s) fed into the set-up one at a time by means of syringes of 5 mL (BD Plastipak). Temperature inside the meso-OFR was regulated by a thermostatic bath maintained at 37 ºC.

5.2.1.4 Experimental apparatus for pH monitoring

As pH is a crucial parameter in HAp precipitation and given the small dimensions of the reactor, monitoring of pH was done with an optical fiber. It allows monitoring pH variation over time during HAp precipitation process. It must be pointed out that the resulting HAp crystals cannot be used for characterization due to the use of a chemical pH indicator in this process. So, this apparatus was only used to obtain the pH profile during HAp precipitation.

In order to validate this methodology, the pH of the final suspensions was measured using a pH microelectrode (SenTix Mic-D, WTW) and compared with the final values obtained using an optical fiber system. The experimental set-up used for pH monitoring is presented below (**Figure 5.6**).

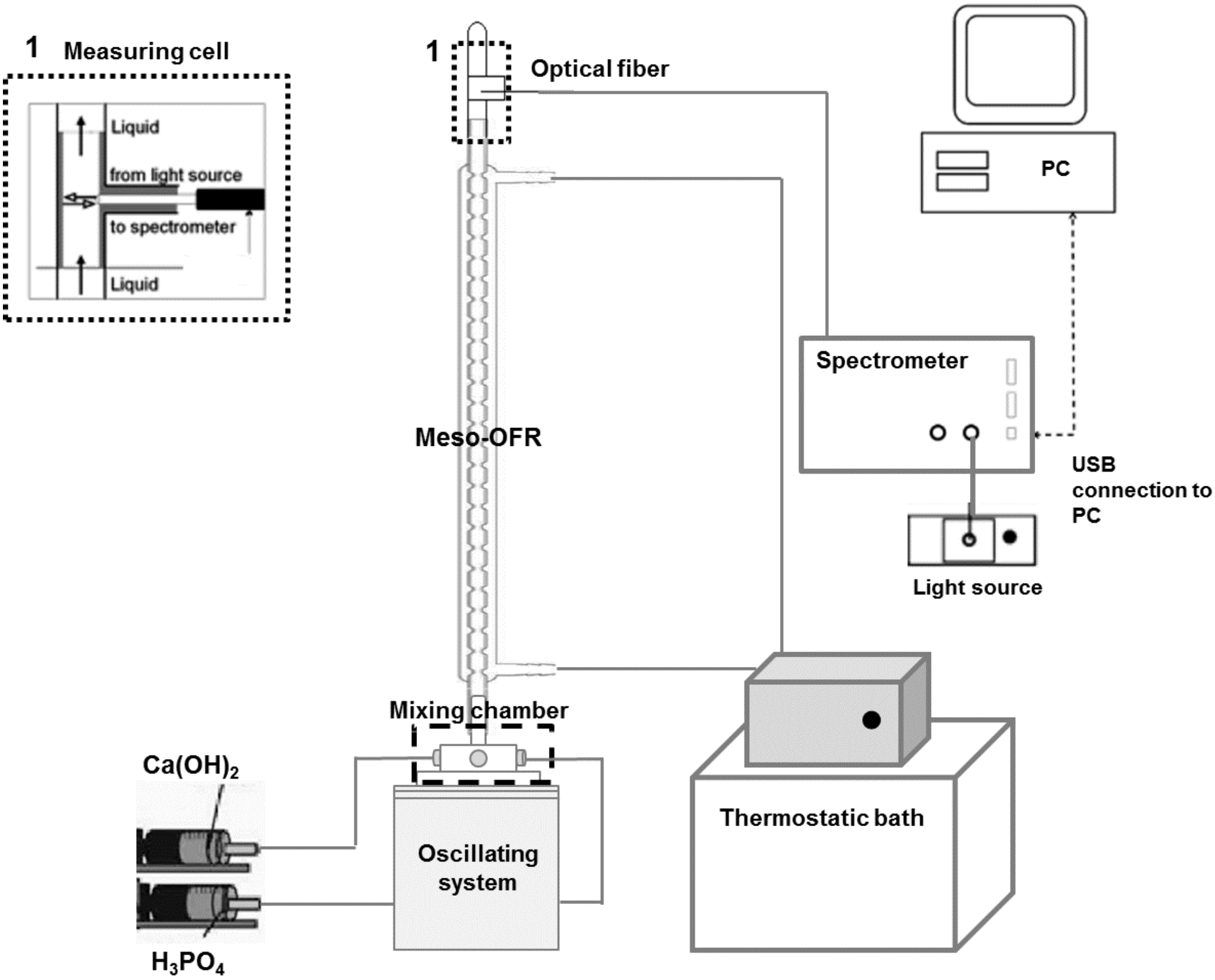

Figure 5.6. Experimental set-up for pH monitoring.

In-line pH value was obtained from the absorbance measured via an optical microprobe (reflection probe, tip 1.5 mm, FCR–7UV200–1.5x100-2, Avantes, Eerbeek, The Netherlands) connected to a multi-channel optic spectrometer system (Avantes, Eerbeek, The Netherlands). The probe was installed at the outlet of the meso-OFR, perpendicularly to the flow direction into a 4 mm internal diameter in-line flow cell with white walls (Swagelok) covered by black adhesive tape (see **Figure 5.6**). Readings were taken every 2 s.

The meso-OFR was completely covered by an aluminum foil to reduce the noise due to ambient light.

5.2.2 Study of the mixing efficiency in the meso-OFR operated in batch mode for a power density of 31.5 W.m^{-3}

Mixing efficiency of the meso-OFR operated in batch was evaluated under the same conditions of power density (31.5 W.m^{-3}) applied in the stirred tank batch reactor. For that, power density of the stirred tank batch reactor was estimated through the following equation (Ni et al. 1995):

$$\frac{\mathrm{P}}{\mathrm{V}}=\frac{\mathrm{N_P}\rho\mathrm{N}^3\mathrm{D_s^5}}{\pi\mathrm{D_t^2}\left(\frac{\mathrm{h}}{4}\right)} \tag{5.3}$$

where $\frac{P}{V}$ is the power density (W.m^{-3}), ρ is the fluid density (kg.m^{-3}), N is the speed of the stirrer (s^{-1}), D_s is the diameter of the stirrer (m), D_t is the diameter of the tank (m) and h is the height of the tank (m) and N_P is the dimensionless power number of the stirrer. The final power density was determined multiplying the power density by the number of agitators that, according to the configuration of the stirrer used is 16 (see 3.2.1.).

Regarding the power density of the meso-OFR, it was estimated from Ni et al. (2002):

$$\frac{P}{V}=\frac{2\rho N_B}{3\pi C_D^2}\,\frac{1-\alpha^2}{\alpha^2}\,x_0^3\omega^3 \tag{5.4}$$

where N_B is the number of constrictions per unit length (m^{-1}), α the baffle free area ratio (=$(D_0/D)^2$) where D_0 is the constriction diameter (m) and D is the tube diameter (m), x_0 the oscillation amplitude (m), ω the angular frequency of oscillation (=$2\pi f$) and C_D the baffle discharge coefficient.

The parameters needed to determine the power density of both reactors are present in **Table 5.1**. The fluid density of water was used since the solutions employed are low concentrated aqueous solutions. As to the power number of the stirrer (N_P), it was estimated based on the stirrer design and on the relationship between the power number (N_P) and the Reynolds number (Re) for Newtonian liquids (Haynes 2012). Concerning the parameters of the meso-OFR, values are based on Reis (2006).

Table 5.1. Parameters for the estimation of the power density of the stirred tank batch reactor and of the meso-OFR.

Stirred tank batch reactor	N_P	ρ **(kg.m^{-3})**	N **(s^{-1})**	D_s **(m)**	D_t **(m)**	L **(m)**
	1.25	993.329	4.5	0.029	0.1	0.15
Meso-OFR	N_B **(m^{-1})**	ρ **(kg.m^{-3})**	α	C_D	x_0 **(m)**	ω **(rad.s^{-1})**
	76.92	993.329	0.13	0.6	-	-

Through Equation (5.4) it is possible to obtain a relation between the oscillation amplitude (x_0) and the frequency of oscillation (f) for a given power input. One of the parameters (x_0 or f) was fixed in order to determine the other one. Values of the amplitude and the frequency are however limited by the experimental set-up. Indeed, in the case of the amplitude, this one cannot be too high to prevent breaking of the membrane. According to this, three different mixing conditions were defined (**Table 5.2**).

Table 5.2. Operating conditions for a power density of 31.5 W.m^{-3}.

f **(Hz)**	x_0 **(mm)**
3.67	1.00
1.67	2.25
0.83	4.50

Values of the amplitudes correspond to the center-to-peak amplitude and these measurements were performed in the tube without constrictions.

The mixing performance was evaluated using a colorimetric technique employing the hue, enabling thus the use of multiple colors. This method has been developed by Rezk et al. (2012) to evaluate the mixing performance of paper-based microfluidic systems. They proposed the hue instead of the intensity (or brightness) as an independent means to quantify mixing. In fact, each color is characterized by a base hue value (**Figure 5.7**), independently of intensity, and hence independently of the method and consistency of the illumination (Rezk et al., 2012). While traditional colorimetric methods are based on grayscale or a specific color channel, for example, the red component of the RGB color space (Rezk et al., 2012), this technique enables the use of multiple colors. In addition, the method provides the ability to dynamically track the progression of the color change both in space and time without requiring a large color contrast as required when using grayscale analysis. Moreover, the hue values vary linearly with the color scale, turning it a robust method under different lighting conditions.

Figure 5.7. Hue values for different colors (Rezk et al. 2012).

A camera (SONY Cyber-shot DSC-H10) was used to photograph the fluid inside the meso-OFR at different time intervals. Hue of the fluid was determined at four specific locations (**Figure 5.8**) by specific software (NIS-Elements) for the different mixing conditions presented in **Table 5.2**.

Two buffer solutions, $(NH_4)H_2PO_4$ (0.2 $mol.dm^{-3}$) (Merck) and NH_3 (0.1 $mol.dm^{-3}$) (Pronalab), were prepared. A pH indicator, bromothymol blue 1$g.L^{-1}$ (Panreac), was added to both solutions (2mL per 100 mL of solution), resulting in two solutions of different colors, one yellow corresponding to the acidic solution, and one blue corresponding to the basic solution. The average hue of each buffer solution, as well as of the resulting solution of the mixture in equal amounts of the two buffer solutions, were estimated. For that, the solutions were fed into the meso-OFR (see **Figure 5.5**) and their corresponding hue was estimated based on the average of the hue values measured at different locations (see **Figure 5.8**). The yellow solution has a hue of approximately 33.52 and the blue solution has a hue around 142.06. The solution resulting from the mixture in equal amounts of the two buffer solutions has a hue of approximately 70.95, corresponding to a green solution and will be referred as “Green Hue” in the rest of the text. Mixing efficiency of the meso-OFR operated in batch was then evaluated by the mixing of equal amounts (2.8 mL) of the buffer solutions under different operating conditions (see **Table 5.2**). The basic solution was first injected slowly, to avoid the formation of bubbles inside the mesoreactor, and then the acidic solution injected rapidly (3 to 4 s), in order to simulate the HAp precipitation process studied.

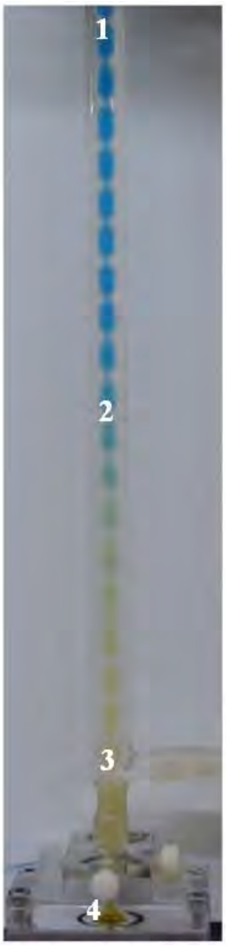

Location Number	1	2	3	4
Part of the meso-OFR	Top	Middle	Bottom	Cone

Figure 5.8. Picture of the meso-OFR. The numeric label indicates the locations at which the quantification of the hue was carried out.

5.2.3 Monitoring of pH

Monitoring of pH was performed in the experimental apparatus presented in **Figure 5.6**. The optical response of the microprobe was calibrated by running several solutions with different pH values. For that, 0.5 dm^{-3} of equimolar (0.01926 mol.dm^{-3}) calcium hydroxide (Riedel-de Haën, 96%) and orthophosphoric acid (Pronalab, 85%) aqueous solutions were prepared, 1 mL of bromothymol blue (1g.L^{-1}) (Panreac) being added to each solution. Then, several solutions with different pH were prepared by mixing the dyed calcium hydroxide and orthophosphoric acid aqueous solutions in different proportions (see Appendix A.2).

Afterwards, the resulting solutions were injected in the meso-OFR for the measurement of the absorbance.

The addition of bromothymol blue allows monitoring the changes of pH through the measurement of the absorbance. Bromothymol blue has two peaks of absorption, one at 430-435 nm for acidic solutions, and one at 615-618 nm for basic solutions (**Table 5.3**).

Table 5.3. Transition range of Bromothymol blue.

	Acidic solutions	**Transition range**	**Basic solutions**
pH	5.8	5.8 - 7.6	7.6
Solution color	yellow	green	blue

In this study, the pH varies between approximately 6 and 12, therefore it was only used the information relative to the blue absorption peak (615-618 nm).Three parameters were measured simultaneously:

- Spectrum in the visible $\lambda = 400 – 700$ nm;
- $F_1 = \int_{610\text{ nm}}^{620\text{ nm}} A(\lambda)d\lambda$, which corresponds to the blue absorption peak;
- $F_2 = \int_{690\text{ nm}}^{700\text{ nm}} A(\lambda)d\lambda$, which corresponds to a “neutral” zone;

where λ is the wavelength and $A(\lambda)$ is the light absorbance.

F_2 was measured in order to monitor the noise. F_1-F_2 (Abs) corresponds to the parameter used for the construction of the calibration curve. The experiments were carried out at 37 °C and repeated three times. The reference blank used was ultra-pure water.

Experiments showed that the relation between absorbance (Abs) and pH is linear only for pH between 6.3 and 8 (**Figure 5.9** and **Figure 5.10**).

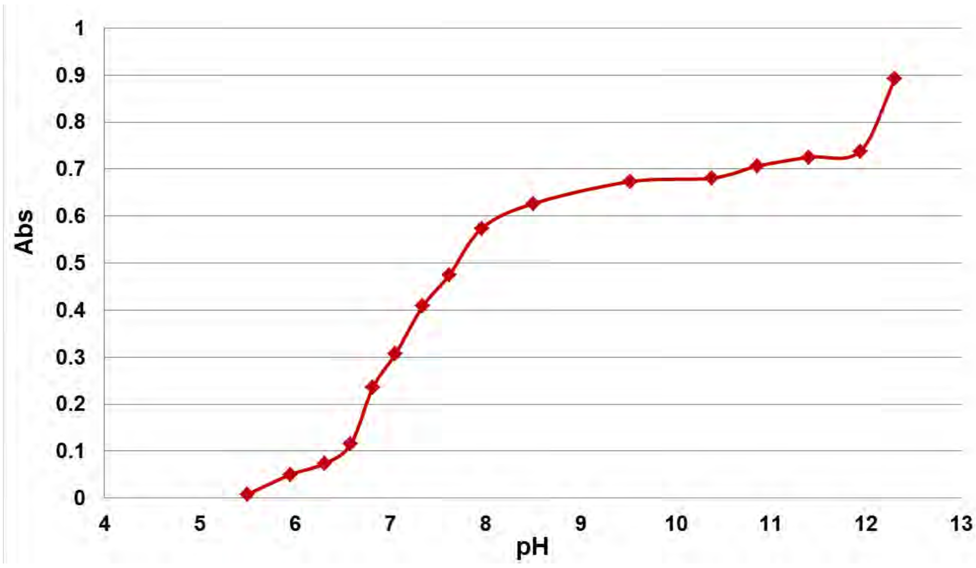

Figure 5.9. Absorbance (Abs = F_1-F_2) versus pH.

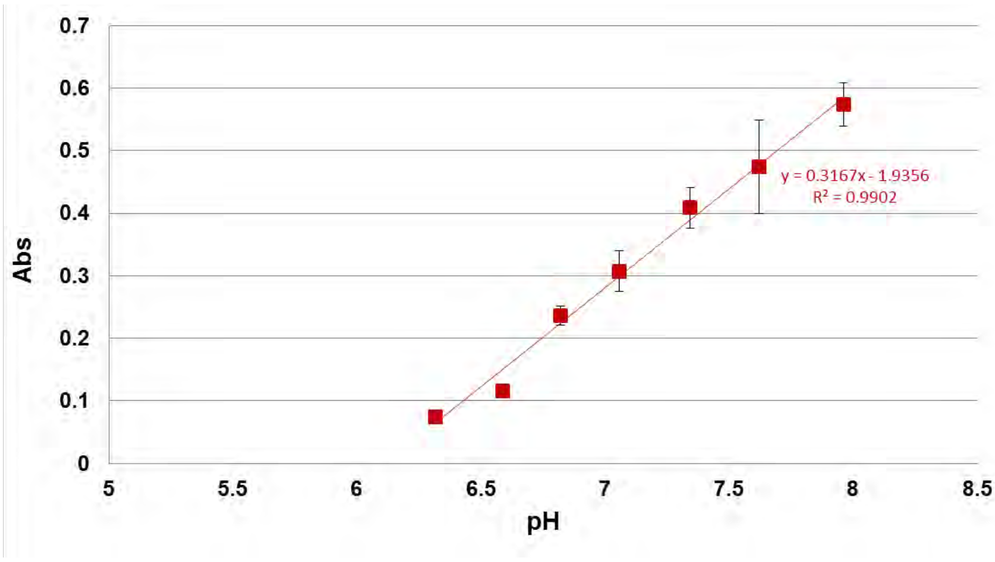

Figure 5.10. Relation between absorbance (Abs = F_1-F_2) and pH.

Error bars show the standard deviation of the absorbance values measured.

The pH of the final suspension was also measured by a pH electrode (SenTix Mic-D, WTW) in order to compare with the final values obtained from the absorbance measurement.

It is important to mention that this methodology was used exclusively for pH monitoring. Due to the use of the pH indicator, bromothymol blue, crystals obtained cannot be used for characterization. Indeed, bromothymol blue can affect the composition of the resulting precipitated HAp particles.

5.2.4 Precipitation of HAp

5.2.4.1 Powder preparation

HAp was synthesized by the mixing of a saturated calcium hydroxide (Riedel-de Haën, 96%) aqueous solution and an orthophosphoric acid (Pronalab, 85%) aqueous solution. 0.5 dm^3 of both reactants were prepared with ultra-pure water (Milli Q water, resistivity of 18.2 MΩ.cm^{-1} at 25 ºC) and their ionic force adjusted by the addition of 6 mL of potassium chloride (Mallinckrodt, 99.8%) 4 mol.dm^{-3} solution. To facilitate the dissolution of calcium hydroxide, the solution was agitated in a closed vessel for 24 h at 500 rpm and at 25 ºC, as its solubility decreases with temperature increase (Johannsen and Rademacher 1999). Then, both reactants were heated and kept at 37 ºC.

The precipitation process was carried out under the same conditions of temperature (37 °C), reactants concentration and power density (31.5 W.m^{-3}) used in the stirred tank batch reactor (see 3.2.1). Further, HAp precipitation was studied for three different mixing Ca/P molar ratios, 1.00, 1.33 and 1.67 (**Table 5.4**). Equal volumes (2.8 mL) of reactant solutions were injected. The calcium hydroxide aqueous solution was first injected slowly in the mesoreactor (see **Figure 5.5**) in order to avoid the formation of bubbles in the system. The orthophosphoric acid aqueous solution was then injected rapidly (3 to 4 s).

Table 5.4. Operating conditions for the precipitation of HAp.

[$CaOH_2$] (M)	[H_3PO_4] (M)	Mixing Ca/P molar ratio
0.01926	0.01926	1.00
	0.01448	1.33
	0.01154	1.67

5.2.4.2 Powder characterization

Samples were withdrawn at the outlet of the mesoreactor, centrifuged (at 1500 rpm for 5 min), washed twice with ultra-pure water and conserved in pure ethanol (Koptec 200 proof pure), which stops the solid-liquid reaction (Bernard et al. 2000). X-ray diffraction (XRD), scanning electron microscopy (SEM), Fourier transform infrared spectroscopy (FTIR), particle size distribution and determination of the final Ca/P molar ratio were performed. Preparation of the samples for each characterization technique and equipment used are described in 3.2.2.

5.3 Results and Discussion

5.3.1 Mixing study in the meso-OFR operated in batch mode

Hue was measured over time at different locations in the meso-OFR (see **Figure 5.8**) and at different operating conditions (see **Table 5.2**). The average values are presented below, being the "Green Hue" the hue value that corresponds to the hue of the solution when the two buffer solutions employed are completely mixed.

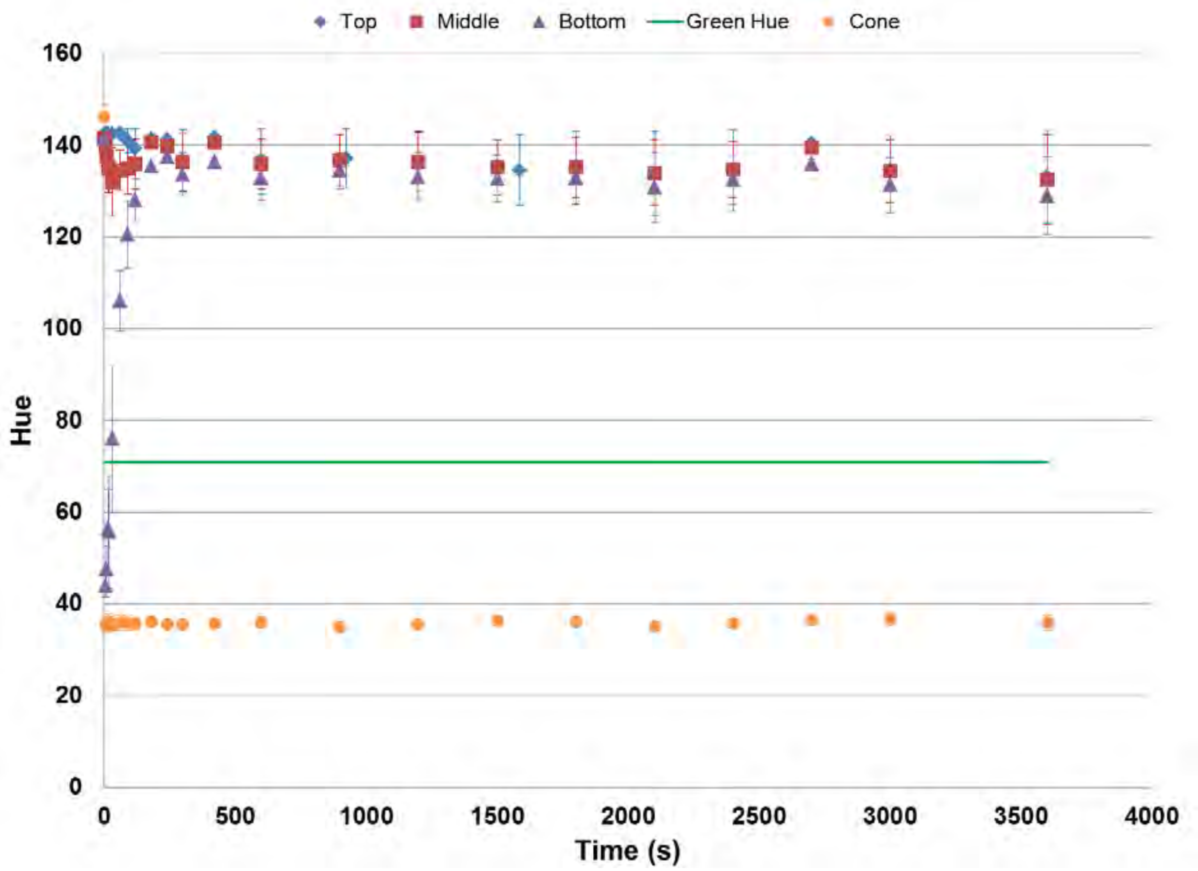

Figure 5.11. Hue values for different locations in the meso-OFR over time for $f = 3.67$ Hz and $x_0 = 1$ mm.

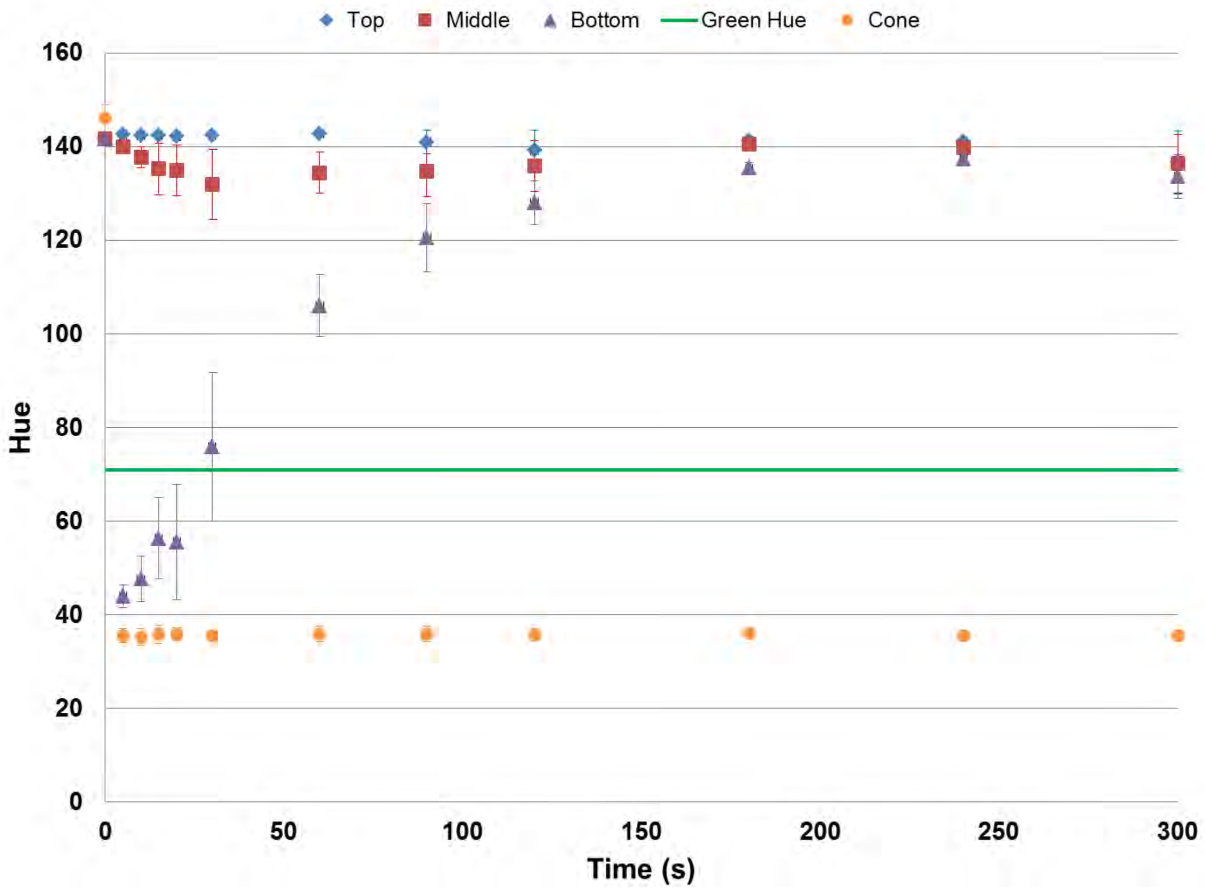

Figure 5.12. Hue values for different locations in the meso-OFR until 300 s for $f = 3.67$ Hz and $x_0 = 1$ mm.

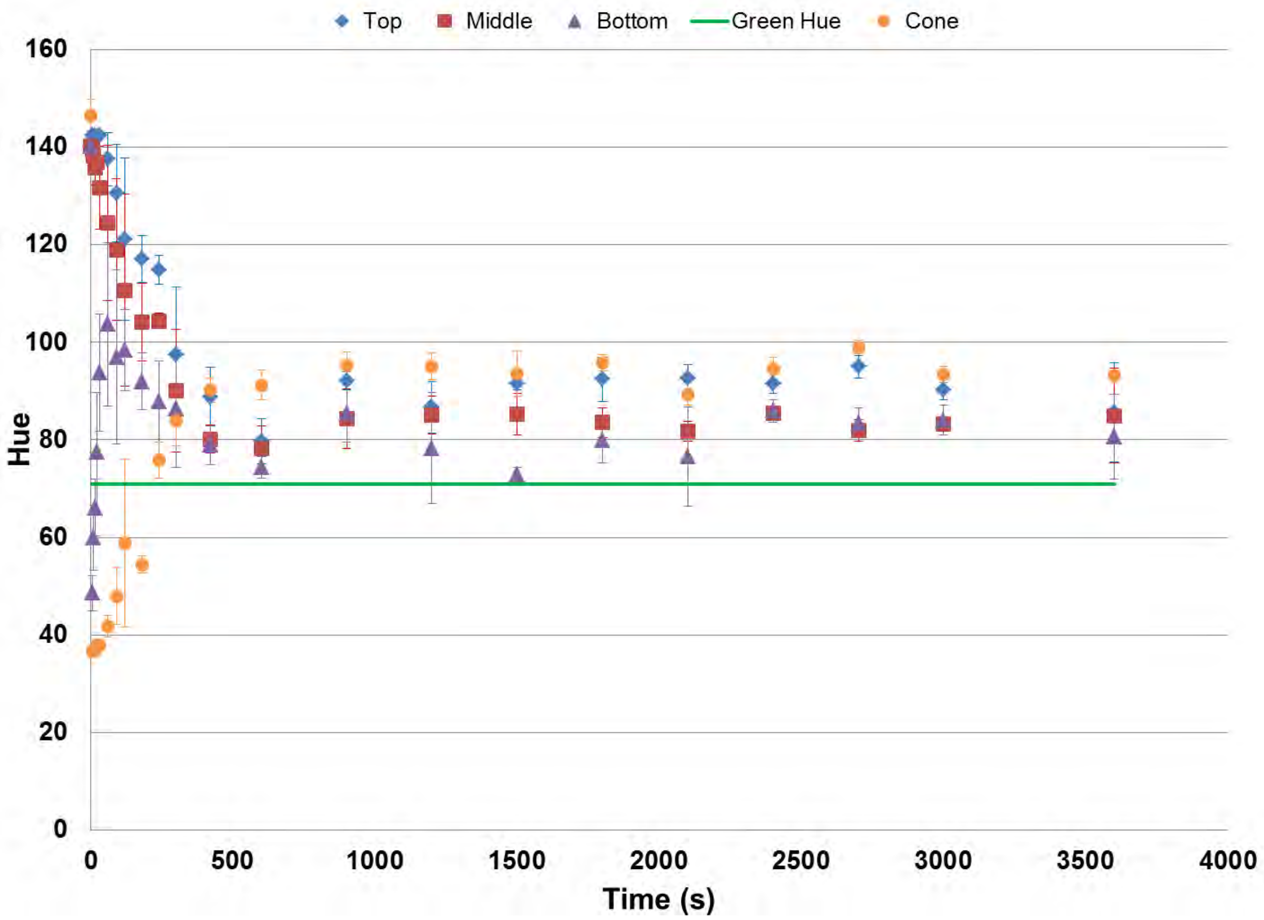

Figure 5.13. Hue values for different locations in the meso-OFR over time for *f* = 1.67 Hz and x_0 = 2.25 mm.

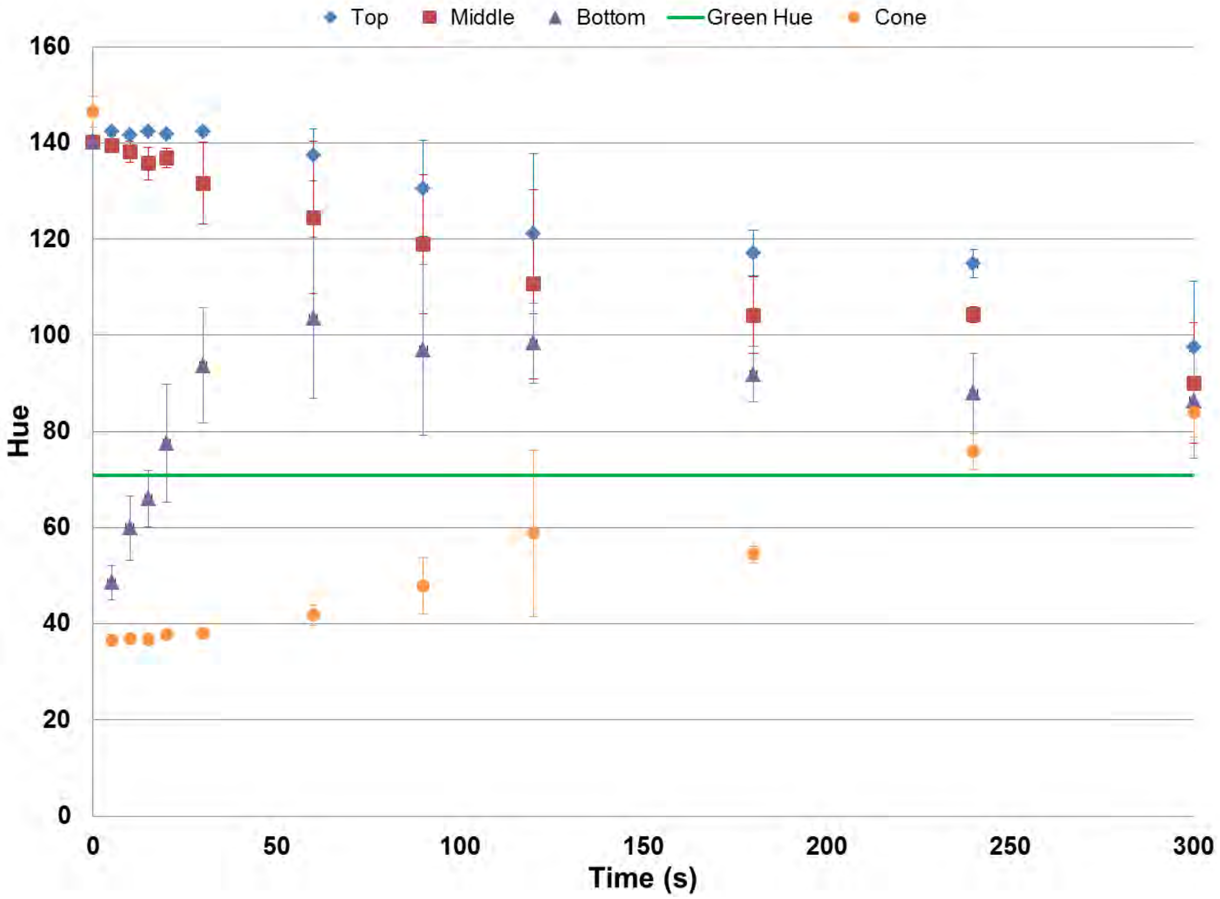

Figure 5.14. Hue values for different locations in the meso-OFR until 300 s for $f = 1.67$ Hz and $x_0 = 2.25$ mm.

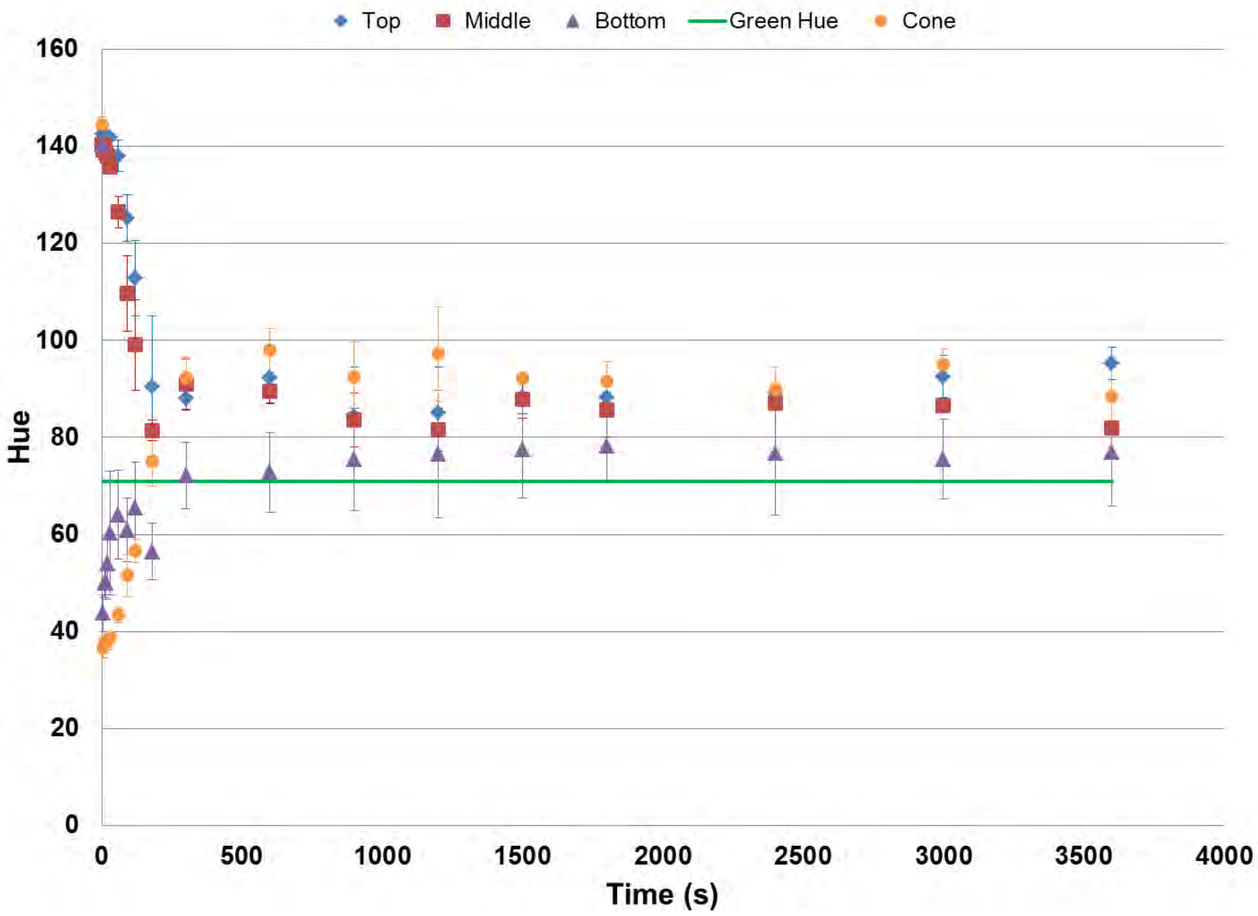

Figure 5.15. Hue values for different locations in the meso-OFR over time for $f = 0.83$ Hz and $x_0 = 4.5$ mm.

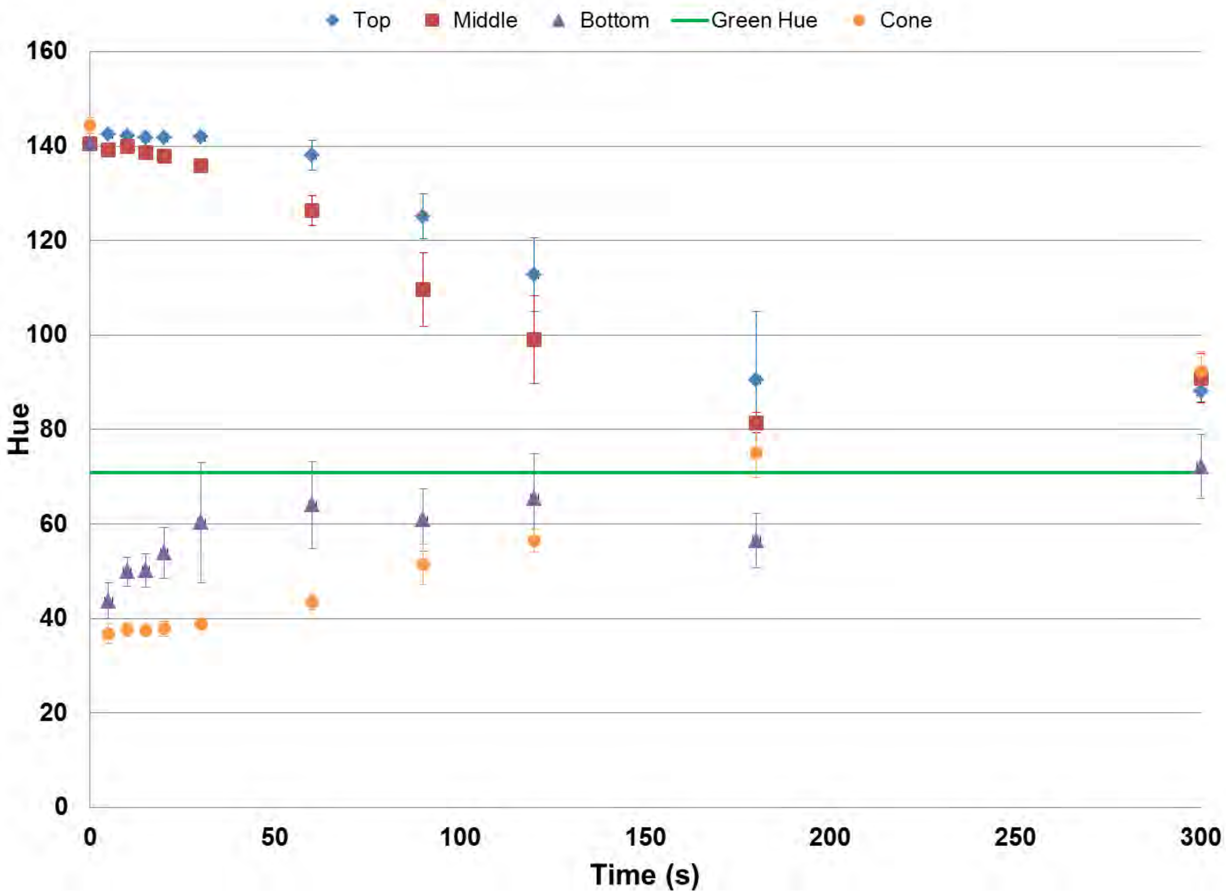

Figure 5.16. Hue values for different locations in the meso-OFR until 300 s for *f* = 0.83 Hz and x_0 = 4.5 mm.

The results obtained (**Figure 5.11** to **5.16**) allow evaluating the mixing efficiency inside the meso-OFR for the different experimental conditions studied, although in some cases the error bars (corresponding to the standard deviation of each measurement) associated to the hue values are significant, particularly at the bottom of the reactor. Based on **Figure 5.15** and **Figure 5.16**, it is possible to verify that for *f* = 0.83 Hz and x_0 = 4.5 mm, hue values measured at each location rapidly converge to the "Green Hue" value and remain close to this value over time. In relation to the two other cases, it takes longer for the two buffer solutions to mix completely. For *f* = 3.67 Hz and x_0 = 1 mm (see **Figure 5.11** and **Figure 5.12**) the solutions remain almost unmixed, since hue values at each location except at the bottom of the reactor, practically do not change. Therefore, the best conditions for fast mixing and a more homogeneous reaction medium were assumed to be obtained for *f* = 0.83 Hz and x_0 = 4.5 mm.

5.3.2 Precipitation of HAp

Precipitation of HAp was carried out in the meso-OFR operated in batch under the same conditions of temperature (37 °C), reactants concentration and power density (31.5 $W.m^{-3}$) applied in the stirred tank batch reactor. The mixing conditions (f and x_0) were defined based on the mixing study results presented above, best mixing being achieved for $f = 0.83$ Hz and $x_0 = 4.5$ mm.

5.3.2.1 Monitoring of pH

pH is an important parameter in determining the likelihood of the formation of calcium phosphate phases (Wang and Nancollas 2008). The influence of pH in the formation of calcium phosphates is linked to the properties of phosphate containing solutions. Due to the triprotic equilibrium in these systems, variations in pH alter the relative concentrations of the four protonated forms of phosphoric acid and thus both the chemical composition and the amount of the CaP formed by direct precipitation (Lynn and Bonfield 2005). Therefore, pH variation over time during HAp precipitation was monitored (**Figure 5.17**).

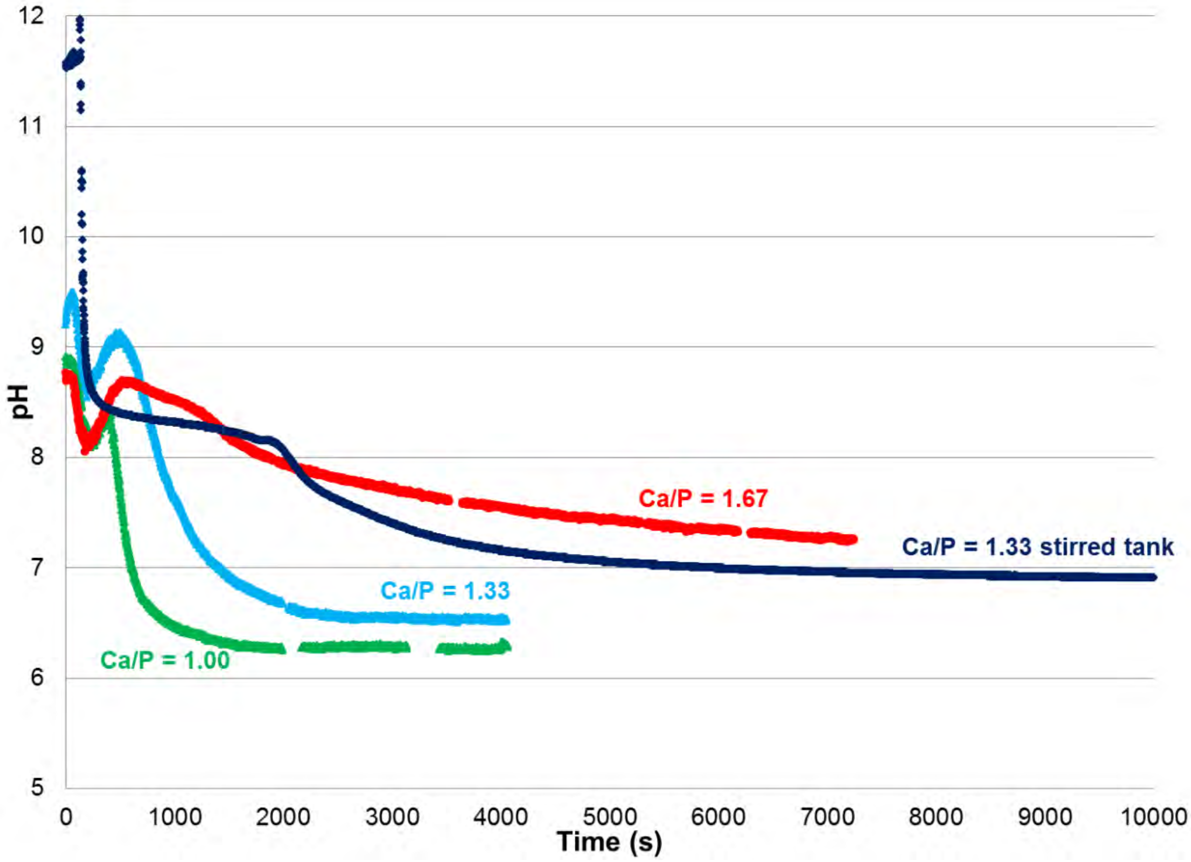

Figure 5.17. Variation of pH with time during HAp precipitation in the meso-OFR operated in batch for different mixing Ca/P molar ratios.

It is important to mention that pH values (see **Figure 5.17**) can only be considered for pH < 8, as calibration curve Abs versus pH was only linear for pH values between 6.3 and 8 (see **Figure 5.17**). **Figure 5.17** shows that for the mixing Ca/P molar ratios 1.00 and 1.33, pH starts to decrease from approximately 500 s and stabilizes at approximately 2000 s and 2500 s, respectively, reaching 6.3 and 6.5, respectively. As to the mixing molar ratio Ca/P = 1.67, pH decreases slowly over time and approaches 7 at approximately 5000 s. Variation of pH over time allows to follow the precipitation reaction, being pH stabilization an indication of the completion of the majority of the reaction. **Figure 5.17** shows that reaction time increases with Ca/P molar ratio.

According to **Table 5.5**, the agreement between final pH values obtained in **Figure 5.17** and final pH values measured by the microelectrode is quite good.

Table 5.5. pH of the product suspensions.

Mixing Ca/P	Final pH measured by the pH microelectrode	Final pH obtained from the absorbance measurements
1.00	5.89	6.3
1.33	6.38	6.5
1.67	7.15	7.3

5.3.2.2 *Phase identification*

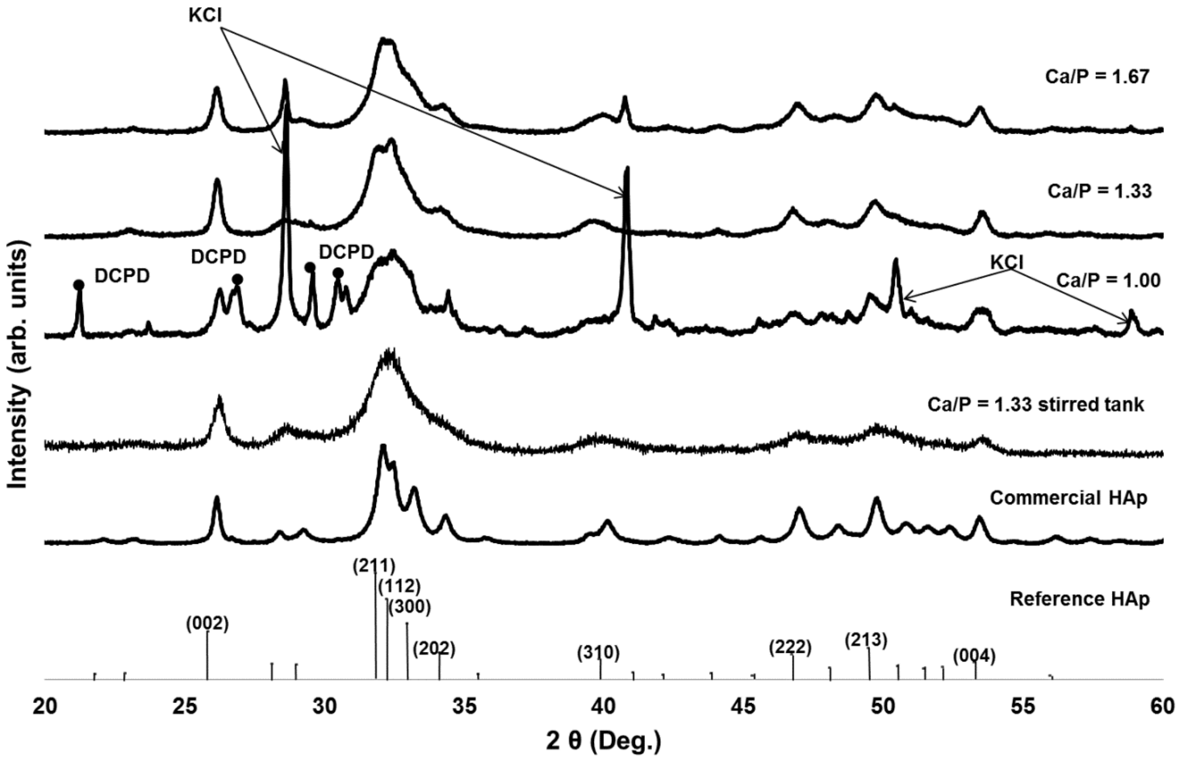

Figure 5.18. XRD patterns of the particles produced in the meso-OFR operated in batch for different mixing Ca/P molar ratios.

According to **Figure 5.18**, single-phased HAp was synthetized for the mixing Ca/P molar ratios 1.33 and 1.67. Diffraction patterns of the prepared powders match well with the diffraction pattern of a reference HAp (JCPDS 9-0432) and a commercial HAp (Spectrum, minimum 40 meshes). However, broader peaks are exhibited, suggesting the presence of amorphous phases or considerably smaller size particles (Wang and Nancollas 2008; Lynn and Bonfield 2005), which is similar to natural bone (Meskinfam et al. 2012). Concerning the

XRD pattern of the particles that were obtained for the mixing molar ratio Ca/P = 1.00, one can notice the presence of peaks assigned to other calcium phosphates, namely dicalcium phosphate dihydrate (DCPD or brushite) (JCPDS 9-0077). In fact, under weakly acidic aqueous environments (pH 4–6), equilibrium conditions can lead to the formation of the brushite phase (Lee and Kumta 2010). Further, brushite grows faster than HAp (Ferreira et al. 2003), the kinetic factors prevailing over the thermodynamics. Sharp and high intensity peaks at 28 º2θ and 40.5 º2θ, assigned to potassium chloride, are observed in the diffraction patterns of the products obtained with the mixing Ca/P molar ratios 1.00 and 1.67. This may be explained by the occlusion of KCl. Indeed, part of the mother liquor could have been trapped between the aggregates, and the KCl contained in the mother liquor crystallized at the drying step.

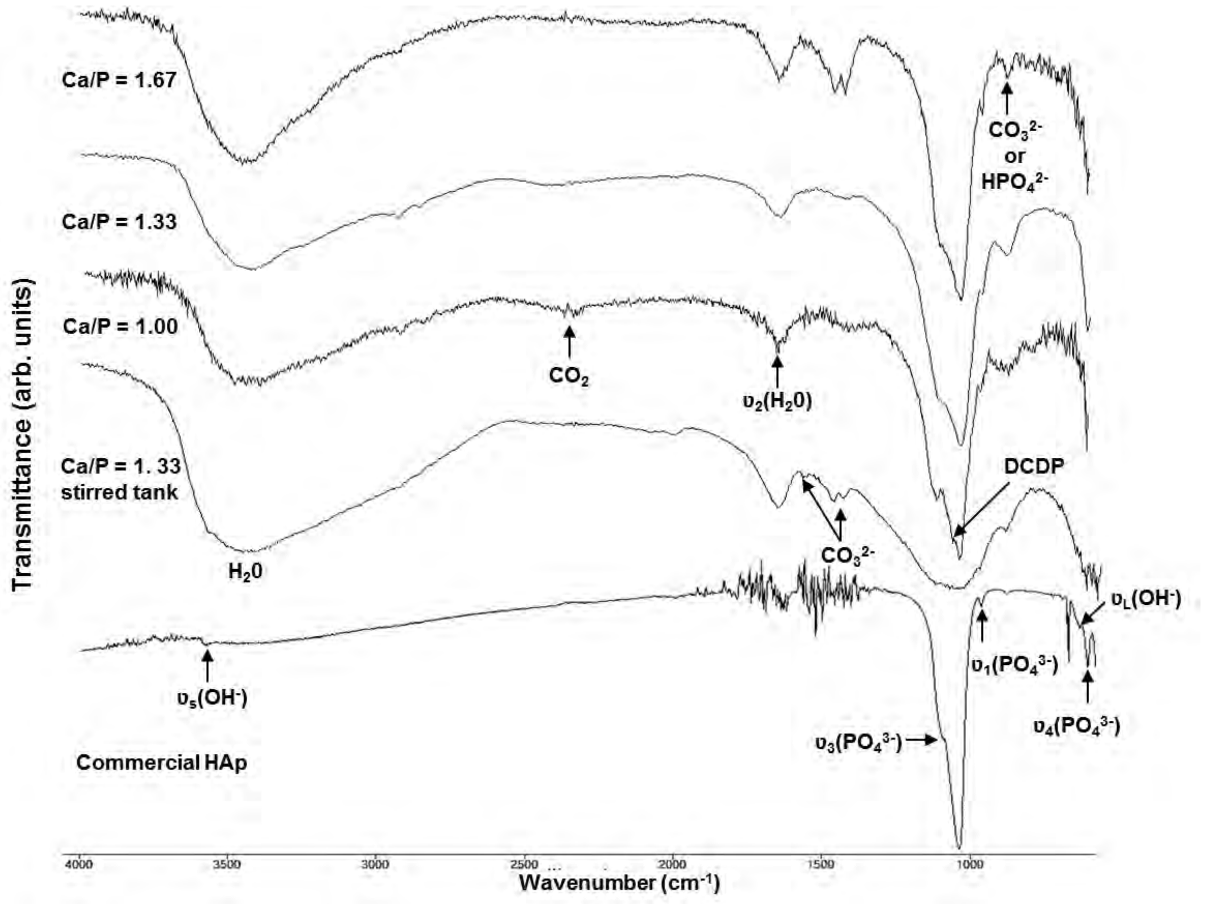

Figure 5.19. FTIR spectra of the particles produced in the meso-OFR operated in batch for different mixing Ca/P molar ratios.

Based on peaks identified (**Figure 5.19**), the synthesis products have a typical apatite structure. Bands of ν_3 PO_4^{3-} mode (around 1037 cm^{-1}) and ν_1 PO_4^{3-} mode (around 962 cm^{-1})

are clearly exhibited in all the spectra, although it is difficult to detect the peak related to ν_4 bending mode of PO_4^{3-}. The broad peak, from approximately 3700 to 3000 cm^{-1}, and the peak at 1643 cm^{-1} (bending mode, υ_2) are assigned to the adsorbed water. This may be justified by the low drying temperature (60 ºC) and the absence of a ripening (ageing) treatment (Osaka et al. 1991; Koutsopoulos 2002; Zhou et al. 2008). The peaks assigned to the vibrational mode of OH^- (around 630 cm^{-1}) and to the stretching mode of OH^- (around 3571 cm^{-1}) are also present, although not well resolved. In the case of the peak assigned to the stretching mode of OH^-, this is due to an overlap with the broad band of the adsorbed water (around 3700 to 3000 cm^{-1}) (Panda et al. 2003). Regarding the vibrational mode of OH^-, the reason why the peak is not clearly visible may be explained by the presence of carbonate ions (Nelson and Featherstone 1982). Bands at 1454 and 1428 cm^{-1} are indicative of the carbonate ion substitution (Koutsopoulos 2002) and are especially observed in the spectrum of the precipitate obtained for the mixing Ca/P molar ratio 1.67, since alkaline solutions readily absorb CO_2 (Osaka et al. 1991). The presence of these bands is characteristic of a carbonated HAp of B-type, where the carbonate ions occupy the phosphate ions sites (Osaka et al. 1991; Zhou et al. 2008). The small band around 875 cm^{-1} can be attributed to the vibrational frequencies of carbonate ions or HPO_4^{2-} group (Koutsopoulos 2002), which is consistent with a carbonated HAp or calcium-deficient HAp. The noise observed in the commercial HAp spectrum (1800 to 1400 cm^{-1}) is due to water vapor.

Precipitates were also characterized in terms of their final Ca/P molar ratio.

Table 5.6. Ca/P molar ratio of the final products formed for different mixing Ca/P molar ratios.

Mixing Ca/P molar ratio	Final Ca/P molar ratio
1.00	1.36 ± 0.02
1.33	2.10 ± 0.02
1.67	1.46 ± 0.03
Commercial HAp	1.811 ± 0.0025

According to **Table 5.6**, precipitates are non-stoichiometric HAp, since their molar ratio is different from the stoichiometric value. The product obtained for the mixing Ca/P molar ratio 1.67 seems to be calcium deficient HAp, once its Ca/P molar ratio is lower than 1.67.

Actually, HAp is a compound with a variable composition existing over Ca/P molar ratios from 1.67 for stoichiometric to ≈1.5 for fully calcium deficient HAp (Wang and Nancollas 2008), and sometimes even outside this range (Elliot 1994). Regarding the Ca/P molar ratio of the final product obtained for the mixing Ca/P molar ratio 1.33, it is higher than the stoichiometric value, showing therefore the formation of a carbonated HAp of B-type (Kumta et al. 2005; Nelson and Featherstone 1982).

5.3.2.3 Particle size, size distribution and morphology

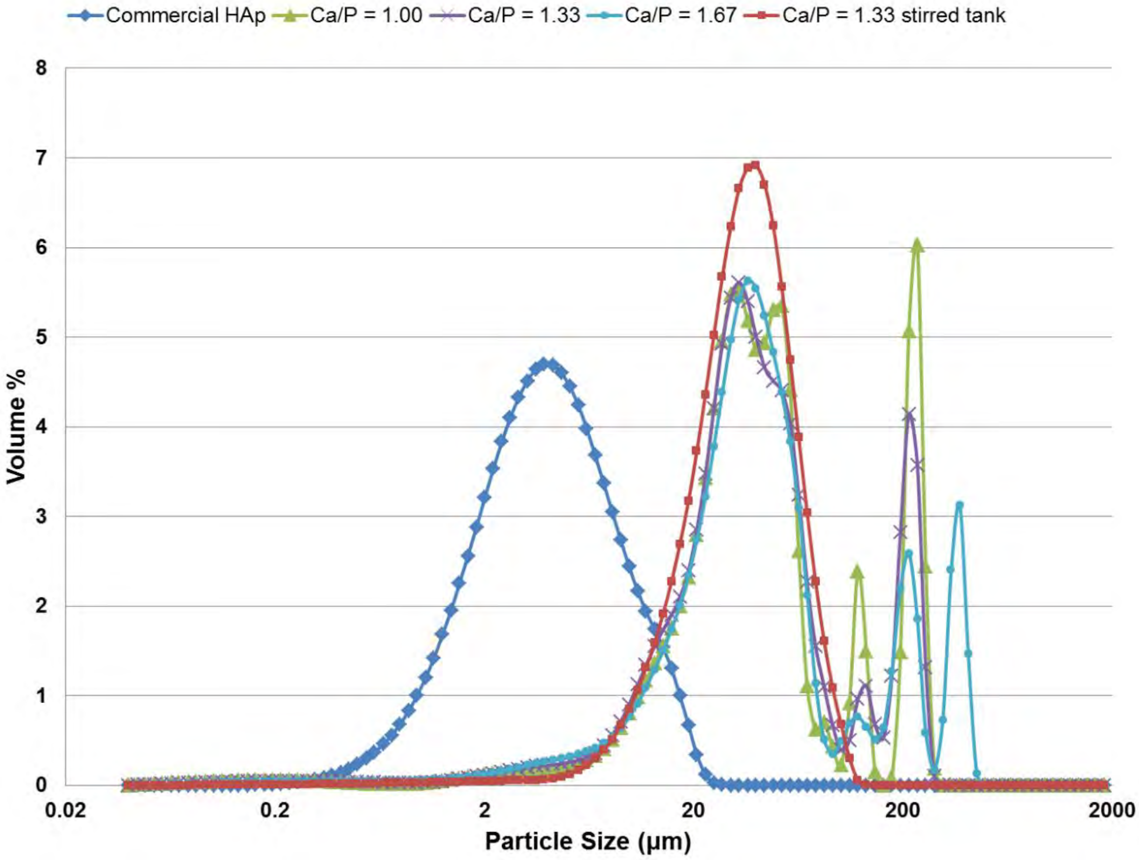

Figure 5.20. Particle size distribution in volume of the particles produced in the meso-OFR operated in batch mode for different mixing Ca/P molar ratios.

Table 5.7. Parameters of the particle size distribution in volume of the powders produced in the meso-OFR operated in batch for different mixing Ca/P molar ratios. d_{10}: 10% of the particles are smaller than this value, d_{50}: 50% of the particles are smaller than this value; d_{90}: 90% of the particles are smaller than this value; span: width of the distribution based on the 10%, 50% and 90% quantile.

Reactor	**Mixing Ca/P molar ratio**	**Particles size (μm)**			**Span**
		d_{10}	d_{50}	d_{90}	
Meso-OFR operated in batch	1.00	14.20	40.38	228.2	5.30
	1.33	13.25	38.96	207.3	4.98
	1.67	13.26	40.64	239.7	5.57
Stirred tank batch reactor	1.33	15.48	36.22	68.11	1.45
Commercial HAp	-	1.29	3.72	10.19	2.39

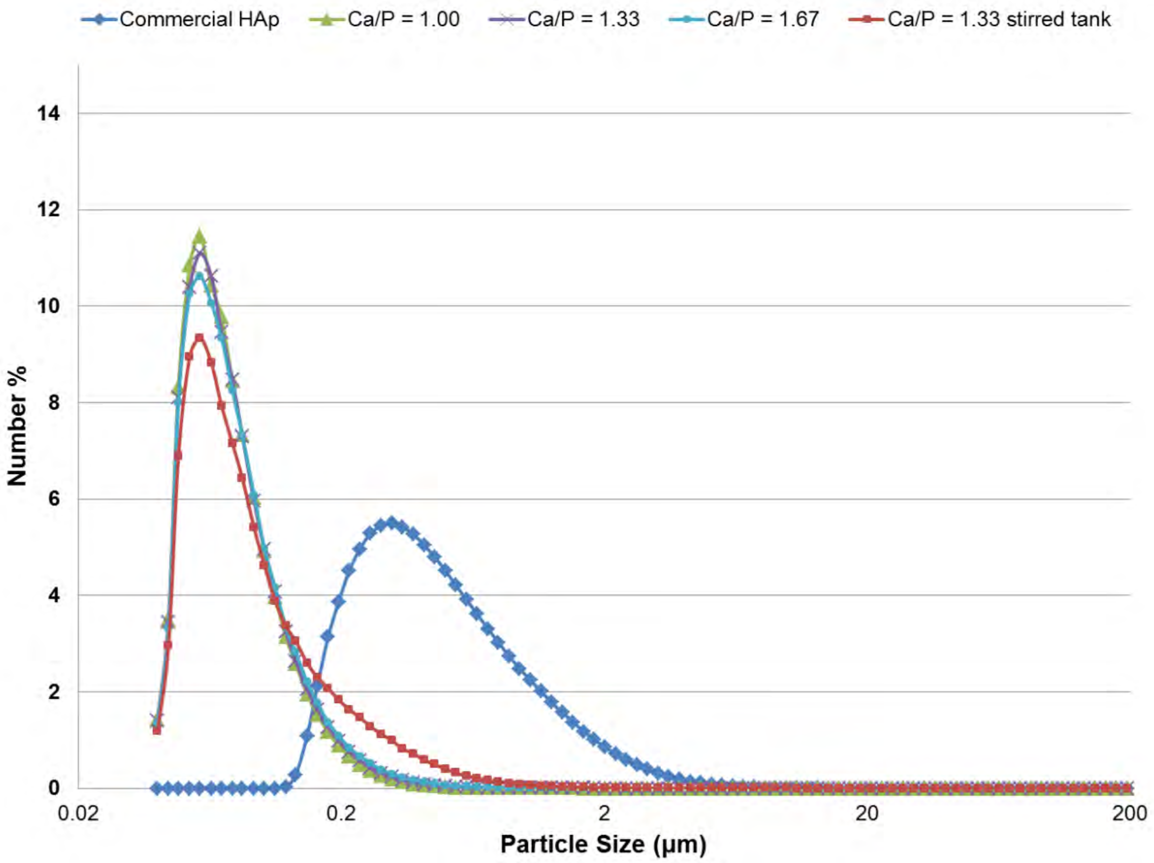

Figure 5.21. Particle size distribution in number of the particles produced in the meso-OFR operated in batch for different mixing Ca/P molar ratios.

Table 5.8. Parameters of the particle size distribution in number of the powders produced in the meso-OFR operated in batch for different mixing Ca/P molar ratios. d_{10}: 10% of the particles are smaller than this value, d_{50}: 50% of the particles are smaller than this value; d_{90}: 90% of the particles are smaller than this value; span: width of the distribution based on the 10%, 50% and 90% quantile.

Reactor	**Mixing Ca/P molar ratio**	**Particles size (µm)**			**Span**
		d_{10}	d_{50}	d_{90}	
Meso-OFR operated in batch	1.00	0.046	0.066	0.125	1.18
	1.33	0.047	0.067	0.123	1.23
	1.67	0.047	0.068	0.134	1.29
Stirred tank batch reactor	1.33	0.047	0.074	0.209	2.18
Commercial HAp	-	0.19	0.40	1.22	3.03

According to **Figure 5.20**, **Figure 5.21** (obtained from the conversion of the particle size distribution in volume), **Table 5.7** and **Table 5.8** (obtained from the conversion of the particle size distribution in volume), particle size distributions for all the mixing molar ratios studied are similar. The particles formed seem to consist in two types of populations, particles formed by aggregates at the micrometer range and nanometer-sized primary particles. However, based on **Figure 5.21** and **Table 5.8**, the as-prepared HAp particles are mainly at the nanometer range with a mean size (d_{50}) of about 67 nm, being smaller than the commercial HAp particles (Spectrum, minimum 40 meshes), originally submitted to granulometric separation. It is very important to underline that particles produced were directly obtained from the system without thermal treatment and without granulometric separation. Besides, the parameters of the particle size distribution in number (see **Table 5.8**) reveal that the size distribution of the particles formed in the meso-OFR is narrower than the size distribution of the commercial powder.

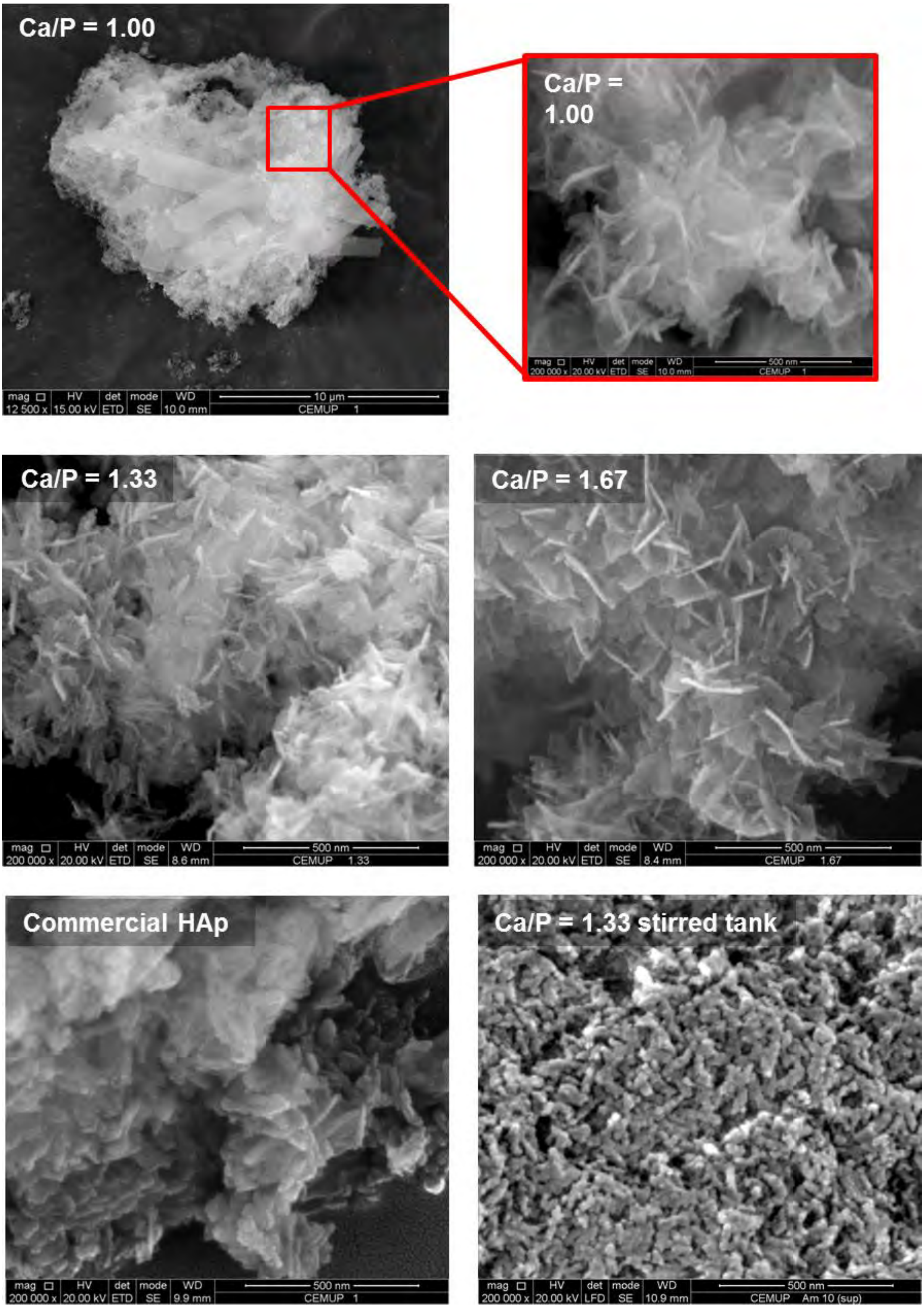

Figure 5.22. SEM images of the particles obtained in the meso-OFR operated in batch for different mixing Ca/P molar ratios.

SEM images (**Figure 5.22**) corresponding to particles obtained for the mixing molar ratio Ca/P = 1.00 show two types of crystals: crystals that exhibit well defined platelet morphology and a smooth surface, with an average crystallite size around 10 to 20 μm, and aggregated plate-shaped crystals with crystallites at the nanometer range. The well-defined platelet morphology is characteristic of DCPD (Panda et al. 2003; Siddharthan et al. 2005) and the nanocrystallites are characteristic of HAp (Zhuang et al. 2012). As mentioned before, DCPD could also be precipitated in the present operating conditions. DCDP, which easily forms a plate-shaped crystal morphology (Zhuang et al. 2012), could then be transformed into HAp by maintaining the plate-shaped particle morphology. Concerning the mixing Ca/P molar ratios 1.33 and 1.67, powders mostly consist of crystals exhibiting a plate-like (predominant) and rod-like morphology with typical sizes in the nanometer range, being in agreement with the literature. According to Neira et al. (2009), phase-pure HAp products can be characterized as either rod-like (whiskers, needles, wires, fibers, etc.) or plate-like. Further, the precipitated particles for the mixing molar ratio Ca/P = 1.67 seem slightly bigger and have a well-defined morphology when compared to the precipitated particles for the mixing molar ratio Ca/P = 1.33.

Based on the results presented above, the mixing molar ratio Ca/P = 1.33 was chosen for the continuation of the work, once stable HAp nanoparticles were generated faster and under near-physiological conditions of temperature and pH. This is particularly important when preparing HAp for medical purposes. Indeed, it is important to follow specific criteria for pH and temperature in order to promote more conductive conditions for the survival of bone-related cells (Kumta et al. 2005).

5.3.2.4 Comparison between the powder produced in the meso-OFR operated in batch and the powder produced in the stirred tank batch reactor

HAp nanoparticles prepared under the optimized experimental conditions in a stirred tank batch reactor (Castro et al. 2012) and in the meso-OFR operated in batch were compared. HAp precipitation process was carried out in both reactors under the same conditions of temperature (37 °C), mixing Ca/P molar ratio (Ca/P = 1.33) and power density (31.5 $W.m^{-3}$). The constant power density applied to both reactors was used as the reference criterion in this comparative study. Despite mixing mechanisms being different in each system, and thereby hydrodynamic conditions being not directly comparable, this criterion is quite informative, because it enables assessing the effectiveness of both reactors for a given power input, in terms of quality of the precipitated particles.

According to **Figure 5.17**, pH stabilizes at approximately 2500 s in the meso-OFR, while in the stirred tank batch reactor pH stabilizes around 10000 s, meaning that the majority of the precipitation reaction is completed about four times faster in the meso-OFR.

The diffraction patterns (see **Figure 5.18**) indicate that the HAp prepared in the stirred tank batch reactor is single phased HAp with low crystallinity degree compared with the diffraction pattern of the HAp prepared in the meso-OFR operated in batch. This result is also confirmed by the FTIR spectra. Based on **Figure 5.19**, HAp prepared in the stirred tank is more amorphous, since its spectrum exhibits broader peaks, especially phosphate characteristic bands at 900-1200 cm^{-1}. Besides, carbonate contamination seems to be minimized in the meso-OFR, as carbonate bands at approximately 1454 and 1428 cm^{-1} are barely detected in the spectrum of the powder obtained in the meso-OFR (see **Figure 5.19**).

Based on particle size distribution in volume (see **Figure 5.20**) and particle size distribution in number (see **Figure 5.21**) and in their respective parameters (see **Table 5.7** and **Table 5.8**), the as-prepared HAp particles are composed by primary particles at the nanometer range and micrometric-size aggregates in both the meso-OFR and the stirred tank. However, the particle size distribution in number shows that most of the as-prepared HAp particles are at the nanometer size (see **Figure 5.21** and **Table 5.8**) for both reactors. Further, it is possible to confirm that smaller particles were prepared in the meso-OFR (see **Table 5.8**). On the other hand, particle size distribution in volume data (see **Figure 5.20** and **Table 5.7**) evidences the presence of larger aggregates (around 200 μm) in the meso-OFR. This may be explained by the fact that smaller particles were formed in the meso-OFR, as verified, and have thus higher tendency to aggregate. It is also possible to confirm that the HAp particles prepared in the meso-OFR have a narrower size distribution compared with the size distribution of the HAp particles prepared in the stirred tank (see **Table 5.8**).

Figure 5.22 revealed the characteristic morphology of the precipitated HAp particles in both reactors. It can be observed that HAp nanoparticles prepared in the stirred tank appear typical rod-like shaped, while the HAp nanoparticles prepared in the meso-OFR mostly consists in plate-shaped HAp particles, although some particles appear to be rod-like shaped.

In short, this work showed the feasibility of a meso-OFR for process intensification for HAp nanoparticles production. By comparison with a stirred tank reactor, the proposed meso-OFR has the capacity of yielding HAp nanoparticles in about four times faster. Further, the mesoreactor yielded HAp particles with improved characteristics, namely higher crystallinity, smaller size and narrower size distribution. Moreover, the meso-OFR is a mesoscale (millilitre) device, thus reducing reagent requirements and waste generated.

5.4 Conclusion

Precipitation of HAp was investigated in a vertical meso-OFR operated batchwise under near physiological conditions of pH and temperature. Mixing efficiency of the meso-OFR under batch operation was first evaluated. Values of $f = 0.83$ Hz and $x_0 = 4.5$ mm proved to be the best operating conditions for fast mixing and more homogeneous reaction environment, e.g. conditions that favor the formation of small and uniform HAp particles with consistent characteristics. Precipitation of HAp was carried out for different mixing Ca/P molar ratios, formation of single-phased calcium-deficient and/or B-type carbonated HAp being confirmed for the mixing Ca/P molar ratios 1.33 and 1.67. It also has been shown that for the mixing molar ratio Ca/P=1.33, stable HAp nanoparticles were obtained at a pH close to 7, which is particularly important in the preparation of HAp for medical purposes. Constant power density was used as the reference operation criterion and applied to the meso-OFR operated in batch and to a stirred tank batch reactor, thus enabling to compare the performance of both reactors, in terms of quality of the precipitated particles, for a given power input. Based on the aforementioned results, the reactor type affects the crystallinity, carbonate content, morphology, size and size distribution of the as-prepared HAp nanoparticles. In the proposed meso-OFR, operated under oscillatory flow, HAp nanoparticles were generated about four times faster than in the stirred tank batch reactor operated under a similar power density. Further, HAp particles formed showed improved characteristics, namely higher crystallinity, smaller size and narrower size distribution. Therefore, besides the meso-OFR proved to be more efficient in the production of HAp nanoparticles, it turns the process more clean and safe due to the reduction of waste generated and reagents requirements, making it an interesting tool for high throughput experimentation.

Finally, we believe that even if the reactor studied in this work does not represent a full-scale production unit, it may be a useful contribution to the development of a platform for the production of valuable and high-quality HAp nanoparticles.

5.5 References

Bernard, L, M Freche, J.L Lacout, and B Biscans. 2000. “Modeling of the Dissolution of Calcium Hydroxyde in the Preparation of Hydroxyapatite by Neutralization.” *Chemical Engineering Science* 55 (23): 5683–5692.

Chew, C. M., and R. I. Ristic. 2005. “Crystallization by Oscillatory and Conventional Mixing at Constant Power Density.” *AIChE Journal* 51 (5): 1576–1579.

Ferreira, A, C. Oliveira, and F. Rocha. 2003. “The Different Phases in the Precipitation of Dicalcium Phosphate Dihydrate.” *Journal of Crystal Growth* 252 (4): 599–611.

Fitch, A. W. Hongbing, J. and X. Ni. 2005. “An Investigation of the Effect of Viscosity on Mixing in an Oscillatory Baffled Column Using Digital Particle Image Velocimetry and Computational Fluid Dynamics Simulation.” *Chemical Engineering Journal* 112 (1-3): 197–210.

Harvey, A, M R Mackley, N Reis, J A Teixeira, and A A Vicente. 2003. “Fluid Mixing and Particle Suspension in a Novel Microreactor.” *Museum* (1993): 26–30.

Haynes, W.M. 2012. *CRC Handbook of Chemistry and Physics*. 93RD ed.

Johannsen, K., and S. Rademacher. 1999. “Modelling the Kinetics of Calcium Hydroxide Dissolution in Water.” *Acta Hydrochimica Et Hydrobiologica* 27 (2): 72–78.

Koutsopoulos, S. 2002. “Synthesis and Characterization of Hydroxyapatite Crystals: a Review Study on the Analytical Methods.” *Journal of Biomedical Materials Research* 62 (4): 600–12.

Kumta, P. N, C. Sfeir, D.-H. Lee, D. Olton, and D. Choi. 2005. “Nanostructured Calcium Phosphates for Biomedical Applications: Novel Synthesis and Characterization.” *Acta Biomaterialia* 1 (1): 65–83.

Landi, E. 2003. “Carbonated Hydroxyapatite as Bone Substitute.” *Journal of the European Ceramic Society* 23 (15): 2931–2937.

Lawton, S., G. Steele, P. Shering, L. Zhao, I. Laird and X. Ni. 2009. “Continuous Crystallization of Pharmaceuticals Using a Continuous Oscillatory Baffled Crystallizer.” *Organic Process Research & Development* 13 (6): 1357–1363.

Lee, D., and P. N. Kumta. 2010. “Chemical Synthesis and Stabilization of Magnesium Substituted Brushite.” *Materials Science and Engineering: C* 30 (7): 934–943.

Lopes, A. M., D. P. Silva, A. A. Vicente, A. Pessoa-Jr, and J. A. Teixeira. 2011. “Aqueous Two-phase Micellar Systems in an Oscillatory Flow Micro-reactor: Study of

Perspectives and Experimental Performance.” *Journal of Chemical Technology & Biotechnology* 86 (9): 1159–1165.

Lynn, A.K., and W Bonfield. 2005. “A Novel Method for the Simultaneous, Titrant-Free Control of pH and Calcium Phosphate Mass Yield.” *Accounts of Chemical Research* 38 (3): 202–207.

Ma, M.-G., and J.-F. Zhu. 2009. “Solvothermal Synthesis and Characterization of Hierarchically Nanostructured Hydroxyapatite Hollow Spheres.” *European Journal of Inorganic Chemistry* (36): 5522–5526.

Meskinfam, M, M S Sadjadi, and H Jazdarreh. 2012. “Synthesis and Characterization of Surface Functionalized Nanobiocomposite by Nano Hydroxyapatite” *International Journal of Chemical and Biological Engineering* 6: 192–195.

Neira, I. S., Y. V. Kolen’ko, O. I. Lebedev, G. Van Tendeloo, H. S. Gupta, F. Guitian, and M. Yoshimura. 2009. “An Effective Morphology Control of Hydroxyapatite." *Crystals and Design*.

Ni, X, D C Bennett, K C Symes, and B D Grey. 1999. “Inverse Phase Suspension Polymerization of Acrylamide in a Batch Oscillatory Baffled Reactor.” *Polymer*: 1669–1676.

Ni, X, S Gao, R. H. Cumming, and D. W. PRITCHARD. 1995. “A Comparative Study of Mass Transfer in Yeast for a Batch Pulsed Baffled Bioreactor and a Stirred Tank Fermenter.” *Chemical Engineering Science* 50 (13): 2127–2136.

Ni, X, H Jian, and A W Fitch. 2002. “Computational Uid Dynamic Modelling of Ow Patterns in an Oscillatory Ba Ed Column.” *Chemical Engineering Science* 57: 2849–2862.

Ni, X, J C Johnstone, K.C. Symes, B.D. Grey, and D.C. Bennett. 2001. “Suspension Polymerization of Acrylamide in an Oscillatory Baffled Reactor : from Drops to Particles.” *AIChE Journal* 47 (8).

Ni, Xiongwei, K.R Murray, Y. Zhang, D. Bennett, and T. Howes. 2002a. “Polymer Product Engineering Utilising Oscillatory Baffled Reactors.” *Powder Technology* 124 (3): 281–286.

Ni, Xiongwei, Y. S. De Gélicourt, J. Neil, and T. Howes. 2002b. “On the Effect of Tracer Density on Axial Dispersion in a Batch Oscillatory Baffled Column.” *Chemical Engineering Journal* 85: 17–25.

Osaka, A., Y. Miura, K. Takeuchi, M. Asada, and K. Takahashi. 1991. “Calcium Apatite Prepared from Calcium Hydroxide and Orthophosphoric Acid.” *Journal of Materials Science: Materials in Medicine* 2 (1): 51–55.

Phan, A. N., and A. P. Harvey. 2011. “Effect of Geometrical Parameters on Fluid Mixing in Novel Mesoscale Oscillatory Helical Baffled Designs.” *Chemical Engineering Journal* 169 (1-3): 339–347.

Reis, N., A. Harvey, M. R. Mackley, A. A. Vicente, and J. A. and Teixeira. 2005. “Fluid Mechanics and Design Aspects of a Novel Oscillatory Flow Screening Mesoreactor.” *Chemical Engineering Research and Design* 83: 357–371.

Reis, N., A. A. Vicente, J. A. Teixeira, and M. R and Mackley. 2004. “Residence Times and Mixing of a Novel Continuous Oscillatory Flow Screening Reactor.” *Chemical Engineering Science* 59: 4967–4974.

Reis, N. M. F.. 2006. “Novel Oscillatory Flow Reactors for Biotechnological Applications.”

Rezk, A. R, A. Qi, J. R Friend, W. H. Li, and L. Y. Yeo. 2012. “Uniform Mixing in Paper-based Microfluidic Systems Using Surface Acoustic Waves.” *Lab on a Chip* 12 (4): 773–9.

Ristic, R. 2007. “Oscillatory Mixing for Crystallization of High Crystal Perfection Pharmaceuticals.” *Chemical Engineering Research and Design* 85 (7): 937–944.

Wang, L., and G. H. Nancollas. 2008. “Calcium Orthophosphates: Crystallization and Dissolution.” *Chemical Reviews* 108 (11): 4628–69.

Zhou, W., M. Wang, W. Cheung, B. Guo, and D. Jia. 2008. “Synthesis of Carbonated Hydroxyapatite Nanospheres Through Nanoemulsion.” *Journal of Materials Science: Materials in Medicine* 10 (1): 103–110.

Zhuang, Z., H. Yamamoto, and M. Aizawa. 2012. “Synthesis of Plate-shaped Hydroxyapatite via an Enzyme Reaction of Urea with Urease and Its Characterization.” *Powder Technology* 222: 193–200.

6 CONTINUOUS-FLOW PRECIPITATION OF HAp AT 37 °C IN A MESO OSCILLATORY FLOW REACTOR

Continuous-flow precipitation of HAp was investigated in a meso oscillatory flow reactor (meso-OFR). HAp precipitation was also studied in a scaled-up meso-OFR, obtained by associating in series eight vertical meso-ORFs. Experiments were carried out by mixing a calcium aqueous solution with phosphate aqueous solution under near-physiological conditions of temperature and pH, using fixed frequency (f = 0.83 Hz) and amplitude (x_0 = 4.5 mm). Further, HAp precipitation was studied at different residence times from 0.4 to 6.7 min. It has been shown that the mean particle size and the aggregation degree of the prepared HAp particles decrease with decreasing residence time. HAp nanoparticles with a mean size (d_{50}) of 77 nm, narrow size distribution and uniform morphology were obtained at a residence time τ of 0.4 and 3.3 min, in the meso-OFR and the scaled-up meso-OFR, respectively. These results show the capability of the meso-OFR and the scaled-up meso-OFR for continuous production of uniform HAp nanoparticles, while also confirming the possibility of OFR scale-up by in series association of individual OFRs.

6.1 Introduction

Traditional stirred tank batch reactors for synthetic production of hydroxyapatite (HAp) provide only limited amounts of material and crystallization conditions may change during multiple syntheses (Lawton et al. 2009). The problem is magnified as the scale of operation increases since the control of mixing is very difficult in large vessels (Jongen et al. 2003), particularly in fast precipitation systems owing to the very fast reaction kinetics (Jones et al. 2005).This can lead to problems in achieving consistent product specifications (Lawton et al. 2009). Even small differences in stoichiometry, morphology or size may affect the chemical, biological and physical behavior of the material (Tadic et al. 2002). On one hand, scale up is necessary to increase production rate, and on the other hand the science of reactive precipitation makes it difficult to apply precipitations into industrial scale batch operations under well-defined and reproducible conditions.

Continuous operation offers significant advantages in terms of process and costs (Lawton et al. 2009; Mcmullen and Jensen 2010; Lopes et al. 2011). It allows more efficient use of reagents, solvents, energy and space whilst minimizing the production of waste materials and reactor downtime for reactor maintenance and cleaning. Further, it affords the advantage of enhanced reproducibility of results because all material crystallizes under uniform conditions, resulting in the formation of crystals with consistent properties (Lawton et al. 2009). In addition, continuous operations allow higher productivity and permit the continuous variation of the chemical composition of the reaction medium.

In this work, a simple apparatus for the continuous preparation of HAp nanoparticles under near-physiological conditions of temperature and pH is presented. Continuous-flow precipitation of HAp was performed in a meso-OFR presented in the previous section, and in a scaled-up meso-OFR, being suitable for continuous high throughput screening due to their small volume (millilitre). The fluid mechanics of the meso-OFR operated in continuous are governed by dimensionless dynamic groups (Chew and Ristic 2005; Reis 2006; Phan et al. 2011): the Strouhal (*St*) and the oscillatory Reynolds (Re_o), already described in the previous chapter, and the net flow Reynolds number (Re_n). Re_n can be defined as:

$$\mathrm{Re_n} = \frac{\rho D u}{\mu} \tag{6.1}$$

where u is the superficial velocity of the liquid (m.s^{-1}).

HAp precipitation was carried at 37 °C, for a mixing Ca/P molar ratio of 1.33, and at different residence times (τ = 0.9 and 0.4 min for the meso-OFR, and τ = 6.7 and 3.3 min for the scaled-up meso-OFR). Characteristics of the prepared powders (purity, size, size distribution and morphology) were evaluated for all the operating conditions.

6.2 Materials and Methods

6.2.1 Precipitation of HAp

6.2.1.1 Description of the experimental set-ups

Continuous-flow precipitation of HAp was carried out in the following experimental installation (**Figure 6.1**).

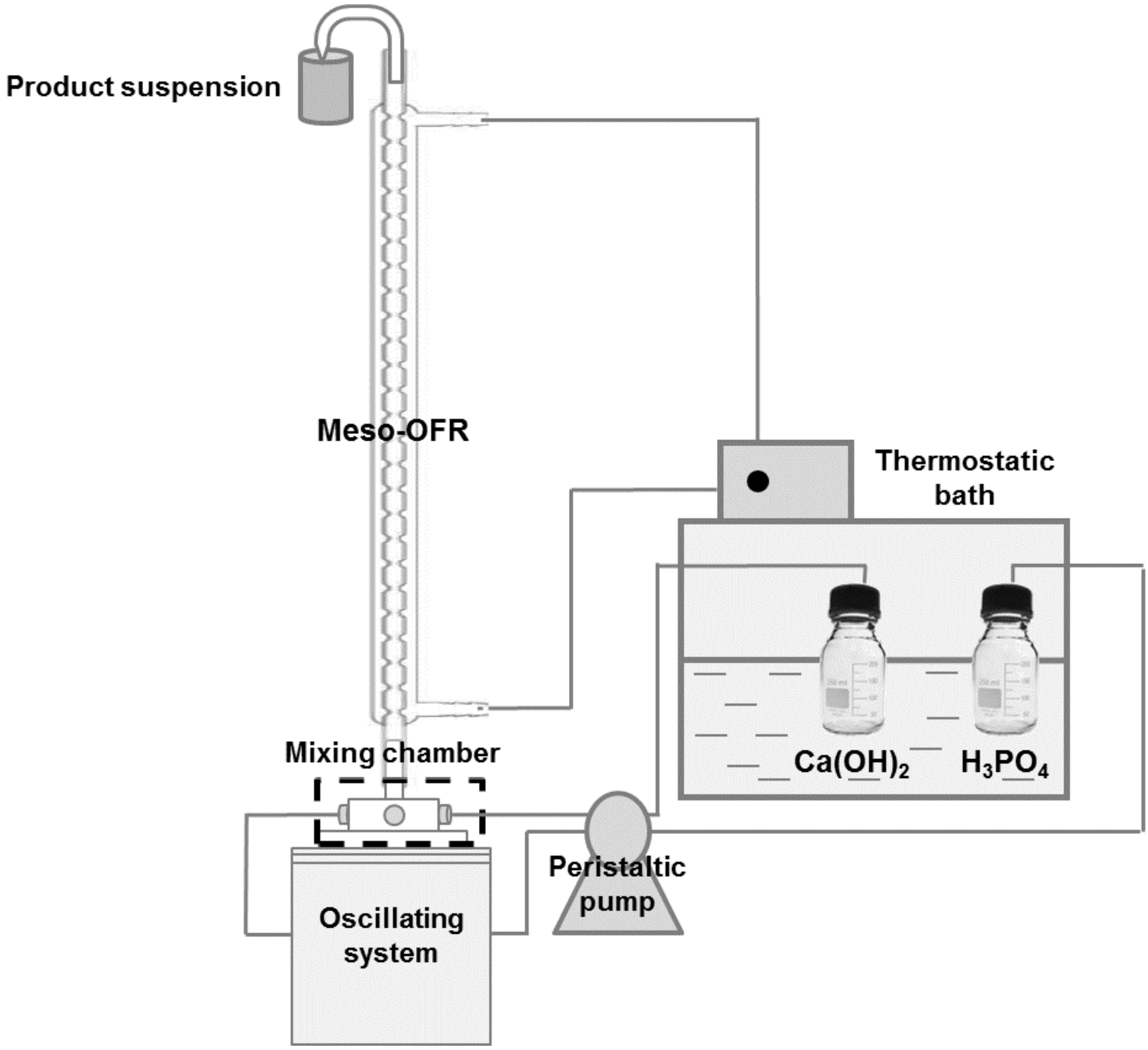

Figure 6.1. Experimental apparatus for the continuous-flow precipitation of HAp.

HAp precipitation was then carried out in the scaled-up meso-OFR. For this, eight meso-OFRs were positioned in series, each meso-OFR placed vertically (**Figure 6.2**).

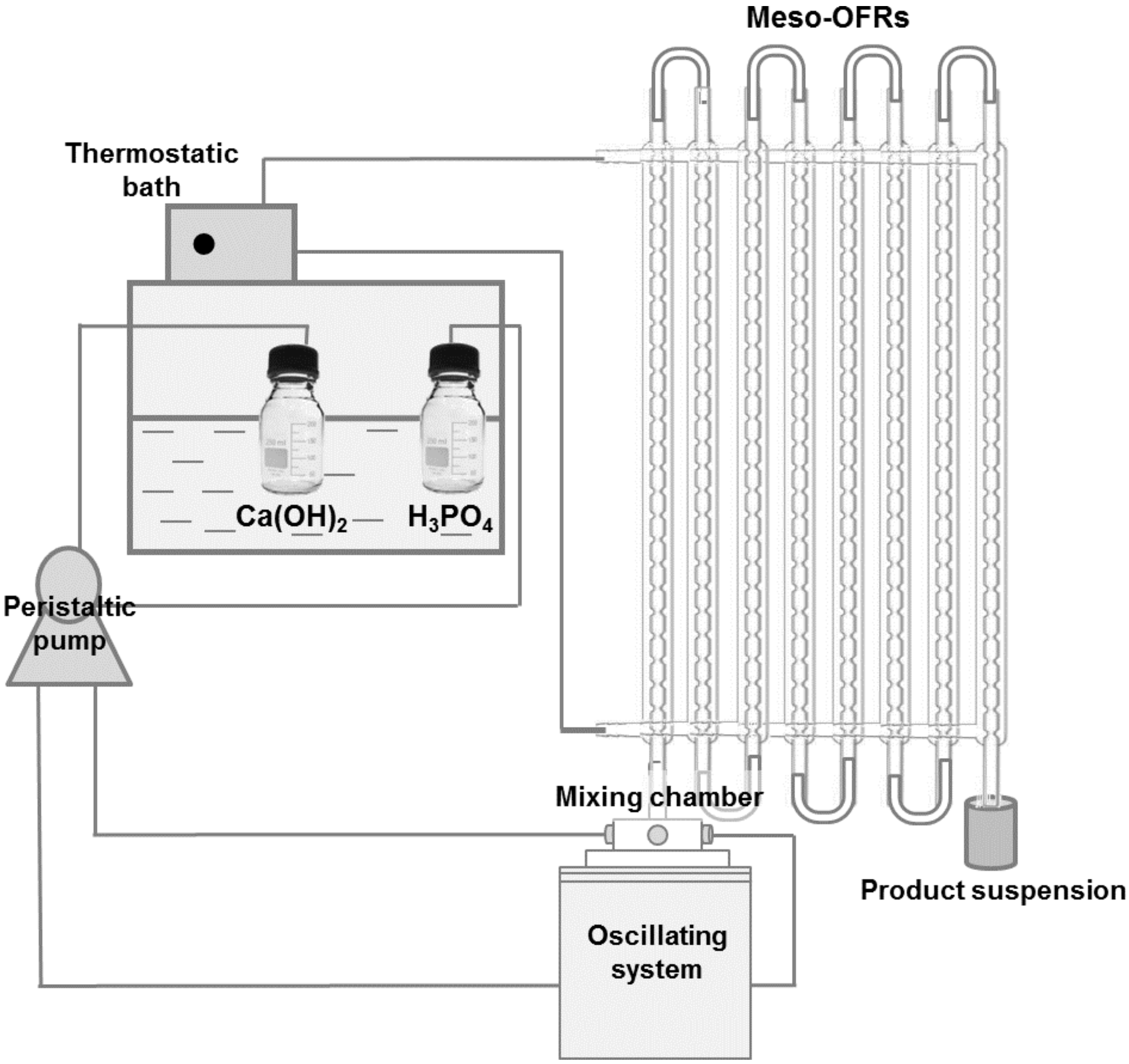

Figure 6.2. Experimental apparatus for the scale-up of the continuous-flow precipitation of HAp.

For both experimental apparatuses, the fluid was oscillated using a custom-built oscillating system. Oscillation amplitude (x_0) and frequency (*f*) were fixed to 4.5 mm and 0.83 Hz, respectively. Reactants were fed into the set-ups by means of a peristaltic pump (ISMATEC IPS 8, Switzerland). Temperature of the reactants and temperature inside the meso-OFRs were regulated by a thermostatic bath maintained at 37 ºC.

6.2.1.2 Powder preparation

HAp synthesis was achieved by the mixing of a saturated calcium hydroxide (Riedel-de Haën, 96%) aqueous solution (0.01926 mol.dm^{-3}) and an orthophosphoric acid (Pronalab, 85%) aqueous solution (0.01448 mol.dm^{-3}), being reactant solutions prepared according to the protocol used in 3.2.1.

Continuous-flow precipitation of HAp was performed under the same conditions of temperature (37 °C), mixing Ca/P molar ratio (1.33), and frequency (0.83 Hz) and amplitude (x_0 = 4.5 mm) applied in the batch mode. Further, HAp precipitation was carried out at different residence times in one and eight vertical meso-OFRs. The operating conditions are presented in **Table 6.1**.

Table 6.1. Operating conditions for the continuous-flow precipitation of HAp in the meso-OFR and in the scaled-up meso-OFR.

Reactor	Liquid flow rate (mL/min)	N° of meso-OFRs	Total Volume (mL)	τ (min)
Meso-OFR	4.5	1	≈ 4	0.4
	9.0			0.9
Scaled-up meso-OFR	4.5	8	≈ 30	6.7
	9.0			3.3

Temperature (inoLab, WTW) and pH (SenTix Mic-D, WTW) were measured at different time intervals at the outlet of the mesoreactor. The pH electrode was calibrated with two buffer solutions at pH=7.00 and pH=10.00 at 25 ºC.

Samples were collected after approximately two residence times, until pH stabilization.

6.2.2 Powder characterization

Samples were withdrawn at the outlet of the mesoreactor, centrifuged (at 1500 rpm for 5 min), washed twice with ultra-pure water and kept in pure ethanol (99.8%), which stops the solid-liquid reaction (Bernard et al. 2000). X-ray diffraction (XRD), scanning electron microscopy (SEM), Fourier transform infrared spectroscopy (FTIR), particle size distribution and determination of the final Ca/P molar ratio were performed. Preparation of the samples for each characterization technique and equipment used are described in 3.2.2. The final precipitate was also dried and weighed for the estimation of the mass of the crystals obtained.

6.3 Results and Discussion

6.3.1 Important parameters in the precipitation of HAp

pH is an important parameter in determining the likelihood of the formation of calcium phosphate phases (Wang and Nancollas 2008). The influence of pH on the formation of calcium phosphates is linked to the properties of phosphate-containing solutions. Due to the triprotic equilibrium in these systems, variations in pH alter the relative concentrations of the four protonated forms of phosphoric acid (3.1) and thus both the chemical composition and the amount of the CaP that forms by direct precipitation (Lynn and Bonfield 2005).

In this work, experiments were conducted under near-physiological conditions of temperature and pH (**Table 6.2**), which is particularly important when preparing HAp for medical purposes. As already mentioned, it is important to follow specific criteria for pH and temperature in order to promote more conductive conditions for the survival of bone-related cells (Kumta et al. 2005). Furthermore, from a thermodynamic point of view, these conditions favor the precipitation of HAp, since at body temperature and pH between 4 and 12, HAp is the most stable calcium phosphate salt (Elliot 1994). Concerning the quantity of the precipitate obtained, results presented in **Table 6.2** show that the mass of precipitate prepared per mL is similar for all the operating conditions.

Table 6.2. Parameters measured during continuous-flow precipitation of HAp in the meso-OFR and in the scaled-up meso-OFR, for different operating conditions.

Reactor	**Operation type**	**Residence time τ (min)**	**pH**	**Precipitate (mg/mL)**
Meso-OFR	Continuous-flow	0.9	6.90	0.87
		0.4	7.10	0.93
Scaled-up meso-OFR	Continuous-flow	6.7	6.63	0.80
		3.3	6.65	0.83
Meso-OFR	Batch	67	6.38[a]	0.81
Stirred tank	Batch	330	6.9[a]	0.91

[a] pH value corresponds to the final value

6.3.2 Continuous-flow HAp precipitation

6.3.2.1 Phase identification

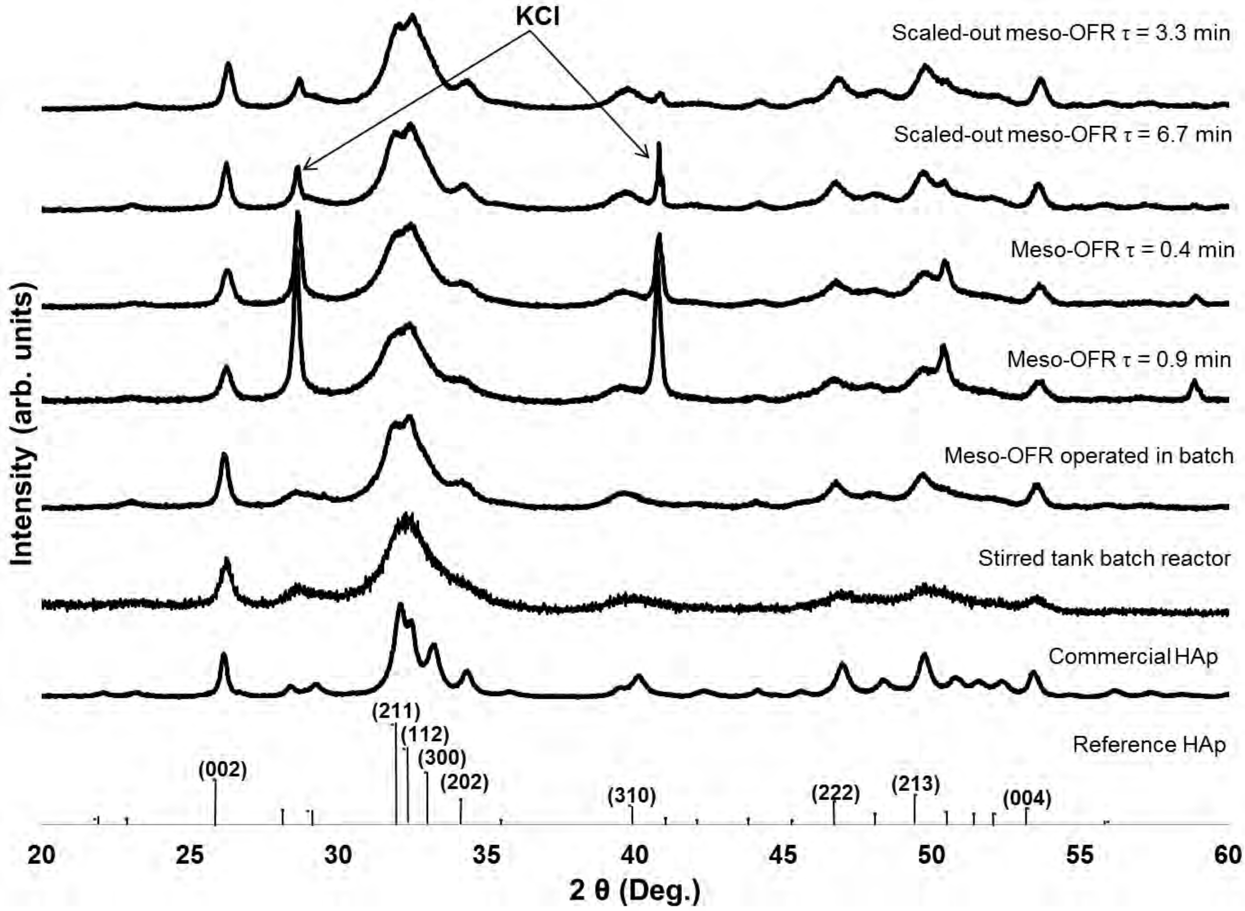

Figure 6.3. XRD patterns of the particles produced in the meso-OFR and the scaled-up meso-OFR operated in continuous for different operating conditions.

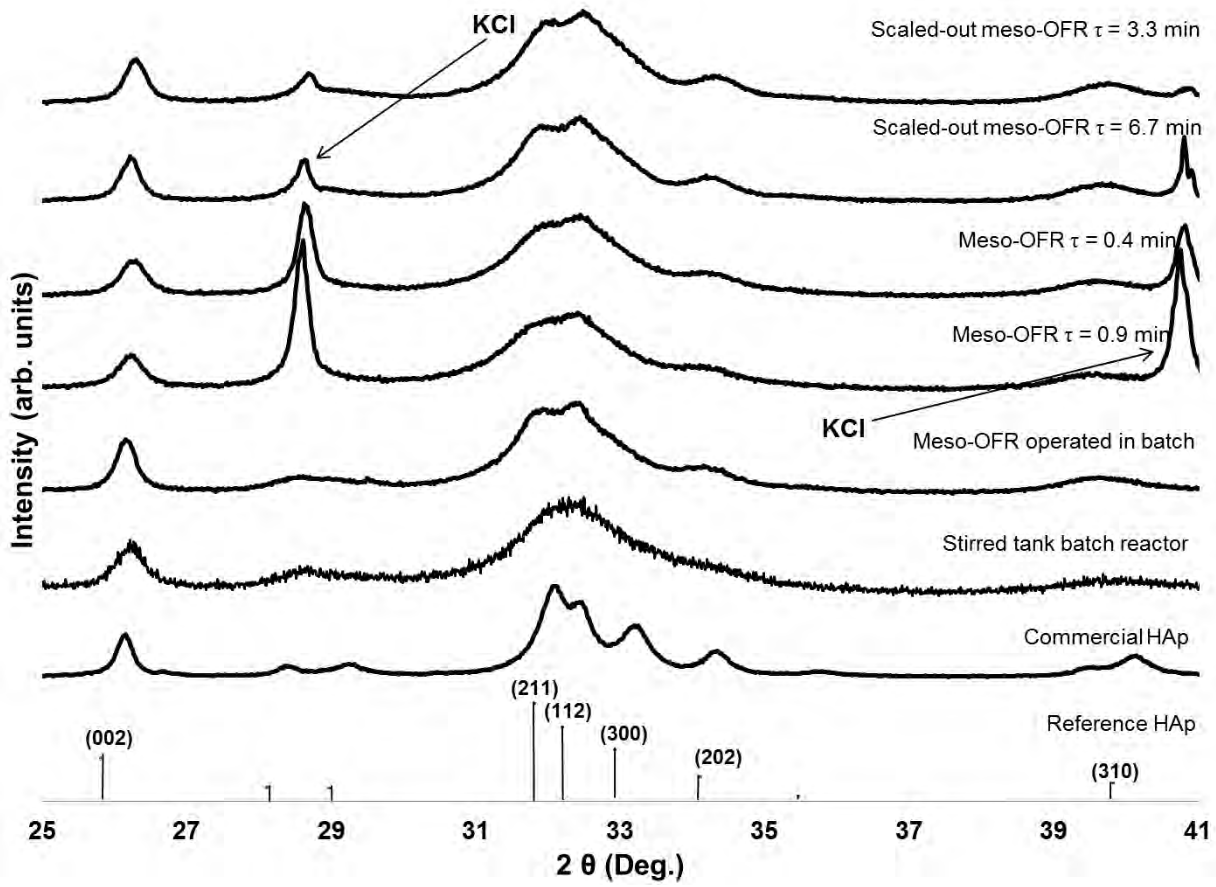

Figure 6.4. Magnified XRD patterns of the particles produced in the meso-OFR and the scaled-up meso-OFR operated in continuous for different operating conditions.

The XRD analysis of the prepared powders revealed no secondary phases (**Figure 6.3** and **Figure 6.4**) besides the apatitic phase, for all the operating conditions studied. XRD patterns of the different powders obtained match well the XRD pattern of the commercial HAp (Spectrum, minimum 40 meshes). However, broadening and overlap of the peaks are observed, being more pronounced in the diffraction pattern of the particles produced in the scaled-up meso-OFR. This may imply small crystallites and low crystallinity (Meskinfam et al. 2012). Peaks assigned to KCl (namely at 28 º2θ and 40.5 º2θ) are also exhibited, especially in the diffraction patterns of the particles prepared in the scaled-up meso-OFR. As already mentioned, this may be explained by the occlusion of KCl present in the mother liquor, which could have been trapped in the aggregates and crystallized at the drying step. KCl peaks are less detected for the lower residence times.

It can also be seen that there is a slight shift between the XRD patterns of the prepared powders and the XRD reference pattern of HAp. This is probably due to the experimental conditions under which XRD analyses were performed, since a slight shift is also visible in the diffraction pattern of commercial HAp.

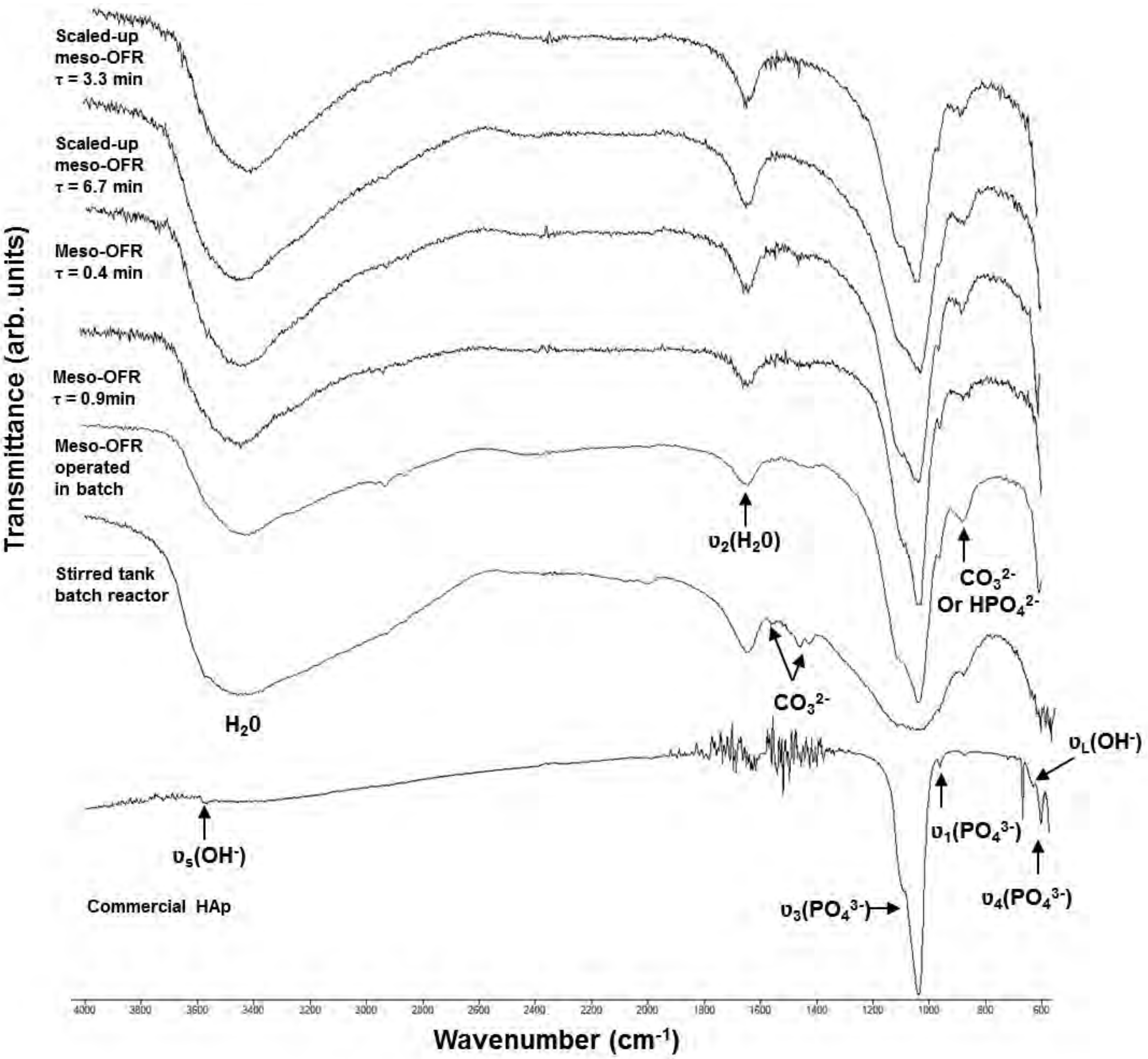

Figure 6.5. FTIR spectra of the particles produced in the meso-OFR and scaled-up meso-OFR operated in continuous for different operating conditions.

According to **Figure 6.5**, FTIR spectra exhibit stretching and bending vibrations of the phosphate, PO_4^{3-}, and the hydroxyl, OH^-, functional groups, characteristic of a typical apatite structure (Koutsopoulos 2002), although it is difficult to detect the peak related to ν_4 bending mode of PO_4^{3-}, and the peaks assigned to the vibrational mode (around 630 cm^{-1}) and stretching mode (around 3571 cm^{-1}) of OH^- are not well resolved. Concerning the peak assigned to stretching mode of OH^-, this can be due to the overlap with the broad peak (from approximately 3700 to 3000 cm^{-1}) of the adsorbed water on HAp particles (Ma and Zhu

2009). A second peak assigned to adsorbed water is also observed at 1643 cm^{-1} (bending mode, υ_2). Presence of adsorbed water on the HAp prepared particles can be explained by the low drying temperature (60 ºC) and the absence of a ripening (ageing) treatment (Osaka et al. 1991; Koutsopoulos 2002; Zhou et al. 2008). In addition, presence of a peak (around 875 cm^{1}) assigned to the vibrational frequencies of carbonate ions or HPO_4^{2-} group (Koutsopoulos 2002), suggests the formation of a carbonated HAp or calcium-deficient HAp.

6.3.3 Particle size, size distribution and morphology

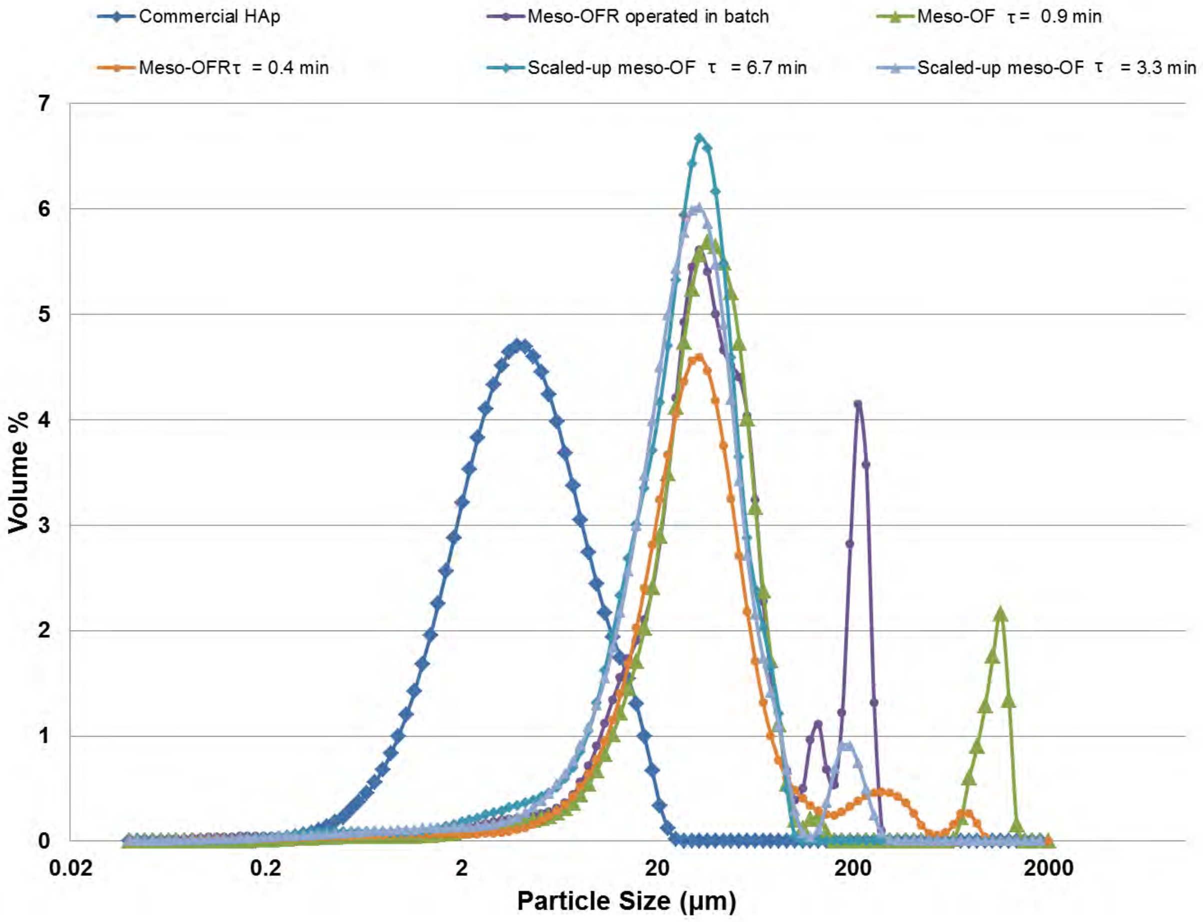

Figure 6.6. Particle size distribution in volume of the particles produced in the meso-OFR and scaled-up meso-OFR operated in continuous for different operating conditions.

Table 6.3. Parameters of the particle size distribution in volume of the powders produced in the meso-OFR and scaled-up meso-OFR operated in continuous for different operating conditions. d_{10}: 10% of the particles are smaller than this value, d_{50}: 50% of the particles are smaller than this value; d_{90}: 90% of the particles are smaller than this value; span: width of the distribution based on the 10%, 50% and 90% quantile.

Reactor	**Operation type**	**Residence time τ (min)**	**Particles size (µm)**			**Span**
			d_{10}	d_{50}	d_{90}	
Meso-OFR	Continuous-flow	0.9	14.68	38.31	110.1	2.49
		0.4	12.75	32.88	93.98	2.47
Scaled-up meso-OFR	Continuous-flow	6.7	10.07	30.18	59.12	1.60
		3.3	9.62	27.60	62.74	1.92
Meso-OFR	Batch	67	13.25	38.96	207.3	4.98
Stirred tank	Batch	330	15.48	36.22	68.11	1.45
Commercial HAp		-	1.29	3.72	10.19	2.39

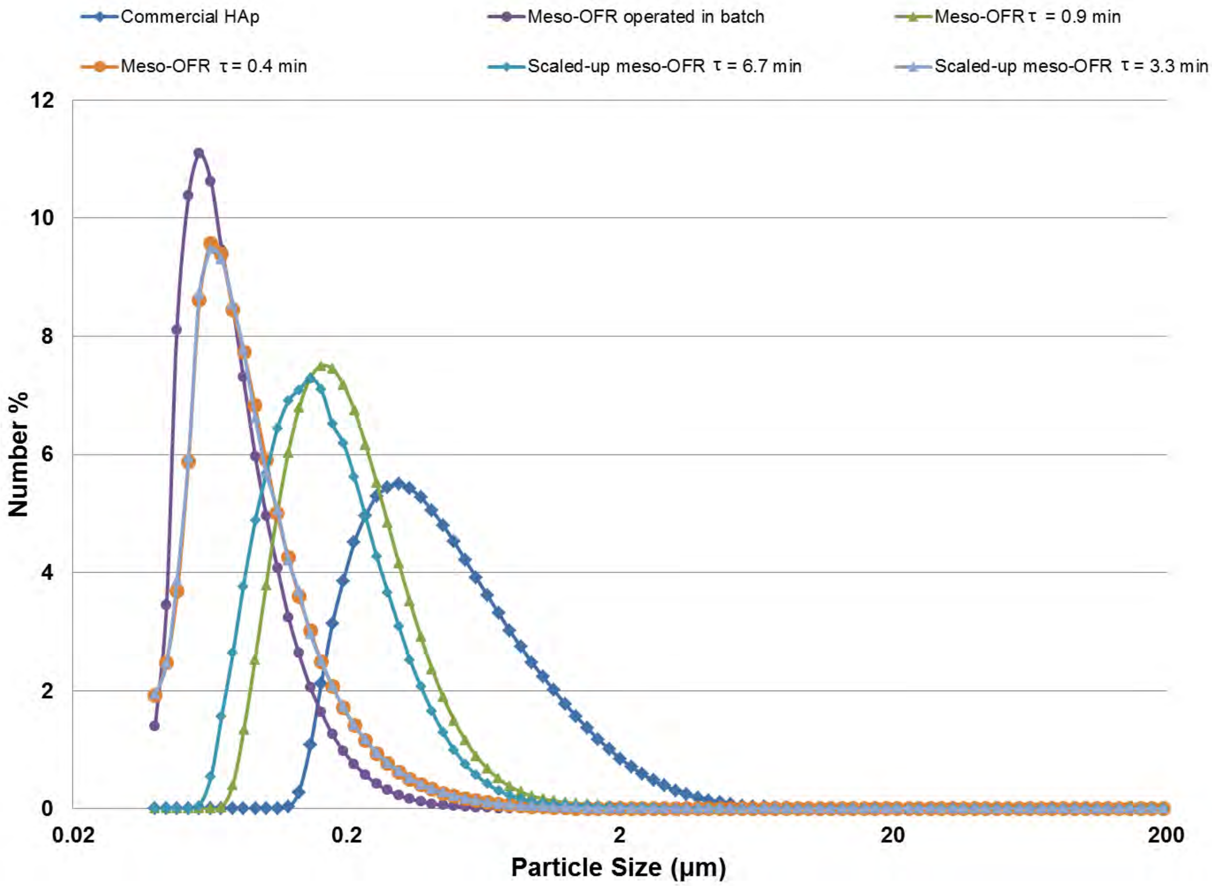

Figure 6.7. Particle size distribution in number of the particles produced in the meso-OFR and scaled-up meso-OFR operated in continuous for different operating conditions.

Table 6.4. Parameters of the particle size distribution in number of the powders produced in the meso-OFR and scaled-up meso-OFR operated in continuous for different operating conditions. d_{10}: 10% of the particles are smaller than this value, d_{50}: 50% of the particles are smaller than this value; d_{90}: 90% of the particles are smaller than this value; span: width of the distribution based on the 10%, 50% and 90% quantile.

Reactor	Operation type	Residence time τ (min)	Particles size (µm)			Span
			d_{10}	d_{50}	d_{90}	
Meso-OFR	Continuous-flow	0.9	0.106	0.183	0.389	1.55
		0.4	0.050	0.077	0.171	1.57
Scaled-up meso-OFR	Continuous-flow	6.7	0.087	0.154	0.332	1.59
		3.3	0.049	0.077	0.172	1.60
Meso-OFR	Batch	67	0.047	0.067	0.123	1.23
Stirred tank	Batch	330	0.047	0.074	0.209	2.18
Commercial HAp		-	0.19	0.40	1.22	3.03

According to **Figure 6.6** and **Figure 6.7** (obtained from the conversion of the particle size distribution in volume), and **Table 6.3** and **Table 6.4** (obtained from the conversion of the particle size distribution in volume), the as-prepared powders consist of a population of primary particles in the nanometer range and a population of micrometric-sized aggregates that given the considerable difference in size, could be separated. Aggregates probably result from the aggregation of primary nanoparticles, since small particles possess a high surface area to volume ratio, resulting in a high surface tension which they tend to lower by adhering to one another (Luque de Castro and Priego-Capote 2007). Further, the peak observed at 1000 µm (see **Figure 6.6**) is probably due to the presence of bubbles in the suspension analyzed. Results also show that the mean size and the aggregation degree of the as-prepared particles increase with increasing residence time. Based on **Figure 6.7** and **Table 6.4** (obtained from the conversion of the particle size distribution in volume), HAp particles with a mean size (d_{50}) of 77 nm were obtained at the residence time $\tau = 0.4$ and 3.3 min, for the meso-OFR and the scaled-up meso-OFR, respectively. Indeed, for higher liquid flow rates, Reynolds numbers are higher and mixing efficiency enhances. This results in a more homogeneous reaction medium and therefore in a more homogeneous distribution of supersaturation (Mersmann 1999; Günther and Jensen 2006; Wang et al. 2007), thus affecting size distribution of the particles (Mersmann 1999; Ying et al. 2008). When compared with the commercial HAp particles, originally submitted to granulometric separation, the HAp particles prepared at the lowest residence times (τ = 0.4 min for the meso-OFR and τ = 3.3 min for the scaled-up meso-OFR) have a smaller mean size (d_{50}) and a narrower size distribution (see **Table 6.4**). However, it is very important to underline that particles produced were directly obtained from the system without thermal treatment and without granulometric separation.

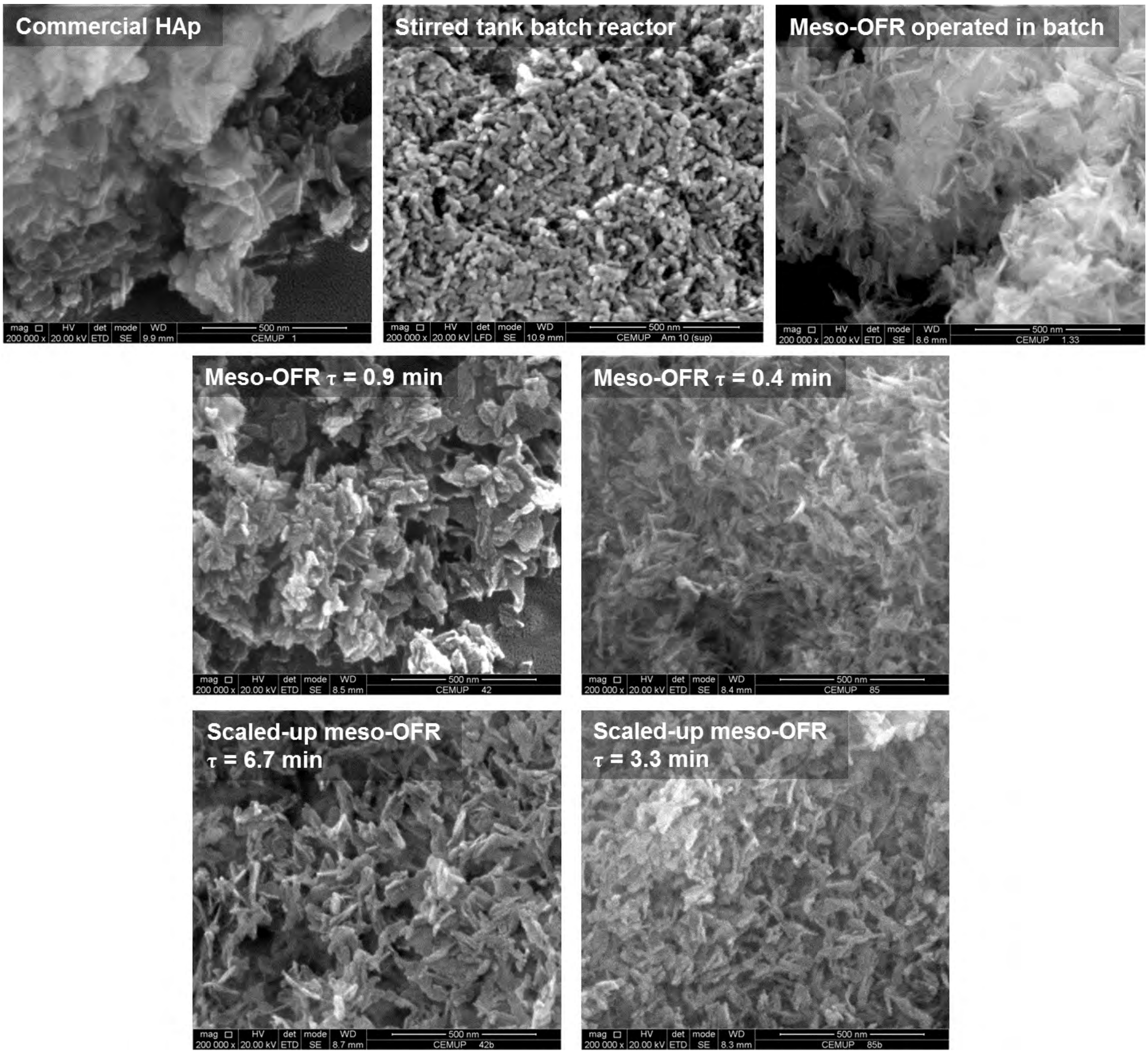

Figure 6.8. SEM images of the particles produced in the meso-OFR and scaled-up meso-OFR operated in continuous for different operating conditions.

Figure 6.8 shows two types of particles for the residence time τ = 0.9 and 6.7 min, for the meso-OFR and the scaled-up meso-OFR, respectively: ones with a rod-like shape and others with a plate-shape. Regarding particles produced at τ = 0.4 and 3.3 min, morphology seem more uniform and particles apparent to be mostly rod-like shaped. As already said, mixing is more efficient for higher Reynolds numbers, providing more homogeneous reaction conditions (Mersmann 1999; Günther and Jensen 2006; Wang et al. 2007), and improving thus the monodispersity of synthesized nanoparticles (Jähnisch et al. 2004; Hung and Lee 2007; Kockmann et al. 2008; Song et al. 2008).

Based on the above-mentioned results, the feasibility of the meso-OFR and the scaled-up meso-OFR was demonstrated for the continuous production of uniform HAp nanoparticles. In both the meso-OFR and the scaled-up meso-OFR operated in continuous, single-phase HAp nanoparticles with a mean size (d_{50}) of 77 nm and a narrow size distribution were obtained.

6.3.4 Comparison between the HAp particles obtained in the different reactors studied

According to**Table 6.2**, experiments carried out in the different reactors were all conducted under near-physiological conditions of temperature and pH. Besides, the mass of precipitate per mL obtained in the different reactors is similar. However, one can note that the meso-OFR was operated at a shorter residence time when compared with the stirred tank batch reactor.

Diffraction patterns (see **Figure 6.3** and **Figure 6.4**) indicate that the HAp prepared in the meso-OFR operated in batch and in continuous is single phased HAp with a higher crystallinity degree compared with the HAp prepared in the stirred tank batch reactor.

From **Figure 6.5**, there is no major difference between FTIR spectra of the particles obtained in the meso-OFR operated in both batch and continuous modes, and in the scaled-up meso-OFR operated in continuous. On the other hand, FTIR spectrum of the particles prepared in the stirred tank batch reactor possess broader peaks, especially the phosphate characteristic bands at 900-1200 cm^{-1}, suggesting the formation of a more amorphous phase. Besides, carbonate contamination seems to be minimized in the meso-OFR and the scaled-up meso-OFR, as CO_3^{2-} bands are barely detected in spectra of the particles produced in the meso-OFR and in the scaled-up meso-OFR.

Figure 6.6, **Figure 6.7**, **Table 6.3** and **Table 6.4** show that the as-prepared powders are mainly formed by particles at the nanometer range, for all the reactors and operating conditions studied. According to **Table 6.4**, the size distributions in number of the as-prepared particles in the meso-OFR are narrower than the size distribution in number of the particles obtained in the stirred tank batch reactor, and even than the size distribution in number of the commercial HAp powder. It is important to underline that the particles produced were directly obtained from the system without thermal treatment and without granulometric separation, while commercial HAp was originally submitted to granulometric separation.

As shown in **Figure 6.8**, the reactor type and the residence time affect the morphology of the as-prepared HAp nanoparticles. HAp particles obtained in the stirred tank batch reactor seem rod-like shaped and rather amorphous, while both plate-shaped and rod-like shaped HAp particles were produced in the meso-OFR and the scaled-up meso-OFR. However, the HAp particles precipitated in both the meso-OFR and the scaled-up meso-OFR operated in continuous mode for the lowest residence times (τ = 0.4 min for the meso-OFR and τ = 3.3 min for the scaled-up meso-OFR), only exhibit a rod-like shape. Besides, particles seem to have a more defined shape compared with the particles prepared in the stirred tank batch reactor.

Based on the aforementioned results, the reactor type affects the crystallinity, carbonate content, morphology, size, size distribution and aggregation degree of the as-prepared HAp nanoparticles. The proposed continuous reactors offer an alternative mixing mechanism (known as the oscillatory flow mixing) (Chew and Ristic 2005; Reis 2006), which provides intense and fast mixing, favoring thus the formation of small and uniform nanoparticles, as well as well-defined and reproducible conditions for the production of particles with consistent characteristics. Further, they provide an interesting platform for continuous high throughput screening due to their small volume (millilitre).

6.4 Conclusion

Continuous-flow precipitation of HAp was investigated in the meso-OFR and in the scaled-up meso-OFR. Calcium-deficient and/or carbonated HAp nanoparticles were successfully produced in both reactors. The influence of the residence time on HAp particles size and size distribution was also studied. For both reactors, it was found that the mean particle size and the aggregation degree of the particles decrease with the decrease of the residence time. In addition, HAp particles more uniform in size were precipitated for both the meso-OFR and the scaled-up meso-OFR at the lower residence times. Single-phase HAp nanoparticles with a mean size (d_{50}) of 77 nm and a narrow size distribution were obtained in both the meso-OFR and the scaled-up meso-OFR. Furthermore, the precipitated HAp particles show improved quality, namely in terms of size and size distribution, when compared with a commercial HAp powder and HAp particles prepared in the stirred tank batch reactor. Thus, the proposed scaled-up meso-OFR may be useful as a high throughput screening tool, namely for performing reactions which require longer reaction times.

In summary, the present study demonstrates the capability of a meso-OFR and a scaled-up meso-OFR for the continuous production of HAp nanoparticles, taking advantage of both oscillatory flow mixing and continuous operation.

6.5 References

Bernard, L, M Freche, J.L Lacout, and B Biscans. 2000. “Modeling of the Dissolution of Calcium Hydroxyde in the Preparation of Hydroxyapatite by Neutralization.” *Chemical Engineering Science* 55 (23): 5683–5692.

Chew, C. M., and R. I. Ristic. 2005. “Crystallization by Oscillatory and Conventional Mixing at Constant Power Density.” *AIChE Journal* 51 (5): 1576–1579.

Elliot, J.C. 1994. *Structure and Chemistry of the Apatites and Other Calcium Orthophosphates*. Amsterdam: Elsevier.

Günther, A., and K. F Jensen. 2006. “Multiphase Microfluidics: From Flow Characteristics to Chemical and Materials Synthesis.” *Lab on a Chip* 6 (12): 1487–503.

Harvey, A, M R Mackley, N Reis, J A Teixeira, and A. A. Vicente. 2003. “Fluid Mixing and Particle Suspension in a Novel Microreactor.” 30th International Conference of Slovak Society of Chemical Engineering, (2003) 26–30.

Hung, Lung-hsin, and Abraham Phillip Lee. 2007. “Microfluidic Devices for the Synthesis of Nanoparticles and Biomaterials.” *Journal of Medical and Biological Engineering* 27 (1): 1–6.

Johannsen, K., and S. Rademacher. 1999. “Modelling the Kinetics of Calcium Hydroxide Dissolution in Water.” *Acta Hydrochimica Et Hydrobiologica* 27 (2): 72–78.

Jones, A., S. Rigopoulos, and R. Zauner. 2005. “Crystallization and Precipitation Engineering.” *Computers & Chemical Engineering* 29 (6): 1159–1166.

Jongen, N., M. Donnet, P. Bowen, J. Lemaître, H. Hofmann, R. Schenk, C. Hofmann, et al. 2003. “Development of a Continuous Segmented Flow Tubular Reactor and the ‘Scale-out’ Concept - In Search of Perfect Powders.” *Chemical Engineering and Technology* 26: 303–305.

Jähnisch, K., V. Hessel, H. Löwe, and M. Baerns. 2004. "Chemistry in Microstructured Reactors". *Angewandte Chemie International Edition* 43: 406-446.

Kockmann, N, J Kastner, and P Woias. 2008. “Reactive Particle Precipitation in Liquid Microchannel Flow.” *Chemical Engineering Journal* 135: S110–S116.

Koutsopoulos, S. 2002. “Synthesis and Characterization of Hydroxyapatite Crystals: a Review Study on the Analytical Methods.” *Journal of Biomedical Materials Research* 62 (4): 600–12.

Kumta, P. N, C. Sfeir, D.-H. Lee, D. Olton, and D. Choi. 2005. "Nanostructured Calcium Phosphates for Biomedical Applications: Novel Synthesis and Characterization." *Acta Biomaterialia* 1 (1): 65–83.

Lawton, S., G. Steele, P. Shering, L. Zhao, I. Laird and X. Ni. 2009. "Continuous Crystallization of Pharmaceuticals Using a Continuous Oscillatory Baffled Crystallizer." *Organic Process Research & Development* 13 (6): 1357–1363.

Lopes, A. M., D. P. Silva, A. A. Vicente, A. Pessoa-Jr, and J. A. Teixeira. 2011. "Aqueous Two-phase Micellar Systems in an Oscillatory Flow Micro-reactor: Study of Perspectives and Experimental Performance." *Journal of Chemical Technology & Biotechnology* 86 (9): 1159–1165.

Luque de Castro, M D, and F Priego-Capote. 2007. "Ultrasound-assisted Crystallization (sonocrystallization)." *Ultrasonics Sonochemistry* 14 (6): 717–24.

Lynn, A.K., and W Bonfield. 2005. "A Novel Method for the Simultaneous, Titrant-Free Control of pH and Calcium Phosphate Mass Yield." *Accounts of Chemical Research* 38 (3): 202–207.

Ma, M.-G., and J.-F. Zhu. 2009. "Solvothermal Synthesis and Characterization of Hierarchically Nanostructured Hydroxyapatite Hollow Spheres." *European Journal of Inorganic Chemistry* (36): 5522–5526.

Mcmullen, J. P, and K. F Jensen. 2010. "An Automated Microfluidic System for Online Optimization in Chemical Synthesis." *Organic Process Research & Development* 14 (5): 1169–1176.

Mersmann, A. 1999. "Crystallization and Precipitation." *Chemical Engineering and Processing: Process Intensification* 38: 345–353.

Meskinfam, M, M S Sadjadi, and H Jazdarreh. 2012. "Synthesis and Characterization of Surface Functionalized Nanobiocomposite by Nano Hydroxyapatite" *International Journal of Chemical and Biological Engineering* 6: 192–195.

Ni, X, S Gao, R. H. Cumming and D. W. Pritchard. 1995. "A Comparative Study of Mass Transfer in Yeast for a Batch Pulsed Baffled Bioreactor and a Stirred Tank Fermenter." *Chemical Engineering Science* 50 (13): 2127–2136.

Ni, X, H Jian, and A W Fitch. 2002. "Computational Uid Dynamic Modelling of Ow Patterns in an Oscillatory Ba Ed Column." *Chemical Engineering Science* 57: 2849–2862.

Ni, X, J C Johnstone, K. C. Symes, B. D. Grey, and D. C. Bennett. 2001. "Suspension Polymerization of Acrylamide in an Oscillatory Baffled Reactor : from Drops to Particles." *AIChE Journal* 47 (8).

Ni, X., K.R Murray, Y. Zhang, D. Bennett, and T. Howes. 2002. “Polymer Product Engineering Utilising Oscillatory Baffled Reactors.” *Powder Technology* 124 (3): 281–286.

Ni, Xiongwei, Yann Sommer, De Gélicourt, John Neil, and Tony Howes. 2002. “On the Effect of Tracer Density on Axial Dispersion in a Batch Oscillatory Baffled Column.” *Chemical Engineering Journal* 85: 17–25.

Osaka, A., Y. Miura, K. Takeuchi, M. Asada, and K. Takahashi. 1991. “Calcium Apatite Prepared from Calcium Hydroxide and Orthophosphoric Acid.” *Journal of Materials Science: Materials in Medicine* 2 (1): 51–55.

Reis, N., A. Harvey, M. R. Mackley, A. A. Vicente, and J. A. and Teixeira. 2005. “Fluid Mechanics and Design Aspects of a Novel Oscillatory Flow Screening Mesoreactor.” *Chemical Engineering Research and Design* 83: 357–371.

Reis, N., A. A. Vicente, J. A. Teixeira, and M. R and Mackley. 2004. “Residence Times and Mixing of a Novel Continuous Oscillatory Flow Screening Reactor.” *Chemical Engineering Science* 59: 4967–4974.

Reis, Nuno Miguel Fernandes. 2006. “Novel Oscillatory Flow Reactors for Biotechnological Applications.”

Ristic, R. 2007. “Oscillatory Mixing for Crystallization of High Crystal Perfection Pharmaceuticals.” *Chemical Engineering Research and Design* 85 (7): 937–944.

Song, Yujun, J. Hormes, and C. S S R Kumar. 2008. “Microfluidic Synthesis of Nanomaterials.” *Small (Weinheim an Der Bergstrasse, Germany)* 4 (6): 698–711.

Tadic, D, F Peters, and M Epple. 2002. “Continuous Synthesis of Amorphous Carbonated Apatites.” *Biomaterials* 23 (12): 2553–9.

Wang, K, Y J Wang, G G Chen, G S Luo, and J D Wang. 2007. “Enhancement of Mixing and Mass Transfer Performance with a Microstructure Minireactor for Controllable Preparation of CaCO 3 Nanoparticles.” *Industrial & Engineering Chemistry Research* 46: 6092–6098.

Wang, L., and G. H Nancollas. 2008. “Calcium Orthophosphates: Crystallization and Dissolution.” *Chemical Reviews* 108 (11): 4628–69.

Ying, Y, G Chen, Y Zhao, S Li, and Q Yuan. 2008. “A High Throughput Methodology for Continuous Preparation of Monodispersed Nanocrystals in Microfluidic Reactors.” *Chemical Engineering Journal* 135 (3): 209–215.

Zhou, W., M. Wang, W. Cheung, B. Guo, and D. Jia. 2008. "Synthesis of Carbonated Hydroxyapatite Nanospheres Through Nanoemulsion." *Journal of Materials Science: Materials in Medicine* 10 (1): 103–110.

7 CONTINUOUS-FLOW PRECIPITATION OF HAp AT 37 °C IN TWO ULTRASONIC MICROREACTORS

The present chapter investigates the continuous-flow precipitation of HAp in two ultrasonic microreactors. Precipitation of HAp was first carried out in a tubular microreactor immersed in an ultrasonic bath, where single-phase (laminar) flow and segmented gas-liquid flow were both evaluated. The single-phase flow study was then conducted in a novel microfluidic device developed at MIT. It consists of a Teflon stack microreactor with an integrated piezoelectric element (Teflon microreactor), thereby allowing the direct transmission of ultrasound to the reactor. Rod-like shape HAp nanoparticles were yielded in both microreactors under near-physiological conditions of pH and temperature. The as-prepared particles, especially particles prepared in the segmented-flow tubular microreactor and in the Teflon microreactor, show improved characteristics compared to commercial powder or powder obtained in the stirred tank batch reactor. Primary particles are smaller, particle shape is more homogeneous, and the aggregation degree of the particles is lower.

7.1 Introduction

The application of microfluidic devices in chemical processes, namely in nanoparticles synthesis, is advantageous in many aspects, including enhanced transfer processes and mixing, high throughput experimentation, cost savings and safer operation. The main feature of the microreactors, in comparison to conventional chemical reactors, is their high surface-area-to-volume ratio (Jähnisch et al. 2004). This implies that heat and mass transfer distances are significantly reduced (Hartman and Jensen 2009), improving considerably heat and mass transport. Further, mixing times (down to several milliseconds) are generally smaller than in conventional systems, resulting in an efficient and rapid mixing of the reactants. This provides homogeneous reaction environments and allows thus a better control of the reaction steps that govern particle size distribution, i.e., nucleation and growth, thereby improving the monodispersity of synthesized nanoparticles (Jähnisch et al. 2004; Hung and Lee 2007; Kockmann et al. 2008; Song et al. 2008). Further, microreactors have the ability to operate within continuous flow regimes, which besides being more productive and able to promote more homogeneous reaction conditions, also permits the continuous variation of the chemical composition of the reaction medium (Song et al. 2008; Marre and Jensen 2010; Zhao et al. 2011). An additional advantage of continuous-flow synthesis is that scale-up is straightforward either by increasing the running time or by simply running reactions in parallel (Zhao et al. 2011). Finally, the intrinsic small volume of microreactors allows a reduction of energy costs, reagent consumption and waste generated, as well as improved safety from reduced consumption of hazardous chemicals and reagents (Hung and Lee 2007).

However, there are difficulties accompanying the handling of solids in microfluidics, such as transport behaviour (Hung and Lee 2007; Leng and Salmon 2008; Song et al. 2008) and channel clogging (Poe et al. 2006; Kockmann et al. 2008). Microreactors are usually characterized by geometries with a low Reynolds number. In such channels, laminar flow is dominant and is characterized by a parabolic velocity profile, leading to wide residence time distribution and thus to wide particle size distribution (**Figure 7.1**a). In this context, segmented-flow microreactors have been proved to narrow the residence time distribution by carrying out reactions in segmented liquid slugs, gas-liquid segmented-flow reactors being particularly attractive due to the simple separation process of the gas from the liquid (Günther and Jensen 2006; Khan and Jensen 2007; Zhao et al. 2011). The segmented gas is used to create recirculation and thus enhance mixing within an individual liquid slug (**Figure 7.1**b). In addition, in gas-liquid flow microreactors small liquid entities are separated from each other by gas bubbles (**Figure 7.1**b), hence reducing axial dispersion. These two effects provide a well-defined residence time, which in turn reduces particle size polydispersity (Zhao et al. 2011).

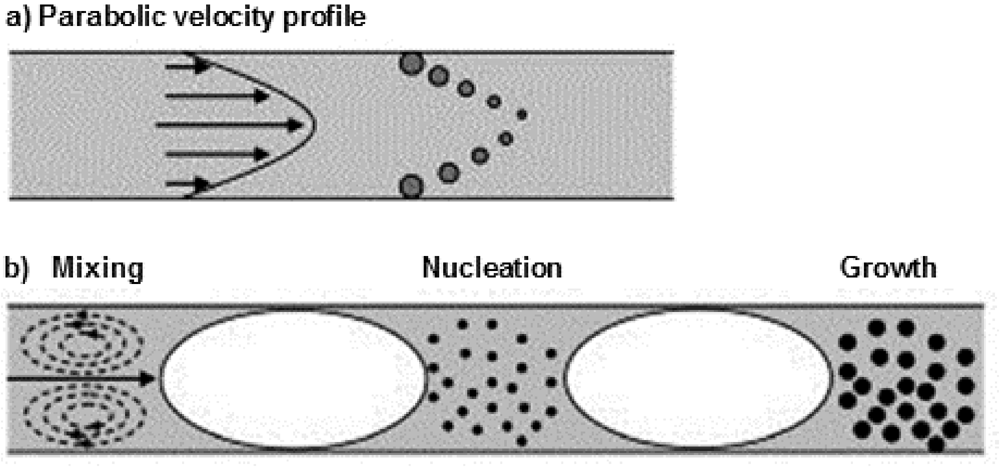

Figure 7.1. a) Schematic of parabolic velocity profile in continuous-flow microreactors and b) schematic of the flow pattern in segmented flow microreactors.

As to channel clogging, it is mainly caused by wall attachment of particles and by particle aggregation. In the first case, an accurate choice of the tube material and/or coating of the wall can solve the problem. In the case of particle aggregation, it can be significantly reduced by the use of ultrasound, as shock waves created by cavitation can shorten the contact time between particles and prevent their bonding together (Luque de Castro and Priego-Capote, 2007). The application of ultrasound produces stable cavitation by degassing the solvent (Mason 1964). The so generated pressure waves cause the particles to collide into one another with great force, promoting faster nucleation and aggregates breakage (Luque de Castro and Priego-Capote 2007). Therefore, the use of ultrasound provides a non-invasive (no added chemicals or additional mechanical treatment) way of improving crystal properties and process control.

In the present chapter, two ultrasonic microsystems were used for the synthesis of HAp nanoparticles. Initially, continuous-flow precipitation of HAp was carried out in a tubular microreactor immersed in an ultrasonic bath, where single-phase (laminar) flow and gas-liquid flow experiments were both performed. Continuous-flow precipitation of HAp in single-phase flow was then done in a novel microreactor made of Teflon plates, this time with the direct transmission of the ultrasound to the reactor through the integration of a piezoelectric actuator. Finally, the operating conditions, namely temperature, reactants concentration and mixing Ca/P molar ratio, were defined in order to promote spontaneous formation of HAp under near-physiological conditions of temperature and pH.

7.2 Materials and Methods

7.2.1 Description of the experimental set-ups

7.2.1.1 Ultrasonic tubular microreactor

Continuous-flow precipitation of HAp was carried out in a tubular microreactor (**Figure 7.2** and **Figure 7.3**a) immersed in an ultrasonic bath, where single-phase flow and gas-liquid flow studies were both performed. As it is exemplified in **Figure 7.2** and **Figure 7.3**a, the reactor is constituted by two main parts: a mixing chamber (Upchurch Scientific), with two different configurations depending on the flow type, a T-mixer for the single-phase flow (see **Figure 7.2**) and a cross-mixer for the gas-liquid flow (see **Figure 7.3**a); and the tubular reactor (Teflon PFA, Upchurch Scientific) itself of 600 μL, that consists of a spiral tube with 1.02 mm in inner diameter and 1.59 mm in external diameter. The function of the first part of the reactor is to mix thoroughly the reactants and in the case of the gas-liquid flow its function is also to segment the liquid mixture. The reaction progresses in the second part of the reactor. The segmented gas is used to separate the liquid phase in small entities (**Figure 7.3**b).

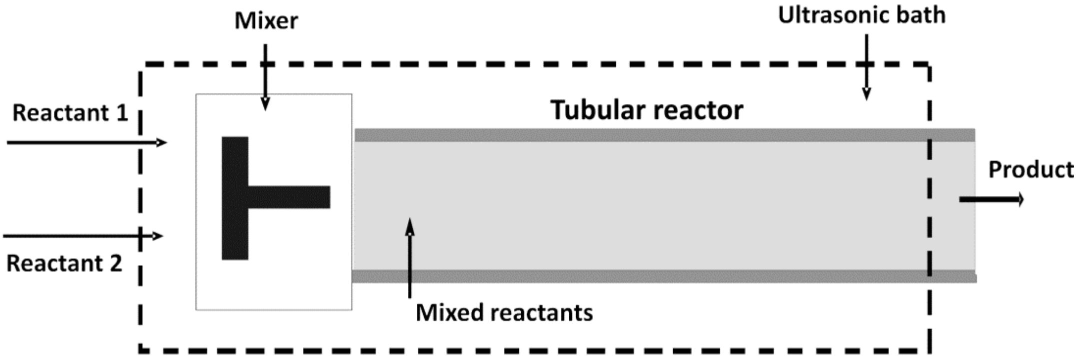

Figure 7.2. Schematic representation of the ultrasonic single-phase flow tubular microreactor.

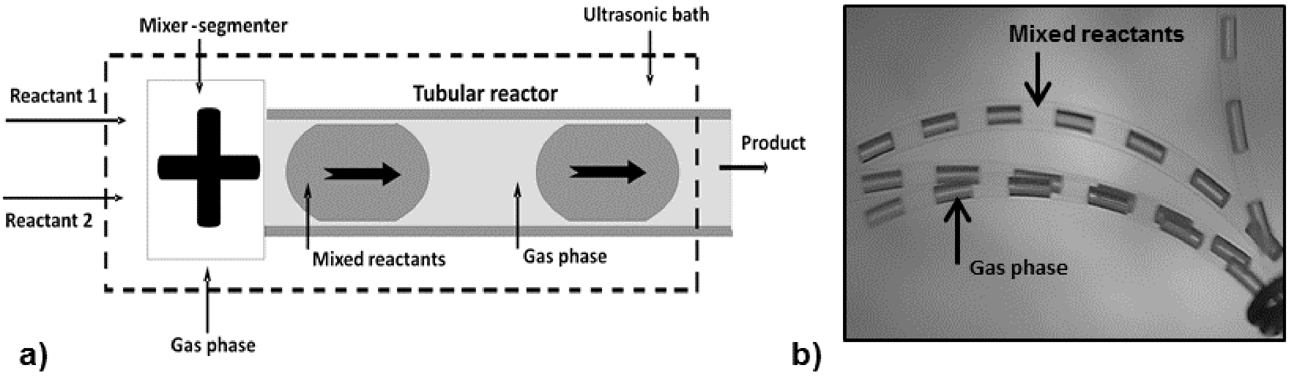

Figure 7.3. a) Schematic representation of the ultrasonic gas-liquid flow tubular microreactor; b) picture of a section of the gas-liquid flow tubular microreactor.

The reactants were fed into the set-up by means of a syringe pump (Harvard PHD 2000) and kept at 37 ºC through the use of thermal jackets (McMaster-Carr). With regard to the gas phase, the flow rate of nitrogen was adjusted by a mass flow controller (Sierra FlowBox). The microfluidic connections were provided by Teflon tubing (Upchurch Scientific) with 1.02 mm in inner diameter. The reactor was immersed in an ultrasonic bath (VWR model 50HT, frequency of 40 kHz and power input of 4-8 W) to minimize the potential for clogging the reactor and to enhance mixing. The experiments were started with a temperature of 37 ºC in the ultrasonic bath.

7.2.1.2 Teflon reactor

Continuous-flow precipitation of HAp was also carried out in a Teflon microreactor with integrated piezoelectric actuator developed at MIT (Massachusetts Institute of Technology) (**Figure 7.4**) (Kuhn et al. 2011). The microreactor is made of Teflon (PTFE) plates, with an integrated piezoelectric element with a thickness of 1 mm. The channel width is 600 µm and the total volume is 1000 µL. The system has two inlets and one outlet. The microfluidic connections were made of Teflon tubing (Upchurch Scientific) with 1.02 mm inner diameter. Reactants were mixed in a T-mixer (same mixing chamber used in the tubular microreactor for the single-phase study) (**Figure 7.5**) before entering in the reactor, and thus only one inlet was used. As in the previous systems, the reactants were fed into the reactor by means of a syringe pump (Harvard PHD 2000), where syringes were kept at 37 ºC through the use of thermal jackets (Upchurch Scientific).

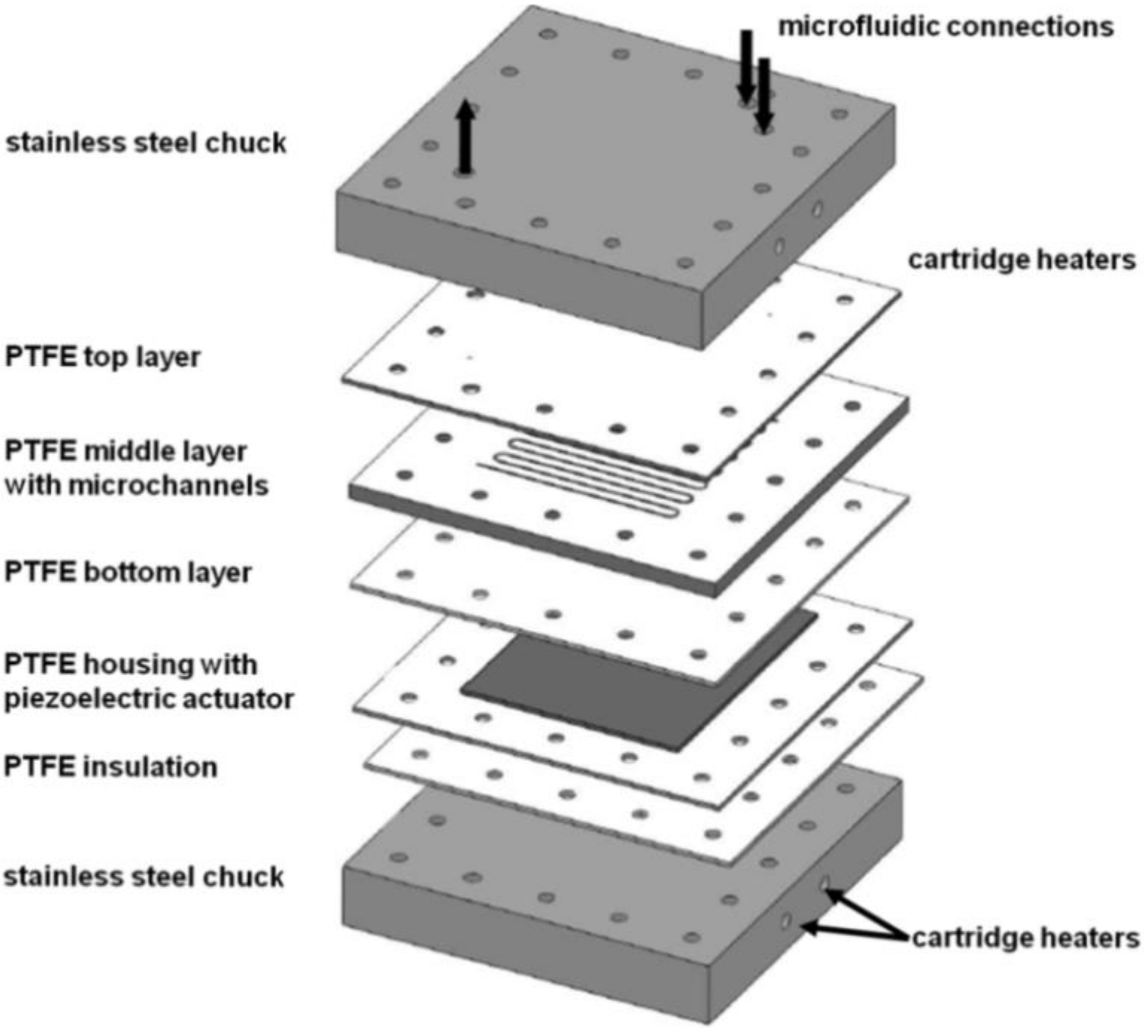

Figure 7.4. CAD representation of the microreactor assembly: The microreactor consists of 3 PTFE plates, with the middle layer providing the microchannel structure, and the top layer the inlet and outlet holes. The piezoelectric actuator is integrated using PTFE housing for mechanical stability and a PTFE layer for electrical insulation. These plates are compressed using two stainless steel chucks, with holes for the insertion of cartridge heaters, and the top chuck providing the microfluidic connections (Kuhn et al. 2011).

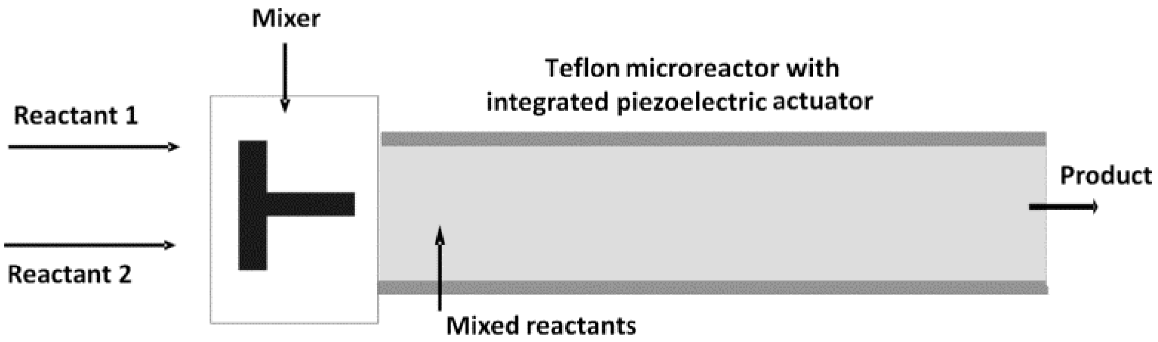

Figure 7.5. Schematic representation of the Teflon microreactor with integrated piezoelectric actuator.

7.2.2 Powder preparation

HAp was synthesized by the mixing of a saturated calcium hydroxide (Sigma-Aldrich, 95%) aqueous solution and an orthophosphoric acid (Mallinckrodt, 85%) aqueous solution at 37 ºC, with a mixing molar ratio Ca/P=1.33. Reactant solutions were prepared according to the protocol used on Chapter 3, section. The operating conditions used are presented in **Table 7.1**. Suspensions were collected after two to three residence times, until pH stabilization.

Temperature (J-KEM Scientific) and pH (needle-like tip micro pH electrode, Thermo Fisher Scientific ORION) were continuously measured at different time intervals at the outlet of the microsystem. The pH electrode was calibrated with two buffer solutions with pH=7.00 and pH=10.00 at 25 ºC.

Table 7.1. Operating conditions for the continuous-flow precipitation of HAp.

Sample	Flow type	Liquid flow rate (mL/min)	Gas flow rate (standard mL/min)	Liquid residence time τ (min)	[Ca(OH)$_2$] (M)	[H$_3$PO$_4$] (M)	Ca/P Molar ratio	Ultrasound frequency and power input
Tubular microreactor								
SPF 1	Single-phase flow	0.152	-	3.94	0.01926	0.01448	1.33	40 kHz and 4-8 W
SPF 2		0.304	-	1.97				
SPF 3		0.608	-	0.99				
SPF 4		2.0	-	0.30				
SPF 5		4.0	-	0.15				
GLF 1	Gas-liquid flow	0.152	1.2	0.43	0.01926	0.01448	1.33	
GLF 2		0.304	1.2	0.39				
GLF 3		0.608	1.2	0.34				
GLF 4		2.0	1.2	0.19				
GLF 5		2.0	2.0	0.15				
GLF 6		4.0	1.2	0.12				
GLF 7		4.0	4.0	0.08				
Teflon microreactor								
SPF 6	Single-phase flow	3.3	-	0.30	0.01926	0.01448	1.33	50 kHz and 30 W
Stirred tank batch reactor								
Batch	-	-	-	330	0.01926	0.01448	1.33	-

7.2.3 Powder characterization

Samples were withdrawn at the outlet of the microreactor, centrifuged (at 1500 rpm for 5 min), washed twice with ultra-pure water and conserved in ethanol (Koptec 200 proof pure), which stops the solid-liquid reaction (Bernard et al. 2000). For X-ray diffraction (XRD) (PanAlytical X'Pert PRO MPD) and scanning electron microscopy (SEM) (FEI Quanta 400FEG ESEM/EDAX Genesis X4M, with an accelerating voltage of 20 kV) and transmission electron microscopy (TEM) (HR-(EF)TEM JEOL, 2200FS / EDS Oxford, INCA Energy TEM 250) studies, suspensions were dried at T = 80 ºC during 24 h. As to SEM analysis, samples were covered by a 10 nm gold layer and for TEM analysis powders were suspended in ethanol and a small drop of the suspension was fixed on a support (Carbon film on 400 meshes, Monocomp). For FTIR spectroscopy (Bruker Vertex 70 with MCT detector), a small drop of the suspension was put on a 1 mm thick ZnSe support, dried (80 ºC) to evaporate the ethanol and then analyzed. Finally, for particle size distribution analysis, suspensions were collected at the end of each experiment and directly analyzed using a Malvern Mastersizer 2000 apparatus.

7.3 Results and Discussion

7.3.1 Important parameters in the precipitation of HAp

According to **Table 7.2**, experiments were conducted under near-physiological conditions of temperature and pH. An increase in the temperature value was however observed. This may be due to the continuous use of ultrasound. In fact, ultrasonic waves produce heat when passed through a substance due to the transfer of ultrasonic energy, making the maintenance of isothermal conditions difficult in the systems used. The problem is magnified in the Teflon microreactor, not only because of the higher power input but also because of the smaller area of irradiation (Pankaj and Ashokkumar 2010) as compared to the tubular microreactor immersed in the ultrasonic bath. In the case of the tubular microreactor, the emitted ultrasonic waves first need to cross the liquid inside the ultrasonic bath (e.g. water) before reaching the microreactor. Therefore, ultrasonication intensity inside the microreactor is lower than expected. In the Teflon microreactor, the acoustic waveform is directly transmitted to the reactor, being thus energetically more efficient and further allowing for a precise control of the operating frequency (Kuhn et al. 2011). A considerable increase in the temperature value was also observed in the tubular microreactor for the higher residence times. This is probably due to the longer exposition to ultrasound. Moreover, it should be noted that the precipitation reaction of HAp is exothermic, which also could explain the observed increase in the temperature. Thereby, the factors mentioned above may contribute to the temperature increase. Although the temperature variation may influence the characteristics of the final product (Martins et al. 2008), namely HAp solubility, no significant differences in the studied parameters are expected for most experimental conditions given the differences observed in the temperature. However, for some cases (SPF 1, GLF 1 and GLF 2) the increase in temperature is considerable and may affect the end product.

Table 7.2. Parameters measured during continuous-flow precipitation of HAp.

	Sample	**Liquid residence time τ (min)**	**pH**	**Precipitate (mg/mL)**	**Initial T (ºC)**	**Final T (ºC)**
Tubular microreactor	SPF 1	3.94	7.2	0.71	37.0	46
	SPF 2	1.97	6.7	1.34		42
	SPF 3	0.99	7.0	0.94		41
	SPF 4	0.30	7.2	1.13		38
	SPF 5	0.15	7.4	0.77		37.5
	GLF 1	0.43	7-7.5	0.81		52.6
	GLF 2	0.39	6.5-7	0.87		45.1
	GLF 3	0.34	6.5-7	1.30		41.3
	GLF 4	0.19	7-7.5	1.20		37.7
	GLF 5	0.15	7	1.22		37
	GLF 6	0.12	7-7.5	1.47		37
	GLF 7	0.08	7-7.5	1.39		37
Teflon microreactor with integrated piezoelectric actuator	Teflon-SPF	0.30	7.23	1.39	38.3	42.0
Stirred tank	Batch	330	6.9 [a]	0.91	36.7	37.9

7.3.2 Phase identification

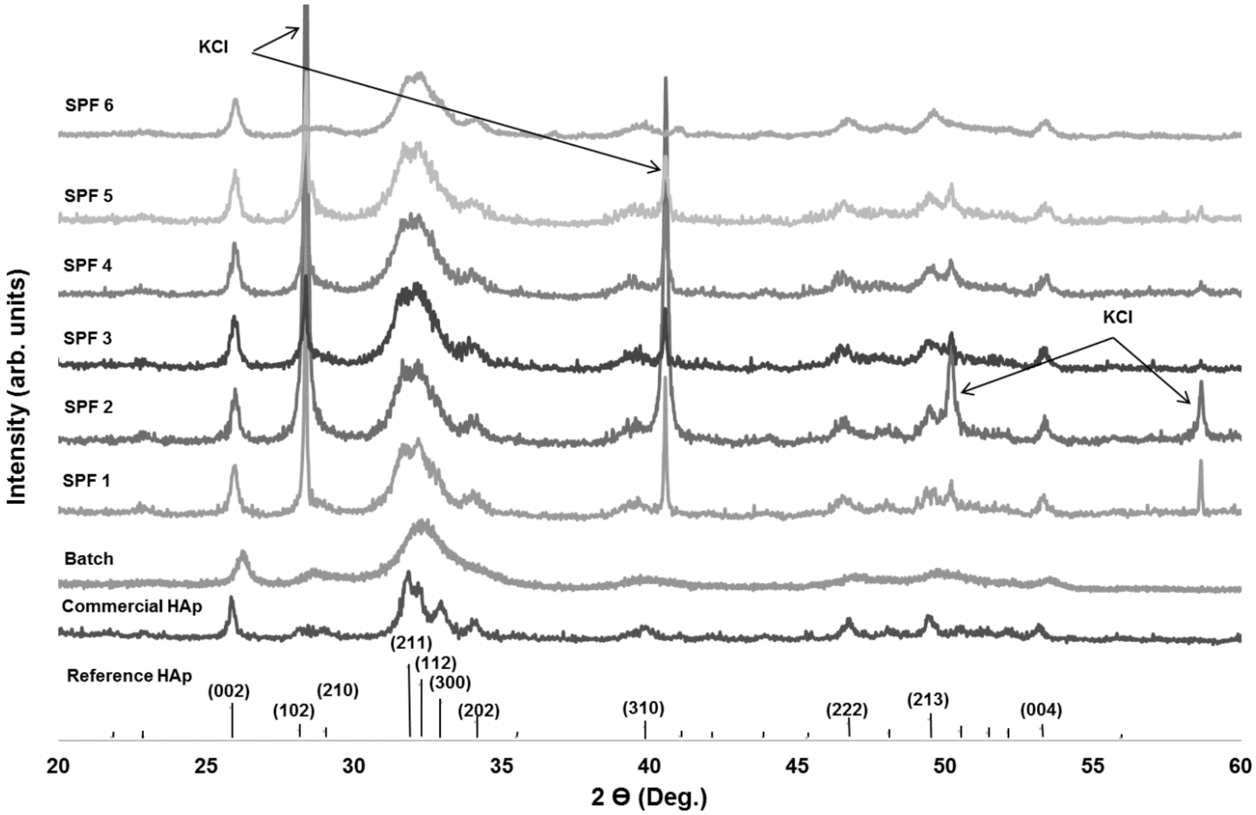

Figure 7.6. XRD patterns of the HAp particles produced in single-phase flow in the ultrasonic microreactors.

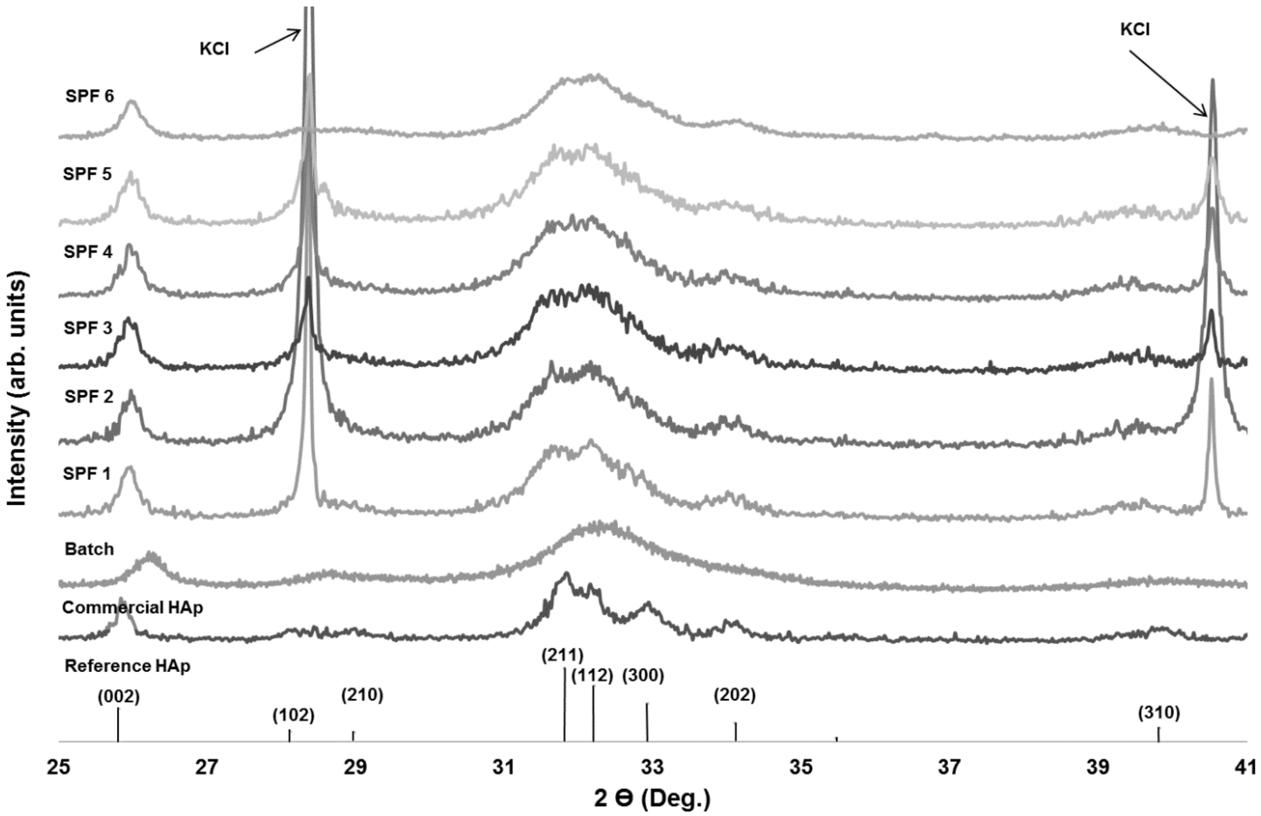

Figure 7.7. Magnified XRD patterns of the HAp particles produced in single-phase flow in the ultrasonic microreactors.

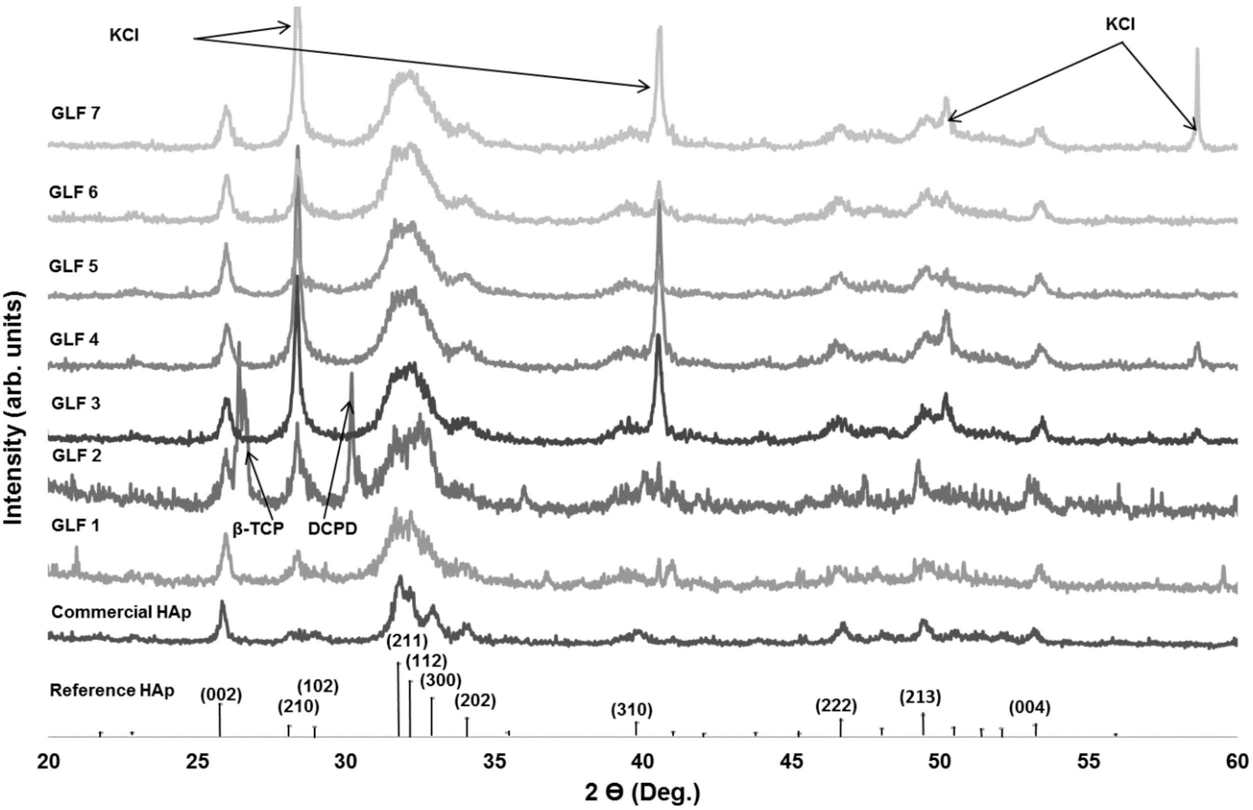

Figure 7.8. XDR patterns of the HAp particles produced in gas-liquid flow in the ultrasonic tubular microreactor.

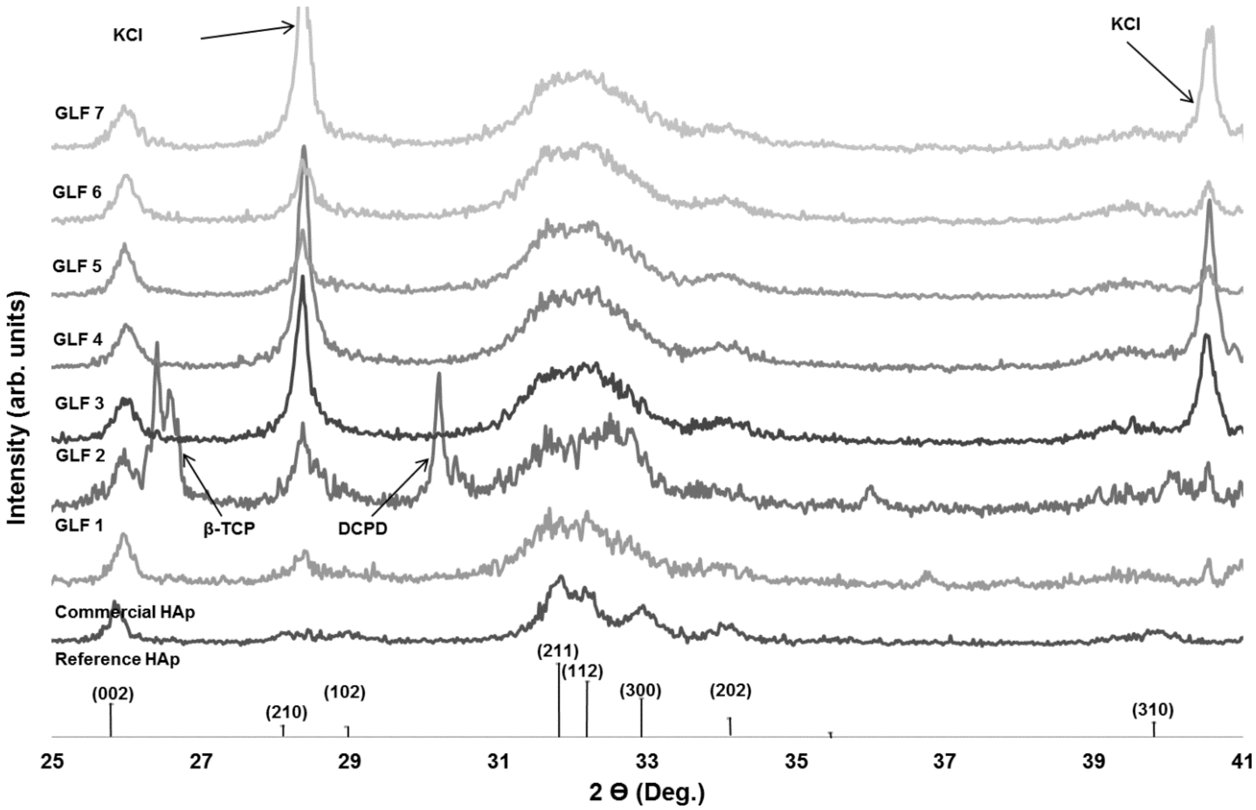

Figure 7.9. Magnified XDR patterns of the HAp particles produced in gas-liquid flow in the ultrasonic tubular microreactor.

XRD patterns of the as-prepared particles are shown in **Figure 7.6** and **Figure 7.8**. Besides, magnified diffraction patterns (**Figure 7.7** and **Figure 7.9**) show the dominant peaks. The diffraction patterns show characteristic peaks of HAp (JCPDS 9-0432), though GLF 2 pattern also exhibits peaks assigned to dicalcium phosphate dehydrate (DCPD) (JCPDS 9-77) and to beta-tricalcium phosphate (β-TCP) (JCPDS 9-169) (see **Figure 7.7** and **Figure 7.9**). XRD patterns of the products formed show broader peaks when compared to the pattern of a commercial HAp (Spectrum, minimum 40 meshes). This can suggest the presence of amorphous phases or considerably small size particles (Victoria and Gnanam 2002; Siddharthan et al. 2005). Further, diffraction patterns show sharp and high intensity peaks at 28 º2θ and 40.5 º2θ, unlike the commercial HAp pattern. Such peaks are characteristic of high crystallinity and large grain size. These peaks are assigned to potassium chloride and are observed in most of the samples' patterns. This may be explained by the occlusion of KCl. Indeed, part of the mother liquor could have been trapped between the aggregates, and the KCl contained in the mother liquor crystallized at the drying step. Regarding experiments performed under laminar flow (see **Figure 7.7**), there is no major difference between diffraction patterns of the powders obtained. The only difference observed is in the pattern of sample SPF-6, where KCl's peaks are barely detected. This may due to a lower degree of particle aggregation, as it will be seen later, allowing thus a better removal of the mother liquor during the washing step. In relation to powders prepared under segmented-flow (see **Figure 7.9**), the main differences between the precipitates are due to the presence of KCl peaks, which in some cases are barely detected, and the presence of peaks assigned to other calcium phosphate phases. As mentioned before, peaks assigned to DCPD and β-TCP are visible in the diffraction pattern of sample GLF 2. Despite HAp being thermodynamically the most stable calcium phosphate at the existing conditions, other calcium phosphates grow faster and therefore may appear. In these conditions the kinetic factors can assume a decisive role and may thus explain the formation of other calcium phosphates.

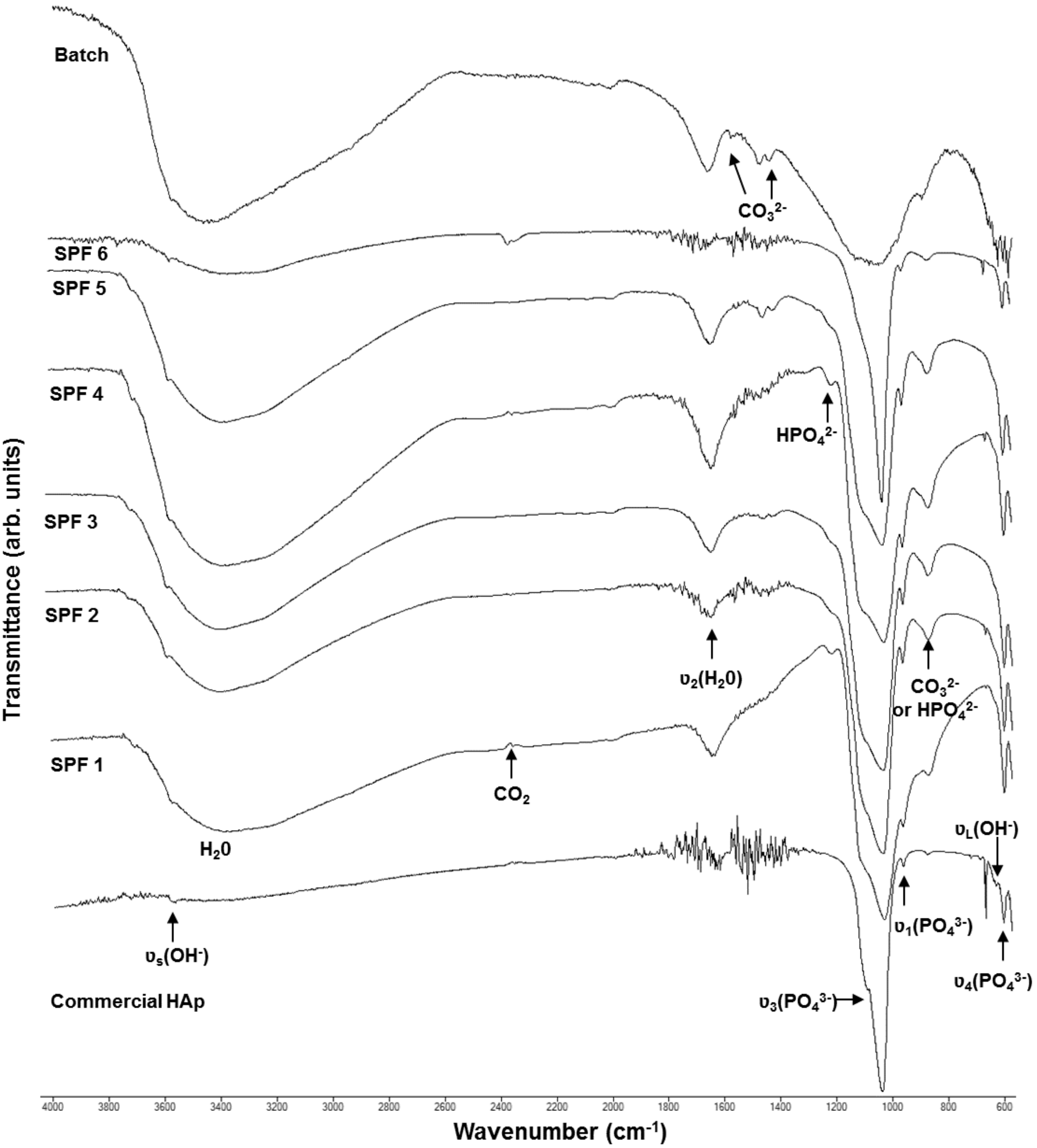

Figure 7.10. FTIR spectra of the HAp particles produced in single-phase flow in the ultrasonic microreactors.

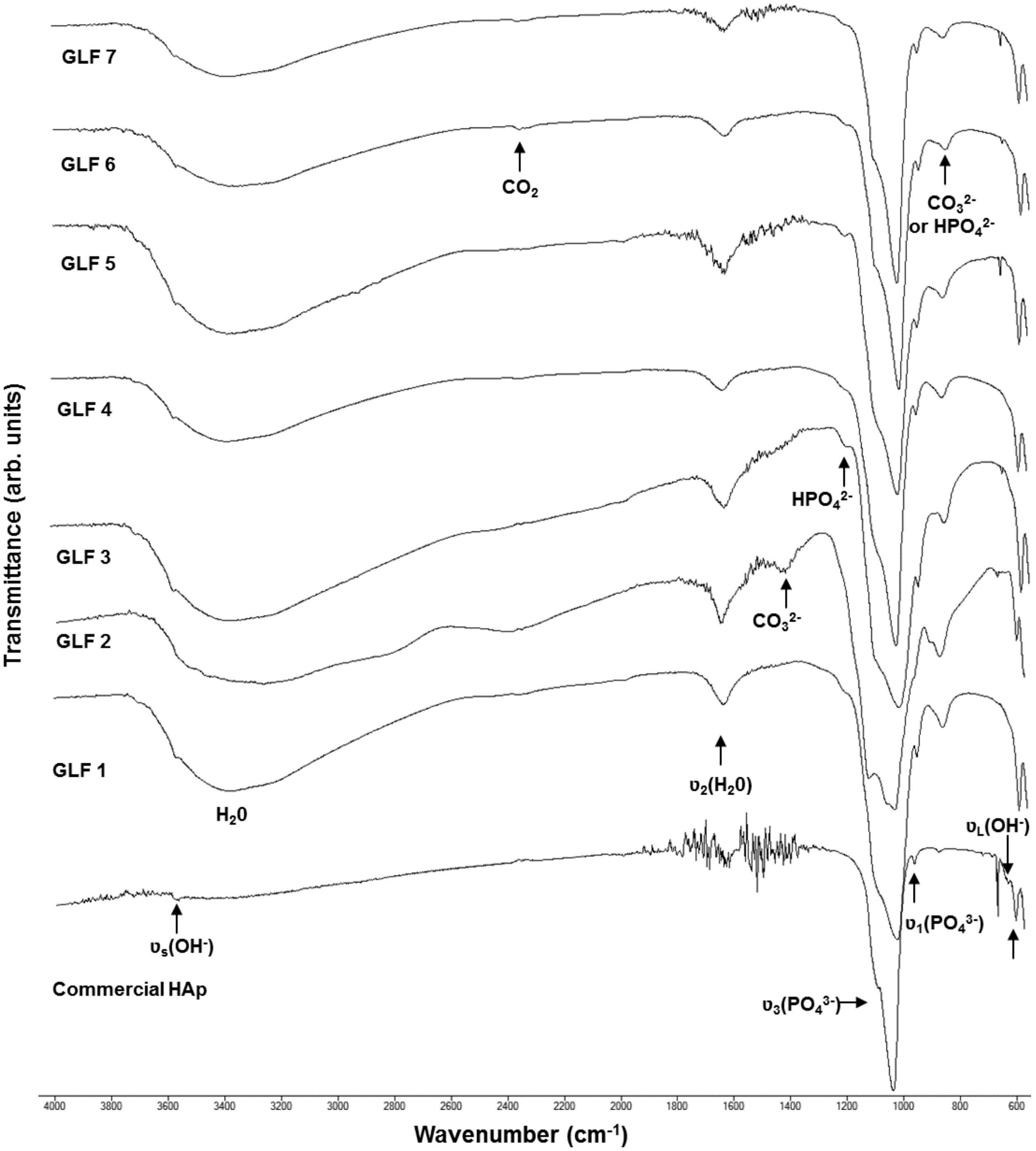

Figure 7.11. FTIR spectra of the HAp particles produced in gas-liquid flow in the ultrasonic tubular microreactor.

FTIR spectra of the as-prepared particles are given in **Figure 7.10** and **Figure 7.11**. All spectra exhibit the stretching and bending vibration modes of the phosphate and the hydroxyl groups, characteristic of a typical apatite structure (Koutsopoulos 2002). The peaks at 603 and 962 cm^{-1} indicate the presence of a υ_4 phosphate bending mode and a υ_1 phosphate stretching mode, respectively. The strong broad band around 1037 cm^{-1} confirms the presence of the υ_3 PO_4 mode. The sharp peaks at 630 (vibrational mode, υ_L) and 3571 cm^{-1} (stretching mode, υ_s) belong to the stretching vibrations of the hydroxyl group, although the peak attributed to the vibrational mode of OH^- is not clearly visible in most of the spectra. Presence of adsorbed water in the products formed is also verified, as a broad band from approximately 3700 to 3000 cm^{-1} and a peak at 1643 cm^{-1} are observed (Koutsopoulos 2002; Zhou et al. 2008). This may be justified by the low drying temperature (80 ºC) and the absence of a ripening (ageing) treatment (Osaka et al. 1991). The small band around 875 cm^{-1} can be attributed to the vibrational frequencies of carbonate ions or HPO_4^{2-} group (Koutsopoulos 2002), which is consistent with a carbonated HAp or calcium-deficient HAp. In some cases, spectra show a doublet at 1454 and 1428 cm^{-1} that confirms the CO_3^{2-} carbonate mode of vibration. These bands are characteristic of a carbonated HAp of B-type, where the carbonate ions occupy the phosphate ions sites (Koutsopoulos 2002; Landi 2003). The presence of carbonate ions can be explained by the absorption of CO_2 from air and water. Therefore, HAp formed seems to present characteristics similar to biological apatites, as they generally are considered calcium-deficient carbonated apatites (Kumta et al. 2005). In what concern sample GLF 2, a band attributed to DCPD (around 1110 cm^{-1}) is detected. In addition, υ_s hydroxyl stretching mode and υ_1 phosphate stretching mode are not clearly exhibited. Information on the crystallinity is also available by IR spectroscopy. It can be seen that the precipitates SPF 6 and GLF 7 are more crystalline when compared to the others precipitates, especially when observing the phosphate bands around 1000 cm^{-1}, which are broad and unresolved in the other samples, indicating poor crystallinity (Tadic et al. 2002). Moreover, the broad band corresponding to the adsorbed water (3700 to 3000 cm^{-1}) is much smaller than in the other spectra. The noise observed in almost all the spectra and especially in the commercial HAp spectrum (1800 to 1400 cm^{-1}) is due to water vapor.

7.3.3 Particle size, particle morphology and particle size distribution

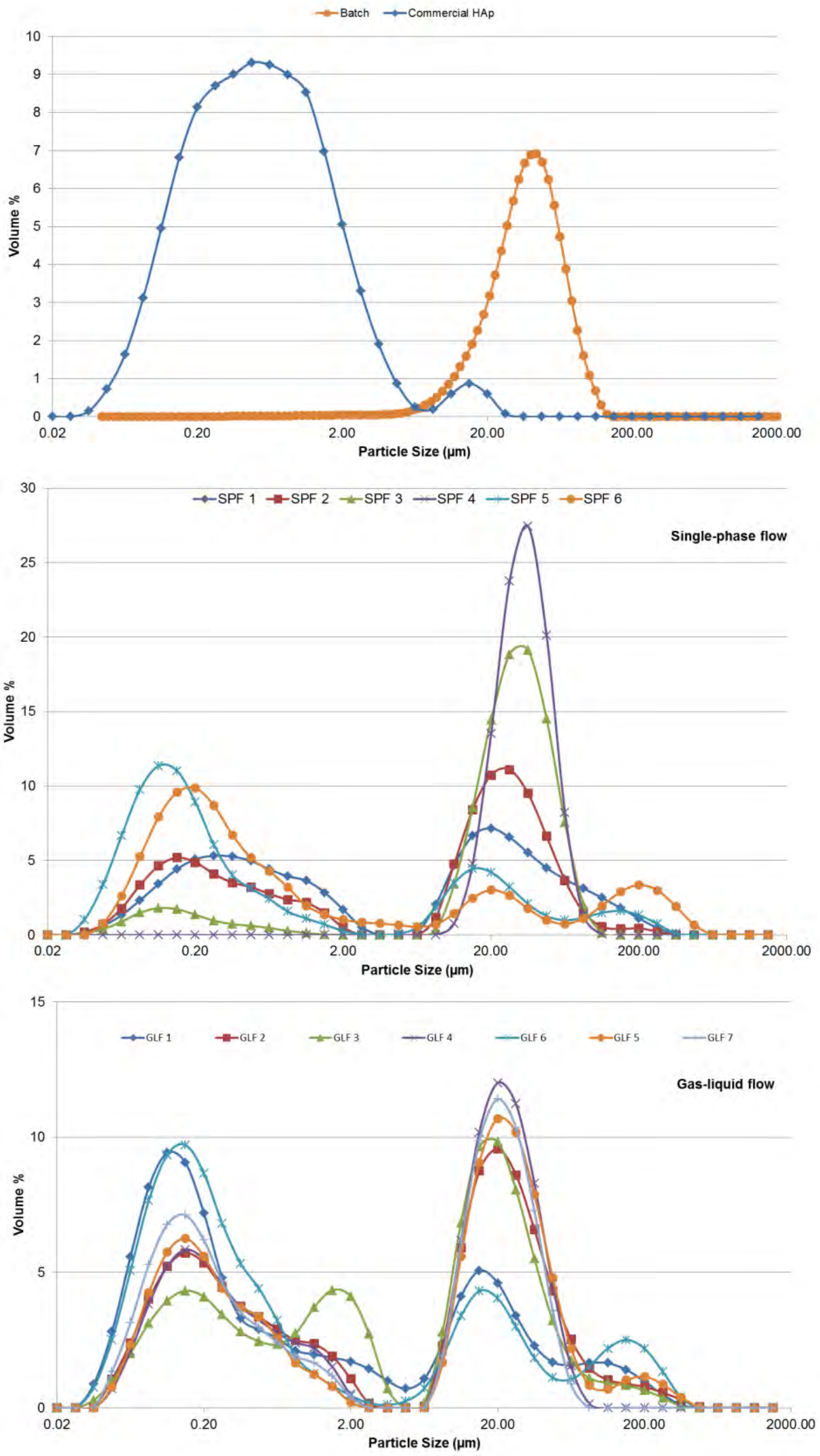

Figure 7.12. Size distribution in volume of the HAp particles produced in the ultrasonic microreactors.

Table 7.3. Parameters of the particle size distribution in volume of the powders produced in the ultrasonic microreactors and in the stirred tank batch reactor. d_{10}: 10% of the particles are smaller than this value, d_{50}: 50% of the particles are smaller than this value; d_{90}: 90% of the particles are smaller than this value; span: width of the distribution based on the 10%, 50% and 90% quantile.

Sample	**Particles size (µm)**			**Span**
	d_{10}	d_{50}	d_{90}	
SPF 1	0.15	1.24	43.42	34.90
SPF 2	0.14	16.96	54.20	3.19
SPF 3	0.60	32.29	62.83	1.93
SPF 4	22.59	38.30	62.70	1.05
SPF 5	0.08	0.25	38.97	155.56
SPF 6	0.09	0.33	136.67	413.88
GLF 1	0.09	0.42	44.56	105.88
GLF 2	0.13	12.23	53.00	4.32
GLF 3	0.15	10.35	44.23	4.26
GLF 4	0.14	13.90	40.94	3.96
GLF 5	0.13	14.88	52.33	3.51
GLF 6	0.09	0.35	87.26	249.06
GLF 7	0.11	10.76	37.67	3.49
Batch	15.48	36.22	68.11	1.45
Commercial HAp	0.15	0.59	2.44	3.88

As to particle size distribution in volume, for both segmented and laminar flows, a bimodal distribution (and in some cases trimodal distribution) has been obtained, except for powder SPF 4 (**Figure 7.12** and **Table 7.3**). The as-prepared powders consist of a population of primary particles in the nanometer range and a population of micrometric-sized aggregates that given the considerable difference in size could be separated. When compared to commercial HAp particles, the as-prepared powders possess smaller primary particles (see **Figure 7.12**). It is also important to underline that particles produced were directly obtained from the system without thermal treatment and without granulometric separation. In the case of precipitates produced in the single-phase flow tubular microreactor, it is clear that as the liquid flow rate increases the aggregation phenomenon is more pronounced, except for the higher liquid flow rate (see **Figure 7.12**). Smaller particles would be expected for higher liquid flow rates, since Reynolds numbers are higher and mixture efficiency enhanced. This results in a high degree of supersaturation and a more homogeneous medium (Mersmann

1999; Günther and Jensen 2006; Wang et al. 2007), which in its turn results in rapid nucleation and growth, favoring the formation of small particles (Mersmann 1999; Ying et al. 2008; Yang et al. 2010). However, smaller particles are more susceptible to aggregation than bigger particles at the same conditions, namely at the same ionic strength and pH conditions (He et al. 2007). In this case, smaller particles may have formed as the liquid flow rate increases, but aggregate later on given their small size. In what concerns flow segmentation, results show a larger primary particles population, when compared to the powders formed in single-phase flow (see **Figure 7.12** and **Table 7.3**). Analyzing parameters of the particle size distributions (see **Table 7.3**), one can see that d_{10} and d_{50} decrease with segmentation of the flow, approximating to the particle size distribution of the commercial HAp. A third population appears in some cases, consisting in large aggregates of about 200 µm, probably because primary particles are smaller and thus have higher tendency to aggregate.

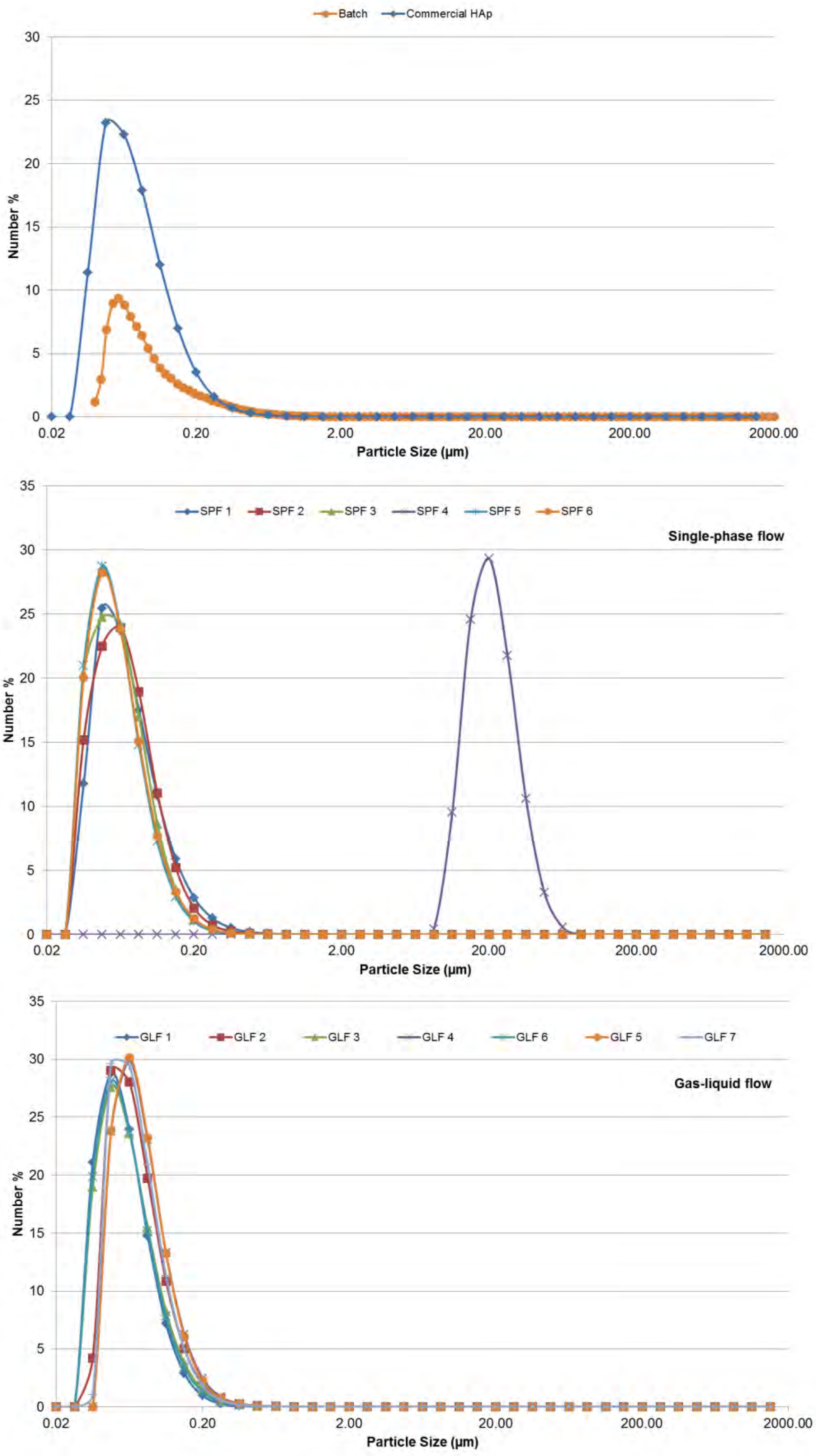

Figure 7.13. Size distribution in number of the HAp particles produced in the ultrasonic microreactors.

Table 7.4. Parameters of the particle size distribution in number of the powders produced in the ultrasonic microreactors and in the stirred tank batch reactor. d_{10}: 10% of the particles are smaller than this value, d_{50}: 50% of the particles are smaller than this value; d_{90}: 90% of the particles are smaller than this value; span: width of the distribution based on the 10%, 50% and 90% quantile.

Sample	Particles size (µm)			Span
	d_{10}	d_{50}	d_{90}	
SPF 1	0.034	0.056	0.118	1.50
SPF 2	0.033	0.056	0.108	1.37
SPF 3	0.031	0.051	0.097	1.30
SPF 4	11.26	17.65	30.42	1.09
SPF 5	0.031	0.048	0.091	1.25
SPF 6	0.031	0.049	0.095	1.31
GLF 1	0.031	0.637	2.07	3.20
GLF 2	0.038	0.057	0.107	1.22
GLF 3	0.031	0.050	0.099	1.37
GLF 4	0.041	0.061	0.113	1.18
GLF 5	0.041	0.061	0.111	1.16
GLF 6	0.031	0.049	0.096	1.32
GLF 7	0.039	0.058	0.107	1.17
Batch	0.047	0.074	0.209	2.18
Commercial HAp	0.034	0.058	0.130	1.64

However, it is possible to observe from the particle size distribution in number (**Figure 7.13** and **Table 7.4**) that the powders prepared are mostly constituted by nanoparticles. **Table 7.4** also shows that the parameters of the size distribution of the as-prepared particles are really close to the parameters of the particle size distribution of the commercial HAp. Besides, most of the powders present a narrow particle size distribution and in some cases even narrower than the particle size distribution of the commercial HAp.

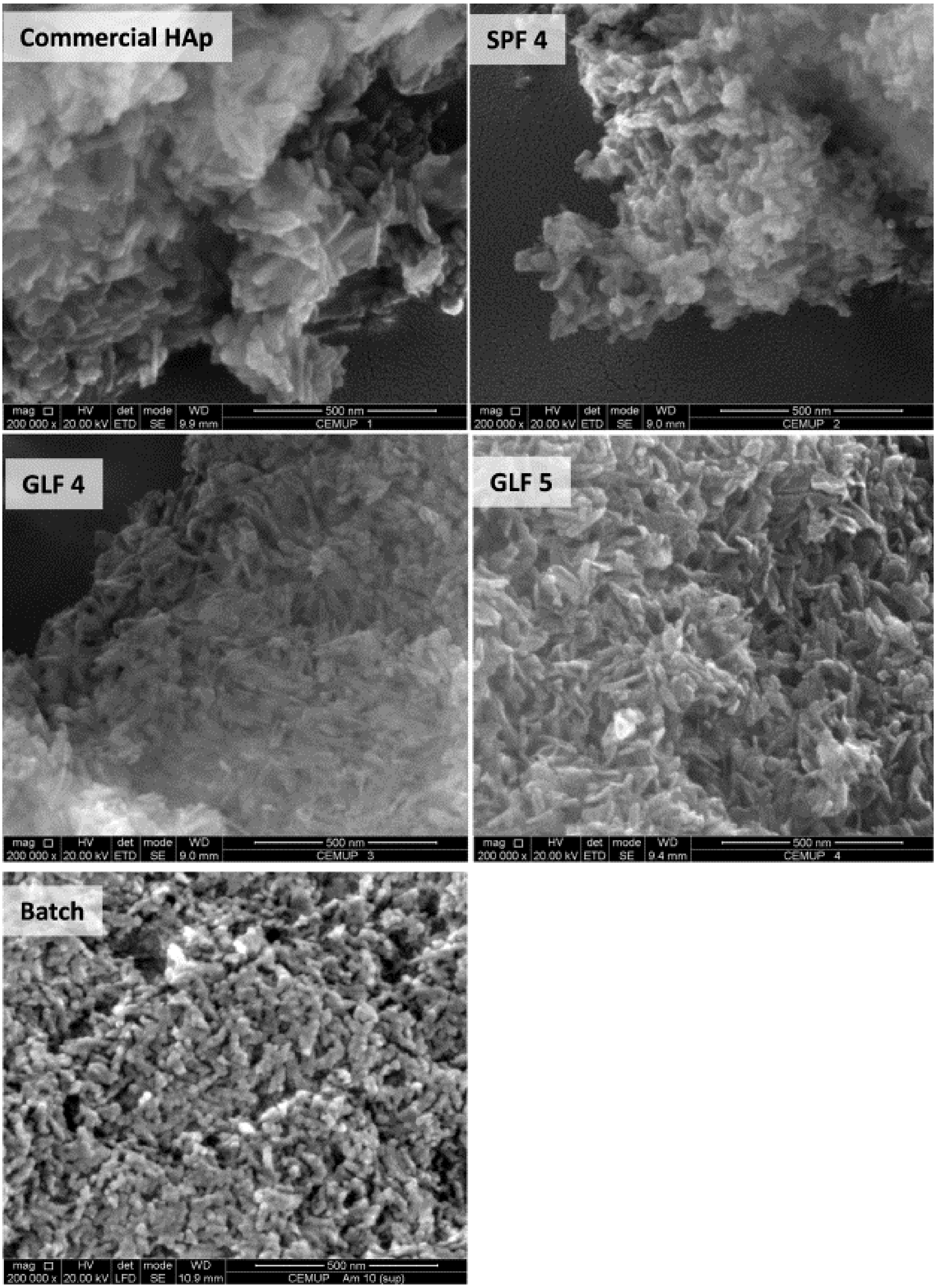

Figure 7.14. SEM images of the powders produced in the ultrasonic microreactors.

According to **Figure 7.14**, the powders prepared consist of rod-like shape and nanometric-sized particles. Primary particles are more easily seen for the powders prepared in the gas-liquid flow tubular microreactor (GLF 4 and GLF 5), when compared to commercial HAp particles and particles prepared in the single-phase flow tubular microreactor (SPF 4). Particles produced under segmented flow seem to have a more defined shape, while particles produced under laminar flow seem to be more amorphous and hence have higher tendency to form aggregates (see **Figure 7.14**). Indeed, using gas to create a segmented flow results in the formation of small reacting entities separated from each other by gas bubbles, which reduces particle-to particle interactions, and thus the formation of aggregates (Kuhn et al. 2011). Besides, the introduction of the gas phase creates recirculation and thus enhances mixing within the individual liquid slugs. This leads to a narrow residence time and reduced axial dispersion, resulting thereby in a high degree of supersaturation and a more homogeneous medium, favouring the formation of small and uniform particles (Günther and Jensen 2006; Mersmann 1999; Wang et al. 2007).

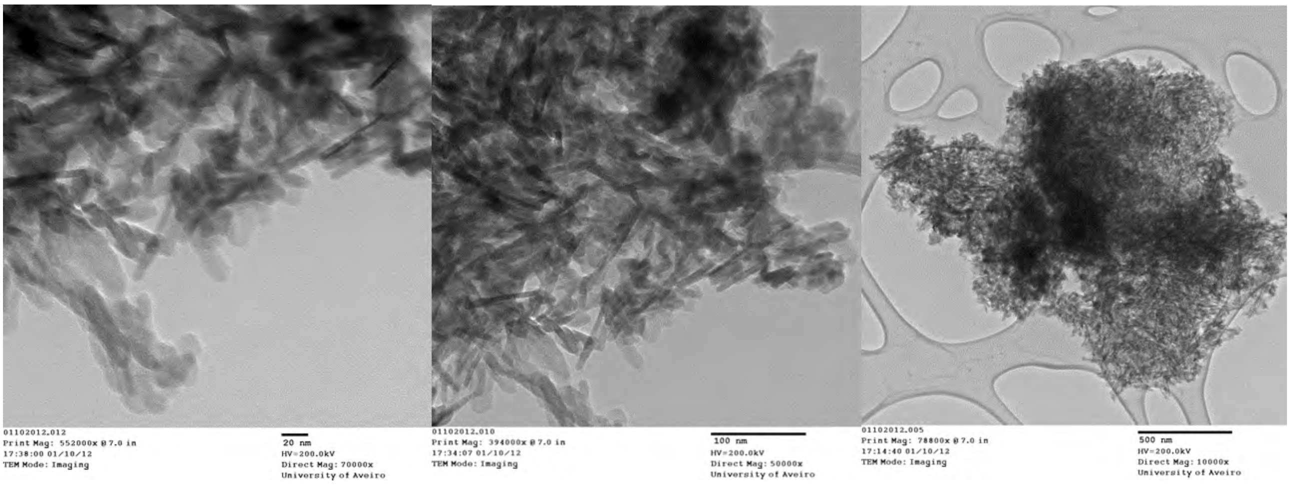

Figure 7.15. TEM images of the particles produced in the ultrasonic microreactors.

The microstructure of the HAp particles was also observed by TEM analysis (**Figure 7.15**). Primary particles seem uniform in size and shape, presenting less than 100 nm in length and around 20 nm in width, and a rod-like shape.

The as-prepared particles present therefore interesting characteristics for biomedical applications. Actually, nanocrystalline HAp powders exhibit greater surface area (Mobasherpour et al. 2007) when compared to microscale HAp. Moreover, it is desirable that the HAp for use in implants be bioresorbable so that it can be replaced, over a period of time, with regenerated bone upon implantation. In this context, nanoparticles of HAp have shown higher rates of bioresorbability than micrometric HAp and close to biological apatite

(Murugan and Ramakrishna 2005). Further, the resorbability of HAp can be developed with improving its crystallinity degree similar to biological HAp (60–70%) (Fathi et al. 2008).

7.3.4 Comparison between HAp particles prepared in a stirred tank batch reactor and in the ultrasonic microreactors

Particles synthesized in the stirred tank batch reactor appear to be less crystalline than the particles formed in the ultrasonic microreactors, since its XRD pattern and its FTIR spectrum exhibit broader peaks when compared to XRD patterns and FTIR spectra of the powders prepared in the microreactors (see **Figure 7.6** and **Figure 7.11**). Carbonate contamination seems to be minimized in the ultrasonic microreactors, as carbonate bands at approximately 1454 and 1428 cm^{-1} are clearly exhibited in the spectrum of the HAp powder prepared in batch and in most cases are not present in the spectra of the powders obtained in the microsystems (see **Figure 7.10** and **Figure 7.11**). Indeed, systems were not open to air and carbonate ions could only come from the water used in the preparation of the reagents.

According to **Figure 7.12** and **Figure 7.13**, the powder formed in the stirred tank batch reactor has higher primary particle size and wider particle size distribution when compared to HAp particles produced in the ultrasonic microreactors. Regarding morphology and size of the HAp particles, in all the reactors rod-like shape particles of about 100 nm long and 20 to 50 nm width were formed (see **Figure 7.14**).

7.4 Conclusion

Continuous-flow precipitation of HAp was studied in two ultrasonic microreactors, a tubular microreactor immersed in an ultrasonic bath and a Teflon microreactor with integrated piezoelectric actuator. All the samples prepared, irrespective of the system used, consisted of nano-size calcium-deficient carbonated HAp particles, thus approaching biological apatites. Moreover, particles were obtained under near-physiological conditions of pH and temperature, making them promising compounds for bone substitution application.

Several configurations were tested in the tubular microreactor (single-phase flow and gas-liquid flow), and segmentation of the flow was successful in reducing particle aggregation.

Control of particle aggregation was however best achieved in the Teflon microreactor, primarily due to the higher intensity of the ultrasound.

Synthesis products were also compared to the product obtained in the stirred tank batch reactor. The HAp particles formed have proved to be more crystalline and less carbonate contaminated than the HAp particles obtained in the stirred tank batch reactor. Moreover, microreactors used yielded HAp particles in a very short residence time and at a constant pH.

Finally, we believe that even if the reactor studied in this section does not represent a full scale production unit, it can be a useful contribution to the development of a platform for the continuous production of high quality HAp nanoparticles.

7.5 References

Bernard, L, M Freche, J.L Lacout, and B Biscans. 2000. “Modeling of the Dissolution of Calcium Hydroxyde in the Preparation of Hydroxyapatite by Neutralization.” *Chemical Engineering Science* 55 (23): 5683–5692.

Fathi, M, A. Hanifi, and V. Mortazavi. 2008. “Preparation and Bioactivity Evaluation of Bone-like Hydroxyapatite Nanopowder.” *Journal of Materials Processing Technology* 202 (1-3): 536–542.

Günther, A., and K. F Jensen. 2006. “Multiphase Microfluidics: From Flow Characteristics to Chemical and Materials Synthesis.” *Lab on a Chip* 6 (12): 1487–503.

Hartman, R. L, and K. F Jensen. 2009. “Microchemical Systems for Continuous-flow Synthesis.” *Lab on a Chip* 9 (17): 2495–507.

He, Y. Thomas, J. Wan, and T. Tokunaga. 2007. “Kinetic Stability of Hematite Nanoparticles: The Effect of Particle Sizes.” *Journal of Nanoparticle Research* 10 (2): 321–332.

Hung, L.-H., and A. P. Lee. 2007. “Microfluidic Devices for the Synthesis of Nanoparticles and Biomaterials.” *Journal of Medical and Biological Engineering* 27 (1): 1–6.

Jähnisch, K., V. Hessel, H. Löwe, and M. Baerns. 2004. "Chemistry in Microstructured Reactors." *Angewandte Chemie International Edition* 43: 406-446.

Khan, S. A, and K. F Jensen. 2007. “Microfluidic Synthesis of Titania Shells on Colloidal Silica.” *Advanced Materials* 19 (18): 2556–2560.

Kockmann, N, J Kastner, and P Woias. 2008. “Reactive Particle Precipitation in Liquid Microchannel Flow.” *Chemical Engineering Journal* 135: S110–S116.

Koutsopoulos, S. 2002. “Synthesis and Characterization of Hydroxyapatite Crystals: a Review Study on the Analytical Methods.” *Journal of Biomedical Materials Research* 62 (4): 600–12.

Kuhn, S., T. Noel, L. Gu, P. L. Heider, and K. F. Jensen. 2011. “A Teflon Microreactor with Integrated Piezoelectric Actuator to Handle Solid Forming Reactions.” *Lab on a Chip* 11 (15): 2488–2492.

Kumta, P. N, C. Sfeir, D.-H. Lee, D. Olton, and D. Choi. 2005. “Nanostructured Calcium Phosphates for Biomedical Applications: Novel Synthesis and Characterization.” *Acta Biomaterialia* 1 (1): 65–83.

Landi, E. 2003. “Carbonated Hydroxyapatite as Bone Substitute.” *Journal of the European Ceramic Society* 23 (15): 2931–2937.

Leng, J., and J.-B. Salmon. 2008. “Microfluidic Crystallization.” *Lab on a Chip* 9: 24–34.

Marre, S., and K. F. Jensen. 2010. “Synthesis of Micro and Nanostructures in Microfluidic Systems.” *Chemical Society Reviews* 39 (3): 1183–1202.

Martins, M. A., C. Santos, M. M. Almeida, and M. E. V. Costa. 2008. “Hydroxyapatite Micro- and Nanoparticles: Nucleation and Growth Mechanisms in the Presence of Citrate Species.” *Journal of Colloid and Interface Science* 318: 210–216.

Mason. 1964. *Physical Acoustics: Principles and Methods,*. New York: Academic Press.

Mersmann, A. 1999. “Crystallization and Precipitation.” *Chemical Engineering and Processing: Process Intensification* 38: 345–353.

Mobasherpour, I., M. S. Heshajin, A. Kazemzadeh, and M. Zakeri. 2007. “Synthesis of Nanocrystalline Hydroxyapatite by Using Precipitation Method.” *Journal of Alloys and Compounds* 430 (1-2): 330–333.

Murugan, R, and S Ramakrishna. 2005. “Aqueous Mediated Synthesis of Bioresorbable Nanocrystalline Hydroxyapatite.” *Journal of Crystal Growth* 274 (1-2): 209–213.

Osaka, A., Y. Miura, K. Takeuchi, M. Asada, and K. Takahashi. 1991. “Calcium Apatite Prepared from Calcium Hydroxide and Orthophosphoric Acid.” *Journal of Materials Science: Materials in Medicine* 2 (1): 51–55.

Pankaj, A., and M. Ashokkumar. 2010. *Theoretical and Experimental Sonochemistry Involving Inorganic Systems*. New York: Springer.

Poe, S. L., M. A. Cummings, M. P. Haaf, and D. T. McQuade. 2006. “Solving the Clogging Problem: Precipitate-Forming Reactions in Flow.” *Angewandte Chemie International Edition* 45 (10): 1544–1548.

Siddharthan, A, S K Seshadri, and T S Sampath Kumar. 2005. “Rapid Synthesis of Calcium Deficient Hydroxyapatite Nanoparticles by Microwave Irradiation .” *Trends in Biomaterials & Artificial Organs* 18 (2): 110–113.

Song, Y., J. Hormes, and C. S S R Kumar. 2008. “Microfluidic Synthesis of Nanomaterials.” *Small (Weinheim an Der Bergstrasse, Germany)* 4 (6): 698–711..

Tadic, D., F. Peters, and M. Epple. 2002. “Continuous synthesis of Amorphous carbonated apatites.” *Biomaterials* 23 (12): 2553–2559.

Victoria, E Caroline, and F D Gnanam. 2002. “Synthesis and Characterization of Biphasic Calcium Phosphate.” *Trends in Biomaterials & Artificial Organs* 16 (1): 12–14.

Wang, K, Y J Wang, G G Chen, G S Luo, and J D Wang. 2007. “Enhancement of Mixing and Mass Transfer Performance with a Microstructure Minireactor for Controllable Preparation of CaCO 3 Nanoparticles.” *Industrial & Engineering Chemistry Research* 46: 6092–6098.

Yang, Q., J.-X. Wang, L. Shao, Q.-A. Wang, F. Guo, J.-F. Chen, L. Gu, and Y.-T. An. 2010. “High Throughput Methodology for Continuous Preparation of Hydroxyapatite Nanoparticles in a Microporous Tube-in-Tube Microchannel Reactor.” *Industrial & Engineering Chemistry Research* 49: 140–147.

Ying, Y, G Chen, Y Zhao, S Li, and Q Yuan. 2008. “A High Throughput Methodology for Continuous Preparation of Monodispersed Nanocrystals in Microfluidic Reactors.” *Chemical Engineering Journal* 135 (3): 209–215.

Zhao, C.-X., L. He, S. Z. Qiao, and A. P.J. Middelberg. 2011. “Nanoparticle Synthesis in Microreactors.” *Chemical Engineering Science* 66 (7): 1463–1479.

Zhou, W., M. Wang, W. Cheung, B. Guo, and D. Jia. 2008. “Synthesis of Carbonated Hydroxyapatite Nanospheres Through Nanoemulsion.” *Journal of Materials Science: Materials in Medicine* 10 (1): 103–110.

8 CONCLUSION

This chapter presents the major conclusions of this thesis and recommendations for further research in this field.

8.1 Conclusions

The problem that was addressed in this thesis was finding out how to obtain hydroxyapatite (HAp) crystals with a precise controlled size, with a controlled (and narrow) size distribution and with high purity, rendering them suitable for bone substitution. Experimental studies conducted, as well as modeling of the HAp precipitation process, allow drawing some important conclusions. Firstly, this thesis refers to a simple and non-polluting method for the precipitation of nano-sized HAp particles with a narrow size distribution, under near-physiological conditions of temperature and pH. It provides an understanding of the mechanism of HAp formation and gives a good indication of the precipitation process chemistry over time. This thesis also explores the advantages of scaled-down reactors for process intensification and optimization of HAp nanoparticles production. To sum up, the work developed may be a valuable contribution for the development of a cost-effective platform for the continuous production of high quality HAp nanoparticles.

This work proposes a simple approach for the synthesis of HAp nanoparticles. It consists in preparing HAp from neutralization between diluted aqueous solutions of calcium hydroxide and orthophosphoric acid. Furthermore, HAp particles were produced under near-physiological conditions of pH and temperature, which is particularly relevant for the preparation of HAp for medical purposed. Indeed, it is important to follow specific criteria for pH and temperature in order to promote more conductive conditions for the survival of bone-related cells.

HAp precipitation was first carried out in a “conventional” stirred tank reactor provided with a new metal stirrer. The study provided information on the composition of the precipitate formed and on the precipitation process chemistry over time. Characterization of the HAp precipitation process, based on the variation of pH and calcium concentration with time, revealed the existence of three stages: spontaneous precipitation of amorphous calcium phosphate (ACP); transformation of ACP to HAp; and growth of HAp. The definition of the reaction system, based on mass balance and equilibrium equations, and calcium supersaturation, provided information on the chemical species present in solution over time. A satisfactory agreement between the predicted conductivity value by the proposed model and the experimental conductivity value was obtained, at the exception of the early moments of the precipitation process, where the proposed system was not adequate.

The advantages of a meso oscillatory flow reactor (meso-OFR) operated in batch over the stirred tank batch reactor for the production of uniform HAp nanoparticles under near-physiological conditions of pH and temperature were demonstrated. A constant power density was applied to both reactors and used as the reference criterion. The effectiveness of both mixing methods, for a given power input, was evaluated in terms of reaction time and characteristics of the precipitated particles. Based on the aforementioned results, the reactor type affects the crystallinity, carbonate content, morphology and size distribution of the prepared HAp nanoparticles. In the proposed meso-OFR, the alternative mixing mechanism (oscillatory flow mixing) generates intense eddy mixing, hence intensifying micromixing and promoting the formation of small and uniform HAp nanoparticles about four times faster when compared with the stirred tank batch reactor operated under a similar power density.

The capability of the meso-OFR and two ultrasonic microreactors for the continuous production of HAp nanoparticles under near-physiological conditions of pH and temperature was illustrated. Regarding the meso-OFR and the scaled-up meso-OFR, calcium-deficient carbonated HAp nanoparticles were successfully produced in both reactors. For both cases, it was found that the mean particle size and the aggregation degree of the particles decrease with the decrease of the residence time. In addition, particles more uniform in size were precipitated for both the meso-OFR and the scaled-up meso-OFR at lower residence times. The obtained results confirm the possibility of OFR scale-up by in series association of individual OFRs.

In relation to the two ultrasonic microreactors (a tubular microreactor immersed in an ultrasonic bath and a Teflon microreactor with integrated piezoelectric actuator), the prepared particles consisted of nano-size calcium-deficient carbonated HAp particles. Several configurations were tested in the tubular microreactor (single-phase flow and gas-liquid flow), and segmentation of the flow was successful in reducing particle aggregation. Control of aggregation was however best achieved in the Teflon microreactor, primarily due to the higher intensity of the ultrasound. Moreover, microreactors used yielded HAp particles in a very short residence time and at a constant pH. Finally, particle aggregation and primary particle size were significantly reduced in the segmented-flow tubular microreactor and especially in the Teflon microreactor.

Despite mixing mechanisms being different in all the reactors studied, and thereby hydrodynamic conditions being not directly comparable, the effectiveness of each reactor type was evaluated in terms of the characteristics (purity, size, size distribution, morphology) of the precipitated particles. In general, the microreactors used yielded HAp nanoparticles with improved characteristics, smaller primary particles, more homogeneous particle shape, lower aggregation degree, higher crystallinity and less carbonate contamination, when compared with the HAp nanoparticles produced in the stirred tank batch reactor, as well with a commercial HAp powder. Furthermore, they were operated in continuous, thus offering significant advantages in terms of process and costs, namely more uniform reaction environment, reduced costs and wasted materials. Although numerous advantages are associated with microreactors, going down also creates difficulties in product analysis. In this context, the meso-OFR offers advantages over the microreactors. The passage from μL to mL is useful for subsequent product evaluations. Besides, the aforementioned results show the capability of the meso-OFR in both batch and continuous operations for the production of uniform HAp nanoparticles.

Finally, we believe that even if the reactors studied do not represent a full-scale production unit, they may be a useful contribution to the development of a cost-effective platform for the production of high quality HAp nanoparticles.

8.2 Future work

The results documented in this research are significant and provide the basis for several research opportunities. The present thesis has dealt with reactive crystallization for HAp nanoparticles formation under near-physiological conditions of pH and temperature, and the importance of mixing in the determination of the size and size distribution of the HAp particles. It provides fundamental information on the mechanism of HAp formation and showed the feasibility of scaled-down reactors for the production of HAp particles with small size, narrow size distribution and uniform morphology, rendering them suitable for bone substitution application. Thus, this thesis provides a good background to go to the next steps and obtain more information about the characteristics of the prepared HAp particles and test different operating conditions to study how they affect particle size and size distribution.

Firstly, further product characterization, namely to evaluate the "biological" properties of the HAp particles, is recommended. The determination of the specific surface area of the prepared HAp nanoparticles could give an indication of the surface area that is available for the attachment of bone-related cells. It would also be interesting to evaluate the "biocompatibility" of the prepared HAp powders, by first investigating the cytotoxicity of the prepared powders over bone-related cells (osteoblasts) and then studying their ability for stimulating bone-related cells activity (cell adhesion/proliferation).

HAp precipitation was studied in the presence of KCl, added to adjust the ionic strength. Although apparently KCl does not significantly affect the process or the characteristics of the particles, it would be interesting to study the process without the presence of KCl and thus assess the characteristics of the obtained particles. In fact, it is known that the presence of KCl in the reaction medium can affect the solubility of HAp. Also, it would be important to assess the solubility of HAp in the operating conditions studied with and without the presence of KCl.

The influence of some of the operating parameters (initial Ca/P molar ratio, residence time, mixing conditions) on purity, size, size distribution and morphology of HAp particles was investigated. The initial insights aforementioned can be extended by studying the influence of other operating parameters such as the concentration of reagents and different hydrodynamic conditions. For instance, in the case of the stirred tank, the influence of stirring speed and the way reagents are mixed together can be investigated. Concerning the meso-OFR operated in batch, other amplitudes and frequencies can be studied. In relation to the meso-OFR and the microreactors operated in continuous, the study can be extended to other residence times.

Finally, once the meso-OFR was developed to suit some of the bioprocess applications requirements, namely reduce the high shear regions that may be crucial to some cell cultures, and once HAp particles were obtained under near-physiological conditions of pH and temperature, it would be interesting to apply the meso-OFR for bone-related cells growth in the presence of HAp particles. As further tasks, we recommend the optimization of the meso-OFR operating parameters, frequency (f) and amplitude (x_0), during bone-related cells growth. We also suggest assessing the functionality of the meso-OFR containing previously produced HAp particles in order to investigate the combined effect of dynamic conditions with the chemistry of the environment in the resulting cell function.

APPENDIXES

A.1 - Modeling of the HAp precipitation process at 37 °C in a stirred tank batch reactor – MATLAB application

The resolution of the system of equations resulting from the mass balance and equilibrium equations, as well as the calcium supersaturation, presented in Chapter 4, was done through the following MATLAB application:

```
clear all;

%*****************  PARAMETROS PARA CADA FICHEIRO  *********************
runi=input('Initial run:');
runf=input('Final run:');

for iei=runi:runf

%---------- LOAD THE DATA FILE --------

filenamein=['run', num2str(iei),'.txt'];
disp(['reading ' filenamein])
fid=fopen(filenamein,'r');
%z=[velocd Kla errorb Texp Tgas sat];
    [n1,n2,n3,n4,n5] = textread(filenamein,'%f %f %f %f %f',-1);
  m=1;
  k1=1e-14;
  k4=10.^(-11.984);
  k6=10.^(-6.337);
  k8=10.^(-1.288);
  CKCl=0.048; %KCl concentration, mol dm-3

 for i=1:size(n1);
 if n2(i,1)> 0 && n2(i,1)< 20 && n3(i,1)> 0 && n4(i,1)> 0 && n4(i,1)< 40 &&
n5(i,1)> 0 && n5(i,1)< 14

     n1a(m,1)=n1(i,1);%t(s)
     n2a(m,1)=n2(i,1)*.001;%k(S cm-1)
     n3a(m,1)=n3(i,1)/(1000*40.082);%[ca2+]mol/dm3
     n4a(m,1)=n4(i,1);%T(°C)
     n5a(m,1)=n5(i,1);%pH

     %Equilibrium constant, mol dm-3

     %k1(m,1)=10.^-(4471.33/(273.15+n4a(m,1))+.017053*(273.15+n4a(m,1))-
6.0846);
     k2(m,1)=10.^-(799.31/(273.15+n4a(m,1))-
4.5535+0.013486*(273.15+n4a(m,1)));
     k3(m,1)=10.^-(1979.5/(273.15+n4a(m,1))-
5.3541+0.019840*(273.15+n4a(m,1)));
     k5(m,1)=10.^(148.15-22188/(273.15+n4a(m,1))-0.2554*(273.15+n4a(m,1)));
     k7(m,1)=10.^(53.335-8413.5/(273.15+n4a(m,1))-
0.08660*(273.15+n4a(m,1)));
     ksp(m,1)=10.^-
(8219.41/(273.15+n4a(m,1))+1.6657+0.098215*(273.15+n4a(m,1)));
     %HAP Solubility - [Ca2+](ppm)
```

```
      SOL(m,1)=10.^(-0.0067*n5a(m,1)^4+0.2237*n5a(m,1)^3-
2.4647*n5a(m,1)^2+10.18*n5a(m,1)-15.545);

     %Supersaturation

     S(m,1)=((n3a(m,1)))/(SOL(m,1));

     m=m+1;
 end

 end



  for in=1:size(n1a);
      Y1(in,1)=1; Y2(in,1)=1; Y3(in,1)=1;
      for ji=1:20;
          %[H+]
          Ar(in,1)=10^(-n5a(in,1));
          %[OH-]
          Br(in,1)= k1/((Y1(in,1))^2*Ar(in,1));
          %[PO43-]

Fr(in,1)=((ksp(in,1)*(S(in,1))^9)/(n3a(in,1)^5*Y2(in,1)^5*Y1(in,1)*Br(in,1)
*Y3(in,1)^3))^(1/3);
          %[HPO42-]
          Er(in,1)=(Y3(in,1)*Y1(in,1)*Ar(in,1)*Fr(in,1))/(Y2(in,1)*k4);
          %[H2PO4-]
          Cr(in,1)= (Y2(in,1)*Ar(in,1)*Er(in,1))/k3(in,1);
          %[H3PO4]
          Dr(in,1)=((Y1(in,1))^2*Ar(in,1)*Cr(in,1))/k2(in,1);
          %[CaHPO4]
          Gr(in,1)=((Y2(in,1))^2*n3a(in,1)*Er(in,1))/k5(in,1);
          %[CaPO4-]
          Hr(in,1)=(Y2(in,1)*Y3(in,1)*n3a(in,1)*Fr(in,1))/(Y1(in,1)*k6);
          %[CaH2PO4+]
          Ir(in,1)=(Y2(in,1)*n3a(in,1)*Cr(in,1))/k7(in,1);
          %[CaOH]
          Jr(in,1)=(Y2(in,1)*n3a(in,1)*Br(in,1))/k8;
          %TCA
          Kr(in,1)= n3a(in,1)+Gr(in,1)+Hr(in,1)+Ir(in,1)+Jr(in,1);
          %TPO

Lr(in,1)=Cr(in,1)+Dr(in,1)+Er(in,1)+Fr(in,1)+Gr(in,1)+Hr(in,1)+Ir(in,1);
          %Ionic strength, mol dm-3

ION(in,1)=0.5*(Br(in,1)+Cr(in,1)+9*Fr(in,1)+4*Er(in,1)+Hr(in,1)+4*n3a(in,1)
+Ir(in,1)+Jr(in,1)+Ar(in,1)+2*CKCl);
          F1(in,1)=-(0.51*(ION(in,1))^(1/2))/(1+(ION(in,1))^(1/2));
          Y1(in,1)=10^(F1(in,1));
          Y2(in,1)=10^(4*F1(in,1));
          Y3(in,1)=10^(9*F1(in,1));
          %Conductivity, Scm-1
kcond(in,1)=(349.65*(Ar(in,1)*Y1(in,1))/1000+198*(Br(in,1)*Y1(in,1))/1000+3
6*(Cr(in,1)*Y1(in,1))/1000+2*57*(Er(in,1)*Y2(in,1))/1000+3*92.8*(Fr(in,1)*Y
3(in,1))/1000+2*59.47*(n3a(in,1)*Y2(in,1))/1000+73.48*CKCl/1000+76.31*CKCl/
1000)*1.2356;

      end
```

```
 end
end


%---------- Plotting --------

xmin=100;

for pl=xmin:size(n1a);
    ml=pl-xmin+1;
     n1pl(ml,1)=n1a(pl,1);%t(s)
     n2pl(ml,1)=n2a(pl,1);%k(S cm-1)
     n3pl(ml,1)=n3a(pl,1);%[ca2+]mol/dm3
     n4pl(ml,1)=n4a(pl,1);%T(°C)
     n5pl(ml,1)=n5a(pl,1);%pH
     kcondpl(ml,1)=kcond(pl,1);%Conductivity, Scm-1
end



subplot (2,1,1);[haxes, hline1, hline2]= plotyy(n1pl, n5pl, n1pl, n3pl);
xlabel('t(s)','Fontsize',8)
axes(haxes(1))
ylabel('pH','Fontsize',8)
axes(haxes(2))
ylabel('Ca2+(mol dm-3)','Fontsize',8)
%set(get(gca,'YLabel'),'Rotation',0.0)
title('\it{pH and Ca2+ variation}','Fontsize',12)

subplot (2,1,2); plot(n1pl, n2pl, n1pl, kcondpl)
legend ('Measured','Estimated')
xlabel('t(s)','Fontsize',8)
ylabel('k(S cm-1)','Fontsize',8)
title('\it{k variation}','Fontsize',12)

%---------- Save Data --------

z1=[n1a n2a n3a n4a n5a];
save(['CleanData_', num2str(runi),'.txt'],'z1','-ascii')
z2=[Ar Br Cr Dr Er Fr Gr Hr Ir Jr Kr Lr ION kcond SOL S];
save(['results_', num2str(runi),'.txt'],'z2','-ascii')
% clear all
```

A.2 - Calibration curve Abs *versus* pH

For the construction of the calibration curve Abs versus pH presented in Chapter 5, the following solutions with different pH were prepared:

Table A.1. Solutions with different pH prepared from equimolar aqueous solutions of $Ca(OH)_2$ and H_3PO_4.

Solution	**1**	**2**	**3**	**4**	**5**	**6**	**7**	**8**	**9**	**10**	**11**	**12**	**13**	**14**	**15**	**16**
V $CaOH_2$ 0,01926 M (mL)	10	8	6.7	6.3	6.2	6.1	6	5.9	5.8	5.7	5.5	5.3	5	4.5	4	3.5
V H_3PO_4 0.01926 M (mL)	0	2	3.3	3.7	3.8	3.9	4	4.1	4.2	4.3	4.5	4.7	5	6.5	6	6.5
pH (average)	12.30 ± 0.01	11.93 ± 0.01	11.40 ± 0.01	10.86 ± 0.03	10.38 ± 0.09	9.53 ± 0.17	8.51 ± 0.14	7.96 ± 0.03	7.62 ± 0.01	7.34 ± 0.02	7.06 ± 0.03	6.82 ± 0.03	6.59 ± 0.02	6.32 ± 0.02	5.95 ± 0.04	5.50 ± 0.02